Universitat Autònoma de Barcelona

# Epitaxial Ferroelectric Thin Films on Si(001): strain tuning of $BaTiO_3$ and stabilization of polar phase in $Hf_{0.5}Zr_{0.5}O_2$

**ADVERTIMENT.** L'accés als continguts d'aquesta tesi queda condicionat a l'acceptació de les condicions d'ús establertes per la següent llicència Creative Commons: 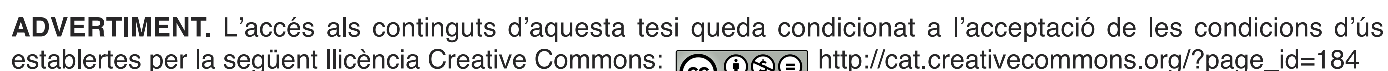 http://cat.creativecommons.org/?page_id=184

**ADVERTENCIA.** El acceso a los contenidos de esta tesis queda condicionado a la aceptación de las condiciones de uso establecidas por la siguiente licencia Creative Commons: http://es.creativecommons.org/blog/licencias/

**WARNING.** The access to the contents of this doctoral thesis it is limited to the acceptance of the use conditions set by the following Creative Commons license: 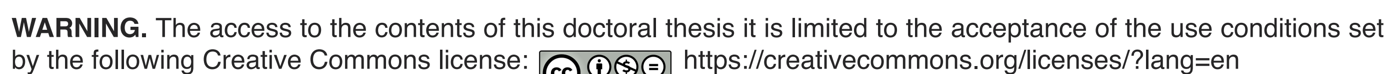 https://creativecommons.org/licenses/?lang=en

Universitat Autònoma de Barcelona

# Epitaxial Ferroelectric Thin Films on Si(001): strain tuning of $BaTiO_3$ and stabilization of polar phase in $Hf_{0.5}Zr_{0.5}O_2$

**Jike Lyu**

Doctoral Thesis

SUPERVISOR

Dr. Florencio Sánchez Barrera

Institut de Ciència de Materials de Barcelona (ICMAB-CSIC)

TUTOR

Prof. Javier Rodríguez Viejo

Universitat Autònoma de Barcelona

Department of Physics, Faculty of Science

Doctoral Program: Material Science

EXCELENCIA SEVERO OCHOA

CSIC

CONSEJO SUPERIOR DE INVESTIGACIONES CIENTÍFICAS

**Dr. Florencio Sánchez Barrera**, tenured scientist at the Institut de Ciència de Materials de Barcelona - Consejo Superior de Investigaciones Científicas, and **Prof. Javier Rodríguez Viejo**, full professor at Universitat Autònoma de Barcelona

CERTIFY

that **Jike Lyu** carried out under their direction the research work entitled "Epitaxial Ferroelectric Thin Films on Si(001): strain tuning of $BaTiO_3$ and stabilization of polar phase in $Hf_{0.5}Zr_{0.5}O_2$". This work has been developed within a PhD program in Materials Science at the department of physics of Universitat Autònoma de Barcelona.

For that record they sign the certificate.

Bellaterra, June 2019

Dr. Florencio Sánchez Barrera

Prof. Javier Rodríguez Viejo

# Acknowledgments

First and foremost, I would like to express my great gratitude to my research supervisor, Dr. Florencio Sánchez Barrera for giving me the opportunity working in ICMAB and Mulfox group. All of his patient guidance, scientific encouragement and fruitful discussions over these four years push me forward in the academic world of functional oxides. There is no thesis without him. Many thanks to Dr. Ignasi Fina for all the assistance in valuable discussions, and experimental measurements about ferroelectricity.

I would like to thank Prof. Josep Fontcuberta for valuable comments and discussions of my research results in group meetings during last four years and Dr. Gervasi Herranz for organizing these group meetings for me to practise and improve.

I also thank Dr. Mateusz Ścigaj for guiding me at the first month. Special thanks to Raul Solanas in PLD lab for all his collaboration on the extensive work of thin film growth. I also acknowledge Saúl Estandía and Dr. Jaume Gazquez for their work with TEM measurements and Dr. Nico Dix for samples preparation and AFM characterization. I want to present my gratitude to Dr. Fanmao Liu, Dr. Mengdi Qian, Yu Chen and Mathieu Mirjolet for their experimental assistance during these years. Furthermore, I also want to thank the other members in Mulfox group, namely Dr. Ferran Macià, Dr. Blai Casals, Dr. Rafael Cichelero, Dr. Mikko Kataja, Morteza Alizadeh, Milena Sulzbach, Marc Font, Xiao Long, Tingfeng Song and Yunwei Sheng for creating a friendly and comfortable academic environment.

I also acknowledge the support and help of the technicians from the scientific service in ICMAB, especially Anna Crespi, Javier Campos and Joan Esquius for the XRD measurements and knowledge sharing, and Maite Simón and Andrés Gómez for AFM measurements. Thank Romain Bachelet and Guillaume Saint-Girons from Institut des Nanotechnologies de Lyon (INL-CNRS) for providing the $SrTiO_3$ buffered Si wafers. Financial support from the Spanish Ministry of Economy, Competitiveness and Universities, through the "Severo Ochoa" Programme for Centres of Excellence in R&D (SEV-2015-0496) and the MAT2017-85232-R (AEI/FEDER, EU), and MAT2015-73839-JIN projects, and from Generalitat de Catalunya (2017 SGR 1377) is also acknowledged.

I would like to extend my gratitude to all my friends in Barcelona for their help and friendship, making me feel like home.

I am also very grateful to China Scholarship Council (CSC) for financial support during my doctoral study.

Lastly, I would like to give the deepest gratitude to my parents for their encouragement and unselfish support for me studying abroad.

# Abstract

Ferroelectrics are widely used materials for nonvolatile memories and other various devices due to their promising characteristics such as low power consumption, high switching speeds and non-volatility. However, the Pb-containing in most commercial devices of ferroelectrics is a major concern. Also, cell size of the commercial ferroelectric memories cannot be scaled down. Therefore, alternative ferroelectric material are needed. In this thesis, we investigated two different lead free ferroelectric materials – barium titanate ($BaTiO_3$) and hafnium zirconium oxide ($Hf_{0.5}Zr_{0.5}O_2$), aiming to grow epitaxial ferroelectric films integrated with Silicon.

We have developed a new strain engineering for integrating epitaxial $BaTiO_3$ films on Si using $LaNiO_3/CeO_2$/YSZ buffer layers by pulsed laser deposition. The strategy is to control the deposition parameters (substrate temperature, oxygen pressure and growth rate) which can affect the balance between thermodynamics and kinetics during the growth of $BaTiO_3$ films. We show that epitaxial growth of the $BaTiO_3$ films with selectable polar axis orientation can be achieved in a broad deposition parameter window with a large impact on the lattice strain of the $BaTiO_3$ polar axis (exceeding 2 % in films thicker than 100 nm) and ferroelectric properties. This flexible strain method overcomes the primary limitations of conventional substrate-based strain engineering: it can be applied to films on specific substrates including Si(001) and perovskites, and it is not restricted to ultrathin films. Then, we investigated the role of electrode-interfaces in a series of $BaTiO_3$ capacitors using different electrodes (perovskite metallic oxides $La_{2/3}Sr_{1/3}MnO_3$ and $LaNiO_3$ and noble metal Pt). The impact of the electrodes on the electrical properties such as ferroelectric polarization, leakage and imprint field of epitaxial $BaTiO_3$ films was determined.

We also present a detailed study of epitaxial growth of $Hf_{0.5}Zr_{0.5}O_2$ on $SrTiO_3$ substrate buffered with $La_{2/3}Sr_{1/3}MnO_3$ electrode by pulsed laser deposition. The growth window of deposition temperature, oxygen pressure and film thickness is mapped and the polar orthorhombic phase with (111) orientation can be stabilized in the $Hf_{0.5}Zr_{0.5}O_2$ films. We find that the growth parameters and thickness determine the relative amount of orthorhombic phase and its lattice strain, permitting the control of the structural and functional properties. Through selection of deposition parameters and film thickness, the electrical properties can be tailored with low leakage and high remnant polarization up to 24 $\mu C/cm^2$ without the need of wake-up. The coercive field – thickness$^{-2/3}$ scaling, often observed in ferroelectric perovskites, is reported for the first time for ferroelectric hafnia films. Then, we investigated the epitaxial integration of $Hf_{0.5}Zr_{0.5}O_2$ film in a capacitor heterostructure on Si(001). High quality (111)-oriented $Hf_{0.5}Zr_{0.5}O_2$ films have been successfully integrated on Si with $La_{2/3}Sr_{1/3}MnO_3/LaNiO_3/CeO_2$/YSZ or simpler $La_{2/3}Sr_{1/3}MnO_3/SrTiO_3$ buffer layers, presenting robust ferroelectric properties, including the remnant polarization above 30

μC/cm$^2$. The notable endurance (above $10^{10}$ cycles) and long retention (over 10 years) either on $SrTiO_3$(001) or Si(001) are also reported.

# Resumen

Hoy en día los materiales ferroeléctricos se usan ampliamente en memoria no volátiles y otros dispositivos. Esto se debe a que permiten excelentes prestaciones como bajo consumo de potencia, alta velocidad y no volatilidad. Sin embargo, la presencia de plomo en la mayoría de los dispositivos comerciales es un gran problema. Por ello es necesario disponer de materiales ferroeléctricos alternativos. En esta tesis investigamos dos materiales ferroeléctricos sin plomo, titanato de bario ($BaTiO_3$) y óxido de zirconio y hafnio ($Hf_{0.5}Zr_{0.5}O_2$), con el objetivo de integrarlos epitaxialmente en silicio.

Mediante la técnica de depósito con láser pulsado hemos integrado epitaxialmente capas finas de $BaTiO_3$ en Si(001), usando la heteroestructura $LaNiO_3/CeO_2$/YSZ como *buffer layer* y desarrollado una nueva ingeniería de deformación de red cristalina, *strain*. La estrategia de *strain* se basa en variar los parámetros de depósito (temperatura de substrato, presión de oxígeno y velocidad de crecimiento), de modo que se controle el balance entre termodinámica y cinética durante el crecimiento de las capas finas de $BaTiO_3$. Hemos conseguido crecimiento epitaxial de $BaTiO_3$ en una ventana amplia de parámetros de depósito, pudiendo seleccionar la orientación del eje polar (en plano y fuera de plano), y teniendo los parámetro una gran influencia en el *strain* del eje polar del $BaTiO_3$ (con valores incluso superiores al 2 %) y en las propiedades ferroeléctricas. La flexibilidad de esta ingeniería de *strain* evita las limitaciones de los métodos convencionales de ingeniería de *strain* basados en la selección del substrato: puede usarse con capas sobre un substrato determinado incluidos Si(001) y perovskitas, y su uso no está restringido a capas ultra delgadas. Hemos investigado también el papel de las interfaces con los electrodos, en una serie de condensadores de $BaTiO_3$ con diferentes electrodos (los óxidos metálicos $La_{2/3}Sr_{1/3}MnO_3$ y $LaNiO_3$, y el metal noble Pt). En este estudio hemos determinado la influencia de los electrodos en la polarización ferroeléctrica, la corriente de fuga y el campo de *imprint*.

La tesis incluye un estudio detallado del crecimiento epitaxial, mediante láser pulsado, de $Hf_{0.5}Zr_{0.5}O_2$ sobre substratos de $SrTiO_3$(001) usando $La_{2/3}Sr_{1/3}MnO_3$ como electrodo inferior. Hemos determinado la formación de fases cristalinas y las propiedades de las capas en una amplia ventana de crecimiento incluyendo temperatura de substrato, presión de oxígeno y espesor. Con ello hemos encontrado las condiciones en las que se estabiliza la fase polar ortorrómbica en las capas de $Hf_{0.5}Zr_{0.5}O_2$. Esta fase presenta, en todas las condiciones en que se obtiene, orientación fuera del plano (111), mientras que su cantidad relativa respecto al la fase no polar monoclínica y la deformación de red dependen de los parámetros de crecimiento y del espesor. Seleccionando adecuadamente los parámetros de crecimiento y el espesor se obtienen capas de $Hf_{0.5}Zr_{0.5}O_2$ con baja corriente de fuga y

polarización remanente de hasta 24 μC/cm$^2$ sin necesidad de procesos de *wake-up*. Hemos observado que el campo coercitivo depende potencialmente del espesor con un exponente -2/3, una dependencia comunmente observada en perovskitas ferroeléctricas pero observada por primera vez en ferroeléctricos basados en $HfO_2$ en esta tesis. Finalmente hemos abrodado la integración epitaxial sobre Si(001) de capas de $Hf_{0.5}Zr_{0.5}O_2$ en una estructura de condensador. Capas epitaxiales de $Hf_{0.5}Zr_{0.5}O_2$, de alta calidad y orientación (111), se han crecido sobre Si(001) usando como *buffer layers* la heteroestructura $La_{2/3}Sr_{1/3}MnO_3$/$LaNiO_3$/$CeO_2$/YSZ o la bicapa $La_{2/3}Sr_{1/3}MnO_3$/$SrTiO_3$. Las propiedades ferroeléctricas son excelentes, incluyendo polarización remanente superior a 30 μC/cm$^2$ y resitencia a la fatiga (superior a $10^{10}$ ciclos) y retención más allá de 10 años.

# Contents

**Chapter 1. Motivation, objectives and outline of the thesis.................. 1**

1.1 Motivation.......................................................................... 1

1.2 Objectives of the thesis.......................................................... 3

1.3 Outline of the thesis.............................................................. 4

**Chapter 2. Introduction.................................................................... 5**

2.1 Perovskite Ferroelectric $BaTiO_3$........................................... 6

2.1.1 $BaTiO_3$.......................................................................... 6

2.1.2 $BaTiO_3$ on Si.................................................................. 6

2.1.3 Strain engineering.............................................................. 8

2.2 Fluorite Ferroelectric $HfO_2$................................................. 11

2.2.1 Ferroelectric $HfO_2$.......................................................... 11

2.2.2 Origin of ferroelectricity in $HfO_2$..................................... 12

2.2.3 Epitaxial doped $HfO_2$ film................................................ 17

**Chapter 3. Experimental Methods...................................................... 21**

3.1 Sample preparation............................................................... 21

3.1.1 Targets............................................................................ 21

3.1.2 Pulsed laser deposition....................................................... 22

3.1.3 Sputtering........................................................................ 23

3.2 Sample characterization........................................................ 24

3.2.1 X-ray diffraction............................................................... 24

3.2.2 Atomic force microscopy.................................................... 27

3.2.3 Electric characterization..................................................... 27

3.2.4 Other techniques............................................................... 31

**Chapter 4. Epitaxial Ferroelectric $BaTiO_3$ thin film on Si................ 33**

4.1 Strain Tuning of Epitaxial $BaTiO_3$ Films on Si(001)...................35

4.1.1 Substrate Temperature........................................................................39

4.1.2 Oxygen Pressure...................................................................................50

4.1.3 Growth rate...........................................................................................63

4.2 Electrode-interface controlled ferroelectric $BaTiO_3$ films...........71

**Chapter 5. Epitaxial Ferroelectric $Hf_{0.5}Zr_{0.5}O_2$ Thin film........................ 85**

5.1 Growth Window of Ferroelectric Epitaxial $Hf_{0.5}Zr_{0.5}O_2$ Films.....87

5.1.1 Growth conditions................................................................................ 88

5.1.2 Structural Study....................................................................................90

5.1.3 Electric characterization....................................................................... 97

5.2 Epitaxial Integration on Si(001) of Ferroelectric $Hf_{0.5}Zr_{0.5}O_2$ Capacitors.. 119

5.2.1 Ferroelectric $Hf_{0.5}Zr_{0.5}O_2$ capacitors epitaxially integrated on $La_{2/3}Sr_{1/3}MnO_3/LaNiO_3/CeO_2$/YSZ/Si(001) structure................... 120

5.2.2 Ferroelectric $Hf_{0.5}Zr_{0.5}O_2$ capacitors epitaxially integrated on $La_{2/3}Sr_{1/3}MnO_3/SrTiO_3$/Si(001) structure......................................139

**Chapter 6. General conclusions..........................................................147**

**Appendix..............................................................................................149**

Texture control of epitaxial $BaTiO_3$ films on silicon........................ 149

**List of symbols and abbreviations...................................................... 157**

**List of publications.............................................................................. 159**

**List of communications...................................................................... 160**

**References.............................................................................................161**

# Chapter 1. Motivation, Objectives and Outline of the thesis

## 1.1 Motivation

Since the discovery of ferroelectricity in *Rochelle salt* in 1921, the ferroelectric (FE) materials have provided functionalities crucial for a diverse range of applications such as logic memory devices,[1-2] pyroelectric energy conversion,[1-4] piezoelectric sensors and actuators,[5-7] neuromorphic computing,[8-9] and optical devices[10]. The most common ferroelectrics have chemical formula $ABO_3$ perovskite structure (Figure 1-1a) such as $BaTiO_3$ and $Pb(Zr,Ti)O_3$. Ferroelectric materials possess a reversible spontaneous polarization in the absence of an external electric field. The spontaneous polarization in ferroelectrics comes from the non-centrosymmetric arrangement of ions in the unit cell that produces an electric dipole moment. As described by the Landau theory of energetics during ferroelectric switching in Figure 1-1 (b),[11-14] the ferroelectrics have two stable states of polarization. As increasing the temperature above the Curie temperature ($T_c$), the phase transition will take place from non-centrosymmetric (ferroelectric) to centrosymmetric (paraelectric) structure in which the global minimum of the Gibbs free energy lies at $P = 0$, and then materials lose the ferroelectricity. When applying electric field to a ferroelectric, the polarization shows a hysteretic behavior with the applied field (Fig 1-1c). At zero bias, there are two states of residual polarization, which is called remnant polarization ($\pm P_r$). In memory devices, these two states can be translated into “0” and “1” for storing information. Since no external field is required to maintain these states, the memory device is so-called “nonvolatile”. To switch the polarization state or rewrite the information, the threshold electric field higher than the coercive field ($\pm E_c$) is required. Usually, the ferroelectric materials are preferred to be processed in the form of thin films for low-power operation.

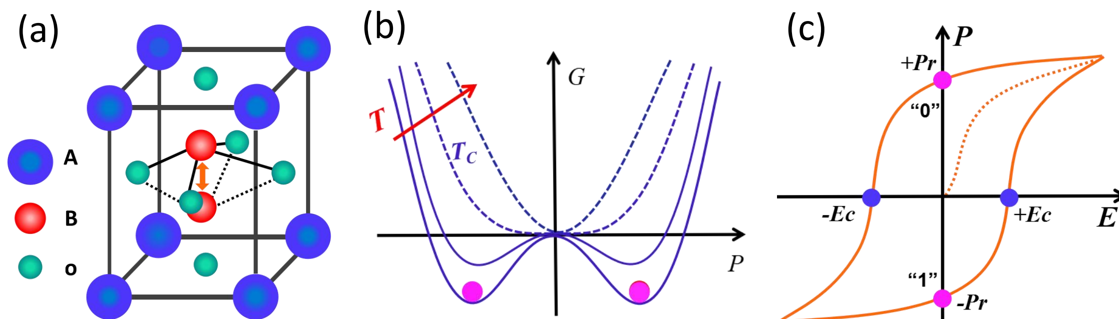


*Figure 1-1 (a) The unit cell of $ABO_3$ type perovskite structure. (b) Landau theory energy potential landscapes: Gibbs free energy potential as a function of the spontaneous polarization. (c) The typical ferroelectric hysteresis loop.*

For the practical non-volatile logic memory devices in most applications of ferroelectrics, the ferroelectric thin films should be integrated on the semiconductor platform, especially on Silicon.[15-17] However, the structure quality of ferroelectric oxide films grown on semiconductor substrates is far from the quality of these films grown on appropriate oxide substrates, leading to the degraded properties in the microelectronic devices.[15-19] The reason is because of the chemical reaction and mechanical incompatibility of dissimilar interfaces between perovskite ferroelectric oxides and Silicon. As a consequence, a significant effort and improvements to integrate functional complex functional oxides on silicon have been made during the past decades.[20-33] However, most of the high quality ferroelectric films grown on silicon are lead (Pb)-containing which is toxic and environmentally unfriendly. This is a drawback affecting its use in commercial devices. Alternative materials, Pb-free and offering superior functional properties are demanded. In this thesis, two different lead-free ferroelectric materials were intensively studied: One is the prototypical perovskite oxide $BaTiO_3$ (BTO); another one is the novel doped $HfO_2$, specifically $Hf_{0.5}Zr_{0.5}O_2$ (HZO), with fluorite-structure.

Firstly, the perovskite-structure $BaTiO_3$ with spontaneous polarization ($P_s$) around 26 $\mu C/cm^2$ in bulk state is a good candidate for lead-free microelectronic devices. Although $BaTiO_3$ films have been recently integrated with Si(001), epitaxial growth and high ferroelectric polarization are very challenging.[15,16] In particular, $BaTiO_3$ films with the polar axis perpendicular to the Si(001) plane, required in devices such as FE field-effect transistors, are elusive.[15-17,19] High quality *c*-oriented $BaTiO_3$ films with large remnant polarization ($P_r$) of 6-10 $\mu C/cm^2$ were integrated with silicon using YSZ (yttria-stabilized zirconia), $CeO_2$, and conducting $LaNiO_3$ in a buffer layer heterostructure by our group.[34] On the other hand, it is well-known that lattice strain generally causes dramatic effects on the properties of ferroelectrics. In particular, epitaxial compressive strain has permitted a notable enhancement of the ferroelectric polarization and the Curie temperature.[52,57] The conventional strain engineering is based on the selection of proper substrate with certain lattice mismatch inducing the epitaxial strain. However, this substrate-based strain engineering is restricted to relatively small ranges of strain and film thickness due to the plastic relaxation. Also, the limited number of substrates for choice will cause the insufficient strain tunability. More importantly, in most applications ferroelectric films are required to be integrated with the specific substrate silicon, putting the serious limits for the use of substrate-based strain engineering. Therefore, alternative strategies to the usual substrate engineering are highly needed.

Secondly, the lead-free fluorite-structure doped $HfO_2$ thin films were first reported to be ferroelectric in 2011.[35] Due to their advantages such as high compatibility with complementary metal oxide semiconductor (CMOS) technology and excellent scalability compared with conventional perovskites,[35-37] the ferroelectric $HfO_2$-based thin films are considered to be a very promising candidate for the further development of future memories applications. It is generally accepted that the origin

of this unexpected ferroelectricity is due to the formation of a metastable non-centrosymmetric orthorhombic phase with space group $Pca2_1$. Several mechanisms [36-37] such as doping, grain size, top electrode capping effect and balance between kinetics and thermodynamics have been put forward as important factors responsible for stabilizing the ferroelectric phase. Currently, this ferroelectric phase is usually stabilized in polycrystalline films where nanometric orthorhombic grains coexist with non-ferroelectric phases.[36-38] The polycrystalline nature and the mixture of phases in $HfO_2$ films challenge the understanding of the intrinsic ferroelectric properties as well as prototyping devices. For this purpose, epitaxial ferroelectric $HfO_2$ films are definitely more convenient. Despite the nascent state of epitaxial ferroelectric hafnia, recent research has reported that the FE orthorhombic phase can be stabilized in epitaxial films. More progress in the fabrication and deeper functional characterization of epitaxial $HfO_2$-based thin films is required.

## 1.2 Objectives of the thesis

The objective of the thesis is to achieve significant progress in the two following directions.

(i) Developing a different strain engineering for ferroelectric $BaTiO_3$ on a specified substrate with the tunability of lattice strain and ferroelectric polarization. Defects engineering could be a viable way for achieving this goal. Defects in thin films offer an opportunity to expand the crystal lattice and engineer the strain if controlled properly. For epitaxial ferroelectric thin films, complex point defects are usually present. Such point defects can be introduced with high energetic techniques like pulsed laser deposition or sputtering. Based on the balance between thermodynamics and kinetics in the growth of $BaTiO_3$ by pulsed laser deposition, the growth conditions (substrate temperature, deposition oxygen pressure and growth rates) have strong influence on the $BaTiO_3$ growth mechanisms, lattice strain, and ferroelectric properties. We have investigated this influence, and we demonstrate that they permit tunable strain and ferroelectric polarization, providing a feasible method that can overcome the main limitations of the conventional strain engineering.
In addition, as the electric properties of ferroelectric $BaTiO_3$ thin films can be largely dominated by the interfaces, the relevant investigation about the role of electrode-interface on the ferroelectricity of $BaTiO_3$ thin films is also performed.

(ii) Stabilization of polar orthorhombic phase in epitaxial $Hf_{0.5}Zr_{0.5}O_2$ thin films. $Hf_{0.5}Zr_{0.5}O_2$ film are grown on $SrTiO_3$(001) substrate buffered with $La_{2/3}Sr_{1/3}MnO_3$ electrode to determine the growth window for the epitaxial orthorhombic phase. The effect of deposition parameters (temperature, oxygen pressure and film thickness) on the structural and ferroelectric properties of $Hf_{0.5}Zr_{0.5}O_2$ films by pulsed laser deposition is investigated. For future device applications in CMOS technology,

integration has to be done on Si(001). Thus, the epitaxial integration of $Hf_{0.5}Zr_{0.5}O_2$ film in a capacitor heterostructure on Si(001) is also addressed.

## 1.3 Outline of the thesis

Chapter 2 firstly introduces the basics of perovskite $BaTiO_3$, how it can be epitaxially integrated on Si and the limitations of classic strain engineering and proposed solutions. Then the novel ferroelectric $HfO_2$-based thin films and the origin of ferroelectricity are presented. The state-of-the-art research for epitaxial doped $HfO_2$ films is also reviewed.

Chapter 3 describes the experimental methods and tools used throughout this work for sample preparation and characterization. The sample preparation summarizes the fabrication process of pulsed laser deposition targets, basics of pulsed laser deposition system and sputtering for top electrodes. Respect to sample characterizations we briefly describe the techniques used for the structural analysis (X-ray diffraction, atomic force microscopy) and the electric measurements.

In chapter 4, we present the study of influence of deposition parameters (substrate temperature, oxygen pressure and growth rate) on the structure and ferroelectric polarization of epitaxial $BaTiO_3$ on Si. It is shown that the epitaxial strain and ferroelectric polarization can be effectively tailored by deposition parameters and then new strategy of strain engineering can be built. Also, the influence of electrodes (perovskite metallic oxides $La_{2/3}Sr_{1/3}MnO_3$ and $LaNiO_3$ and noble metal Pt) on the electric properties of $BaTiO_3$ films is studied and determined.

In chapter 5, we firstly show how the deposition parameters (temperature, oxygen pressure and film thickness) determine the structural and ferroelectric properties of $Hf_{0.5}Zr_{0.5}O_2$ films. The growth window map for epitaxial stabilization of the ferroelectric phase is established. Then we integrate epitaxial $Hf_{0.5}Zr_{0.5}O_2$ films on Si(001) with two different buffer layers $La_{2/3}Sr_{1/3}MnO_3$/$LaNiO_3$/$CeO_2$/YSZ and simpler $La_{2/3}Sr_{1/3}MnO_3$/YSZ heterostructures. The extensively characterization for electric properties such as polarization, leakage, retention and fatigue of epitaxial $Hf_{0.5}Zr_{0.5}O_2$ thin films is presented.

Chapter 6 summarizes the general conclusions of the thesis.

Finally, in Appendix, we show how the texture of epitaxial $BaTiO_3$ films on Silicon wafers can be controlled by selection of wafer orientation and buffer layers.

# Chapter 2. Introduction

Ferroelectric materials present a switchable spontaneous electric polarization that is intrinsic to the crystal lattice. They belong to a broad class of dielectrics which are insulating materials. The applied external electric field can break the space symmetry of the dielectrics and create a transient electric polarization. A subset of dielectrics with a non-centrosymmetric structure is called "piezoelectrics", for which the application of stress induces an electric potential or, conversely, the application of an electric field induces mechanical strain. Some of piezoelectrics possess a unique polar axis, leading to a spontaneous electric polarization. As the polarization is dependent with temperature that create charge flow, these materials are so-called "pyroelectrics". Finally, some polar pyroelectric materials possess two or more stable polarized states in the absence of an electric field, and the application of an electric field can induce switching between these states. These materials are called "ferroelectrics".

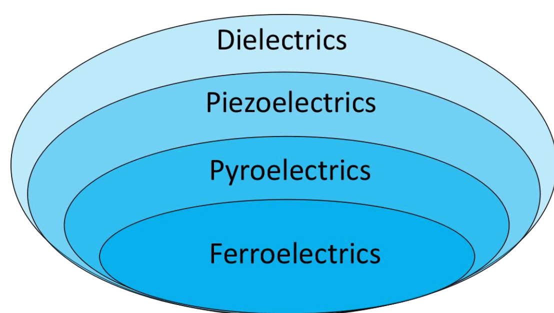


*Figure 2.1 Hierarchy of the dielectric materials according to the piezoelectric, pyroelectric and ferroelectric properties.*

The most widely investigated FE materials are perovskite oxides and related structures such as $BaTiO_3$ , $Pb(Zr,Ti)O_3$ (PZT), $SrBi_2Ta_2O_9$ (SBT) or $Bi_4Ti_3O_{12}$. Due to their chemical and thermal robustness and other attractive characteristics such as high dielectric constant, large spontaneous polarization, and electro-mechanical response, perovskite ferroelectric oxides have been widely used in nonvolatile memories, sensors, actuators, and electro-optic devices.[1-10] However, in most of these oxides, the chemical composition usually includes volatile (Pb, Bi) and toxic elements (Pb). Alternative materials, Pb-free and offering superior functional properties are demanded. The perovskite-structure $BaTiO_3$ which is lead-free with good ferroelectric properties and very high electro-optical coefficients can be a good alternative choice. On the other hand, the novel fluorite-structure ferroelectric $HfO_2$ thin films possessing the advantages of high compatibility with silicon and excellent scalability can be an excellent candidate for lead-free microelectronic devices. Therefore, in the following section we will focus on these two lead-free materials: the perovskite ferroelectric $BaTiO_3$ and fluorite ferroelectric $HfO_2$.

## 2.1 Perovskite Ferroelectric $BaTiO_3$

### 2.1.1 $BaTiO_3$

$BaTiO_3$ is the archetype ferroelectric perovskite oxide. The origin of ferroelectricity for BTO is the shift of Ti atom either up or down from the centrosymmetric position to a configuration of lower energy. This bistability of the Ti position produces the switchable permanent dipole moment characteristic of ferroelectricity. BTO loses its ferroelectricity above the Curie temperature around $T_c$ = 120 °C[39] where it becomes a centrosymmetric cubic structure. At room temperature, ferroelectric BTO has tetragonal structure (space group *P4mm*) with lattice parameters $a$ = 3.994 Å and $c$ = 4.038 Å and spontaneous polarization ($P_s$) around 26 μC/cm$^2$ with [001] polar direction. Continuously lowering the temperature, BTO suffers another two ferroelectric phase transitions to the orthorhombic phase (below 5 °C) and further rhombohedral phase (below -90 °C) with polar axes along [011] and [111] respectively as shown in Figure 2.2. Epitaxial strain can dramatically increase the transition temperature of ferroelectric oxide thin films by several hundred degrees with simultaneous enhancement in ferroelectric polarization.[40,41] Besides the FE memory applications, the strong electro-optic effect with large effective Pockels coefficient of $r_{eff}$ = 148 pm V$^{-1}$ and low propagation losses of only 6 dB/cm achieving in epitaxial films on Si makes BTO potentially useful for integrated Si nanophotonics.[43]

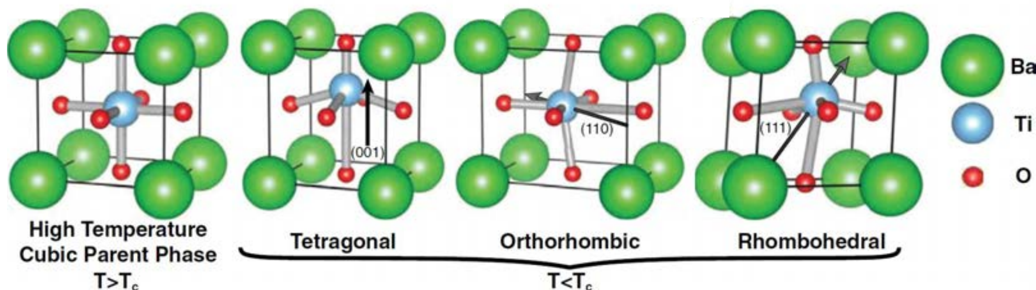


*Figure 2.2 Schematic drawing of the crystal structure of polymorphic states of $BaTiO_3$ including (a) ideal perovskite structure (cubic, paraelectric phase), (b) tetragonal phase with polarization along [001], (c) orthorhombic phase with polarization along [110], and (d) rhombohedral phase with polarization along [111]. [42]*

### 2.1.2 $BaTiO_3$ on Si

In order to use ferroelectric single crystalline $BaTiO_3$ thin films for most commercial

applications, epitaxial integration on silicon wafers is required. The epitaxial integration of BTO on Si (001) remains challenging due to the dissimilarities between Si and BTO. The successful direct growth of BTO on Si would be of significant relevance in devices such as ferroelectric field effect transistors. The reason is that an additional phase (silicide or silicate) is formed at the interface due to the chemical interaction, which prevents epitaxial crystallization of BTO and causes the deteriorated functional properties of the film.[15-17] Another challenge is the large thermal expansion mismatch between Si and BTO, with BTO having a thermal expansion coefficient about three times larger than Si.[44] This thermal mismatch will result in a large residual tensile stress that can cause cracks in the film.[45] Also, tensile stress favors the polar *c*-axis of BTO alignment in the Si(001) plane at the paraelectric-ferroelectric transition when they are cooled down after deposition.[34] The polar axis of BTO on Si should be along the out-of-plane direction in memory devices. Consequently, these difficulties mentioned above challenge the epitaxial growth of *c*-oriented BTO on Si(001).

The common solution to achieve epitaxial growth is the use of a buffer layer. A buffer layer that can be epitaxially grown on Si can be used as a pseudosubstrate for the subsequent deposition of films. The most widely used buffer template for the epitaxial growth of complex oxides on silicon are $SrTiO_3$ (STO) and yttria-stabilized zirconia (YSZ). Both of buffers have been successfully used for the integration of high quality ferroelectric $Pb(Zr,Ti)O_3$ on silicon. In this thesis, YSZ has been employed as buffer layer for epitaxial integration of BTO on Si.

YSZ has been successfully grown epitaxially on Si with PLD since the 1990s.[46,47] Firstly, YSZ is deposited on as-received silicon substrate in low oxygen pressure to perform a redox reaction. The Zr and Y atoms reduce the native silicon oxide due to the lower Gibbs formation free energies of $ZrO_2$ and $Y_2O_3$ compared to $SiO_x$. Crystallization of YSZ on the silicon typically occurs above a thickness of 1.0 - 1.5 nm.[48,49] Then, the nanometric $SiO_x$-free regions act as seeds for epitaxy and subsequent lateral crystallization of the rest of the amorphous YSZ. Finally, a chemically stable YSZ film is grown epitaxially on the Si substrate.[48] In this way, very flat surface can be achieved. Additionally, an epitaxial fluorite $CeO_2$ layer is grown on the YSZ film to obtain a template with better structure compatibility with perovskite oxides.[50] This permits epitaxial integration of (001)-oriented BTO film on buffered Si(001) substrate. Figure 2.3 shows the sketch of heterostructure used in this thesis for $BaTiO_3$ thin films integrated on Si indicated with the corresponding lattice mismatch between each layer.

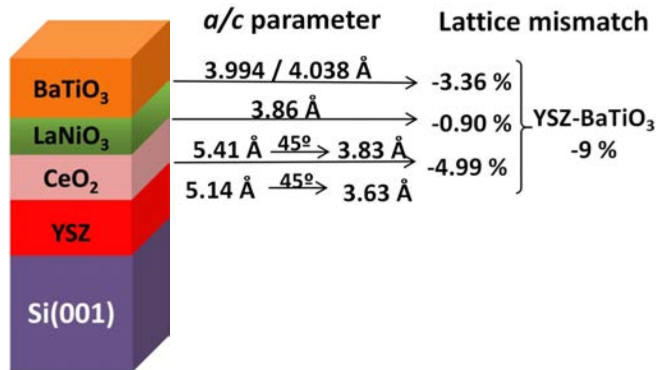


*Figure 2.3 The sketch of the heterostructure for $BaTiO_3$ integrated on Si with corresponding lattice mismatch between each layer.*

## 2.1.3 Strain engineering

The functional properties of oxides can be controlled by modifying the crystal structures due to the inherent coupling between structure and functionality of oxides. In the case of epitaxial films, the classic strategy is based on the use of different substrates which present a tailored lattice mismatch with thin film and further induce the structural distortions for expected functional properties as shown in Figure 2.4. By choosing the appropriate substrate, the perovskite oxide thin films can be grown under compressive (Figure 2.4b) or tensile (Figure 2.4c) strain exerted by the substrates. The commercially available monocrystalline substrates with lattice constants in the 3.7 Å - 4.2 Å range can be seen in Figure 2.5. As a result, epitaxial strain can be tailored from compressive to tensile states. This strain engineering has been widely applied to superconducting, metallic, ferromagnetic, and ferroelectric oxides, among others.[51-56]

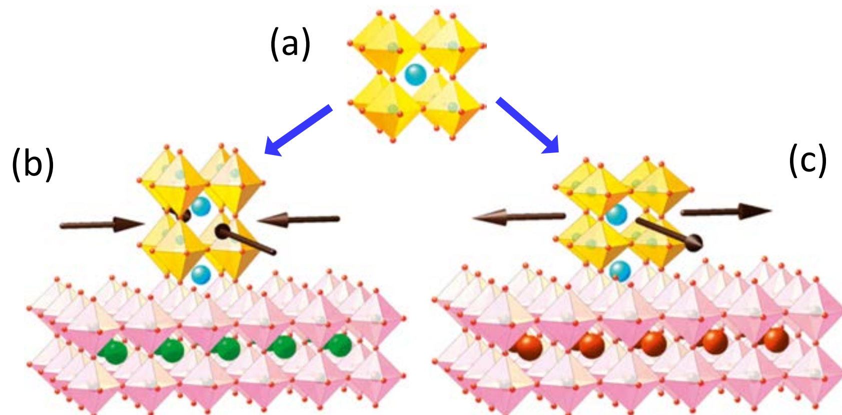


*Figure 2.4 "Strain engineering" - the effect of substrate on the in-plane strain of perovskite thin film. (a) Unstrained state of perovskite oxides; (b) Biaxial compressive strain by a substrate with smaller in-plane lattice constants. (c) Biaxial tensile strain by a substrate with larger in-plane*

*lattice constants. [51]*

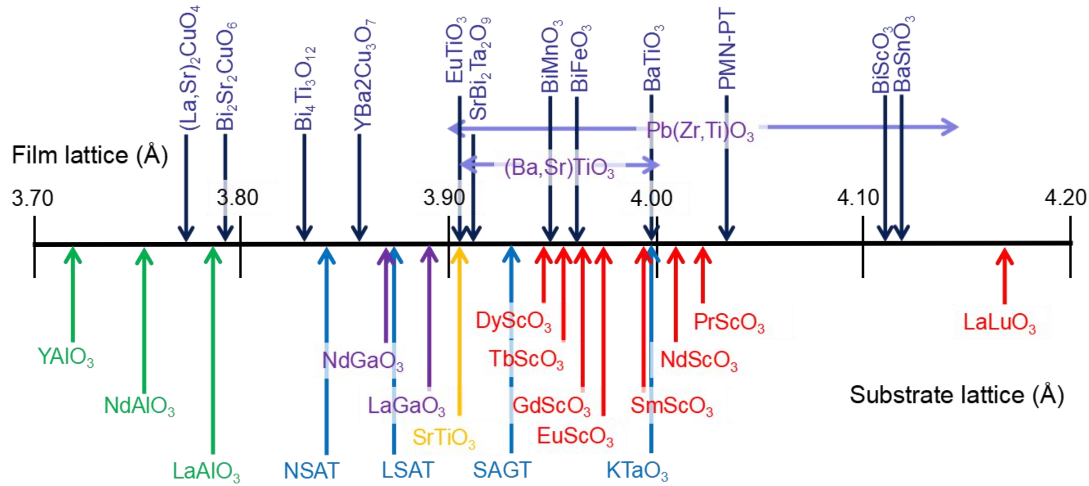


*Figure 2.5 A summary of the pseudocubic in-plane lattice constants of various perovskite and perovskite-related oxides. [Abbreviations in the figure: NSAT, $(NdAlO_3)_{0.39}$—$(SrAl_{0.5}Ta_{0.5}O_3)_{0.61}$; LSAT, $(LaAlO_3)_{0.29}$—$(SrAl_{0.5}Ta_{0.5}O_3)_{0.71}$; SAGT, $Sr_{1.04}Al_{0.12}Ga_{0.35}Ta_{0.5}O_3$] [51]*

For ferroelectric thin films, the large expitaxial strain can hugely enhance the ferroelectric polarization and the Curie temperature. For example, when the biaxial compressive strain has been applied to $BaTiO_3$ thin films by scandate substrates, the curie temperature and the remnant polarization are nearly 500 °C and 250 % respectively, higher than bulk $BaTiO_3$ single crystals.[57] Despite the success of controlling the material properties by elastic strain, this classic substrate-based strain engineering has several restrictions. Firstly, it only permits small ranges of strain and film thickness. The film thickness should be below a critical value or plastic relaxation will occur. It means films should be either very thin or deposited on substrates presenting low lattice mismatch (thus causing low strain). This will limit the practical applications. In addition, there are limited number of single crystalline substrates for choice, hampering the possibility for exploring the targeted structural distortions and properties. More importantly, because of basing on the selection of specific substrates, the conventional strain engineering is not possible to be applied for the many current applications which require integration with silicon wafers. Therefore, alternative strategies to the classic strain engineering, with flexibility to be used on a specified substrate and not restricted to ultrathin films, have to be developed.

Defect engineering has been widely applied in optimizing the electrical, optical, mechanical, and other properties of a wide class of functional materials.[60] For epitaxial ferroelectric thin films, point defects such as self interstitial atoms and ionic vacancies (cation and anion vacancies) are usually presented. If these defects can be

controlled properly, it could provide an opportunity to engineer the strain and expand the crystal lattice during the growth process. Additionally, due to clamping of the film on a bulky substrate, for example, silicon, the thin film can expand anisotropically along the out-of-plane direction and achieve higher lattice strain. Such point defects can be introduced with high energetic techniques like pulsed laser deposition or sputtering to modify epitaxial strain, affecting the electric properties in ferroelectric films.[40,41,61-64] The resulting strain can severely influence the ferroelectric properties with highly enhanced tetragonality ($c/a > 1.1$) and ferroelectric remnant polarization (> 50 μC/cm$^2$) of BTO films on STO(001).[41]

However, precisely controlling these point defects and further tailoring the lattice expansion and properties are another concern. During the film growth process with high energetic techniques like pulsed laser deposition, the laser plasma expansion from the target and deposition on substrate are inherently non-equilibrium phenomena. The film growth process process is governed by the competition between kinetics and thermodynamics as illustrated by Figure 2.6. The type of growth is largely determined by the ratio between diffusion rate D and deposition flux F. Here, for simplicity, a continuous growth process is considered. If deposition is slower than diffusion (large values of *D/F*), film grows close to equilibrium conditions, where the film growth is dominated by the thermodynamics. If deposition is fast relative to diffusion (small *D/F*), films growth will be largely determined by the kinetics.[66] This competition between kinetics and thermodynamics will finally determine the formation and concentration of the defects. Thus, the growth parameters can be used as a knob to tailor the self-formed defects by controlling the kinetics and thermodynamics during the film growth. The generated defects during the growth process can be responsible for the the lattice strain and related properties. Indeed, epitaxial BTO films grown by pulsed laser deposition on $GdScO_3$(110) with controlling the laser fluence present strong variations in lattice strain and Curie temperature, and this was proposed to be due to the existence of dipole defects in the films.[40] The growth rate and deposition pressure in pulsed laser deposition of $SrTiO_3$ (STO) films and ferroelectric BTO/STO superlattices have also been shown to permit control of the lattice strain.[64,65] These reported results signal the importance of growth kinetics on the lattice strain of epitaxial perovskite oxides. Therefore, in this thesis, a complete study of the effects of main growth parameters (substrate temperature, oxygen pressure and growth rate) is performed. Firstly, with fixed deposition flux, the relative influence of kinetics and thermodynamics on the growth can be well controlled by varying the substrate temperature since the diffusion rate is thermally activated. Secondly, for the oxygen pressure presented in PLD chamber, the films can present different oxygen vacancies at various oxygen atmosphere due to the insufficient oxidation and low vapor pressure in BTO films; Moreover, because the high energy ions and atoms of the laser-generated plasma make collisions with oxygen atoms, the oxygen pressure can determine the kinetic energy of the BTO atoms in the PLD plasma. Lastly, the growth rate of BTO films is controlled by changing the energy of laser pulse.

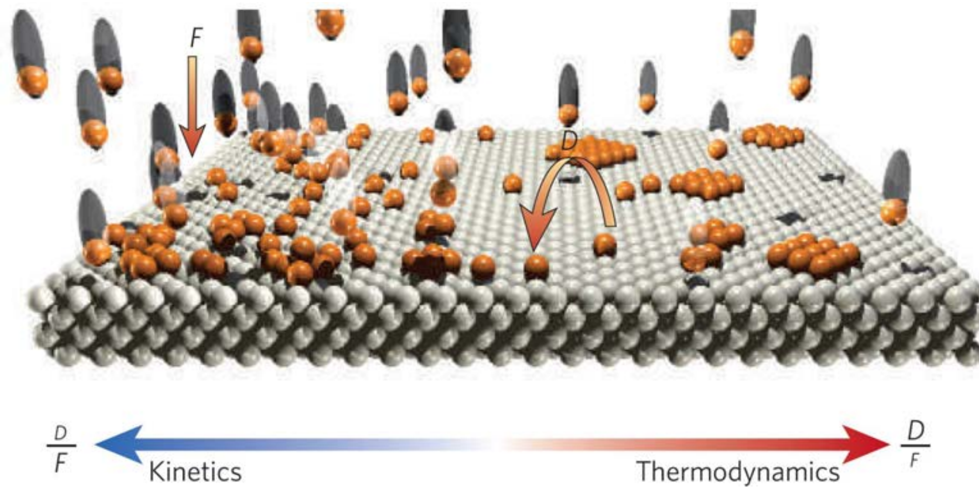


*Figure 2.6 The illustrative image of film surface for growth process at atomic scale. [66]*

## 2.2 Fluorite Ferroelectric $HfO_2$

### 2.2.1 Ferroelectric $HfO_2$

Over the past several decades, ferroelectric materials have been widely investigated for their use in memory devices such as ferroelectric random access memory (FeRAM), ferroelectric field effect transistors (FeFETs) or ferroelectric tunnel junctions (FeTJs). FERAMs are in the market from more than 25 years ago, using currently PZT as ferroelectric material. PZT and other ferroelectric materials such as $BaTiO_3$ (BTO) and $SrBi_2Ta_2O_9$ (SBT)[77] are considered for the emerging FeFETs and FeTJs memories. However, the conventional perovskite ferroelectrics are facing several intrinsic problems. Even though previous studies already reported conventional ferroelectrics can be epitaxially grown on Si substrates,[32,90] the performance stability is much more deteriorated.[15-17,91] The major difficulty is that the perovskite ferroelectrics are not well compatible with silicon-based complementary-metal-oxide-semiconductor (CMOS) technology.[15-17] On one hand, due to the high temperature necessary for crystallization of the ferroelectric thin films, its integration has to be done in the initial steps of CMOS line. On the other hand, for Si-based devices, it is essential to apply the post-metalization annealing process under the hydrogen atmosphere. Due to the weak bonding energy between metal ions and oxygen, H+ is easily incorporated into conventional perovskite films, degrading the device performance.[92-94] The another drawback of conventional ferroelectrics is the limited scalability. As the film thickness is scaled down, the ferroelectric properties degrade, thus limiting the memory density.[1,92,95,96] Also, the conventional FE materials have a relatively small band gap (Eg, 3-4 eV), which

induces a low Schottky barrier height (about 1 eV) with respect to the metal electrodes. This will result in the ferroelectric thin films being more vulnerable to high leakage current, favoring electrical breakdown.[36] Therefore, a relatively large film thickness ($t \geq 70$nm) is required to be successful in FeRAM applications and such large thickness will become the limitation for the fabrication of future three-dimensional capacitor architecture in the technology node with several tens of nanometers.[97] In order to overcome these intrinsic bottlenecks of conventional FE materials, a material innovation is highly demanded for the future development of FE memories and other related devices.

In recent years, hafnium oxide ($HfO_2$) based FE materials have attracted special attention and interest for new generations of high density logic and memory devices since the announcement of its unexpected ferroelectricity by the first time in 2011.[35] Due to the good physical and electrical properties, the excellent compatibility with CMOS processes and scalability, it holds the tremendous potential to replace the conventional perovskite-based ferroelectrics for memory applications. The advantages of $HfO_2$-based materials can be listed below. 1) The $HfO_2$-based films can be extremely thin (film thickness, $t_f \leq 10$nm) with feasible remnant polarization ($P_r$, 10-40 $\mu C/cm^2$) even when $t_f$ scaled down to around several nm.[98,99] This is one of the major advantages compared with the conventional ferroelectric thin film like PZT or SBT where the much thicker thickness ($t_f \geq 100$ nm) are required for realizing stable operation as previously mentioned. 2) The high $E_c$ (1-2 MV/cm) of $HfO_2$, about one order of magnitude larger than those of conventional perovskites, and the lower permittivity can effectively prevent the depolarization effect which often occurs in perovskite ferroelectrics when reducing the film thickness and therefore is beneficial to the polarization stability. 3) $HfO_2$ has a larger bandgap of ≈ 5.3-5.7 eV and much stronger bonding between oxygen and Hf (and other dopants), which makes the possible problems related to leakage current and reliability issues of FE $HfO_2$-based films highly mitigated even with the small thickness ($t_f \leq 10$nm).[35,36,100] More importantly, $HfO_2$ is a standard material for the semiconductor industry, and it has been widely used as buffer layer in ferroelectric field effect transistor (FeFET) to solve the interfacial problems of conventional ferroelectrics and Si substrates. Therefore, in terms of the practical applicability, the $HfO_2$-based films are highly compatible with the currently standard complementary-metal-oxide-semiconductor (CMOS) process and can scale down beyond the present limitation of conventional FE materials.

### 2.2.2 Origin of ferroelectricity in $HfO_2$

Generally, the polar orthorhombic phase (o-phase, space group *Pca2₁*) is believed to be the origin of ferroelectricity in $HfO_2$-based thin films. Figure 2.7 shows the schematic illustrations of the crystal structures of $HfO_2$-related materials. In bulk $HfO_2$ material, the monoclinic phase (m-phase) with space group $P2_1/c$ is the most

stable phase at room temperature and normal pressure. The phase in bulk state highly depends on the temperature and pressure. The tetragonal phase (t-phase, space group $P4_2/nmc$) and cubic (c-phase, space group *Fm3m*) phase can be thermodynamically transformed from monoclinic phase at approximately 1750 °C and 2500 °C, respectively.[101] With applying the hydrostatic compressive pressure, the m-phase transforms into orthorhombic phases with space group *Pbca* at 4 GPa and *Pnma* at 14.5 GPa.[102] All the possible phases mentioned above are centrosymmetric structure, which means they cannot be responsible for the origin of ferroelectricity.

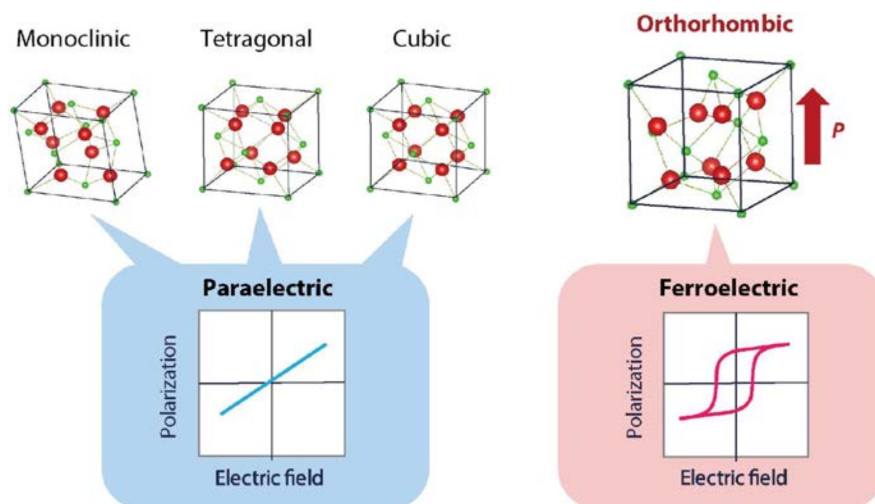


*Figure 2.7 Schematic illustrations of the crystal structures of $HfO_2$-related materials. Ferroelectricity is only expected in a metastable orthorhombic phase. [103]*

However, unexpected ferroelectricity was firstly reported in atomic layer deposition (ALD) deposited Si-doped $HfO_2$ thin films for the first by Boscke *et al.*[35] The authors attributed this observed ferroelectricity to the formation of the metastable non-centrosymmetric orthorhombic phase (space group $Pca2_1$), which is not found in equilibrium phase diagram of $HfO_2$. Actually, this o-phase was first identified in Mg-doped $ZrO_2$ ceramics ($ZrO_2$ and $HfO_2$ are structurally and chemically similar) by neutron powder diffraction.[37] And first discovery of ferroelectricity in thin $HfO_2$-based films in 2007 and the results were first published in 2011. After the experimental confirmation of the ferroelectricity in $HfO_2$-based films, extensive studies were performed.[104-107] Huan *et al.* [104] proposed two possible polar orthorhombic phases with the space groups $Pca2_1$ and $Pmn2_1$ using the first principle calculations and simulated the corresponding X-ray diffraction patterns. The $Pca2_1$ space group is believed to be well matched with reported FE $HfO_2$ thin films. However, experimentally identifying the o-phase is highly challenging with standard X-ray diffraction technique mainly due to the almost identical lattice parameters of o-phase and t-phase in $HfO_2$-based thin films.[35] For example, the (111) reflection of o-phase and (101) reflection of t-phase in standard XRD $\theta$-$2\theta$ scans would share the similar position around 30°. The peaks of o-phase with other m- and t-phases can be

separated at high 2θ angle between 80° − 90° using GIXRD.[35,108-110] Transmission electron microscopy (TEM) observations have revealed the existence of an orthorhombic phase, and the simultaneous position averaged convergent beam electron diffraction (PACBED) has confirmed the this polar orthorhombic phase with space group of $Pca2_1$.[105]

Ferroelectic $HfO_2$-based films can be prepared with various dopants [111-115] and by different deposition techniques such as the most widely employed atomic layer deposition (ALD),[35-37] chemical solution deposition,[116,130] pulsed laser deposition (PLD),[117] sputtering[118,119] and chemical vapour deposition.[120] The commonly used electrode is TiN[121,122] but others including Pt,[123] Ir,[124] TaN[125] and $RuO_2$ were employed.[122] The formation mechanism of the orthorhombic phase ($Pca2_1$) in $HfO_2$-based thin films is usually believed to occur through transition from t-phase, favored by the structure similarities.[126] For undoped $HfO_2$ bulk material, the lattice parameters of o-phase are $a$ = 5.30 Å, $b$ = 5.10 Å, and $c$ = 5.11 Å while $a$ = $b$ = 5.14 Å and $c$ = 5.25 Å are the corresponding lattice parameters for the t-phase.[127,128] The majority of studies involve polycrystalline hafnia oxides, and epitaxial films have been scarcely investigated.[161] Currently, several mechanisms have been widely reported to be responsible for stabilizing the FE o-phase during the film growth as discussed below.

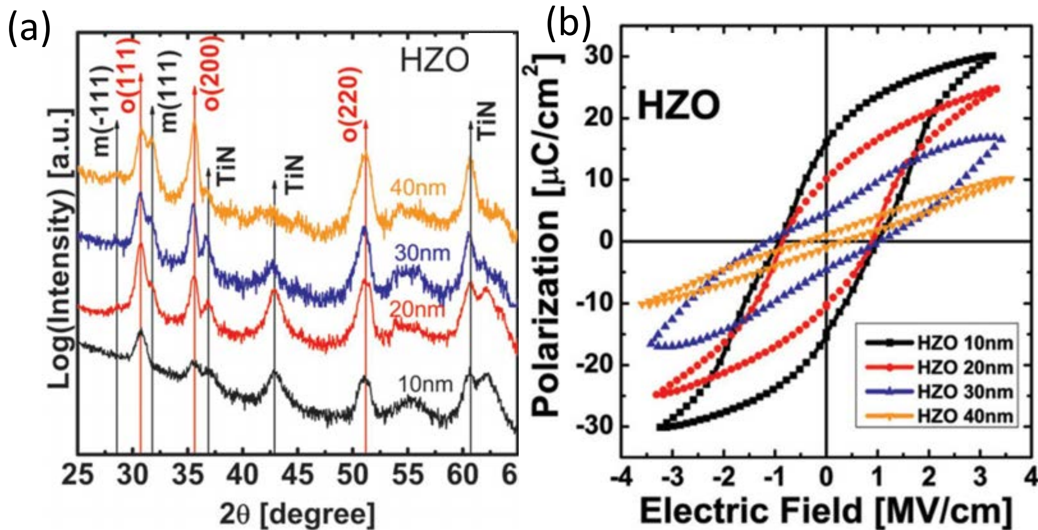


*Figure 2.8 An example of thickness-dependent phase transition (a) GIXRD pattern of the $Hf_{0.5}Zr_{0.5}O_2$ films with various thicknesses and (b) corresponding P-E loops. [129]*

*Grain size.* Grain size is highly dependent on thickness and thermal budget. In case of a higher thermal budget or higher film thickness, the grains grow larger and the proportion of non-polar m-phase increases, then degrading the ferroelectric properties.[116,126,129-131] A clear dependence of m-phase amount and polarization on the film thickness can be seen in Figure 2.8. The reason is because the surface

energy related to the radius $r$ of nanoparticles will create a large internal pressures ($P = 2\sigma/r$) of the order of GPa.[132,133] Also, the recent computational results proved that the small grain sizes with high surface energy will contribute to the stabilization of o-phase in $HfO_2$ and $ZrO_2$ nanoscale films.[134]

*Doping*. Various dopants such as Si, Gd, Al, Y, Sr, Zr and La have permitted stabilizing the ferroelectric o-phase in $HfO_2$ film. The different ionic sizes of dopants with respect to Hf atom can significantly modify the metal-oxygen bonding and balance the relative stabilities of various $HfO_2$ phases.[135] The dopants can be divided in two categories based on the ionic radii:[136] (a) dopants with larger ionic radii larger than that of $Hf^{4+}$ (85 pm), such as $Gd^{3+}$ (108 pm), $Y^{3+}$ (104 pm), $La^{3+}$ (117 pm), $Sr^{2+}$ (132 pm), which favors the c-phase; (b) other dopants, like $Si^{4+}$ (54 pm), $Al^{3+}$ (67.5 pm), and $Zr^{4+}$ (86 pm) with smaller or similar ionic radii to $Hf^{4+}$, tending to stabilize the t-phase. No matter which kind of dopants, the prerequisites for the formation of the o-phase is the preferable transition from m-phase to t-phases, due to the existence of o-phase in the transition region. Besides the dopants, the ferroelectricity of doped $HfO_2$ film can also be dependent on the dopant concentrations. The ferroelectric properties with various dopants and the dopant concentrations are concluded in Figure 2.9(a). Because of the almost same ionic size and the chemical valence of Zr atom to the Hf atom, the $Hf_{1-x}Zr_xO_2$ solid solution can be formed in a broad range in Figure 2.9(b). Ferroelectricity appears at x = 0.3 and peaks at x = 0.5. Increasing the amount of Zr dopant to x = 0.7, antiferroelectricity emerges along with the increase of permittivity as explained by the formation of more t-phases.

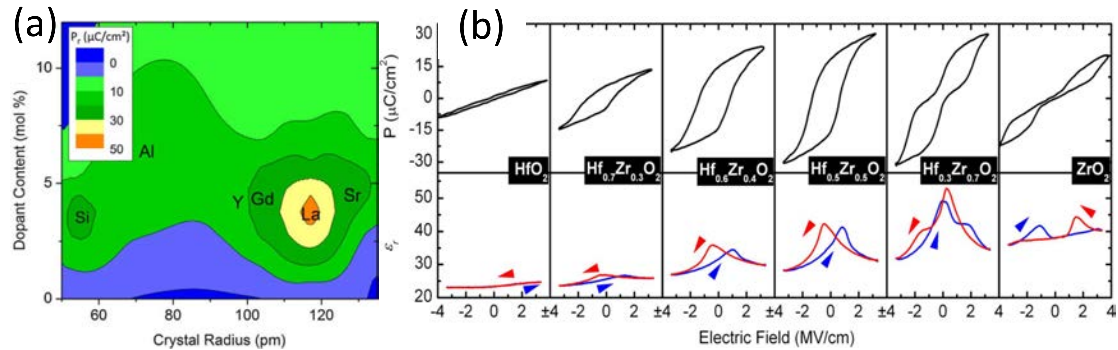


*Figure 2.9 (a) Contour plot of the remanent polarization as a function of crystal radius and dopant content.[137] (b) P-V and C-V hysteresis loops of 9 nm-thick $Hf_{1-x}Zr_xO_2$ thin films sandwiched between TiN top and bottom electrodes.[108]*

*Top electrode capping effect*. The important role of top capping electrode has been frequently emphasized in literature.[36-37] $HfO_2$-based films are usually sandwiched between top and bottom electrode such as TiN electrode, and then followed by post annealing to induce the crystallization of ferroelectric o-phase. The large difference after annealing with and without top capping layers can be seen in the amount of m-phase and o-phase in Figure 2.10. It has been proposed that capping a top electrode

causes a mechanical confinement that avoids shearing and volume expansion of the unit cell during the crystallization process and hence reduces the formation of the m-phase.[36,37] Therefore, the $P_r$ value of the film crystallized with capping electrode is higher than that without capping layer.[109,110,138]

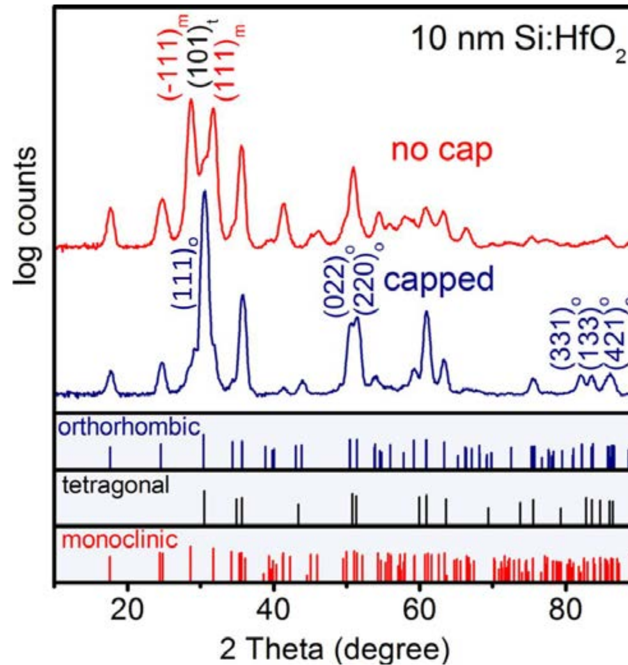


*Figure 2.10 Grazing incidence X-ray diffraction patterns of two different 3% Si-doped $HfO_2$ samples without and with the TiN capping.[35]*

Other factors related to thermal expansion mismatch, formation of oxygen vacancies and island coalescence were put forward for stabilizing the ferroelectric phase.[37] The real mechanism of how this o-phase is stabilized from other competitive phases in $HfO_2$ film is not well understood. However, it is accepted that the structure origin of ferroelectric $HfO_2$-based films is due to the formation of the polar orthorhombic $Pca2_1$ phase.

Until now, the major remaining issues of $HfO_2$-based films related to the reliability for application are the wake up effect and insufficient endurance. The wake up effect as shown in Figure 2.11(a) is usually believed to origin from the non-uniform distribution of oxygen vacancy around the interfaces with electrodes (TiN). Applying the field cycles, the diffusion and redistribution of oxygen vacancies and other charges in thin films causes the ferroelectric wake up.[140-142] Another possible mechanism for the wake up effect is related to the electric filed drived phase transition.[143,144] The wake up effect can be mitigated or overcomed by appropriate doping[145] or growing epitaxial films, which will be discussed in this thesis. The insufficient endurance is usually attributed to the large coercive voltage ($E_c$) arising from the high kinetic barrier between the two spontaneous polarization in FE $HfO_2$-based films.[104,146-148] In general, hard breakdown occurs after significant

increase of leakage current with field cycles.[144,149,150] Figure 2.11(b) summarizes $P_r$ and endurance of ferroelectric $HfO_2$-based film. As $P_r$ increase, the maximum cycling number of endurance usually decreases. The maximum endurance value over $10^{10}$ cycles was recently achieved in La-doped $HfO_2$ film with largest $P_r$ of 15 μC/cm$^2$.[151]

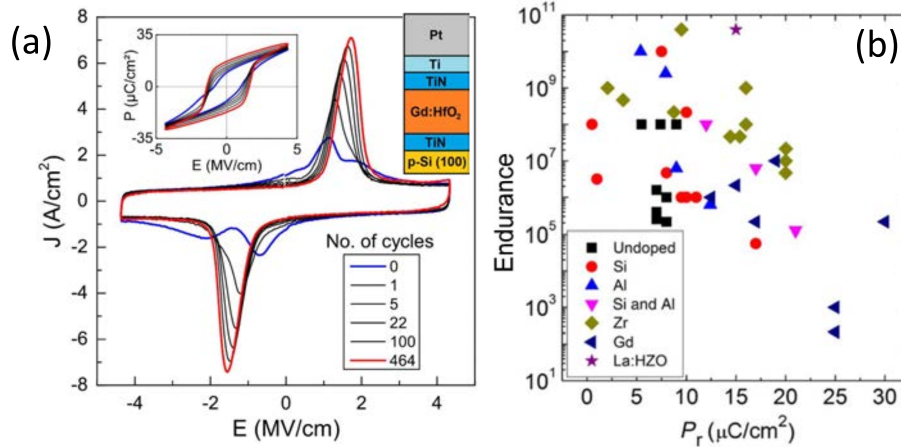


*Figure 2.11 (a) Wake up effects of Current-voltage curves for poly ferroelectric Gd:$HfO_2$ films. Inset: the corresponding P-V loop and structure sketch.[125] (b) Endurance as function of remnant polarization.[139]*

## 2.2.3 Epitaxial doped $HfO_2$ film

The new class of fully silicon-compatible hafnia-based ferroelectrics with high switchable polarization and thickness scalability shows a strong promise for new generations of logic and memory devices. The matured film deposition techniques and compatibility with three-dimensional capacitors make ferroelectric $HfO_2$ films possible to solve the scaling issue in 1-transistor-1-capacitor (1T-1C) ferroelectric random-access memories (FeRAMs) over conventional ferroelectrics. In addition, the low permittivity and high coercive field $E_c$ of hafnia ferroelectrics are beneficial for ferroelectric field-effect-transistors (FeFETs).[98] In contrast to these extensive potential applications and significant progress, the fundamental mechanisms of ferroelectric $HfO_2$ thin films such as spontaneous polarization and domain structures are not yet completely understood. Because the ferroelectric o-phase is usually induced by crystallization of the amorphous HZO film prepared by atomic layer deposition with thermal treatment, and this makes the film polycrystalline with nanometric polar orthorhombic phase and other non-polar phases coexisting in the film. Therefore, up to now, the majority studies for FE $HfO_2$-based films are polycrystalline presenting complex phases (m-, o- and t-phases) and plenty grain boundaries. The polycrystalline nature and the mixture of phases in $HfO_2$ films challenge the understanding of the role of crystal orientation, interfaces, strain, and defects in the ferroelectric properties. Another difficulty is the problem of

reproducibility in devices with ultrathin films or having small lateral size. This is because of the high inhomogeneity of films resulting from polycrystalline nature and grain boundary effects. Furthermore, oxygen vacancies form close to the interfaces with the commonly used TiN electrodes. It is normally accepted that domain boundaries and oxygen vacancies have a prominent role on undesired properties as non-switchable ferroelectric domains, dielectric breakdown, electrical leakage, wake up and fatigue effects,[152-154] all of which are critical to evaluate the performance and reliability of these films for real FE device applications.[1,2,5]

The epitaxial structures hold great advantages in investigating the ferroelectric nature.[96,155-157] The uniform orientation and well-define interfaces of epitaxial films at atomic scale makes it easier to investigate the charge screening mechanism and depolarization field between the nanometric films and electrodes, which is crucial for devices such as ferroelectric tunneling junctions.[158,159] More important, epitaxial films would be convenient to study the fundamental electrical and structure properties and further enhance device reliability.[160] Thus, for better elucidating the crystal structure, the nature of ferroelectricity in $HfO_2$ films as well as prototyping devices, growing epitaxial films which has a highly ordered atomic arrangement with well-defined orientation will be the most suitable approach.

However, in spite of these evident interests, the epitaxial stabilization of the ferroelectric orthorhombic phase is scarcely investigated and achieved in comparison with the huge progress achieved in polycrystalline films. The first demonstration of epitaxial stabilization of the orthorhombic phase, in Y-doped $HfO_2$ films,[161] was published in 2015, four years after the ferroelectricity in polycrystalline films was reported.[35] One years later, in 2016, the first measurements of polarization loops in epitaxial films was reported.[117] Until now, the epitaxial ferroelectric $HfO_2$ films has been demonstrated with two major dopants: yttrium (Y) and zirconium (Zr).

*Epitaxial Y-doped $HfO_2$.* Shimizu *et al.* demonstrated the ferroelectricity and Curie temperature for epitaxial Y-doped $HfO_2$ film grown by PLD on YSZ (110) single crystal using $In_2O_3$ (ITO) as bottom electrodes.[117,161] The saturated polarization for epitaxial Y-doped $HfO_2$ film can be 16 μC/cm$^2$ and Curie temperature was also estimated to be about 450 °C. Increasing the dopant $YO_{1.5}$ from 0 to 15 % favors the transition from low-symmetry monoclinic phase to high-symmetry tetragonal fluorite phases through an orthorhombic phase.[161,162] Further works emphasized the importance of bottom electrode ITO for inducing the ferroelectricity.[163,164,220] Also, the deposition atmosphere has a evident influence on the ferroelectric properties.[165] Under Ar atmosphere, epitaxial Y-doped $HfO_2$ film grown by RF magnetron sputtering presented better ferroelectricity and low leakage than at $O_2$ atmosphere. Recently, it has been reported that Y-doped $HfO_2$ thin films (PLD) can be epitaxially grown on YSZ-buffered Si substrate without bottom electrode.[166]

*Epitaxial Zr-doped $HfO_2$.* In Zr-doped $HfO_2$, the composition of the reported epitaxial

films is $Hf_{0.5}Zr_{0.5}O_2$. The first reported epitaxial $Hf_{0.5}Zr_{0.5}O_2$ was obtained grown on bare YSZ(100) substrate with ion-beam sputtering.[167] Structural analyses of the HZO thin films confirmed the principal orthorhombic phase and partial monoclinic phase both epitaxially coexisted in the HZO films. At the end of 2018, Wei *et al.*[168] reported epitaxial (111)-oriented $Hf_{0.5}Zr_{0.5}O_2$ thin films grown by PLD on (001)-oriented $La_{0.7}Sr_{0.3}MnO_3/SrTiO_3$ substrates. The polarization can be as large as 34 $\mu C/cm^2$ and there was no wake up effects. The structural characterization revealed a rhombohedral structure, different from the polar orthorhombic phase. Tao *et al.*[169] found that epitaxial ferroelectric HZO thin film can stabilized on (001)-, (011)- and (111)-oriented YSZ substrates with TiN bottom electrode. The $TiO_2$ buffer layer formed by the interface reaction was the key to epitaxial growth. Recently, epitaxial HZO film of (111)-oriented orthorhombic phase grown on LAO(001) using LSMO electrode has been demonstrated with a large ferroelectric resistive switching.[170]

Besides the Y and Zr doping, epitaxial $HfO_2$ film can also be stabilized with Fe and Si doping.[171,172] Despite the recent advances in epitaxial $HfO_2$-based films, the investigations in this field is still in a nascent stage. For better understanding the crystal structure and the nature of ferroelectricity, more progress in the fabrication and deeper functional characterization of epitaxial films is needed. In addition, neither application-related ferroelectric properties such as retention and fatigue nor the integration of epitaxial $HfO_2$-based films on Si(001) in a capacitor structure for future device manufacturing were not reported.

In this thesis, we select $Hf_{0.5}Zr_{0.5}O_2$ as target to investigate the epitaxial film growth. The reason is that due to the very similar physical and chemical properties of Zr to those of Hf, $HfO_2$-$ZrO_2$ solid solution system can show ferroelectricity in a wide chemical composition range and peaks at around $Hf_{0.5}Zr_{0.5}O_2$.[108] Since the effect of deposition parameters on structural and ferroelectric properties is of pivotal importance for further development of epitaxial films of ferroelectric hafnia, the influence of deposition parameters (substrate temperature and oxygen pressure) and film thickness on epitaxial $Hf_{0.5}Zr_{0.5}O_2$ film by pulsed laser depositions is investigated to determine the growth window for epitaxial $Hf_{0.5}Zr_{0.5}O_2$ film. Next, the epitaxial $Hf_{0.5}Zr_{0.5}O_2$ films will be integrated on Si with different buffer layers. The extensively characterization for electric properties such as polarization, leakage, retention and fatigue of epitaxial $Hf_{0.5}Zr_{0.5}O_2$ thin films is also performed.

# Chapter 3. Experimental Methods

In this chapter, we will describe the principles of the main experimental techniques used in this thesis for the thin films deposition and characterization. Firstly, we talk about the sample preparation which involves how to prepare targets for pulsed laser deposition and the basic principles of pulsed laser deposition and sputtering for thin film growth of oxides and metal, respectively. Then characterization techniques are introduced, mainly X-ray diffraction and atomic force microscopy for structural characterization and the methods used to measure the ferroelectric properties.

## 3.1 Sample preparation

### 3.1.1 Targets

The ceramic targets used in pulsed laser deposition device for thin film growth were prepared by solid state reaction. The process involved the following steps: (a) stoichiometric weight of commercial oxide powders (above 99 % purity); (b) uniform mixing with hand-mortar; (c) pelletizing with uniaxial pressing; (d) sintering in a tubular furnace. The sintered targets were examined by X-ray diffraction. If needed, the targets were grinded into powder and repeat the steps of pelletizing and sintering until the X-ray diffraction pattern indicated that the chemical reaction is fully completed. The targets with commercial powders used in this thesis are listed in below Table 2.1.

*Table 2.1 Ceramic targets used in this thesis*

| Target | Short name | Chemicals/ Supplier/ Purity | Composition |
|---|---|---|---|
| *$BaTiO_3$* | *BTO* | *Commercial $BaTiO_3$ powder/ Alfa Aesar/ 99.9 %* | *100 mol % BTO* |
| *$Hf_{0.5}Zr_{0.5}O_2$* | *HZO* | *$HfO_2$ powder/ Alfa Aesar/ 99.95 %* | *50 mol % $HfO_2$* |
| | | *$ZrO_2$ powder/ Alfa Aesar/ 99.978 %* | *50 mol % $ZrO_2$* |

### 3.1.2 Pulsed laser deposition

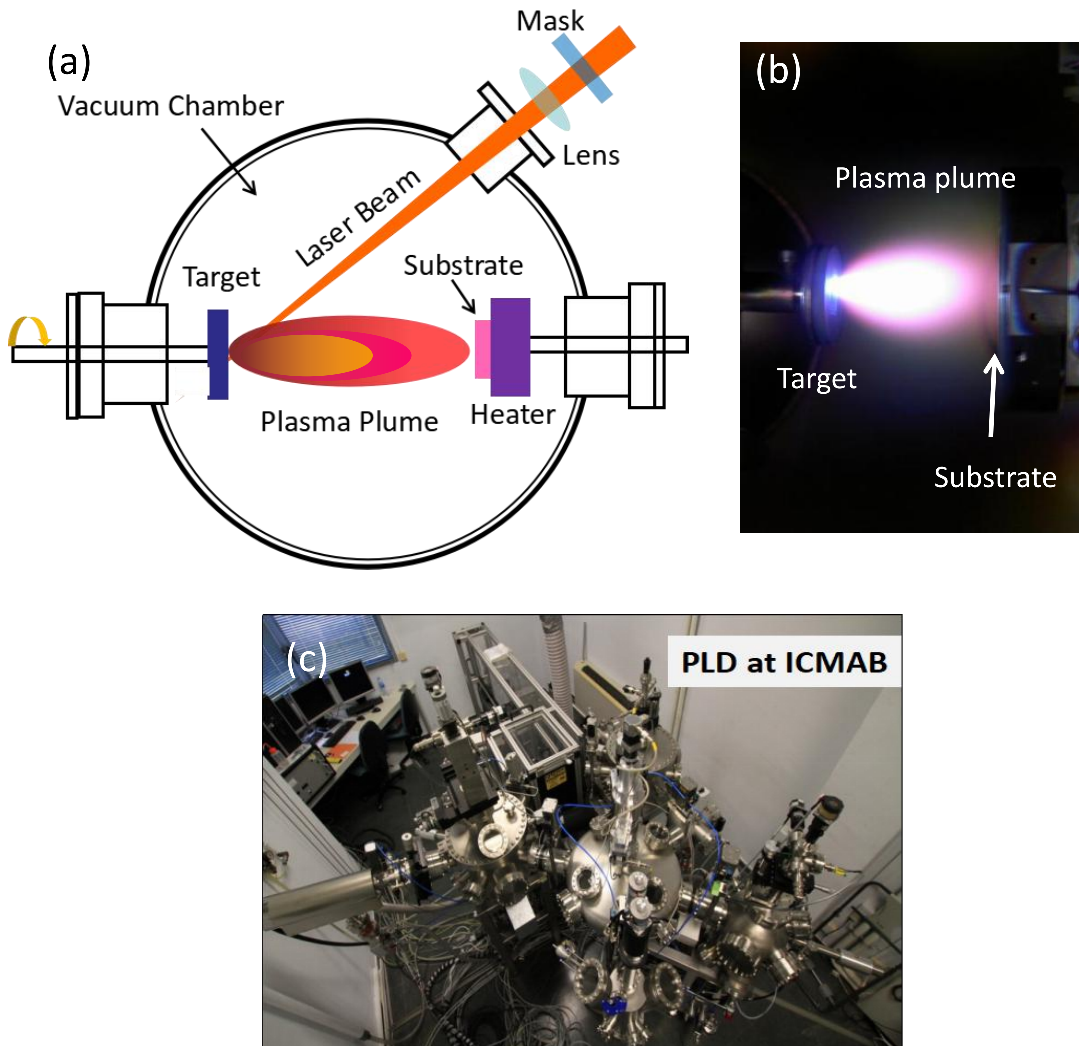


*Figure 3.1 (a) Sketch of a PLD system. (b) Plasma plume generated by the interaction of the laser pulse with a target material. (c) The thin film laboratory at ICMAB.*

Pulsed laser deposition (PLD) was used for growing the oxide thin films investigated in this thesis. It is a physical vapor deposition technique based on the interaction between laser pulses and the target material. PLD has already attracted attention over the last 30 years, as it enables the fabrication of multi-component stoichiometric thin films from a single target. A basic sketch illustrating the PLD working mechanism and the experimental PLD setup in ICMAB are shown in Figure 3.1(a) and (c), respectively. The PLD process can be divided into three stages: (a) Laser ablation and plasma formation. A pulsed ultraviolet laser beam (usually KrF excimer laser with wavelength $\lambda$ = 248 nm and pulse width of 10 ~ 40 ns) is focused through a window on the surface of the ceramic target placed inside the vacuum chamber. The vacuum chamber is usually filled with oxygen background at a given pressure during film

growth. When the high energy laser beam arrives to the target surface, the target material around a small surface region is ablated and vaporizes into a plasma. This plasma plume contains the stoichiometric composition of target material. Also, with varying masks and lens on the laser path, the laser energy and energy density can be controlled; (b) Plasma expansion. Once the plasma is formed, it will expand towards the substrate. A picture of plasma plume is shown in Figure 3.1(b). This step usually takes less than 10 μs, which depends on the background pressure inside the PLD chamber. (c) Deposition and film growth. When the high energetic plasma approaches the substrate surface, the nucleation and thin film growth occurs. The substrate temperature is controlled using a thermocouple inserted in the middle of the heater block.

### 3.1.3 Sputtering

Top metal electrodes were *ex-situ* deposited on the surface of ferroelectric thin films using DC (direct current) magnetron sputtering through stencil masks. The sputtering process involves bombarding a target material with ionized Ar gas, emitting atoms into the plasma. Under the magnetic field created by the magnetron, the sputtering rate is increased. The emitted atoms condense as a thin film on the substrate. TEM grids were placed to deposit the metal electrode through shadow mask. In this thesis, Pt was used as top electrode because Pt is a noble metal with chemical stability and good rectifying characteristic.[85] The DC sputtering conditions for Pt deposition were dynamic Argon pressure of 5 x $10^{-3}$ mbar, power 10 W and room temperature. The thickness of Pt was 20 nm. In this thesis, there are two different sizes of TEM grids used as mask allowing to deposit top Pt contact area. For the BTO samples, the electrode contact is 60 μm x 60 μm square with 15 μm distance apart from each as shown in Figure 3.2(a). For the HZO samples, while 20 μm diameter circle of top Pt contact with 10 μm distance apart from each is deposited as shown in Figure 3.2(b).

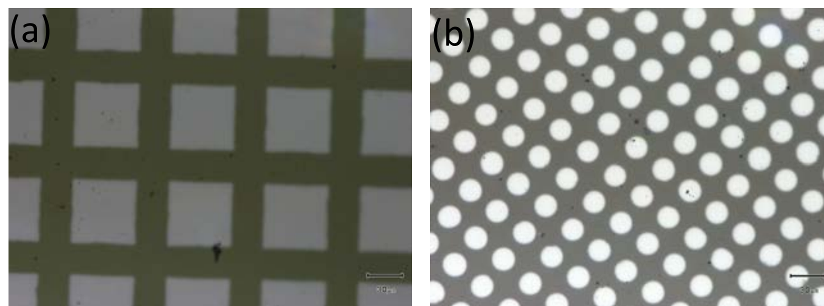


*Figure 3.2 Pt top contacts under optical microscopy for (a) 60 μm x 60 μm square in size on a BTO film (b) for 20 μm diameter in circle on a HZO film.*

## 3.2 Sample characterization

Here we present the experimental techniques used for structural and electrical characterization of the thin films investigation in this thesis.

### 3.2.1 X-ray diffraction

X-ray diffraction (XRD), a non-destructive crystal structure analyzing technique, has been used to acquire the information of the thin films such as lattice constants, crystal orientation, film thickness, epitaxial relationships between films and substrate, etc. For determining these characteristics of crystallographic structure of epitaxial thin films, four-cycle X-ray diffractometers were also used. In addition to the standard two circles ($\omega$ and $2\theta$) in simple X-ray diffraction equipment, the four circle tool has two additional degrees of freedom represented by the angular cycles $\phi$ and $\chi$, which allow the probing of the planes that are not parallel to the substrate surface. The four angles are shown in Figure 3.3(a).

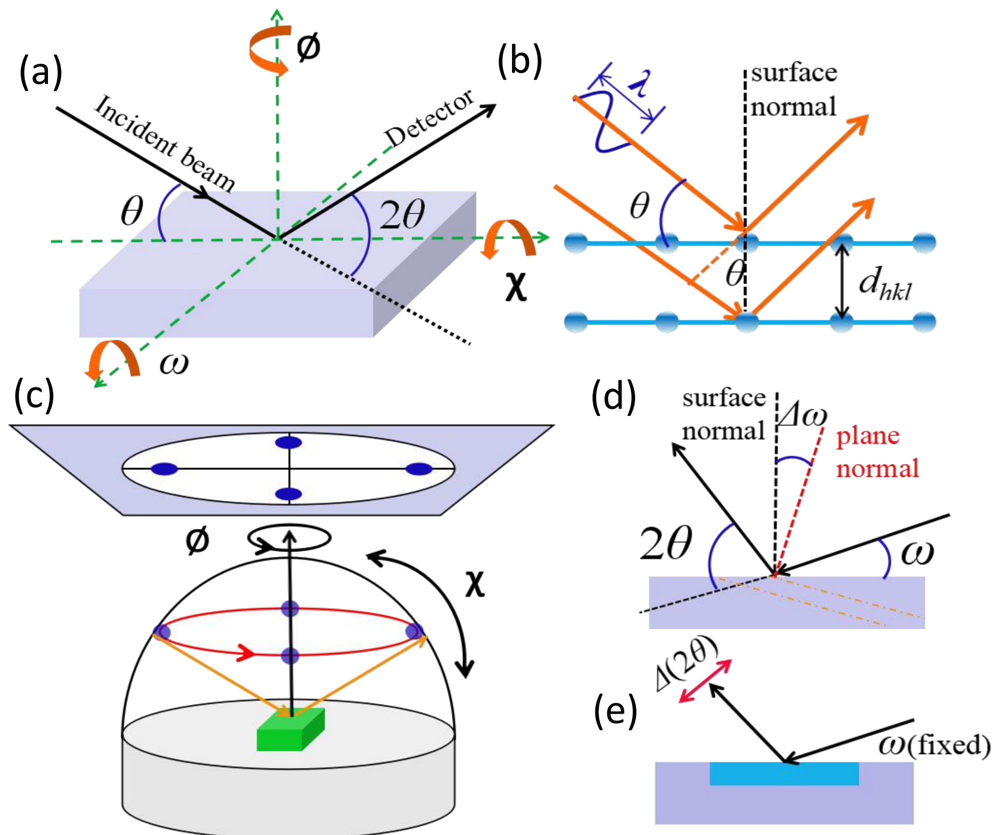


*Figure 3.3 (a) The schematic of geometry for a four cycles diffraction setup. (b) The schematic of Bragg's law. (c) Sphere of the pole figure defined by spherical coordinates $\chi$ and $\phi$ and projection of the pole sphere. (d) Sketch of the asymmetric scan in RSM ($\omega \neq \theta$, $\chi = 0$). (e) Sketch of GIXRD configuration.*

*θ-2θ scan* The symmetric $\theta$-$2\theta$ scan (also called $\omega$-$2\theta$ scan) is the most basic XRD measurements with the $\omega$ and $2\theta$ circles moving simultaneously along the sample surface. It was used in this thesis to determine the crystal phase, out of plane crystal orientation and lattice parameters of thin films. The principle are shown in Figure 3.3(b). When a film with an certain interplanar spacing $d$ (the out of plane parameter in a symmetric scan) is irradiated by a x-ray beam with a comparable wavelength $\lambda$, the constructive interference between elastically scattered x-ray beams can be detected at specific angles $2\theta$ when the Bragg's Law is satisfied:

$$n\lambda = 2d\sin\theta \tag{3.1}$$

where $n$ is any integer. In most diffractometers the $X$-ray wavelength $\lambda$ is fixed and the diffraction angle $\theta$ is varied. The crystal lattice constants can be determined according to the above equation.

*X-ray reflectivity (XRR)* X-ray reflectivity (XRR) measurement was used to determine the thickness of films if the thickness is in about 10 - 100 nm range and the roughness of top surface and interfaces is not too large. It is performed in $\theta$-$2\theta$ scans mode but at low angles ($2\theta$ = 0.5° ~ 8°). In an *XRR* experiment, the incident *x*-ray beam reaches the surface of the thin layer at very low incidence angle. One part of the beam is reflected at the same angle, the other part penetrates the layer with the thickness $d$ and reflected at the interface between the layer and the substrate. Both beams are parallel and they may present interference fringes depending on the angle of incident beam and the layer thickness. In this case, the Bragg reflection takes place at top surface and the interface of the film instead of crystal plane and the Bragg's Law described by equation (3.1) is satisfied. Therefore, the film thickness can be determined.

*Rocking curve (ω scan)* Rocking curve, also called $\omega$ scan, is a useful way to evaluate the crystal perfection. By fixing the detector at the center of the Bragg reflection, the sample is tilted with varying the $\omega$ angle for measurement. The peak width of the rocking curve is an important value to study the crystal quality. The perfect crystal will produce a very sharp peak. The increase in the peak widths is caused by mosaicity (misorientation of crystallites), and inhomogeneity or structural defects can also contribute. Here we use the full width at half maximum (*FWHM*) to quality this information on the crystallinity of the oxide films.

*ϕ scan* In asymmetrical *ϕ scan*, a set of planes not parallel to the surface of the substrate is selected by setting the $\omega/2\theta$ angles and tilting the $\chi$ angle perpendicular to the plane of incidence and then swept by rotating around the $\phi$ cycles while all other angles are kept fixed. This scan reveals information about in-plane alignment for further determining the epitaxial relationship between each layers and substrate.

*Pole figures* Pole figures include multiple $\phi$ scans measurement at a range of $\chi$

angles as shown in Figure 3.3(c). During the pole figure measurement, the $\omega$ angle is fixed for a chosen direction of the film, and the $\phi$ and $\chi$ angles are varied. The pole figure can confirm the epitaxial relationship of each layers and check the crystallinity and other possible minor orientations in the films which can not be distinguished in a *θ-2θ scans*, e.g., because of a relatively weak peak intensity.

*Reciprocal space maps* (*RSM*) Asymmetric reciprocal space maps (RSM) measurement were used to determine the in-plane lattice parameters and strain states of the epitaxial films. The expected Bragg reflections are usually selected and obtained by varying the $\omega$ angles and performing a *ω-2θ scans*, where the tilted angle $\Delta\omega$ is in direction of the diffraction plane as shown in Figure 3.3(d). An area of reciprocal space can be mapped using the relationships:

$$Q_{//} \cong \frac{4\pi}{\lambda}\sin\theta\cos(\omega-\theta); \quad Q_{\perp} \cong \frac{4\pi}{\lambda}\cos\theta\sin(\omega-\theta) \tag{3.2}$$

Data are usually shown in a 2D contour map of the intensity, showing the diffraction peaks from certain layers and substrate. It should be noted that the selected Bragg reflections should be asymmetric with respect to the surface normal to provide the in-plane and out-of-plane information of epitaxial films.

*Glancing incidence X-ray diffraction* (*GI-XRD*) This method uses a fixed angle of incidence $\omega$ and the measurement is carried out by only moving the detector ($2\theta$ scan) as shown in the Figure 3.3(e). GI-XRD measurement was only used for HZO film grown on Si with LNO bottom electrodes.

*Two-dimensional X-ray diffraction (2θ-χ frame)* Two-dimensional (2D) X-ray diffraction measurement refers to 2D diffraction patterns performed by two-dimensional detector in X-ray diffraction. In the conventional diffractometer with one point detector, the diffraction measurement is confined within one plane (diffractometer plane), which makes $2\theta$ scan along a detection circle. With a 2D detector, the measurable diffraction is no longer limited in the diffractometer plane. Instead, 2D detector allows us to collect and integrate the data into a *2θ-χ* frame in a certain range of $\theta$ and $\chi$ angles simultaneously,providing the information about the film orientation, spreading and lattice parameters. The two-dimensional detector was employed in Chapter 5 to investigate the fraction of monoclinic phase and epitaxial quality in HZO films.

In this thesis, three diffractometers located in ICMAB were used to perform the relevant measurements. The *θ-2θ* scan, $\omega$ scan, XRR and GI-XRD measurements were performed at Siemens D5000 diffractometer (one point detector) using a Cu Kα radiation with wavelength of $\lambda$ ($K\alpha_1$) = 1.54056 Å and $\lambda$ ($K\alpha_2$) = 1.54439 Å. And the standard measurement for *θ-2θ* scan is using 0.2 second for data acquisition at each

step (stepsize 0.02°). The $\phi$ scan and reciprocal space mapping (RSM) were measured using a Bruker D8-ADVANCE diffractometer with Cu $K\alpha_1$ radiation. The device of GADDS diffractometer (Cu Kα1) equipped with a two-dimensional (2D) detector was used for the measurement of pole figure and the two-dimensional X-ray diffraction measurements.

### 3.2.2 Atomic force microscopy

Atomic force microscopy (AFM) has been used to study the topography of the thin films. As shown in the working scheme of a AFM device in Figure 3.4(a), the mechanism of AFM is based on the detection of the laser beam reflected by a silicon cantilever with a nanometric tip for sensing the force interacting between the film surface and the tip. AFM can operate in non-contact, tapping and contact modes, depending on the tip force and tip-surface separation. In this thesis, the non-contact mode was used obtain information about the film surface morphology. The tip scans across the film surface based on maintaining the interacting force between the surface atoms and the tip due to van der Waals forces[173] as sketched in Figure 3.4(b). The force changes in maintaining this constant distance can be converted into signals by 4-quadrant photodetector indicating the topographical variation of the film surface in amplitude, phase or frequency.

In this thesis, an Agilent 5100 AFM system equipped with silicon tips in ICMAB was used for performing the AFM measurements. Usually, two regions of 5 x 5 $\mu m^2$ and 1 x 1 $\mu m^2$ on thin film surface were scanned.

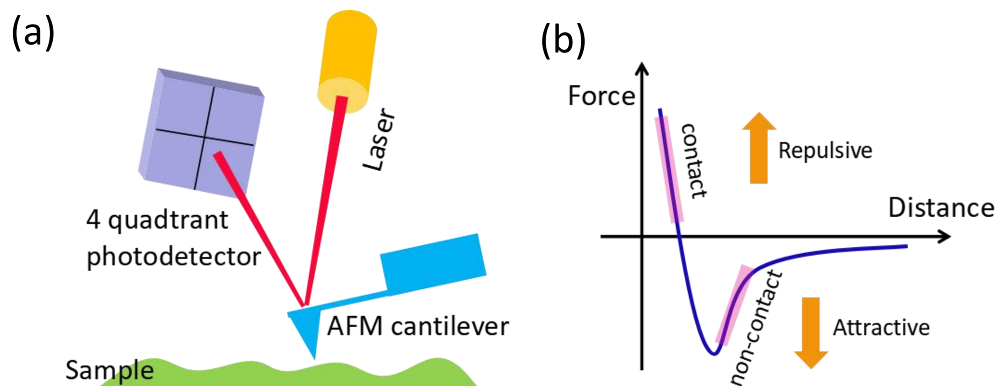


*Figure 3.4 (a) Schematics of an AFM device. (b) Interaction forces (Van del Waals) between the tips and surface atoms.*

### 3.2.3 Electric characterization

Electric characterization of ferroelectrics was performed using *aixACCT* TFAnalyser

2000 system which permits performing polarization hysteresis loops, leakage, retention and fatigue measurements.

*Ferroelectric loops measurement* The ferroelectric polarization - electric field (P - E) hysteresis loops were recorded by applying triangular voltage waveform using two different electrodes configurations, top-bottom (*t-b*) and top-top (*t-t*), as shown in Figure 3.5(a)-(b), respectively. In the t-b configuration, the electric field was applied on the top electrode with virtual grounded bottom electrode and one single capacitor was measured. When employing the different top and bottom electrodes, the loops were usually asymmetric due to the different work function. In the case of the t-t configuration, consisting of two thin film capacitors connected in series through the bottom electrode, the FE loops are symmetric.[175]

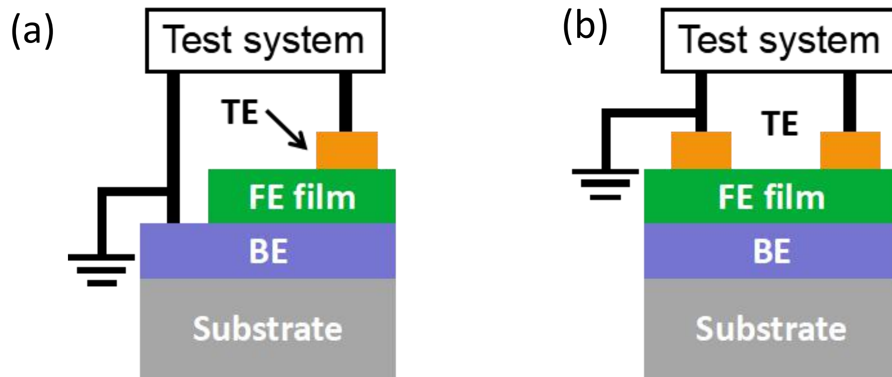


*Figure 3.5 Measurement configurations (a) Top-bottom (b) Top-top configurations. (BE and TE indicate the bottom and top electrode, respectively)*

In this thesis, the hysteresis loops of the ferroelectric thin films were measured with two methods: Dynamic hysteresis measurement (*DHM*) and Dynamic Leakage Current Compensation measurement (*DLCC*).[176] In *DHM* method, four bipolar triangular voltage pulses of frequency $v_0$ are applied with a delay time $\tau$ (1 s) between each pulses as shown in Figure 3.6(a). The first (third) bipolar voltage (V) pulse prepolarizes the sample in the negative (positive) state. The final obtained P-E loop is the combination from the negative part of second pulse and the positive part from the forth part. However, hysteresis loops are calculated with the leakage contribution included, influencing the results especially when leakage is large in ferroelectric thin films. The *DLCC* measurement can effectively remove the leakage current contribution from a ferroelectric polarization loop. Under the assumption of leakage current $I_{leakage}$ independent of the frequency and the displacement current ($I_\varepsilon + I_{FE}$) linearly dependent on the frequency, voltage pulses of two frequencies ($v_0$ and $v_0/2$) in *DLCC* method are applied and allows the subtraction of $I_{leakage}$. The voltage pulses applied for *DLCC* measurement are shown in Figure 3.6(b). In this thesis, ferroelectric hysteresis loops were performed in *DLCC* mode to minimize leakage current effects, unless specified.

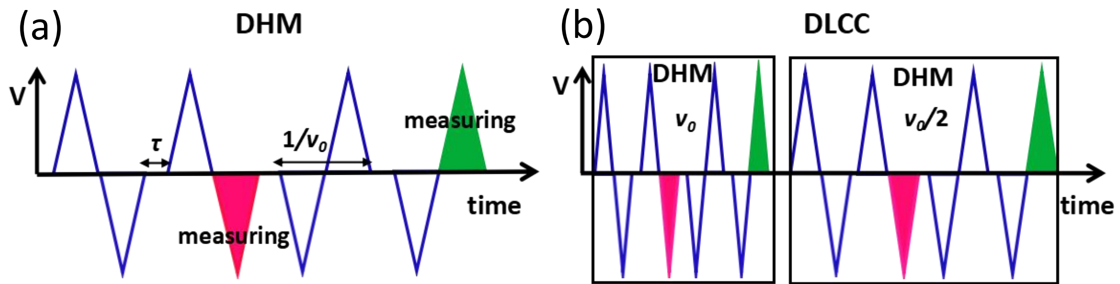


*Figure 3.6 Voltage pulses applied for (a) DHM (b) DLCC modes. τ is the delay time between pulses and $v_0$ is the applied pulse frequency.*

*Leakage measurement* Leakage current through thin dielectric films is usually unavoidable and its magnitude can impact the reliability of a device. The leakage current measurement is performed by applying a step shaped voltage waveform to the sample and measuring the current response. Since a ferroelectric capacitor can be considered as a non-linear capacitor and a voltage dependent resistor in parallel, the pure leakage current can be extracted from the current response due to the applied step waveform voltage with time duration. And the current reading is averaged in the region from 70 % to 90 % of the step time when the current response is stable, giving a precise measurement of the leakage value. In this thesis, the leakage current curves for the ferroelectric thin films were measured by averaging I-V curves increasing and decreasing the voltage using 3 s integration time.

*Retention measurement* Retention is described by the ability of a ferroelectric material to retain the sign and magnitude of the remnant polarization with time (Figure 3.7a). Short retention can cause a memory failure if the polarization drops to the minimum limit which cannot be detected. The retention was measured by poling a sample into a known state and reading out the remaining remnant polarization after defined periods. The signal sequence consisting a writing and five read pulses for retention data is shown in Figure 3.7(b).

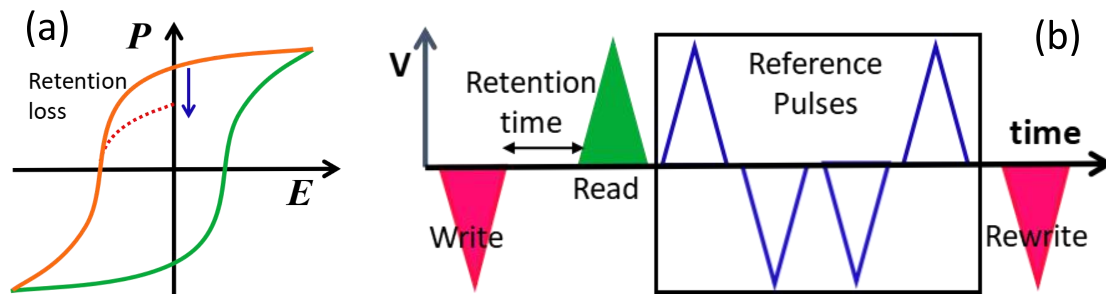


*Figure 3.7 (a) Polarization decrease with time. (b) Voltage pulses applied for acquiring the retention data.*

By prepoling the sample into a known state, the first opposite read pulse measures the

remnant switchable polarization after the defined retention time and the following four pulses determine the absolute polarization value. The variation can be extracted which stands for the polarization loss of the prepoling state. We can obtain the result of retention behavior of $P_r$ with time by repeating this procedure and delay time.

*Fatigue (endurance)* Fatigue describes the loss of polarization due to bipolar field cycling of the ferroelectric capacitor in Figure 3.8(a). In a FeRAM device, switching cycles are performed during writing and reading operations. When the margin between the positive and negative states is below the detection threshold due to the fatigue, the failure of a memory cell will occur. As shown in Figure 3.8(b), a fatigue signal (bipolar rectangle pulses sequence) is applied after measuring the initial hysteresis loop and regularly interrupted for hysteresis measurements to monitor and record polarization value.

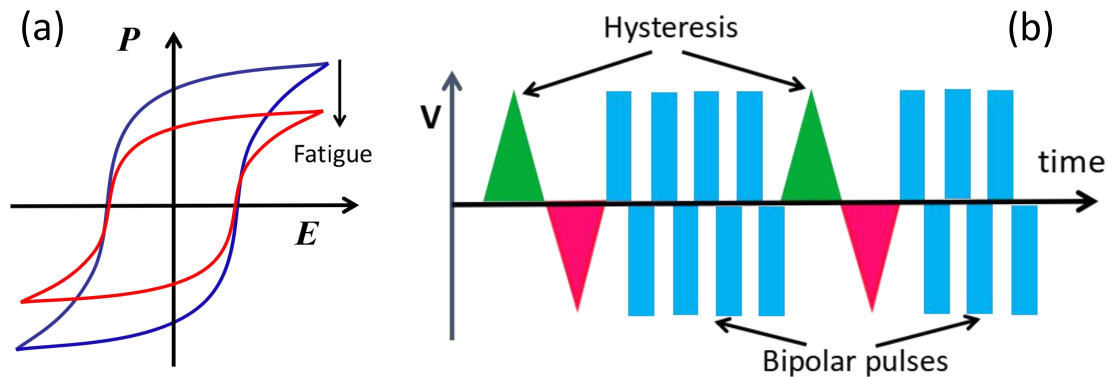


*Figure 3.8 (a) Representative fatigue P-V loops with cycles. (b) Typical voltage pulses for fatigue measurement.*

Typically, rectangular waveform is used to determine the highest amount of switching. If fatigue measurement is performed at high frequencies, it has to be ensured that the sample is switched. Due to the reduced endurance of HZO films compared with perovskite ferroelectric films, we focus on fatigue measurements on epitaxial HZO films in this thesis. To evaluate the appropriate frequency which can be used in endurance measurement of HZO films, two procedures have been considered. One is measuring the fatigue with cycles at different frequency as shown in Figure 3.9(a); another way is to mimic the waveform during the fatigue cycling and further check the effective polarization compared with measurement under the effective condition as shown in Figure 3.9(a)-(c). In Figure 3.9(a), one can see that the $P_r$ loss rate show no dependence with these four frequencies, which means FE domains can be fully switched at 100 kHz. In fact, with higher frequency, slightly small loss rate can be observed. This difference might be related with the thermal effect due to the increasing leakage with cycles, which degrades the $P_r$. The second way as shown in Figure 3.9(b)-(c) is exciting the polarization with the rectangular voltage waveform at different frequencies (1 kHz, 10 kHz and 100 kHz) which were applied in fatigue measurement. From 1 kHz to 100 kHz, the polarization show a negligible drop within

2 μc/cm² drop from 30.5 μc/cm² to 28.7 μc/cm². And at 500 kHz, it cause the dielectric breakdown (results are not shown here). As 1 kHz is effective frequency which is used to obtain the P-V hysteresis loops and the similar switching polarization can also be achieved in 100 kHz, the frequency for endurance measurement is set at 100 kHz finally.

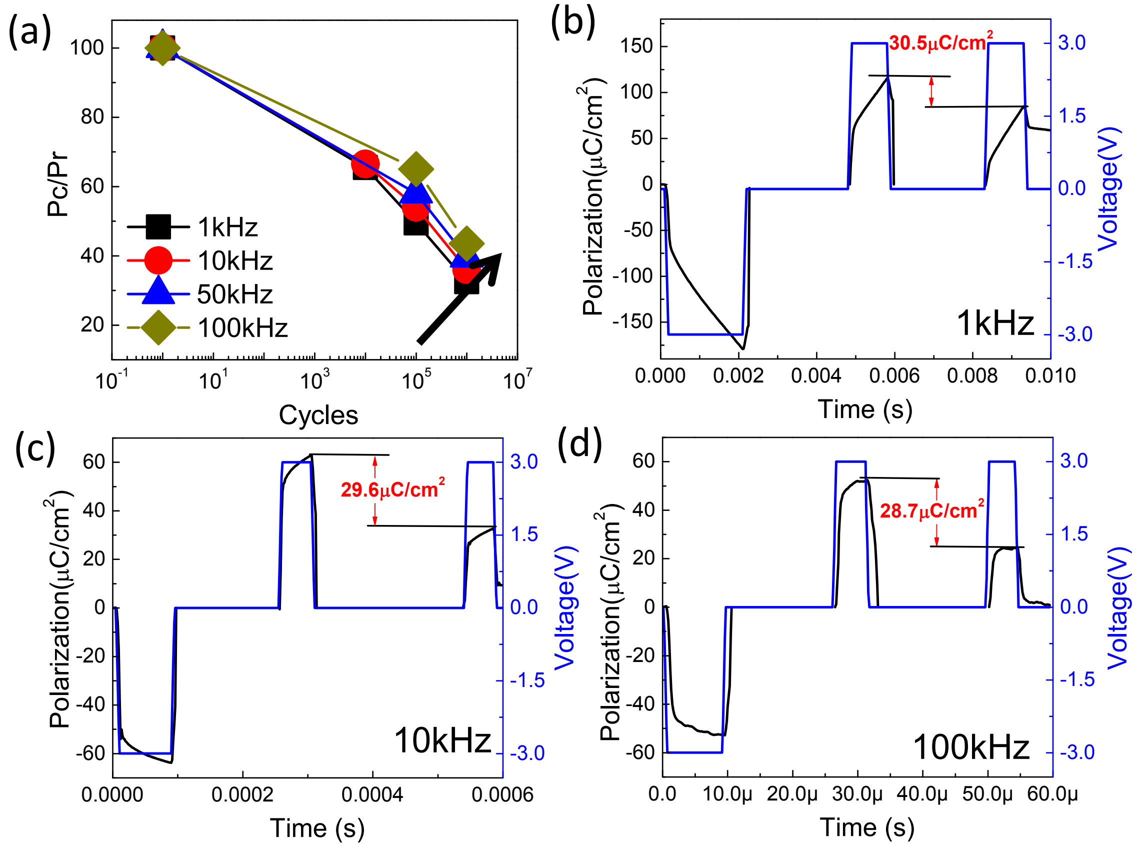


*Figure 3.9 (a) The remnant polarization normalized to its initial value remnant as a function of electric cycling at different fatigue frequencies for 9.7 nm thick HZO on LSMO/LNO/CeO₂/YSZ/Si(001). Applied square voltage and integrated polarization as a function of time at frequency (b) 1 kHz, (c) 10 kHz, and (d) 100 kHz for 4.6 nm thick HZO on LSMO/LNO/CeO₂/YSZ/Si(001).*

## 3.2.4 Other techniques

### Optical Microscope

A optical microscope (Leica DM 1750M) located at ICMAB was used to check the quality of top electrodes and actual contact areas.

**Dielectric measurement**

The dielectric measurements were performed by using an impedance analyzer (HP4192LF, Agilent Co.) operated with an excitation voltage of 50 mV at 20 kHz with top-bottom configuration. The dielectric permittivity ($\varepsilon_r$) - voltage loops can be extracted from capacitance ($C$) value using the $C = \varepsilon A/t$ relation, where $A$ is the electrode area, and $t$ the film thickness.

**Photocurrent measurement**

The identification of randomly distributed point defects in oxide thin films by transmission electron microscopy is quite challenging. Therefore, the photocurrent as an indirect method induced by the illumination is used in this thesis to evaluate the presence of point defects in BTO films. It is known that the point defects in BTO can introduce donor states, either shallow or deep in the bandgap and thus a significant photon absorption, even for sub-bandgap incoming photons, can be anticipated, forming the photocurrent.[174] The amplitude of photocurrent should be proportional to the amount of point defects in oxides films. In this thesis, the short-circuit photocurrent was measured by illuminating the sample with blue laser of wavelength 405 nm (Shenzhen 91 Laser Co.) with energy of 3.06 eV, close but smaller than the optical gap of BTO (3.3 eV) as a probe for point defect concentration. Photoinduced current was monitored as a function of time switching on the illumination at 5 s and off at 15 s. The spot diameter was of 200 μm safely illuminating the measured electrode.

# Chapter 4. Epitaxial Ferroelectric $BaTiO_3$ thin film on Si

*Conventional strain engineering of epitaxial ferroelectric oxide thin films is based on the selection of substrates with a suitable lattice parameter. We demonstrate a flexible strategy of strain engineering for epitaxial ferroelectric $BaTiO_3$ films permitting the tuning of $BaTiO_3$ tetragonality and ferroelectric polarization and the control of polar axis orientation based on balancing the kinetics and thermodynamics during the pulsed laser deposition growth. The new strategy of strain engineering can be applied to films on specific substrates including Si(001) and perovskites, and it is not restricted to ultrathin films.*

*On the other hand, the role of electrode-interfaces is investigated in a series of $BaTiO_3$ capacitors with different electrodes (perovskite metallic oxides $La_{2/3}Sr_{1/3}MnO_3$ and $LaNiO_3$ and noble metal Pt). The impact of the electrode on the electrical properties such as ferroelectric polarization, leakage and imprint field of epitaxial $BaTiO_3$ films was determined.*

## 4.1 Strain Tuning of Epitaxial $BaTiO_3$ Films on Si(001)

*Abstract*

*Ferroelectric $BaTiO_3$ films with large polarization have been integrated with Si(001) by pulsed laser deposition. Here, we show that epitaxial growth of high quality $BaTiO_3$ films on Si(001) can be achieved in broad ranges of deposition parameters, permitting fine tuning of the balance of kinetics and thermodynamics during growth, with huge impact on the $BaTiO_3$ tetragonality and ferroelectric polarization. In particular, (a) c-oriented epitaxial $BaTiO_3$ films are obtained in a substrate temperature range of about 300 °C wide and the deposition temperature critically affects the growth kinetics and thermodynamics balance, resulting on a huge impact on the strain of the $BaTiO_3$ polar axis (exceeding 2 %) and ferroelectric polarization (up to 11 $\mu C/cm^2$) scaling with strain; (b) the oxygen pressure can permit continuous tuning of strain up to over 0.8 % in films and selecting the polar axis orientation to be either parallel or perpendicular to the substrate surface plane; (c) the c-axis strain from -0.8 % to around 2 % can be tuned by the deposition growth rate and the polarization can be as large as over 14 $\mu C/cm^2$ with the polarization not scaling with the lattice strain. This developed strategy provides a feasible way that can overcome the main limitations of the conventional strain engineering methodologies based on substrate selection: it can be applied to films on specific substrates including Si(001) and perovskites, and it is not restricted to ultrathin films.*

As introduced in chapter 2.1, the lattice strain generally causes dramatic effects on the properties of ferroelectrics. By selection of a proper substrate the elastic strain can be controlled in a certain range, which permits increasing the ferroelectric polarization and the Curie temperature.[177] However, the substrate-based strain engineering is limited to relatively small ranges of strain and film thickness due to plastic relaxation. More importantly, it requires the selection of a specific substrate, whereas for most of the applications the ferroelectric films have to be integrated with silicon. Therefore, alternatives to control lattice strain are required. For this purpose, it is relevant that ferroelectric $BaTiO_3$ thin films deposited by energetic techniques like pulsed laser deposition present expansion of the crystalline unit cell.[40,41,61-64] The expansion is likely due to defects, and therefore the relative relevance of thermodynamics and kinetics during deposition of $BaTiO_3$ thin films can influence the amount of defects and consequently of the lattice strain.

In this Section, based on controlling the point defects for generating the strain by tuning the balance between thermodynamics and kinetics in the growth process of BTO, three methods by altering the substrate temperature, deposition oxygen pressure and growth rate are proposed. The illustrative sketch with the three different growth parameters and the heterostructure with the thickness of each layer used in this section can be seen in Figure 4.1.1(a) and (b), respectively.

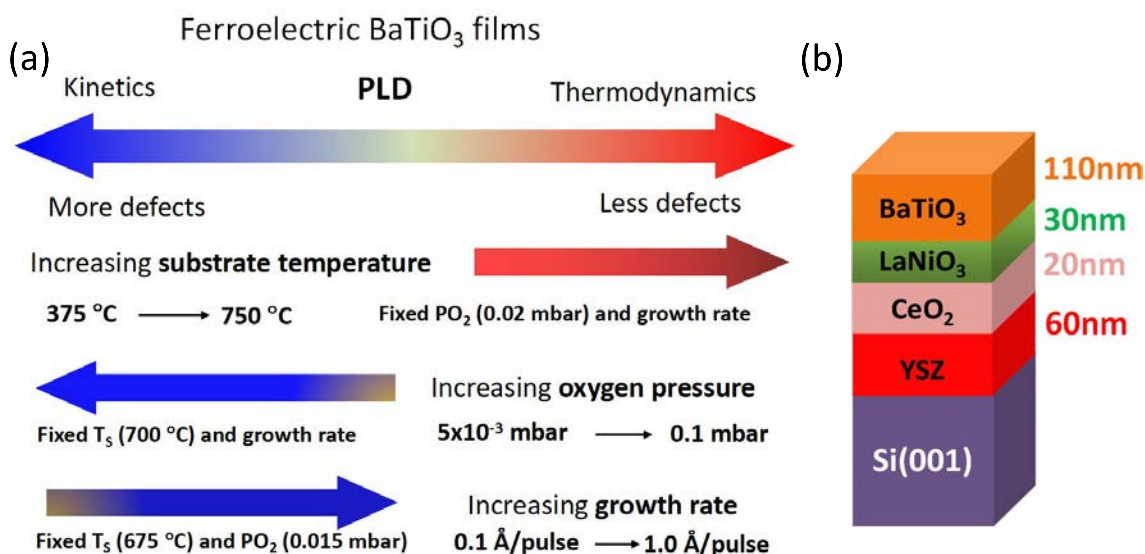


*Figure 4.1.1 (a) The illustrative sketch for deposition process of BTO films with varying the substrate temperature, oxygen pressure and growth rate. (b) Sketch of the heterostructure.*

BTO films were deposited on Si(001) substrates using a LNO/$CeO_2$/YSZ multi buffer layers (Figure 4.1.1a) in a single process by pulsed laser deposition. The choice of the buffers and the related growth process are detailed in Section 2.1.2. The detailed deposition conditions of each layer are summarized in Table 2.

Table 2 The deposition conditions for the BTO/LNO/$CeO_2$/YSZ/Si(001) samples.

| Layer | Temperature (ºC) | Pressure (mbar) | Growth rate (Å/pulse) | Frequency (Hz) |
|---|---|---|---|---|
| YSZ | 800 | $4 \times 10^{-4}$ | 0.24 | 5 |
| $CeO_2$ | 700 | $4 \times 10^{-4}$ | 0.5 | 5 |
| LNO | 700 | 0.15 | 0.2 | 5 |
| BTO | 375 - 750 | 0.005 - 0.1 | 0.099 - 1.05 | 5 |

For the deposition of BTO film, substrate temperature ($T_s$), oxygen pressure ($P_{O2}$) and growth rate (GR) are three variable parameters. The details about these three parameters are:

***$T_s$* series**

Under $P_{O2}$ = 0.02 mbar and GR = 0.550 Å/p, the specific $T_s$ = 375 °C, 400 °C, 410 °C, 425 °C, 450 °C, 500 °C, 550 °C, 600 °C, 650 °C, 675 °C, 700 °C, 725 °C, and 750 °C.

***$P_{O2}$* series**

Under $T_s$ = 700 °C and GR = 0.550 Å/p, the specific $P_{O2}$ = 5 x $10^{-3}$ mbar, 0.01 mbar, 0.015 mbar, 0.02 mbar, 0.05mbar, and 0.1 mbar.

***GR series***

Under $T_s$ = 700 °C and $P_{O2}$ = 0.015 mbar, the specific GR = 0.099 Å/p, 0.184 Å/p, 0.345 Å/p, 0.550 Å/p, 0.647 Å/p, 0.688 Å/p, 0.832 Å/p and 1.050 Å/p.

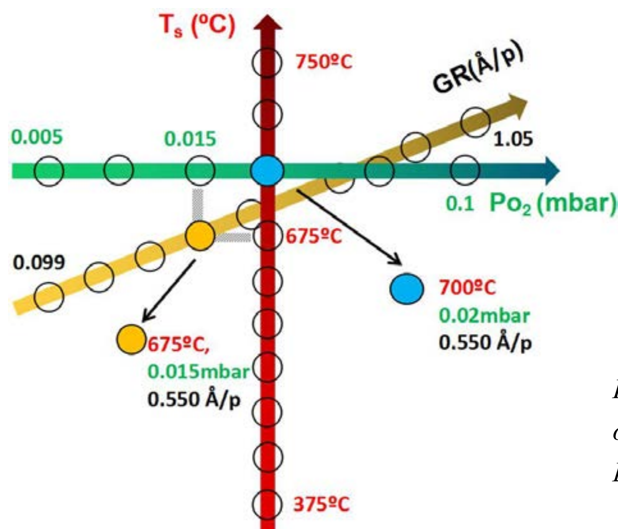


*Figure 4.1.2 Schematic overview of the deposition parameters for $BaTiO_3$ film growth.*

After deposition, the BTO films were cooled down to room temperature under an oxygen atmosphere of 0.2 mbar. Two additional films deposited on Si(001) at $T_s$ = 700 °C were cooled down under 200 mbar of oxygen, adding for one of them an in-situ at 600 °C for 1 hour. The effect of ex-situ annealing (1 hour, 200 mbar) was investigated on the $T_s$ = 450 °C and 600 °C films on Si(001). Both samples were annealed sequentially two times at 450 °C and 600 °C for 1 hour under 200 mbar.

## Results and Discussion

### 4.1.1 Substrate Temperature

**Structural Study**

The specular XRD $\theta$-$2\theta$ scans of the samples on Si(001) are shown in Figure 4.1.3(a). There are (00*l*) reflections from the Si substrate, YSZ, $CeO_2$ and LNO buffer layers, and BTO film, without peaks from spurious phases or other crystal orientations. It is remarkable that in spite of the broad range of BTO growth temperature (close to 400 °C, from $T_s$ = 375 °C to 750 °C), BTO is single (00*l*) oriented in all the samples. A zoomed region of the $\theta$-$2\theta$ scans around the (002) reflections of BTO and LNO is in Figure 4.1.3(b). The solid and dashed vertical lines mark the position of the (002) and (200) reflections of bulk BTO, respectively. The intensity of the BTO(002) peak in the $T_s$ = 375 °C sample, the lowest BTO growth temperature, is much reduced in comparison with the other samples. To quantify the BTO crystallization dependence on deposition temperature, the BTO(002) peak intensity has been normalized to that of YSZ(002) peak of the corresponding sample. The dependence with $T_s$ of the intensity ratio, in logarithmic scale, is plotted in Figure 4.1.3(c). The intensity ratio increases sharply up to around 425 °C, with much lower dependence for higher temperatures. It indicates that the threshold temperature for BTO crystallization by pulsed laser deposition on the used buffer layers is around 375 °C. The dependence with $T_s$ (Figure 4.1.3c, right axis) of the rocking curve ($\Delta\omega$, $\omega$-scan) and particularly the width ($\Delta 2\theta$, $\theta$-$2\theta$ scan) of the BTO(002) reflection also reflect the onset temperature of crystallization. Moreover, the data do not indicate differences in crystal quality between the films deposited at temperature above 425 °C, with similar values of $\Delta\omega$ (~ 1.1°) and $\Delta 2\theta$ (~ 0.4°).

The position of the BTO peak depends on $T_s$, being coincident with the bulk BTO(002) in the film grown at the highest temperature ($T_s$ = 750 °C) and at lower $2\theta$ angles in the other samples. This result indicates that the BTO films are *c*-oriented, the *c*-axis strain depending on the substrate temperature. $\phi$-scans confirmed epitaxial growth. Figure 4.1.3(d) shows $\phi$-scans around BTO(110), LNO(110), YSZ(220) and Si(220) reflections of the $T_s$ = 675 °C sample. Each $\phi$-scan shows a set of four peaks, the BTO and LNO peaks being shifted 45° with respect to the YSZ and Si ones. The lattice parameter of $CeO_2$ is almost coincident with Si, and the $CeO_2$(220) reflections overlap with the high intensity Si substrate peaks. It is concluded that the four layers are epitaxial, with cube-on-cube epitaxial relationship of $CeO_2$ and YSZ with Si(001), whereas BTO and LNO present an in-plane rotation of 45°.[34]

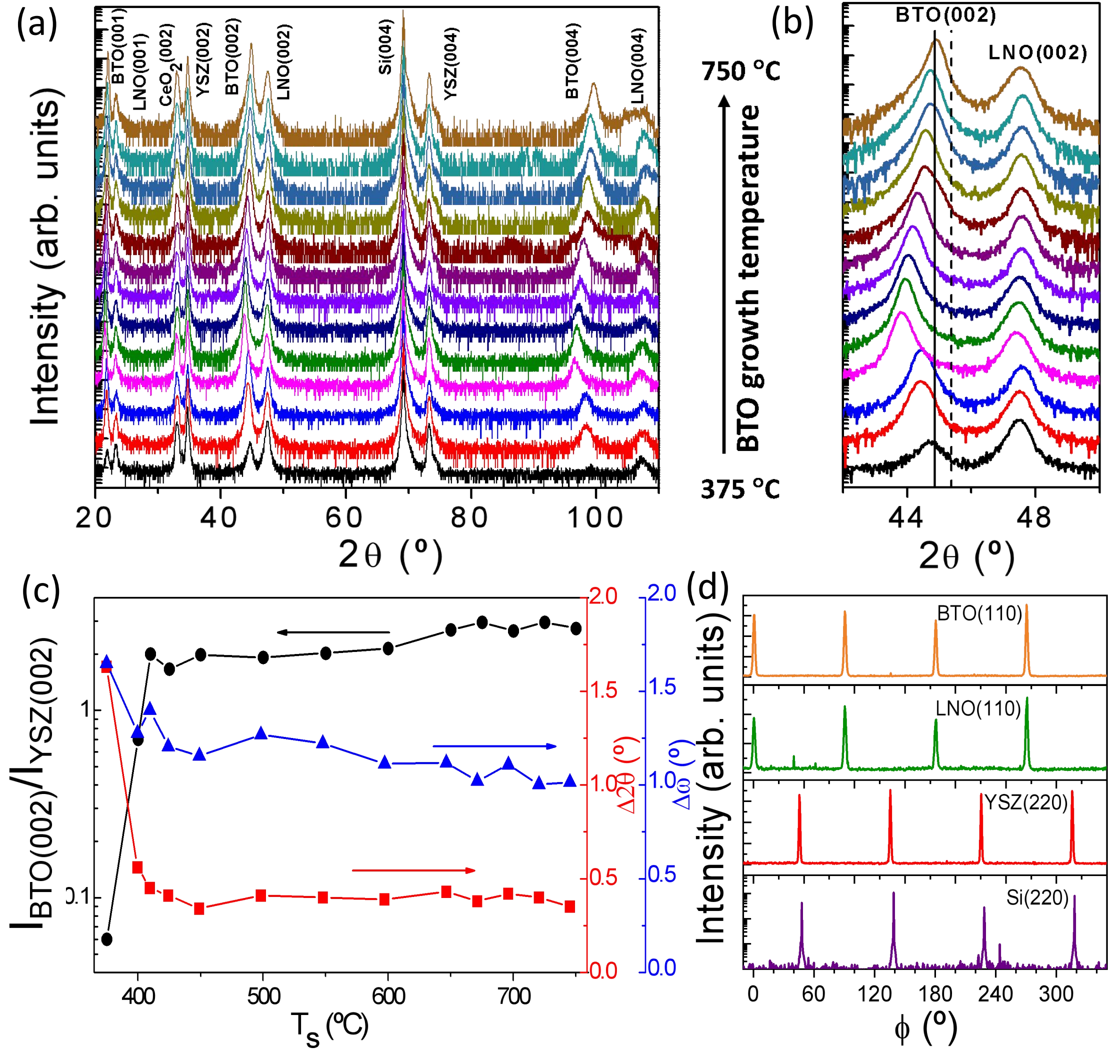


*Figure 4.1.3 (a) XRD θ-2θ scans of the BTO/LNO/$CeO_2$/YSZ/Si(001) series. The intensity is plotted in logarithmic scale, and the diffractograms are shifted vertically for clarity, from the $T_s$ = 375 °C to the 700 °C sample. (b) Zoomed region of the θ-2θ scans around the (002) reflections of BTO and LNO. The vertical solid and dashed lines mark the position of the (002) and (200) reflections in bulk BTO, respectively. (c) Dependence with the deposition temperature of BTO on LNO/$CeO_2$/YSZ/Si(001) of intensity ratio between the BTO(002) and YSZ(002) peaks (black circles, left axis), and full width at half maximum of the 2θ-scan (red squares, right axis), and ω-scan (blue triangles, right axis) of the BTO(002) reflection. (d) ϕ-scans around the BTO(110), LNO(110), YSZ(220) and Si(220) reflections of the $T_s$ = 675 °C sample.*

Reciprocal space maps around the BTO(203) and Si(224) asymmetrical reflections of the samples grown at different substrate temperatures are shown in Figure 4.1.4(a). The BTO peak indicates homogeneous strain in all the measured samples. The in-plane lattice parameter is plotted (red triangles) against $T_s$ in Figure 4.1.4(b), together with the out-of-plane lattice parameter (determined from the specular *θ*-2*θ* scans) of all BTO films on Si. The horizontal dashed lines indicate the values of the *a* (3.994 Å) and *c* (4.038 Å) parameters of bulk BTO. It is observed that the

out-of-plane parameter increases first up to a strain $\varepsilon_{[001]}$ of 2.3 % in the $T_s$ = 425 °C sample, and for higher deposition temperatures decreases monotonically reaching the bulk value of the *c*-axis in the $T_s$ = 750 °C sample.

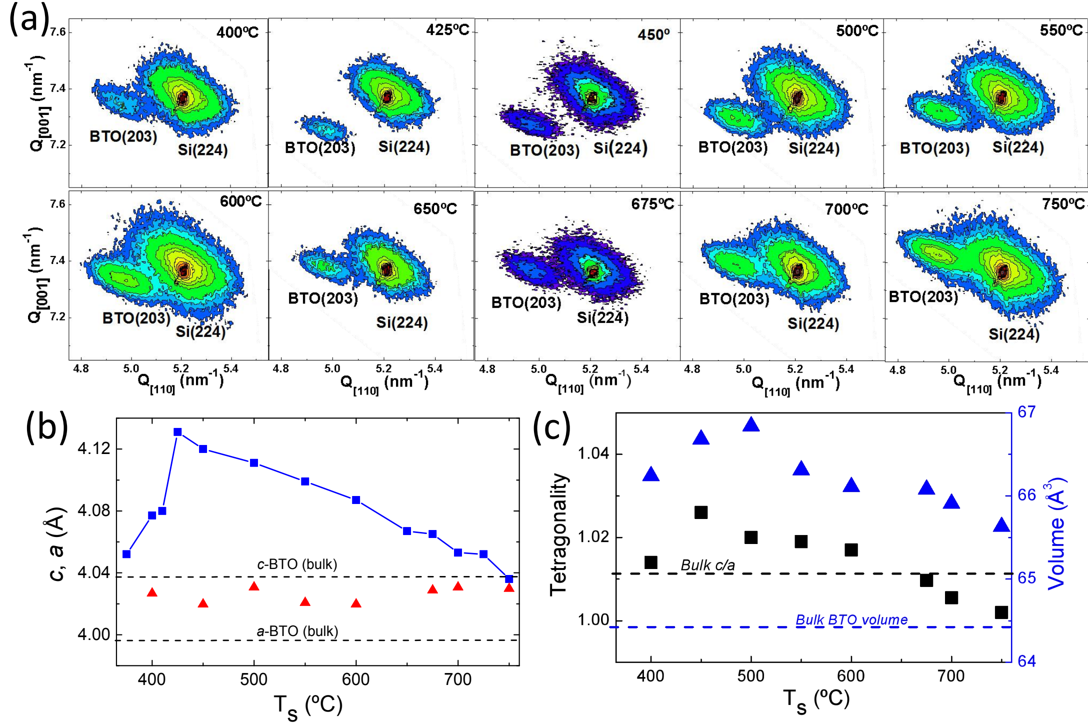


*Figure 4.1.4 (a) Reciprocal space map around the BTO(203) and Si(224) reflections at various substrate temperature $T_s$ (indicated in the top right side of each panel). Note: The samples for $T_s$ = 450 °C and 675 °C were recorded with shorter acquisition time. (b) Dependence of the out-of-plane lattice parameter (blue squares), and in-plane lattice parameter for selected samples (red triangles). The horizontal dashed lines indicate the a- and c-axes length in bulk BTO. (c) Unit cell tetragonality (left axis, black squares) and volume (right axis, blue triangles). The horizontal dashed lines indicate the c/a tetragonality and unit cell volume of bulk BTO.*

The in-plane parameter of the BTO films deposited at different $T_s$ varies slightly between the samples, with values in the 4.021 Å - 4.032 Å range, higher than the in-plane value of bulk BTO (3.998 Å). Three factors can contribute to the expansion of the in-plane parameter: i) the epitaxial strain (it is not expected to be relevant due to the relatively large film thickness and lattice mismatch, anticipating plastic relaxation); ii) the point defects in the films (more relevant for the samples deposited at low $T_s$, although the unit cell is expected to expand mainly along the out-of-plane direction due to the epitaxial in-plane matching); and iii) the higher thermal expansion coefficients of BTO than of silicon, must induce a tensile stress when the films are cooled down to room temperature. The thermal mismatch stress is more important in the high $T_s$ samples. The combined effect of these factors results in similar in-plane parameter in the $T_s$ = 400 - 750 °C range. The unit cell tetragonality (*c*/*a*) and volume (Figure 4.1.3c) increase with $T_s$ up to 450 °C and 500 °C, respectively, and for higher

$T_s$ both decrease monotonically. The tetragonality is smaller than in bulk BTO in the samples deposited at $T_s$ higher than 650 °C. In contrast, the unit cell is expanded in all the samples, with high volume expansions ranging from around 1.9 % (750 °C sample) to above 3.7 % (500 °C sample).

To evaluate the stability of the films, the effect of ex-situ annealing on the lattice parameter *c* value of the $T_s$ = 450 °C and 600 °C samples was investigated. Both samples were annealed sequentially two times at 450 °C and 600 °C for 1 hour under 200 mbar. As shown in Figure 4.1.5(a) and (b), the samples show almost negligible differences after annealing at 450 °C. The annealing at 600 °C has very small effect on the $T_s$ = 600 °C sample, and in the $T_s$ = 450 °C sample there is a small decrease of the out-of-plane parameter. The data before and after ex-situ annealing of the two samples are shown in Figure 4.1.5(c), proving the limited effects of annealing and signaling the high stability of the films.

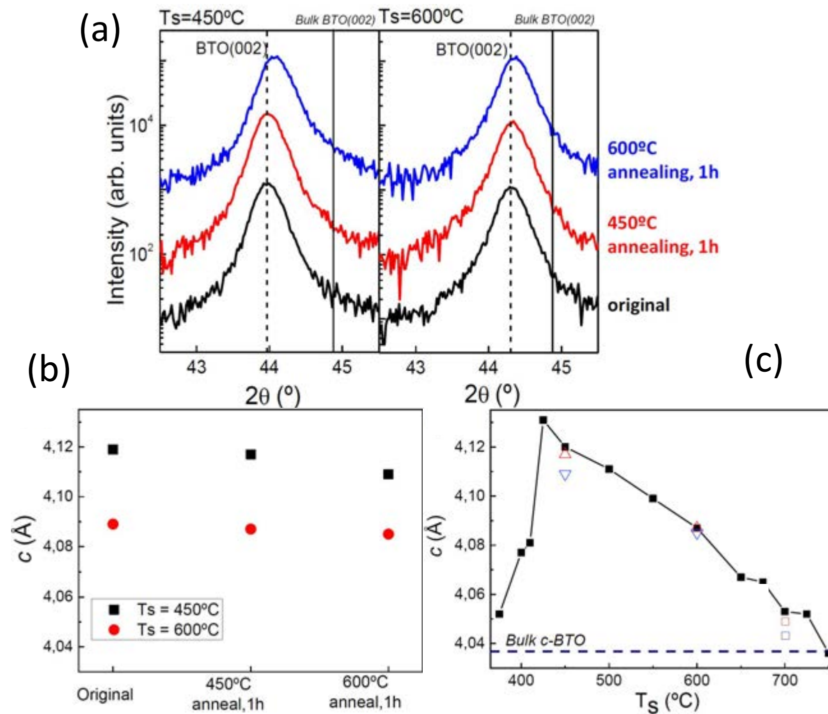


*Figure 4.1.5 (a) XRD θ-2θ scan of the $T_s$ = 450 °C and 600 °C films on Si(001) as-deposited (black curves), after annealing at 450 °C, and after 600 °C. The vertical dashed line mark the corresponding position of the BTO(002) reflections of the as-deposited films. (b) c-axis strain of the as-deposited and annealed films. (c) Dependence of c axis strain with the deposition temperature $T_s$, including the values of the $T_s$ = 450 °C and 600 °C samples after the ex-situ first annealing at 450 °C (open red triangles up) and second annealing at 600 °C (open blue triangles down).*

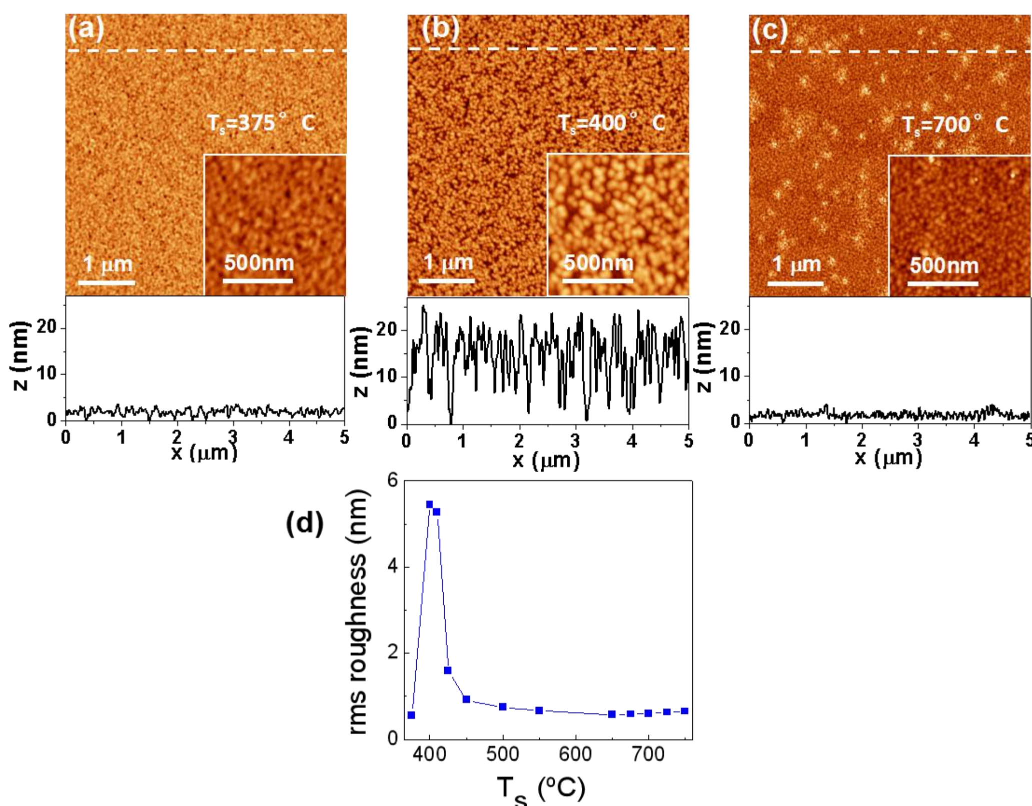


*Figure 4.1.6 Topographic AFM images, 5 µm x 5 µm in size (inset: 1 µm x 1 µm) of the (a) $T_s$ = 375 °C (z-scale: 7 nm), (b) $T_s$ = 400 °C (z-scale: 40 nm), and (c) $T_s$ = 700 °C (z-scale: 7 nm) BTO films on LNO/$CeO_2$/YSZ/ Si(001) with height profiles along the horizontal dashed lines at bottom of each image. (d) rms roughness as a function of $T_s$.*

Topographic AFM images, 5 µm x 5 µm in size, of the $T_s$ = 375 °C, 400 °C, and 700 °C samples on Si are shown in Figure 4.1.6(a)-(c), respectively, with 1 µm x 1 µm images in the corresponding insets. The three images (and the corresponding ones to other films in the series) show islands with lateral size of a few tens of nm. The lateral size is around 40 nm in the $T_s$ = 375 °C and 700 °C samples, and around 80 nm in the $T_s$ = 400 °C sample. The morphology of the $T_s$ = 375 °C sample is very homogeneous, whereas in the $T_s$ = 700 °C sample there is agglomeration of a few islands of higher height in some areas. The morphology of the $T_s$ = 400 °C and the 410 °C samples (the AFM image of the latter not shown here) differs with respect to the other samples, with flat areas between the islands, which are notably larger in height than in the other samples. Notice in Figure 4.1.6(a)-(c) the differences in the z-scales. Indeed, the z-scale ranges in the topographic images are 7 nm in Figure 4.1.6(a) and (c), and 40 nm in Figure 4.1.6(b). The corresponding height profiles at the bottom of each image along the dashed lines evidence the huge difference in islands height. The root means square (rms) roughness of all the samples on Si, calculated from 1 µm x 1 µm areas, is plotted as a function of $T_s$ in Figure 4.1.6(d). There is a sharp increase from 0.56 nm to more than 5 nm as $T_s$ increases from 375 °C to 400 °C. The rms roughness, similarly high in the $T_s$ = 410 °C sample, decreases to

around 1.6 nm and 0.92 nm in the $T_s$ = 425 °C and 450 °C samples, respectively, and is below 0.75 nm for the samples grown at higher temperatures. The peaky dependence of the roughness with deposition temperature is a signature of the onset of BTO crystallization above 375 °C, being the high roughness in the 400 - 425 °C samples likely due to the coexistence of well crystallized islands with other regions presenting lower crystal order or amorphous state. The (001) orientation in the $T_s$ = 400 °C sample, with in-plane epitaxial order confirmed by reciprocal space mapping points to epitaxial columnar growth coexisting with not-epitaxial regions. On the other hand, the low surface roughness of the $T_s$ = 375 °C sample indicates that surface diffusivity at this temperature is low for epitaxial growth but high enough for surface smoothing.

**Electrical Characterization**

The BTO films deposited on Si at 410 °C or higher $T_s$ are ferroelectric. The ferroelectric polarization loops of a selection of the films are plotted in Figure 4.1.7(a). The loops were obtained from current - electric field measurement (the corresponding to the $T_s$ = 425 °C sample is presented in the inset). The remnant polarization $P_r$ and electrical coercive field $E_c$ of the films range within 3 - 11 μC/cm$^2$ and 70 - 160 kV/cm, respectively. The films deposited at the lowest temperatures, 375 °C and 400 °C, did not display current ferroelectric switching peaks. Figure 4.1.7(b) presents the values of remnant polarization and electrical coercive fields of the BTO films on Si as a function of the deposition temperature. The threshold for ferroelectric behavior is $T_s$ = 410 °C, and for higher $T_s$ the remnant polarization increases sharply to a maximum value of around 11 μC/cm$^2$ ($T_s$ = 425 °C). For higher deposition temperatures, $P_r$ decreases monotonically with $T_s$. In the case of the coercive field the dependence is similar, with a reduction from 160 kV/cm ($T_s$ = 425 °C) to 70 kV/cm ($T_s$ = 750 °C).

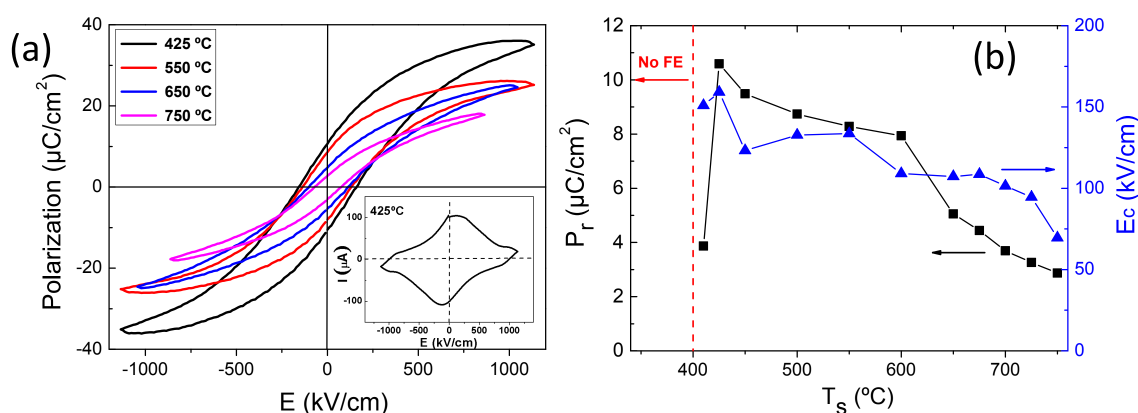


*Figure 4.1.7 (a) Ferroelectric polarization loops of the $T_s$ = 425 °C, 550 °C, 650 °C and 750 °C BTO films on $LNO/CeO_2/YSZ/Si(001)$, with the current (I) – electric field (E) curve corresponding to the $T_s$ = 425 °C sample in the inset. (b) Remnant polarization (black squares, left axis) and*

*coercive field (blue triangles, right axis) as a function of $T_s$.*

The relationship between $P_r$ and *c*-axis strain of epitaxial BTO on Si(001) at different deposition temperatures is plotted in Figure 4.1.8. It can be clearly observed that $P_r$ presents a strong dependence on the lattice strain. With larger *c*-axis strain, BTO film usually present higher $P_r$ value. Therefore, this growth strategy by controlling the deposition temperature during pulsed laser deposition process can provide a feasible way for tailoring the structural and ferroelectric properties of epitaxial BTO thin films on silicon.

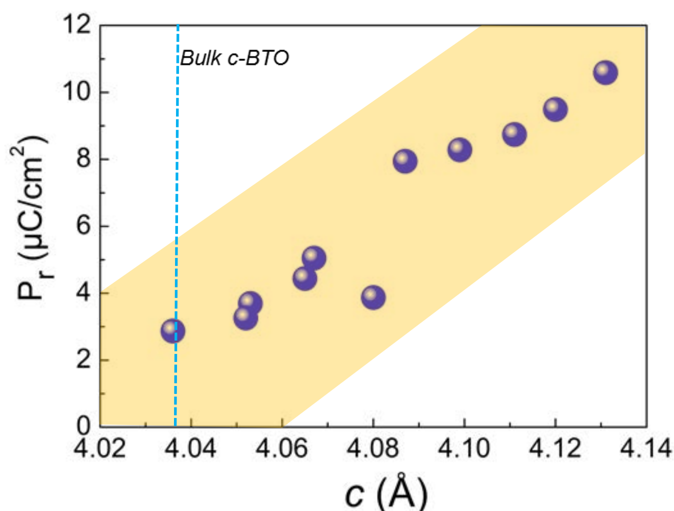


*Figure 4.1.8 The dependence of the remnant polarization (Pr) on c-axis strain of epitaxial $BaTiO_3$ on Si(001).*

The leakage curves of the series of BTO films on Si are shown in Figure 4.1.9(a), and the values of leakage current at 45 and 225 kV/cm are plotted as a function of $T_s$ in Figure 4.1.9(b). The leakage current depends notably on $T_s$, particularly in the samples deposited at low temperatures. The $T_s$ = 375 °C sample was highly insulating and the small area of the contacts did not permit reliable measurements. The conductivity increases sharply with $T_s$, the $T_s$ = 450 °C sample being the most conductive of the series. In particular, the leakage current at 45 kV/cm increases from $10^{-7}$ A/cm$^2$ ($T_s$ = 400 °C) to around 3 x $10^{-5}$ A/cm$^2$ ($T_s$ = 450 °C), and from 4 x $10^{-7}$ A/cm$^2$ to $10^{-3}$ A/cm$^2$ at 225 kV/cm. Films deposited above $T_s$ = 450 °C are more insulating, with a monotonic reduction of the leakage current with $T_s$, presenting the $T_s$ = 750 °C samples leakage current below 1 x $10^{-7}$ A/cm$^2$ and 4 x $10^{-6}$ A/cm$^2$ at 45 and 225 kV/cm, respectively. We emphasize that the leakage of these films is comparable to state of the art BTO films on perovskite single crystalline substrates[178,179] or to thick epitaxial Pb(Zr,Ti)$O_3$ films on Si(001).[60]

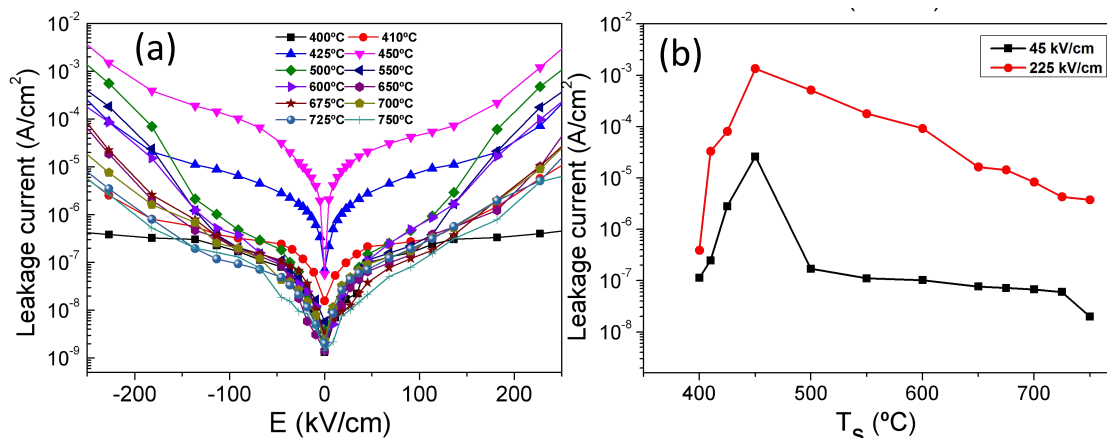


*Figure 4.1.9 (a) Leakage current curves of the BTO films on LNO/$CeO_2$/YSZ/Si(001). (b) Leakage current at 45 kV/cm (black squares) and 225 kV/cm (red circles) as a function of the deposition temperature.*

The impact of the deposition temperature on the properties of BTO is schematized in Figure 4.1.10. Above the crystallization threshold at 375 °C there is a temperature window around 75 °C wide, up to $T_s$ ~ 450 °C where films have a large strain and ferroelectric polarization, but are rough and present high leakage. XRD and AFM characterization point to in-homogeneous crystallinity as the cause. From $T_s$ ~ 450 °C to ~ 750 °C, the films are very flat and highly insulating. In this temperature window, about 300 °C wide, the BTO films are *c*-oriented and show a monotonic variation of the *c*-axis parameter and the ferroelectric polarization. The unit cell of BTO is highly expanded, likely due to the presence of point defects.[48,180-182] The influence of the deposition temperature on these defects permits the control of the *c*-axis parameter and the ferroelectric polarization.

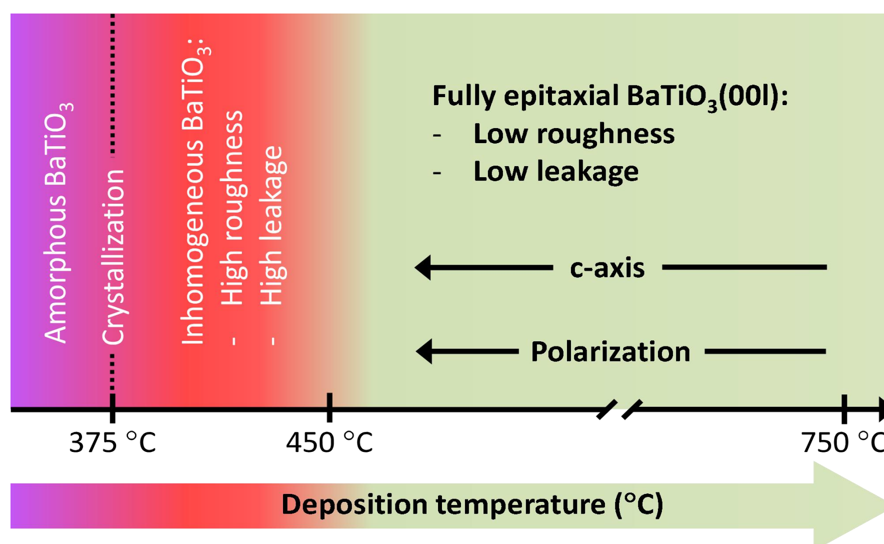


*Figure 4.1.10 Schematics of the influence of the deposition temperature on the crystallinity and*

*properties of $BaTiO_3$ thin films on $LNO/CeO_2/YSZ/Si(001)$.*

In contrast to extended defects, the identification of randomly distributed point defects in oxide thin films by transmission electron microscopy is challenging and indirect methods are typically used.[182] Here we used the photocurrent induced by illumination with 405 nm photons (energy of 3.06 eV, close but smaller than the optical gap of BTO as a probe for point defect concentration. Indeed, it is expected that point defects shall induce in-gap states promoting larger optical absorption of sub-bandgap photons and enlarge the photocurrent. The photocurrent is found to increases with $T_s$ from 8 x $10^{-3}$ μA/cm$^2$ ($T_s$ = 400 °C sample) up to above 0.2 μA/cm$^2$ in the $T_s$ = 425 °C and $T_s$ = 450 °C samples, and then decreases progressively to around 0.1 μA/cm$^2$ in the $T_s$ = 700 °C and $T_s$ = 750 °C samples (Figure 4.1.11). The out-of-plane lattice parameter and the photocurrent display a very similar dependence on the deposition temperature. The photocurrent is higher in the more strained films (The inset of Figure 4.1.11), supporting that cell expansion is caused by defects responsible of the photoresponse.

It is remarkable that the control of strain and polarization by the deposition temperature has been demonstrated in thick BTO films (thicker than 100 nm) integrated epitaxially with Si(001). This is clearly the most convenient substrate for applications, and the demonstration that integration of epitaxial BTO with high polarization can deposited at temperature as low as 450 °C is also of relevance towards the integration in silicon chips.

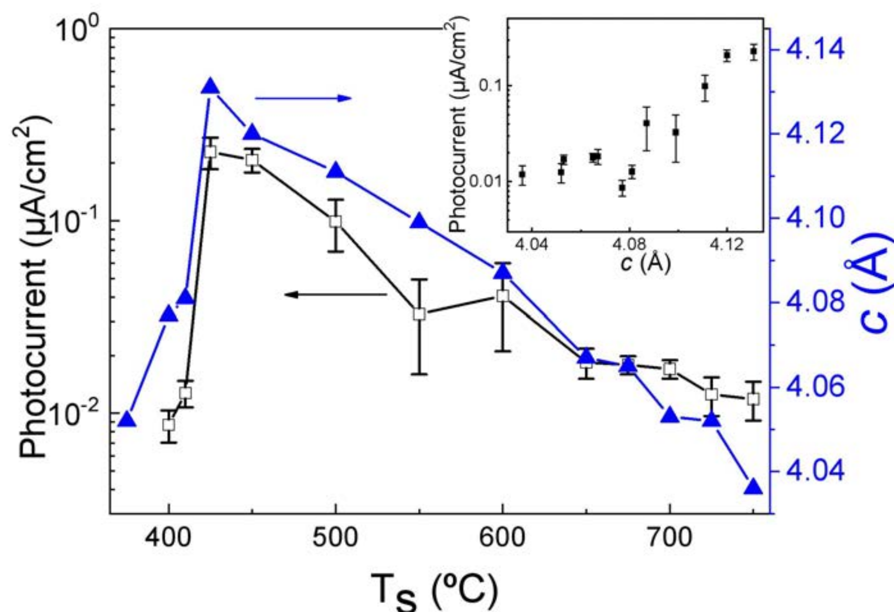


*Figure 4.1.11 Dependence with the deposition temperature of the photocurrent (left axis, open black squares) and the out-of-plane lattice parameter (right axis, solid blue triangles). Photocurrent was measured in at least ten pairs of contacts in each film. The vertical lines in the photocurrent data indicate the ranges of values measured. Inset: photocurrent against*

*out-of-plane lattice parameter.*

**$BaTiO_3$ films on $LaAlO_3$(001) with varied $T_s$**

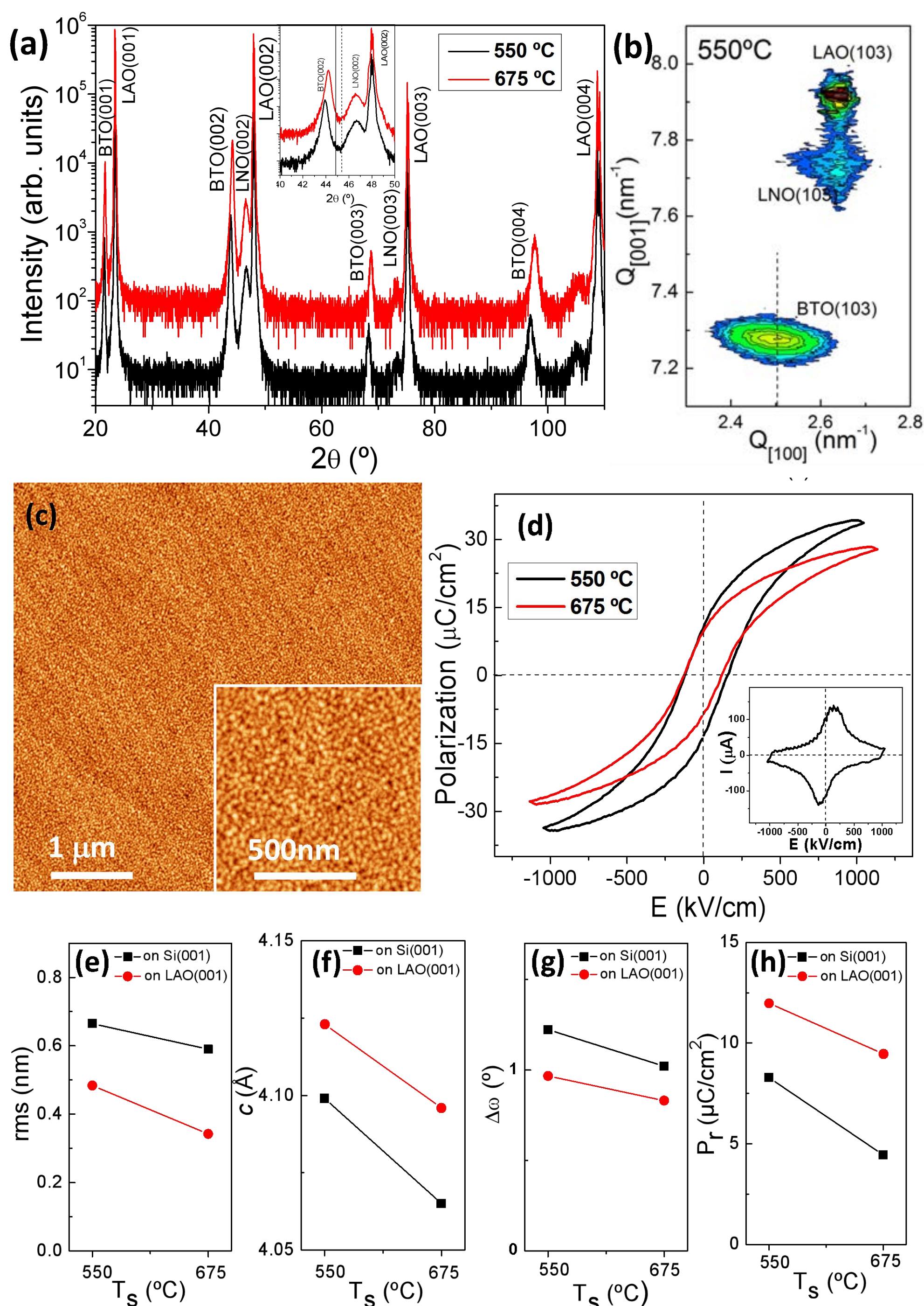


*Figure 4.1.12 (a) XRD θ-2θ scans of the films deposited on LNO/$LaAlO_3$(001) at $T_s$ = 550 °C (black line) and $T_s$ = 675 °C (red line). Inset: zoomed region around the (002) reflections of BTO. (b) XRD reciprocal space maps (RSM) of BTO films deposited on LNO/$LaAlO_3$(001) at $T_s$ =*

*550 °C around asymmetrical (103) reflections of BTO, LNO and LAO. (c) Topographic AFM 5 μm x 5 μm image (inset: 1 μm x 1 μm) of the film deposited at $T_s$ = 675 °C (z-scale: 3 nm). (d) Ferroelectric polarization loops of the $T_s$ = 550 °C (black line) and 675 °C films on LAO, with the current – electric field curve corresponding to the 425 °C sample in the inset. Comparison of rms roughness (e), out-of-plane lattice parameter (f), full width at half maximum of the ω-scan (g), and remnant polarization (h) of BTO films on Si (black squares) and LAO (red circles) at $T_s$ = 550 °C and $T_s$ = 675 °C.*

To confirm if the growth strategy presented here is also valid for BTO films grown on single crystalline oxide substrates which are commonly used as platforms to grow BTO films, we have deposited two BTO/LNO bilayers on LAO at 550 °C and 675 °C. Due to the moderately small lattice mismatch (~1.3 %) between the LNO electrode and the LAO substrate, the XRD specular $\theta$-$2\theta$ scans of the bilayers in Figure 4.1.12(a) only display (00*l*) reflections. The zoom of the scans around the (002) reflections shows narrow BTO peaks at positions that confirm the expected *c*-orientation and expanded *c*-axis, being the strain in the $T_s$ = 550 °C sample (*c* = 4.123 Å) higher than in the $T_s$ = 675 °C one (*c* = 4.096 Å). Reciprocal space maps around asymmetrical (103) reflections for $T_s$ = 550 °C sample is shown in Figure 4.1.12(b). The LNO bottom electrode is fully strained, whereas BTO presents in-plane lattice parameter coincident with the *a*-axis of bulk BTO. It indicates that the films are plastically relaxed, and that the defects cause anisotropic unit-cell deformation, with expansion of the unit cell along the out-of-plane direction. Topographic AFM images show that the films are very flat, and in the case of the $T_s$ = 675 °C sample rms roughness below 0.4 nm and morphology of terraces and steps can be observed in the 5 μm x 5 μm image in Figure 4.1.12(c) in spite of the very small islands, usually present in BTO films.[34,181,182] The ferroelectric loops (Figure 4.1.12d) show larger polarization in the $T_s$ = 550 °C film, in agreement with its higher lattice strain. The values of rms roughness, *c*-axis parameter, BTO(002) rocking curve width and remnant polarization are plotted (red circles) against $T_s$ (550 °C or 675 °C) in Figures 4.1.12(e)-(h), respectively. The Figures include the data of the corresponding samples on Si (black squares). Obviously, the BTO films deposited on Si(001) and LAO(001) substrates display the same trend of film morphology (rms), crystallinity (*c*-axis parameter and rocking curve) and polarization.

### 4.1.2 Oxygen Pressure

**Structural Study**

In this $P_{O2}$ series, BTO films were deposited at different oxygen pressure. The relevance of the oxygen pressure to the crystalline texture of BTO film in the deposition chamber is due to two reasons. On one hand, oxygen present in the ceramic BTO target used for PLD is insufficient for complete oxidation of the growing film (oxygen has low vapor pressure and it is easily re-evaporated). Thus, films deposited under low oxygen pressure can present oxygen vacancies. On the other hand, the laser-generated plasma contains high energy ions and atoms, the energy depending on the chamber oxygen pressure.[213] Under vacuum conditions, the PLD plasma expands free and atoms and ions having large energy of even tens of electron volts impact the substrate.[214] However, in the presence of an oxygen background, the energy of the PLD plasma decreases with increased oxygen pressure due to collisions.[213,215] The energetic plasma can generate point defects when it impacts on the film,[214,216] and thus the amount of defects increases with reduced oxygen pressure. Oxygen vacancies and defects, both favored under low oxygen pressure deposition, cause expansion of the unit cell of the oxide film.[217-219] As the growth rate can change with oxygen pressure, a series of amorphous BTO films deposited at room temperature on bare (without buffer layers) Si(001) and their thicknesses were measured by XRR to evaluate the dependence of growth rate on oxygen pressure. The amorphous films are thicker than epitaxial films, but the dependence of thickness on oxygen pressure between the amorphous films and epitaxial one should be proportional (inset in Figure 4.1.13) and can be accurately determined. The film deposited at the highest pressure ($P_{O2}$ = 0.1 mbar) was rough and there were no XRR oscillations. The thickness of two epitaxial films ($P_{O2}$ = 0.01 and 0.1 mbar samples) deposited at high temperature on buffered Si(001) was determined by TEM[1]. The dependence of growth rate on the oxygen pressure, plotted combining the XRR and TEM results (red colour), is presented in Figure 4.1.13. Finally, the growth rate was in the 0.47 − 0.56 Å/laser pulse range, thus resulting in the film thicknesses in the range of 94 − 112 nm.

[1] The thicknesses of two films grown at $P_{O2}$ = 0.01 and 0.1 mbar confirmed by TEM image are measured by Saúl Estandía (a PhD candidate) and Dr. Jaume Gázquez (a scientist) working at ICMAB, in collaboration with the STEM Group of the Oak Ridge National Laboratory, USA. Details are reported elsewhere [*ACS applied materials & interfaces, 10(30), 25529*].

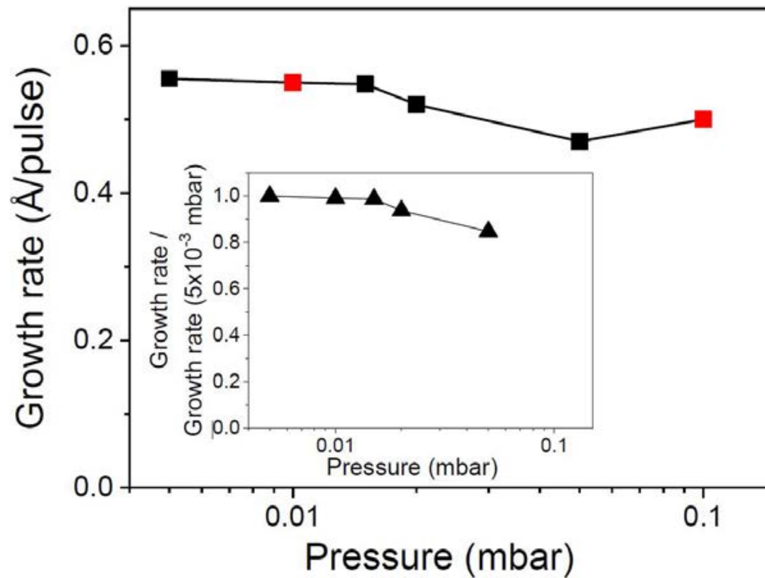


*Figure 4.1.13 Growth rate of BTO as a function of the oxygen pressure. Data corresponding to $P_{O2}$ = 0.01 and 0.1 mbar (red squares) were directly determined by cross sectional TEM images of the epitaxial films on buffered Si(001). The growth rate corresponding to the other pressures has been estimated from XRR measurements of amorphous BTO films deposited at room temperature on bare Si(001). Since amorphous films have smaller density than epitaxial ones, the thickness ratio between epitaxial and amorphous films grown at $P_{O2}$ = 0.01 mbar was used as correction factor for the $P_{O2}$ = 5 x $10^{-3}$, 0.015, 0.02, and 0.05 mbar films.*

The symmetrical XRD *θ-2θ* scan of the $P_{O2}$ = 0.02 mbar sample is shown in Figure 4.1.14(a). The diffraction peaks correspond to (00*l*) reflections of the silicon substrate, buffer layers, or BTO films. Zoomed *θ-2θ* scans (in the 42° − 75° range) of the samples deposited at varied $P_{O2}$ are presented in Figure 4.1.14(b). The patterns are vertically shifted for clarity, from bottom to top as $P_{O2}$ increases from 5 x $10^{-3}$ to 0.1 mbar. The vertical solid and dashed lines mark the position of (002) and (200) reflections of bulk BTO, respectively. The corresponding reflection of the BTO film shifts monotonically from an angle lower than bulk BTO(002) to an angle higher than bulk BTO(200), pointing to the transition from *c*-oriented BTO to *a*-oriented BTO as the oxygen pressure increases during growth.

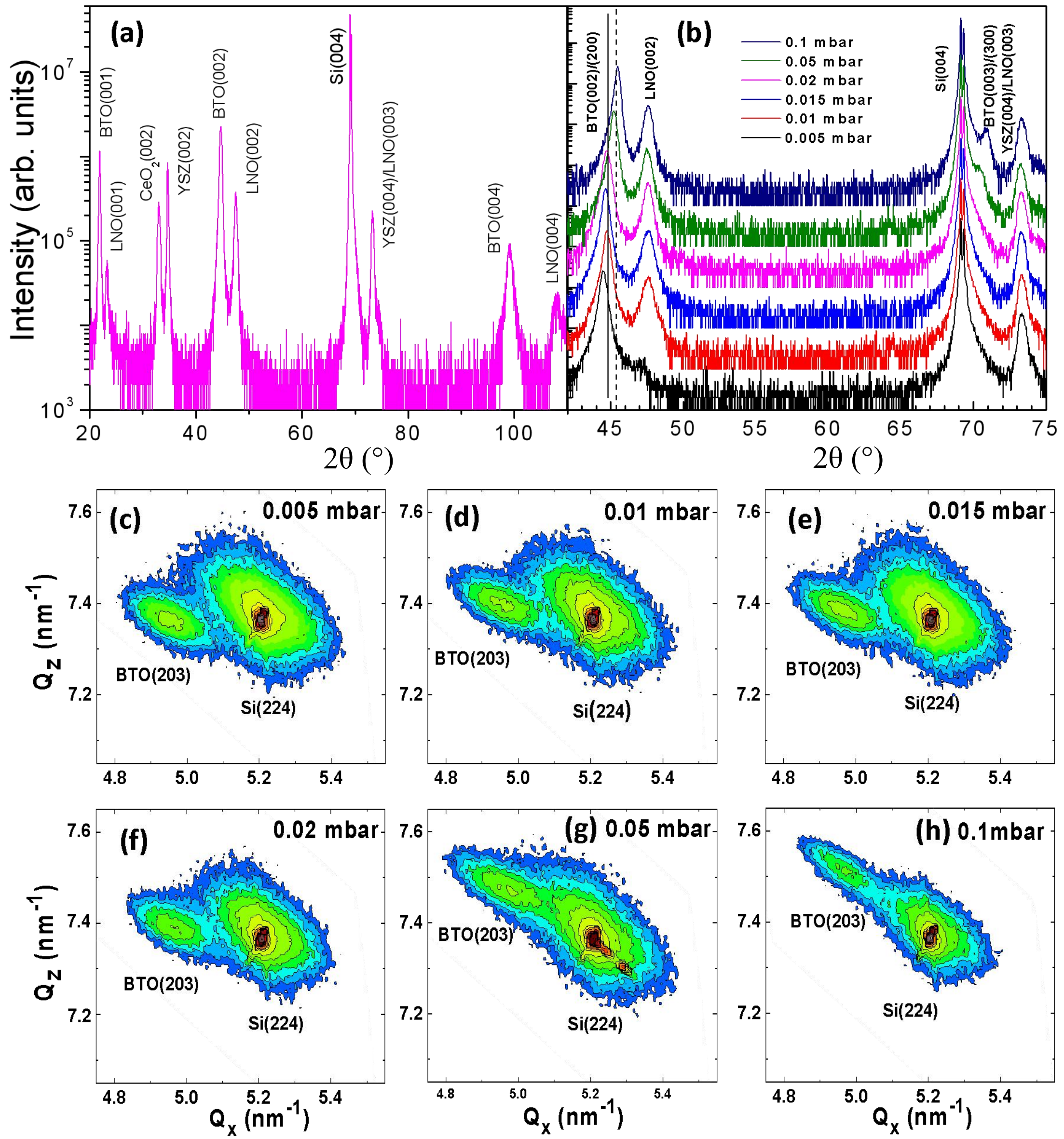


*Figure 4.1.14 (a) Symmetrical XRD θ-2θ scan of the $P_{O2}$ = 0.02 mbar sample. (b) Zoomed θ-2θ scans of the samples deposited at varied $P_{O2}$. Diffractograms are shifted vertically for clarity. The vertical solid and dashed lines mark the position of the (002) and (200) reflections in bulk BTO, respectively. (c-h) XRD reciprocal space maps around Si(224) and BTO(203) asymmetrical reflections.*

The BTO mosaicity, represented by the rocking curve of the specular BTO (002)/(200) reflection in Figure 4.1.15, is similar in all films, with a full width at half-maximum (*FWHM*) in the 1.0° − 1.2° range. It is remarkable that the fwhm of the BTO (002)/(200) specular *θ-2θ* reflections is similar in all of the samples, in the 0.29° − 0.41° range, indicating homogeneous, but different and selectable strain state in the series of films.

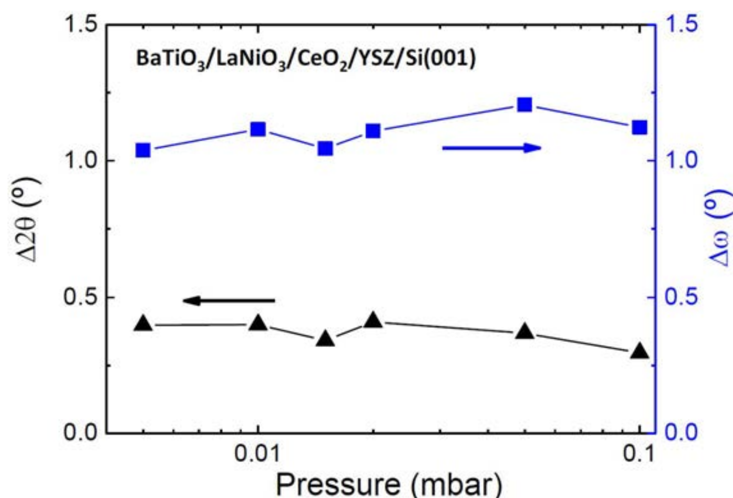


*Figure 4.1.15 Dependence of the FWHM of the specular θ-2θ scan (Δ2θ) and its ω-scan (Δω) around BTO(002)/(200) reflection on the oxygen pressure.*

The out-of-plane (*oop*) and in-plane (*ip*) lattice parameters were determined from the XRD symmetrical $\theta$-$2\theta$ scans in Figure 4.1.14(a)-(b) and asymmetrical RSMs around BTO(203) and Si(224) reflections in the Figure 4.1.14(c)-(h), respectively. The parameters are plotted against $P_{O2}$ in Figure 4.1.16(a). The *oop* lattice parameter (solid triangles) decreases more than 2 % with $P_{O2}$, from 4.072 Å ($P_{O2}$ = 5 x $10^{-3}$ mbar) to 3.987 Å ($P_{O2}$ = 0.1 mbar). The BTO unit cell volume is highly enlarged (3.09 %) in the $P_{O2}$ = 5 x $10^{-3}$ mbar film and shrinks monotonically as the pressure increases (0.32 % in the $P_{O2}$ = 0.1 mbar film), suggesting that the expansion (Figure 4.1.16b, right axis) is likely caused by defects, either those caused by the energetic PLD plasma under low oxygen pressure[28] or oxygen vacancies.[29]

The *oop* parameter in the two highest $P_{O2}$ samples is smaller than the *c*-axis parameter of bulk BTO, and it is even smaller than the bulk *a*-parameter in the $P_{O2}$ = 0.1 mbar sample. In contrast, the *ip* parameter (open squares) of films shows less variation on deposition pressure. The ratio between *oop* and *ip* parameters (Figure 4.1.16b) in the films deposited at 0.02 mbar and lower pressures is larger than 1 and close to the *c/a* ratio in bulk BTO (around 1.01), indicating that the BTO cell is elongated along the *oop* direction. For the two films deposited at 0.05 and 0.1 mbar, the *oop/ip* ratio is smaller than 1 and in the $P_{O2}$ = 0.1 mbar film reaches the *a/c* ratio in bulk (around 0.99), signaling that these two films are *a*-oriented. The variation of polar orientation of BTO films with oxygen pressure is sketched in the inset of Figure 4.1.16(a).

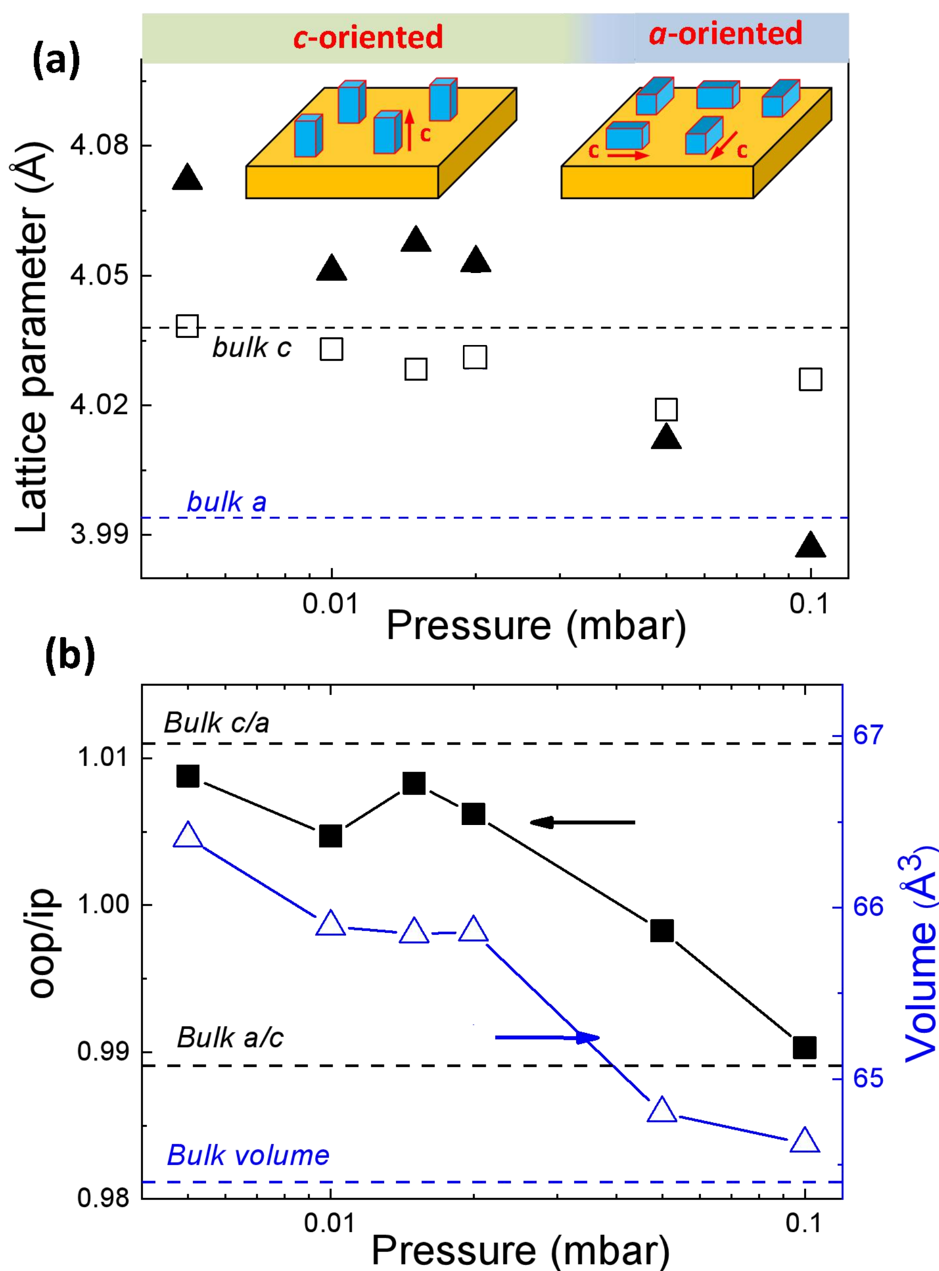


*Figure 4.1.16 (a) ip (open squares) and oop (solid triangles) lattice parameters as a function of deposition pressure. The horizontal dashed lines mark the a and c lattice parameters in bulk BTO. Inset: Sketch of the BTO orientation depending on the deposition pressure. (b) Tetragonality and unit cell volume as a function of deposition pressure. Horizontal dashed lines mark c/a, a/c, and unit cell volume in bulk BTO.*

Topographic AFM images (5 µm x 5 µm area, and 1 µm x 1 µm in the insets) are shown in Figure 4.1.17 with height profiles along the 5 µm long dashed lines. The surface roughness of BTO on LNO/$CeO_2$/YSZ/Si(001) depends on the deposition oxygen pressure. Roughness of films deposited in the $P_{O2}$ = 5 x $10^{-3}$ - 0.02 mbar range is very low with root-mean-square (rms) between 5 - 9 Å, whereas increases in the

films deposited at higher pressure (rms = 2.5 nm for the $P_{O2}$ = 0.1 mbar film). The rms roughness is plotted against the oxygen pressure in bottom panel of Figure 4.1.17. One can see that the rms surface roughness of the *a*-oriented films is notably higher than that of the *c*-oriented films.

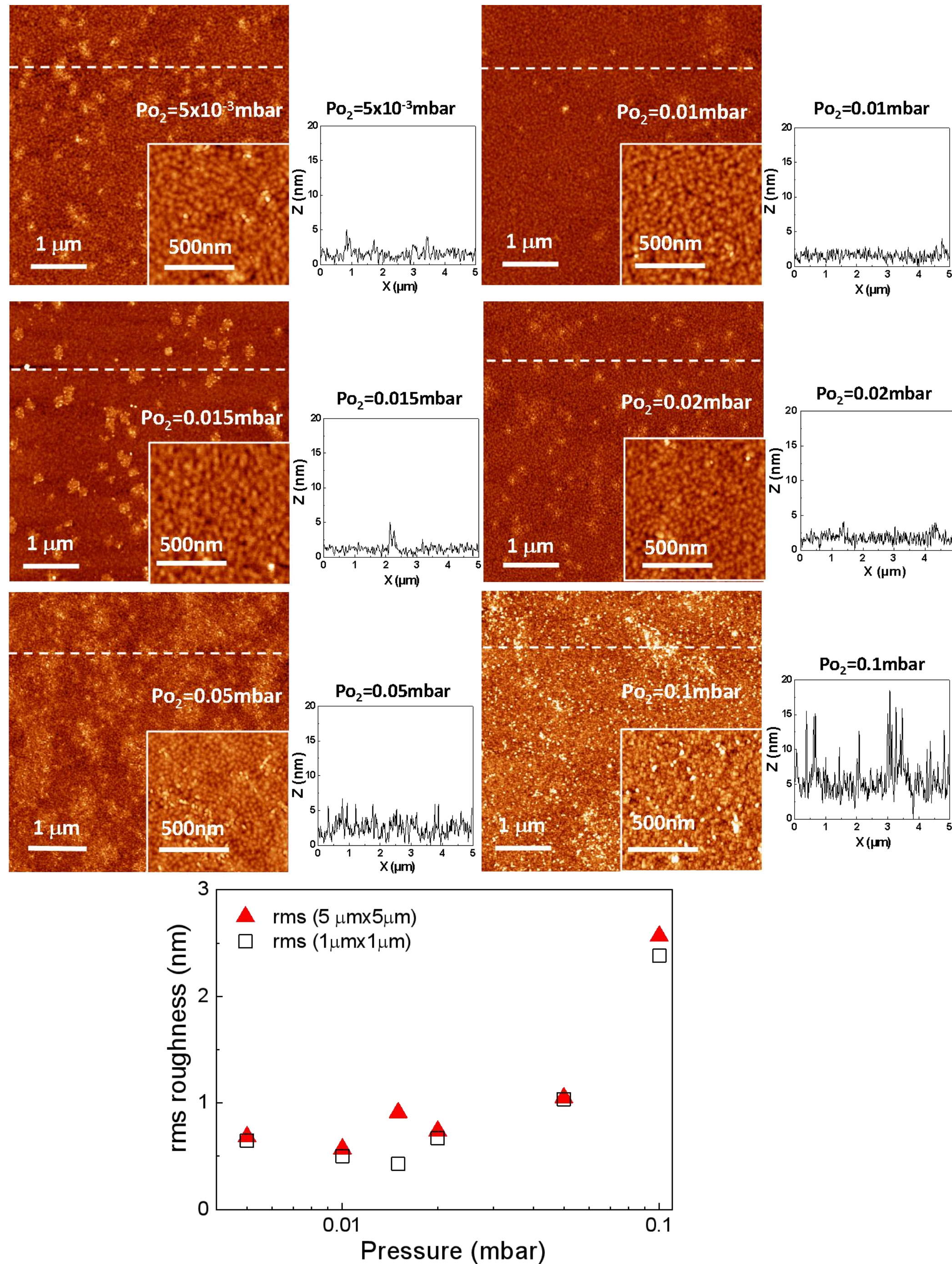


*Figure 4.1.17 Topographic AFM images 5 µm x 5 µm in size (inset: 1 µm x 1 µm) with height profiles (bottom) along the dashed lines. Bottom panel: rms roughness as a function of the oxygen pressure.*

## Electrical Characterization

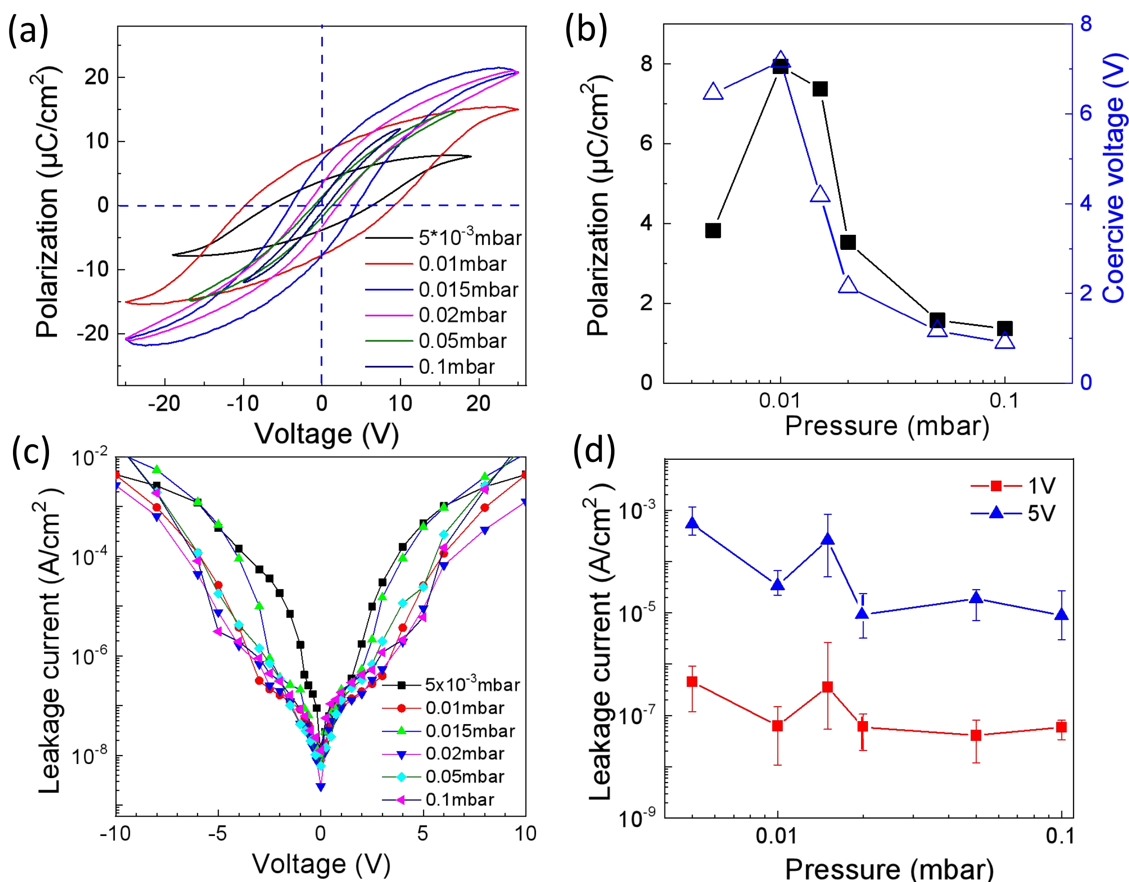


*Figure 4.1.18 (a) Polarization loops of BTO films deposited at varied oxygen pressure on buffered Si(001). (b) Dependence of remnant polarization (left axis, solid symbols) and coercive voltage (right axis, open symbols) on the deposition pressure. Leakage curves of BTO films deposited at varied oxygen pressure (c) and leakage current at 1 V (red squares) and 5 V (blue triangles) as a function of the deposition pressure.*

Figure 4.1.18(a) shows polarization loops of the BTO films deposited at varied oxygen pressure. The films are ferroelectric, with coercive voltage $V_c$ and remnant polarization $P_r$ in the 0.9 − 7.2 V (measuring two capacitors in series) and 1.3 − 8.0 $\mu C/cm^2$ ranges, respectively. Note that near the maximum applied electric field, the loops show a sizeable polarization aperture between the increasing and decreasing voltage curves. This aperture is caused by small leakage current,[183,184] in which contribution to the $P_r$ is small because data have been recorded using the *DLCC* measurement method. The dependence of $V_c$ and $P_r$ on pressure is plotted in Figure 4.1.18(b). The high coercive voltage in the two films deposited at low pressure (above 6 V, corresponding to a coercive electric field $E_c$ higher than 250 kV/cm) decreases to around 1 V ($E_c \approx 50$ kV/cm) in the $P_{O2}$ = 0.05 and 0.1 mbar samples. The coercive electric field of the $P_{O2}$ = 0.02 mbar film fits perfectly in the $E_c$ − thickness scaling dependence reported for epitaxial BTO films on Si(001) deposited under this

pressure.[34] The dependence of the remnant polarization is akin to the coercive voltage, with low $P_r$ values in the high $P_{O2}$ films and enhanced polarization for the lower pressure films excluding the $P_{O2}$ = 5 x $10^{-3}$ mbar one. Thus, ferroelectric polarization and coercive field are controlled by the oxygen pressure. This deposition parameter determines the amount of defects in the BTO film. The effect of the defects is the expansion of the BTO unit cell with increased *oop* lattice parameter. There are more defects with decreasing oxygen pressure, causing *c*-orientation in films deposited below around 0.05 mbar with expanded *oop* parameter and enhanced polarization at lower pressure. It is to be noted that the $P_{O2}$ = 5 x $10^{-3}$ mbar film could only be measured at very low frequency (the loop in Figure 4.1.18(a) was recorded at 150 Hz), most likely because of the degradation of the LNO electrode. Indeed, a detailed view of the XRD pattern of the $P_{O2}$ = 5 x $10^{-3}$ mbar sample in Figure 4.1.12(b) shows low intensity of the LNO(002) reflection, likely because of the low stability of LNO under high temperature and low pressure.[185]

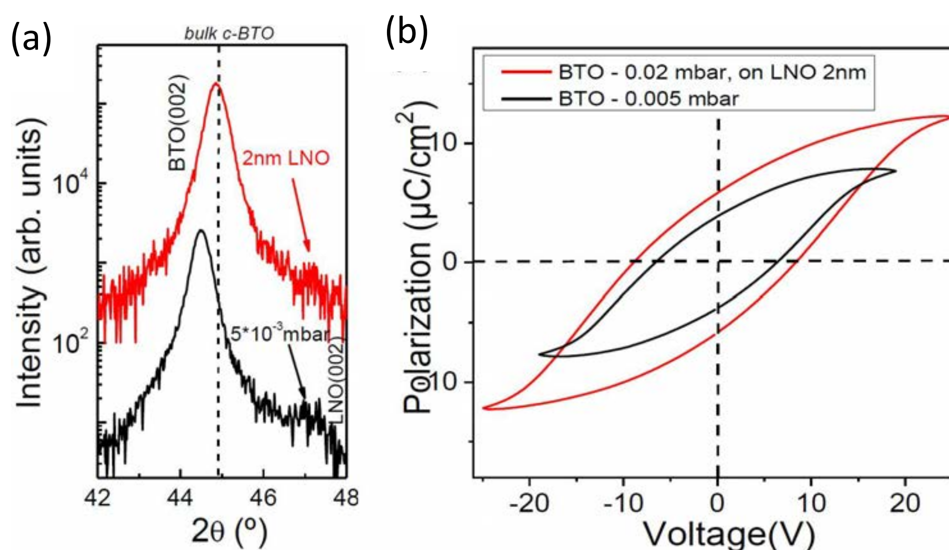


*Figure 4.1.19 XRD θ-2θ scans (a) and polarization loops of BTO films (b) on low conductance LNO bottom electrode, due to either LNO instability at low BTO deposition pressure ($P_{O2}$ = 5 x $10^{-3}$ mbar, LNO thickness around 30 nm) or ultrathin (2 nm) LNO thickness. The loops were measured at 150 and 30 Hz, respectively.*

Whereas LNO degradation does not influence the epitaxial growth and lattice strain of BTO, it reduces the switchable ferroelectric polarization, and does not allow fast polarization screening, hindering high frequency measurement. This causes the compensation of the BTO polarization charges less efficient degrading the ferroelectric properties. To confirm it, a BTO film was deposited at higher oxygen pressure, $P_{O2}$ = 0.02 mbar, but on an ultrathin (2 nm thick) LNO electrode. Indeed, sample with ultrathin LNO present similar FE behaviour. Figure 4.1.19(a) shows the XRD $\theta$-$2\theta$ scans of both samples. The (002) reflections of LNO electrodes on both

samples are very weak. The polarization loops in Figure 4.1.19(b) are similar and the two samples have high coercive voltage with at low frequency, thus pointing that low electrical conductance of the bottom LNO electrode in the $P_{O2}$ = 5 x $10^{-3}$ mbar sample decreased the switchable polarization.

The current − voltage curves of the films (Figure 4.1.18c) do not show big differences, although leakage in the $P_{O2}$ = 0.015 and 5 x $10^{-3}$ mbar samples is higher in most of the voltage range. The observation of similar current − voltage curves in BTO films having different microstructures suggests that current leakage through BTO is dominated by the Schottky barriers at the Pt/BTO and BTO/LNO interfaces. The Schottky barriers at the electrode − ferroelectric interfaces are responsible of the strong dependence of leakage on applied electric field.[186] The current density at 1 and 5 V is plotted against the oxygen pressure in Figure 4.1.16(d). The leakage is similarly low as it is in high quality ferroelectric films on silicon[29] and perovskite[40,41,187,188] substrates.

**Evaluation of point defects**

To evaluate the stability of the defects, and particularly those involving oxygen vacancies, two additional films grown at $P_{O2}$ = 0.02 mbar were prepared and cooled down under high oxygen pressure (200 mbar), one of them with additional annealing for 1 h at 600 °C, labeled (1) and (2), respectively. (Note: samples are normally cooled down under 0.2 mbar of oxygen pressure after deposition.) The XRD $\theta$-$2\theta$ scan and RSMs are presented Figure 4.1.20. The lattice parameters of the annealed samples at these two annealing conditions are similar to those of the sample cooled under $P_{O2}$ = 0.2 mbar.

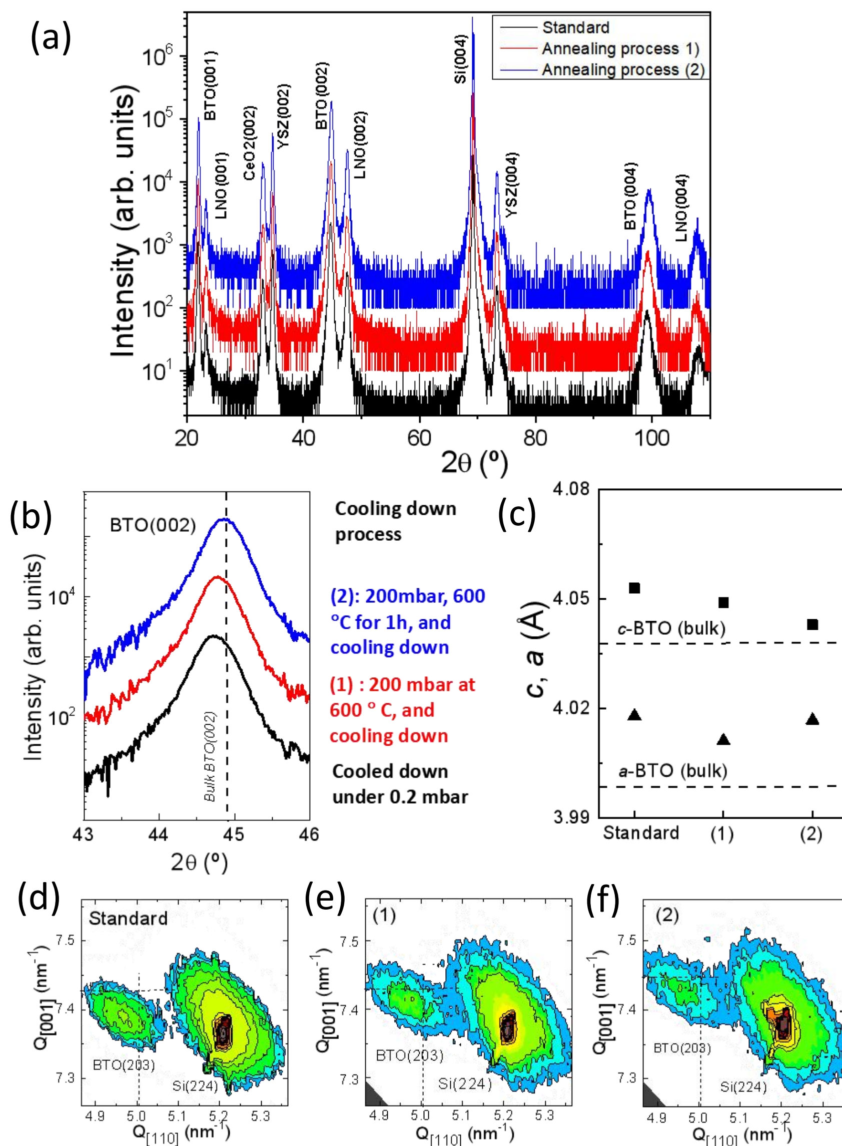


*Figure 4.1.20 (a) XRD θ-2θ scans, with a zoom around the BTO(002) reflection in (b). (c) out-of-plane (square) and in-plane (triangle) lattice parameters. The in-plane parameters were determined from RSMs, shown in (d-f).*

The electrical measurement of the samples with and without annealing are shown in Figure 4.1.21. The annealed samples present remnant polarization and leakage very similar to the corresponding sample cooled down under standard conditions (0.2 mbar). The results signal that low oxygen vacancy concentration and/or highly stable defects ultimately determine lattice strain in the BTO films deposited by PLD, and that their dependence on the deposition oxygen pressure permits growth of films with selectable strain and polar orientation.

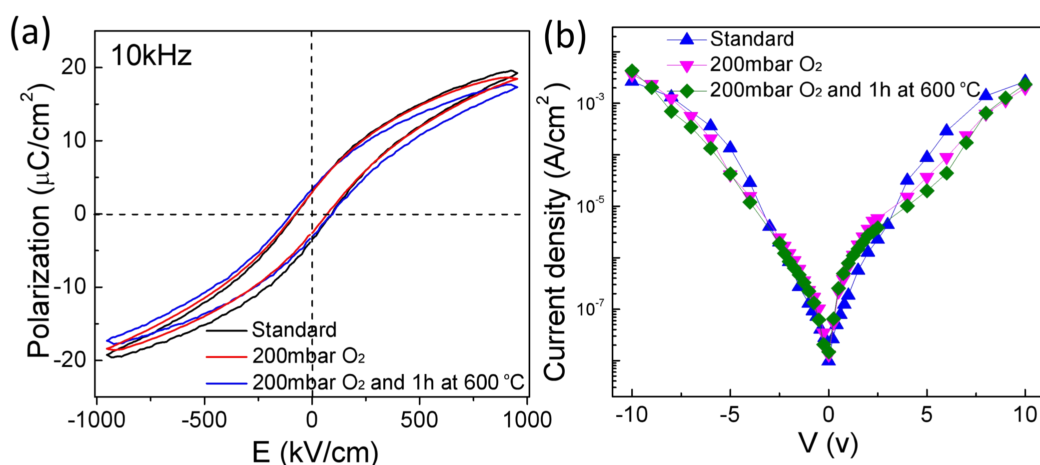


*Figure 4.1.21 (a) Polarization loops and (b) leakage current curves of a standard film (cooled down under 0.2 mbar) and annealed films (1) and (2).*

**$BaTiO_3$ films on $SrTiO_3$(001) and LSAT(001) with varied $P_{O2}$**

To demonstrate if this strategy is applicable for BTO films on other substrates such as perovskite single crystal, BTO films were deposited at 0.01, 0.02, 0.05 and 0.1 mbar oxygen pressure on bare $SrTiO_3$(001) and LSAT(001) perovskite substrates[2]. The two substrates were placed simultaneously in each deposition process. Substrate temperature and laser frequency were the used for deposition on silicon, 700 °C and 5 Hz, respectively.

Figure 4.1.22 shows topographic AFM images of the BTO films on STO and LSAT on the oxygen pressure. It can been seen that on both substrates, BTO films present a flat surface at oxygen pressure below 0.05 mbar and some terrace can be appreciated. Increasing the oxygen pressure to 0.1 mbar, BTO films show a abrupt increase of roughness. This dependence of the surface morphology of the BTO films on STO and LSAT on the oxygen pressure is coincident with the dependence for BTO films on silicon.

[2] Samples were prepared and characterized by Dr. Nico Dix, a Postdoc and former PhD student working at ICMAB. Details are reported elsewhere [*ACS applied materials & interfaces, 10(30), 25529*].

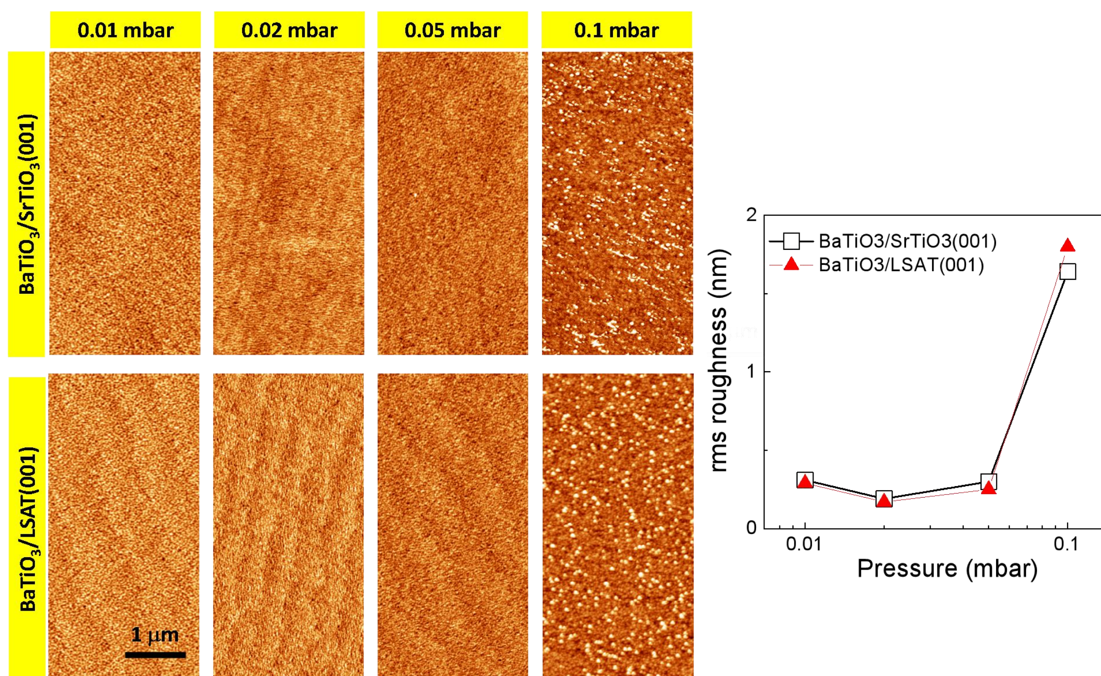


*Figure 4.1.22 Topographic AFM images of BTO films deposited at 0.01, 0.02, 0.05 and 0.1 mbar oxygen pressure on $SrTiO_3$(001) and LSAT(001). Right: dependence of the rms surface roughness on deposition pressure.*

Specular XRD *θ-2θ* scans are shown in Figure 4.1.23(a)-(b). There is a strong dependence of the out-of-plane (*oop*) lattice parameter of BTO on the deposition pressure on both substrates. The values are plotted against pressure in Figure 4.1.23(c)-(d). The dependence is the same that on Si(001): largely expanded *oop* for low deposition pressure and *oop* parameter coincident with lattice parameter in bulk BTO for films deposited under high pressure ($P_{O2}$ = 0.1 mbar). Reciprocal space maps around asymmetrical reflections of the films on STO substrates were measured (not shown) to determine in-plane (*ip*) lattice parameters. The same dependence observed in BTO films on Si(001) are obtained for the BTO film on single crystal: progressive reduction of tetragonality (*oop/ip* ratio) as deposition pressure increases, with tetragonality below 1 in the $P_{O2}$ = 0.1 mbar sample.

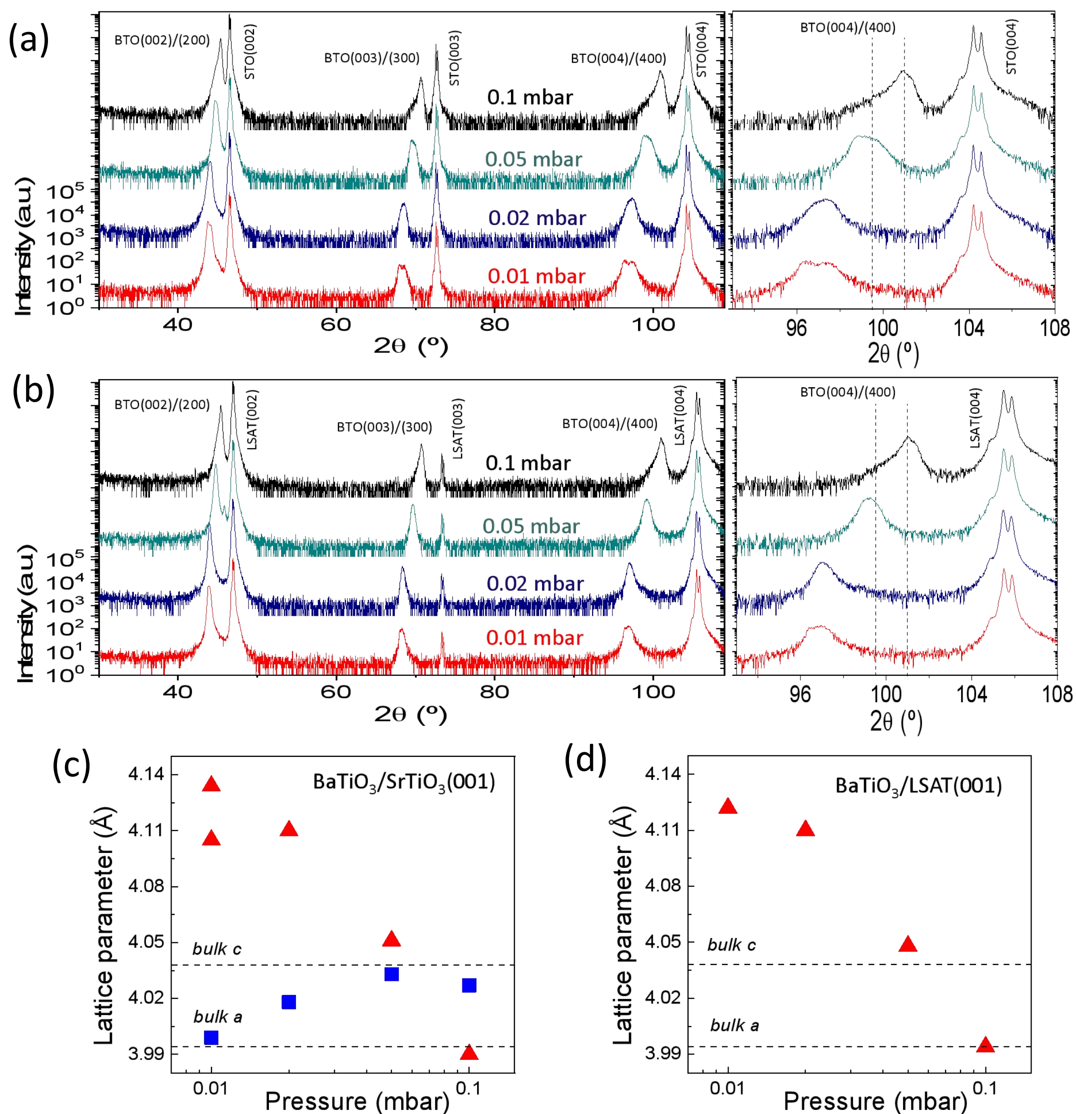


*Figure 4.1.23 Symmetrical XRD θ-2θ scans of BTO films deposited at 0.01, 0.02, 0.05 and 0.1 mbar oxygen pressure on $SrTiO_3$(001) (a) and LSAT(001) (b). The corresponding panels at the right are zooms around (004) substrate and (004)/(400) BTO reflections. Vertical dashed lines at 2θ = 99.494° and 100.984° mark the positions of (004) and (400) reflections in bulk BTO, respectively.*

Therefore, the same dependence of lattice strain, orientation, and surface roughness on pressure can also be achieved on perovskite single crystals. We can conclude that this effectiveness of the oxygen pressure as a tuning knob to tune BTO lattice strain and orientation is not limited to films deposited on Si(001) as a particular substrate,

### 4.1.3 Growth rate

**Structural Study**

Here, the growth rate refers to the instantaneous growth rate (gr/pulse) for depositing the BTO films. Under fixed deposition temperature and oxygen pressure, the growth rate can be varied by changing the size of the mask used to block the less homogeneous part of the laser beam. Using standard mask, the laser energy (E) per pulse is about 97 mJ for buffer layers and bottom electrode. For the deposition of BTO films, masks of different sizes were used to control the laser energy E for obtaining different growth rates. The growth rate of BTO is 0.550 Å/pulse determined by the thickness measurement[34] when the standard mask is used (laser energy E = 97 mJ). In the case of films grown using different masks, the growth rate is estimated indirectly assuming that is proportional to the energy. The number of laser pulses for deposition is varied accordingly in order to have a nominal thickness of 110 nm for all the BTO films.

The symmetric XRD $\theta$-$2\theta$ scans of the BTO films on Si(001) are shown in Figure 4.1.24(a). Only the (00*l*) peaks from BTO, buffer layers and Si substrate can be observed, without sign of parasitic phases. Figure 4.1.24(b) shows a zoom of the $\theta$-$2\theta$ scans around the (002) reflections of BTO and LNO. A continuous shift of BTO(002) peak position to lower $2\theta$ angles when increasing the growth rate from 0.099 Å/p to 0.832 Å/p can be observed, indicating BTO films are more strained when grown at higher growth rate. For the case of the film deposited at highest gr 1.050 Å/p, the peak shifted back towards high angles. In addition, the reflection of the BTO film at lowest gr 0.099Å/p is close to the position of bulk BTO (200), pointing to the transition from *c*-oriented BTO to *a*-oriented BTO when lowering the growth rate. Based on the rocking curve width in Figure 4.1.24(c), the BTO films in all growth rates have similar low mosaicity. Also, fwhm value of the BTO(002) specular $\theta$-$2\theta$ reflections in all of the samples show a small deviation. Therefore, the growth rate has negligible influence on the BTO crystal quality.

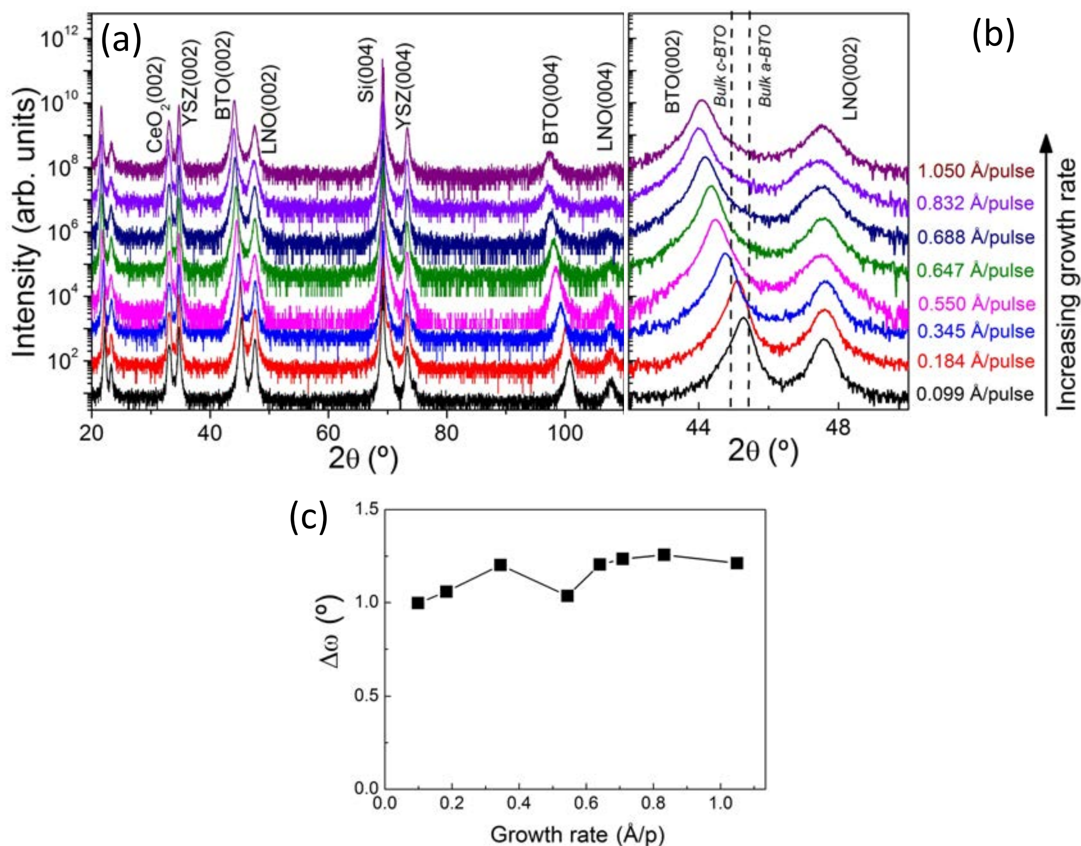


*Figure 4.1.24 (a) XRD θ-2θ scans of the BTO/LNO/CeO$_2$/YSZ/Si(001) series with varying the growth rate of BTO from the gr = 0.099 Å/p to 1.050 Å/p. (b) Zoomed region of the θ-2θ scans around the (002) reflections of BTO and LNO. The vertical solid and dashed lines mark the position of the (002) and (200) reflections in bulk BTO. (c) Dependence of the FWHM of the specular θ-2θ scan (Δ2θ) and its ω-scan (Δω) around BTO(002) reflection on the growth rate.*

Reciprocal space maps around the BTO(203) and Si(224) asymmetrical reflections of the samples grown at growth rates 0.184 Å/p, 0.550 Å/p, 0.831 Å/p and 1.050 Å/p were measured in Figure 4.1.25(a)-(d). The BTO peak indicates homogeneous strain in all the measured samples. The obtained in-plane lattice parameter is plotted against gr in Figure 4.1.25(e), together with the out-of-plane lattice parameter (determined from the specular $\theta$-$2\theta$ scans) of all BTO films on Si. The horizontal dashed lines indicate the values of the $a$ (3.994 Å) and $c$ (4.038 Å) parameters of bulk BTO. It is observed that the out-of-plane parameter increased monotonically up to a strain $\varepsilon_{[001]}$ of 1.9 % in the gr = 0.832 Å/p sample, and slightly relaxed for higher growth rate. While the in-plane lattice parameter does not change significantly due to the pinning of substrate as observed in $T_s$ and $P_{O2}$ series.[189,190] Consequently, the unit cell tetragonality ($c/a$) in Figure 4.1.25(f) increases with gr for the selected samples from below 1 at gr = 0.184 Å/p, smaller than the bulk $c/a$ ratio 1.01, to around 1.02 at gr = 1.050 Å/p. The unit cell volume of BTO is much expanded compared with the bulk value and increases with higher growth rate.

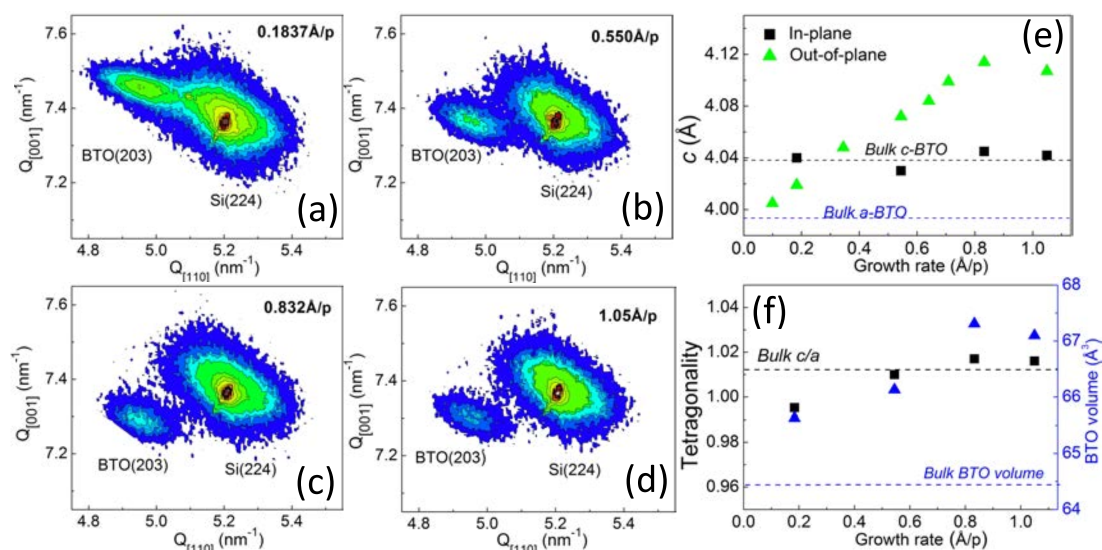


*Figure 4.1.25 (a)-(d) XRD reciprocal space maps around Si(224) and BTO(203) asymmetrical reflections at GR = 0.184 Å/p, 0.550 Å/p, 0.831 Å/p and 1.050 Å/p. (e) Dependence of the out-of-plane lattice parameter, and in-plane lattice parameter for selected samples. The horizontal dashed lines indicate the a- and c-axes length in bulk BTO. (f) Unit cell tetragonality (left axis, black squares) and volume (right axis, blue triangles) for selected samples. The horizontal dashed lines indicate the c/a tetragonality and unit cell volume of bulk BTO.*

Figure 4.1.26 shows the topographic AFM images of BTO films at different growth rates. All the BTO films present very flat and homogeneous surface morphology except for the film at gr = 0.550 Å/p with the agglomeration of a few islands of higher height in some areas. Similar agglomeration of islands are indeed observed in most of BTO films on Si included in the $T_s$ and $P_{O2}$ series. The root means square (rms) roughness of the samples on Si, calculated from 1 μm x 1 μm areas, is plotted as a function of gr in bottom of Figure 4.1.26. The BTO film grown at lowest gr 0.099 Å/p presents the highest roughness with rms around 0.8 nm. The flattest surface with rms below 0.2 nm can be obtained when slightly increasing the gr to 0.184 Å/p. And increasing the growth rate, the films are progressively rougher.

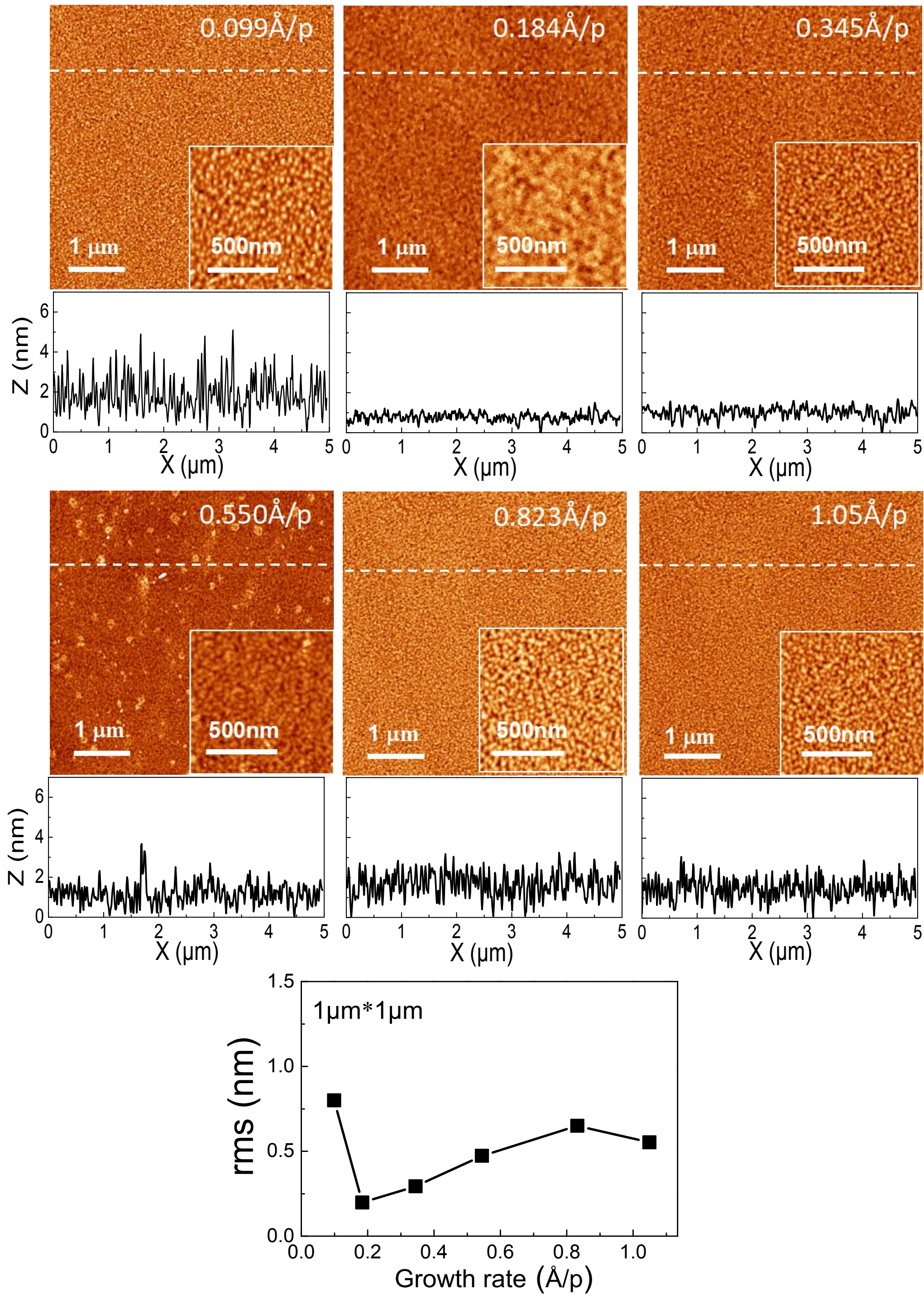


*Figure 4.1.26 Topographic AFM images, 5 μm x 5 μm in size (inset: 1 μm x 1 μm) with height profiles (bottom) along the dashed lines. Bottom panel: rms roughness as a function of the growth rate.*

### Electrical Characterization

All the samples are ferroelectric. The ferroelectric polarization loops for selected samples are measured at 10 kHz with *DLCC* as shown in Figure 4.1.27(a). The

remnant polarization $P_r$ and electrical coercive field $E_c$ of the films range within 2 - 14 μC/cm$^2$ and 1 - 6.5 V, respectively. The values of remnant polarization and coercive voltage as a function of growth rate can be seen in Figure 4.1.27(b). Due to the low growth rate favoring the transition from *c*-oriented BTO to *a*-oriented BTO, the sample at lowest gr 0.099 Å/p has a quite small $P_r$ slightly below 2 μC/cm$^2$. This value is similar to the one of *a*-oriented BTO film at high oxygen pressure (0.05 mbar and 0.1 mbar) as reported in chapter 4.1.2. At slightly higher growth rate 0.184 Å/p, the sample presents the maximum $P_r$ around 14 μC/cm$^2$, which represents the largest value currently achieved of BTO on Si(001) in these three series. Then increasing growth rate to 0.550 Å/p, $P_r$ is decreasing monotonically to around 7 μC/cm$^2$, followed by a dwelling level of $P_r$ between around 6 and 8 μC/cm$^2$ in the growth rate ranging from 0.550 Å/p to 1.050 Å/p. The coercive voltage showed the similar dependence with $P_r$. The current − voltage curves of the films with different growth rates are shown in Figure 4.1.27(c) with the values of leakage current at 1 V, 5 V and 10 V plotted as a function of gr in Figure 4.1.27(d). It can be seen that as increasing the growth rate, the leakage current is getting smaller and the BTO films are more insulting.

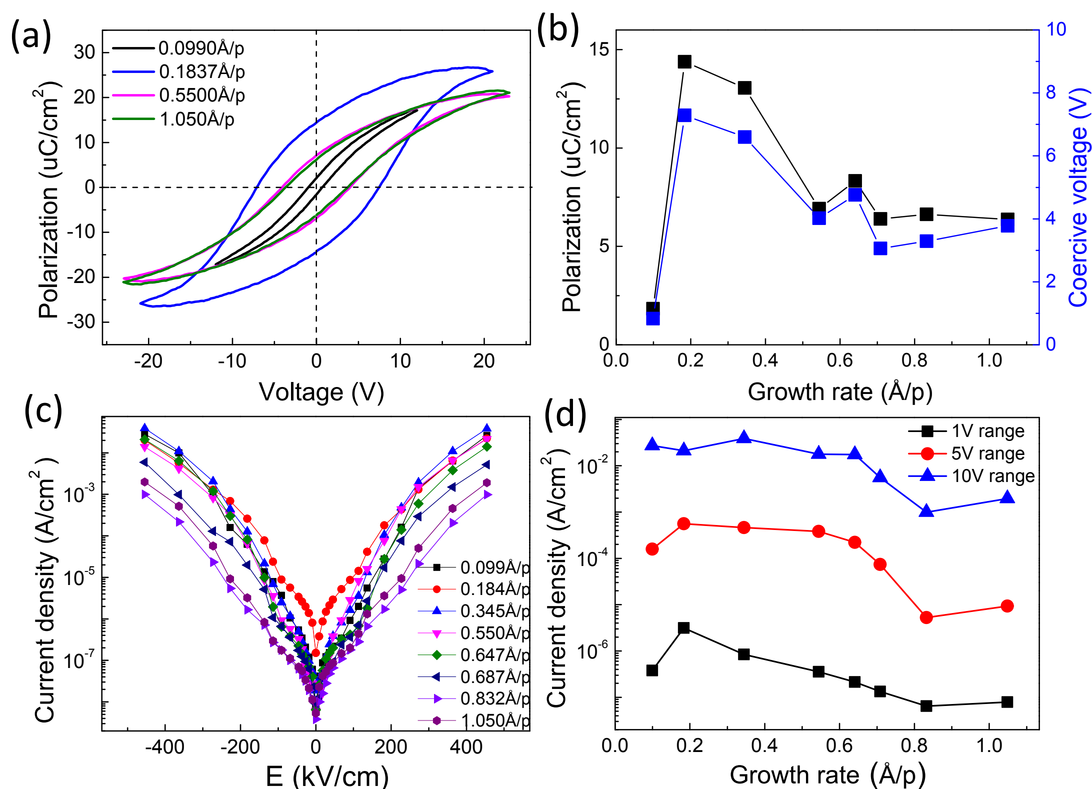


*Figure 4.1.27 (a) Ferroelectric polarization loops of gr = 0.099 Å/p, 0.184 Å/p, 0.550 Å/p and 1.05 Å/p BTO films on LNO/$CeO_2$/YSZ/Si(001). (b) Remnant polarization and coercive field as a function of gr. (c) Leakage curves of BTO films deposited at varied growth rates. (d) Leakage current at 1 V, 5 V and 10 V as a function of the growth rates.*

The remnant polarization and out-of-plane lattice parameters as a function of growth rate are shown in Figure 4.1.28. One can see that the $P_r$ does not scale with the out-of-plane lattice parameters and presents slightly inverse dependence on the c-axis strain. The sample grown at gr = 0.184 Å/p shows $P_r$ is over 14 μC/cm$^2$ with out-of-plane parameter smaller than the *c* value of bulk BTO while $P_r$ for the BTO film grown at gr = 0.832 Å/p with largest out-of-plane parameter 4.114 Å was only 6 μC/cm$^2$. In principle, the $P_r$ should be scaled with the out-of-plane lattice parameters as the unit cell of BTO with more expanded *c*-axis strain will induce larger dipole moment. However, this is not observed in this growth rate series. Other authors reported the dependence of lattice strain on laser fluence in BTO films on $GdScO_3$(110) by pulsed laser deposition.[40] They found huge expansion of the out-of-plane lattice parameter up to 4.1 % with increasing the laser fluence from 1.5 to 2.7 J/cm$^2$. However, in spite of the huge difference in strain, the corresponding polarization was quite similar. The films were stoichiometric and they suggested the defects produced with the high energetics of the PLD growth process as possible cause of lattice expansion. The pinned and shifted hysteresis loops were also signals as consequence of defect dipoles. Defect dipoles could be also present in our films, especially for the sample grown at high growth rate and could cause domain pinning. We note that the *t-t* configuration was used for ferroelectric measurement and thus the imprint field is not determined.[175] Indeed, the BTO film on Si measured using *t-b* configuration presented quite symmetric FE loop with symmetric LNO electrodes (the detailed investigation will be discussed later) without showing the evident imprint. Understanding the nature of these defects and correlation with polarization has not been discussed in this thesis.

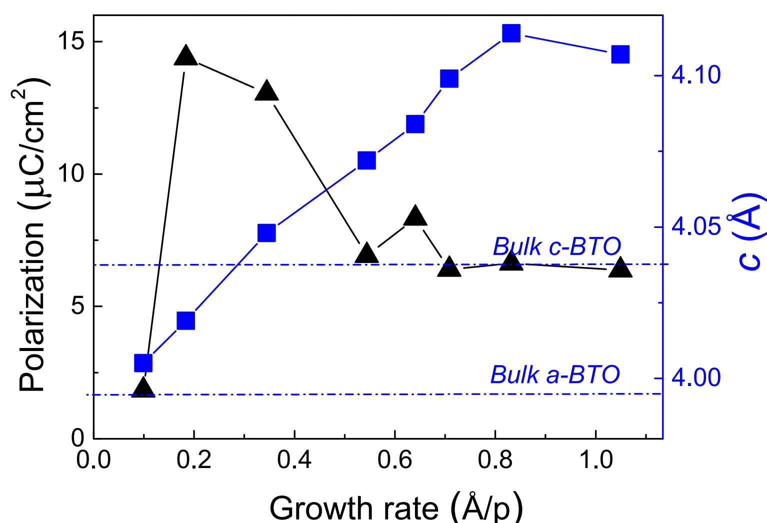


*Figure 4.1.28 The dependence of remanent polarization and c-axis strain on the growth rate of BTO film on $LNO/CeO_2/YSZ/Si(001)$.*

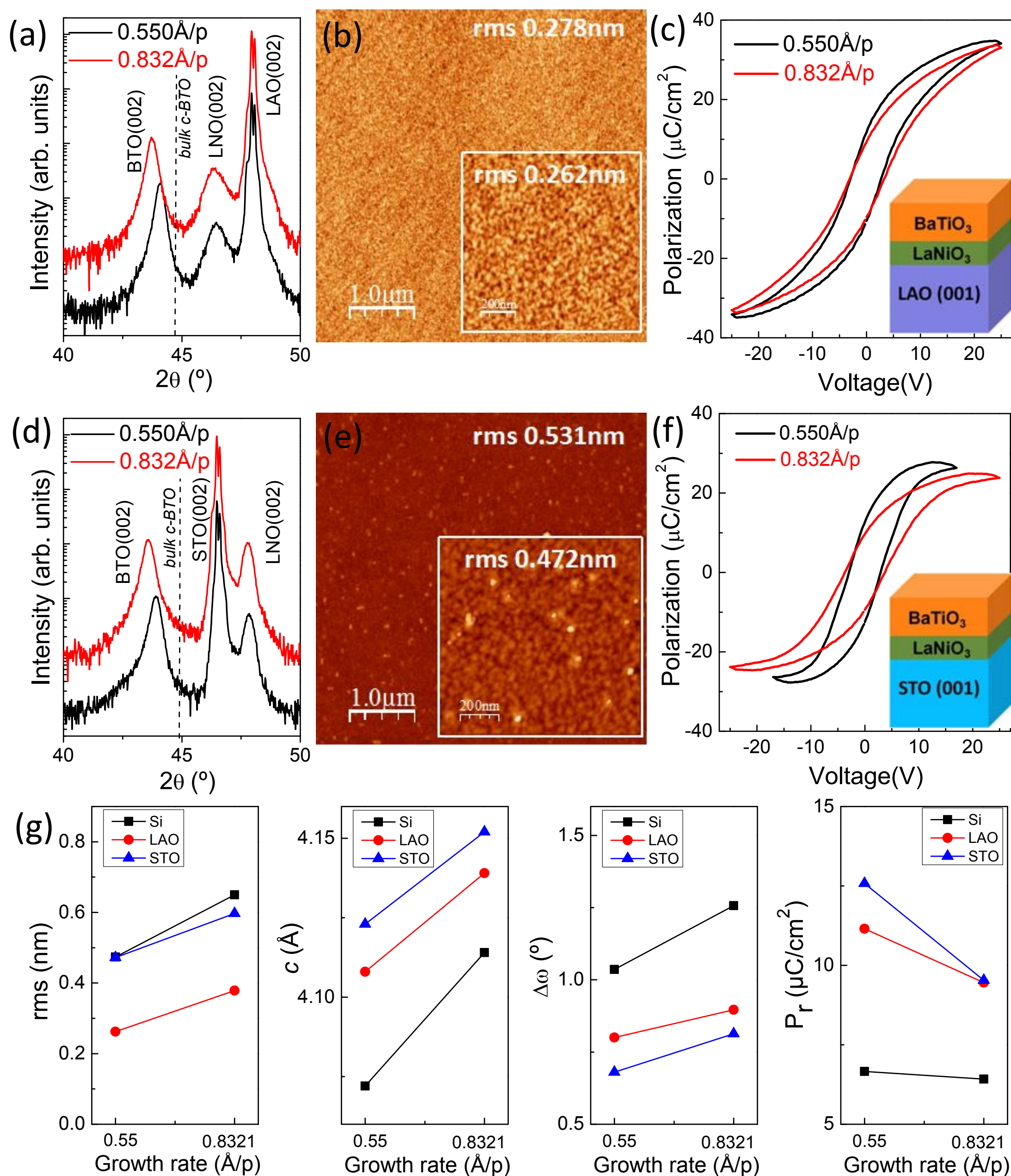


*Figure 4.1.29 (a) and (d) XRD θ-2θ scans of the GR = 0.550 Å/p and 0.832 Å/p films (b) and (e) Topographic AFM 5 μm x 5 μm image (inset: 1 μm x 1 μm) of the GR = 0.550 Å/p film and (c) and (f) Ferroelectric polarization loops of the GR = 0.550 Å/p and 0.832 Å/p films on LNO/$LaAlO_3$(001) and LNO/$SrTiO_3$(001), respectively. Insets of Figure (c) (f) are the sketch of corresponding heterostructures. (g) Comparison of rms roughness, out-of-plane lattice parameter, full width at half maximum of the ω-scan, and remnant polarization (from left to right) of BTO films on Si, LAO and STO at GR = 0.550 Å/p and 0.832 Å/p.*

These intriguing results between the dependence of $P_r$ and *c*-axis strain on the growth rate does not only appeared in sample of BTO films on Si. The similar dependence was also observed on BTO films grown on perovskite substrates. Two additional

samples of BTO/LNO bilayers were prepared on LAO (001) and STO (001) substrates at growth rate 0.550 Å/p and 0.832 Å/p to demonstrate it. As shown in Figure 4.1.29(a) and (d), the XRD $\theta$-$2\theta$ scans of the bilayers only show (00*l*) reflections on both LAO(001) and STO(001), and BTO films are epitaxially strained, being the strain higher at growth rate 0.832 Å/p sample than at growth rate 0.550 Å/p, respectively. Topographic AFM images show that the films on both single crystal substrates are very flat. At growth rate 0.550 Å/p, the rms roughness of BTO on LAO(001) (Figure 4.1.29b) is lower below 0.3 nm with morphology of terraces and steps observed while the BTO sample on STO(001) (Figure 4.1.29e) has high rms roughness around 0.5 nm with the agglomeration of a few islands on the surface. The ferroelectric loops show larger polarization in the GR = 0.550 Å/p BTO films on both substrates as indicated in Figure 4.1.29(c) and (f), basically in agreement with the result of BTO on Si(001) substrate. The values of rms roughness, *c*-axis parameter, BTO(002) rocking curve width and remnant polarization of BTO films on LAO(001), STO(001) and Si(001) against the growth rate (0.550 Å/p or 0.832 Å/p) are concluded in the bottom Figure 4.1.26(g) (from left panel to right), clearly indicating the same trending of BTO films on all three substrates with growth rate.

## Conclusion

In summary, the growth parameters (substrate temperature and oxygen pressure) during pulsed laser deposition can be used as a tuning knob to control lattice strain and ferroelectric polarization of epitaxial $BaTiO_3$ over a broad range with small leakage current. It also permits selecting the polar axis to be *ip* (*a*-oriented $BaTiO_3$) or *oop* (*c*-oriented $BaTiO_3$). In contrast to the usual strain engineering methodology, the selection of a particular strain is achieved without necessity of selecting a specific substrate, and it is not limited to very thin ferroelectric films. This unconventional strain engineering has been demonstrated to be efficient for $BaTiO_3$ films thicker than 100 nm on either perovskite substrates or Si(001) wafers. Important limitations of conventional strain methodology are thus overcome, opening new avenues for better control of strain and polar orientation in ferroelectric oxides and particularly for its integration on semiconducting substrates. However, the nature of defects causing *c*-axis strain and electrical properties of ferroelectric films still requires deeper studies.

## 4.2 Electrode-interface controlled ferroelectric $BaTiO_3$ films

*Abstract*

*Different electrodes ($La_{2/3}Sr_{1/3}MnO_3$, $LaNiO_3$ and Pt) were used in ferroelectric capacitor of epitaxial $BaTiO_3$ on $LaAlO_3$(001) and Si(001) substrates. The ferroelectric properties have a strong dependence on the electrodes. Epitaxial $BaTiO_3$ films using $La_{2/3}Sr_{1/3}MnO_3$ electrode on $LaAlO_3$ and Si substrates present higher remanent polarization, larger coercive field and lower leakage than using $LaNiO_3$ electrode. The larger imprint field ($E_{imp}$) around 90 kV/cm was observed in $BaTiO_3$ films with $LaNiO_3$ electrode on $LaAlO_3$(001) compared with much reduced $E_{imp}$ below 40 kV/cm using $La_{2/3}Sr_{1/3}MnO_3$ electrode. On the other hand, the $E_{imp}$ is quite negligible for $BaTiO_3$ films grown on Si substrate. With noble metal Pt electrode, $BaTiO_3$ films show much shrinked ferroelectric loops with much smaller $P_r$ and $E_c$ compared with using perovskite oxide electrode. In contrast, the leakage is higher in symmetric capacitors with perovskite electrodes than in asymmetric capacitors with top Pt electrodes. This systematic study provides an instructive guide for the selection of different electrode materials, with strong impact on the electric properties of ferroelectric $BaTiO_3$ films.*

Ferroelectric thin film capacitors are generally in a sandwiched structure by two metallic electrodes. The commonly used electrode materials in memory devices can be divided into two groups. One consists of the noble metals such as Pt, Au, Co and Ir while the other is the conducting pervoskite oxide electrodes such as $LaNiO_3$, LSMO, and $SrRuO_3$. It has been widely reported that the ferroelectric-electrode interface has a significant influence on the electrical properties of the ferroelectric thin films. For instance, the use of metallic oxide electrodes can significantly improve the fatigue property of ferroelctric $Pb(Zr,Ti)O_3$ films compared with using the metallic electrode.[82,83] Besides the ferroelectric fatigue, the electrode interface can also have a large influence on the leakage current,[84-86] hysteretic behavior[86-88] and dielectric permittivity[89] of the ferroelectric films. Therefore, the interface state in ferroelectric capacitors must be well understood for controlling and optimizing the design of ferroelectric-based memory devices. However, the extensive work on understanding the electrode interface effects are mainly on ferroelectric $Pb(Zr,Ti)O_3$ films and the effects of electrode interfaces on the electrical properties of $BaTiO_3$ capacitors are less studied, especially when they are integrated with Si substrate. Motivated by this, a systematical investigation about employing the different type of electrodes (perovskite metallic oxides and noble metals) are proposed to investigate the influence of electrode-interface on the electrical properties of ferroelectric epitaxial $BaTiO_3$ thin film on single crystal $LaAlO_3$ and Si substrates.

### 4.2.1 Growth conditions

$BaTiO_3$ films (thickness t = 110 nm) were deposited in a single process on $LaAlO_3$(001) single crystal and Si(001) substrates with $La_{2/3}Sr_{1/3}MnO_3$ and $LaNiO_3$ as bottom electrodes of around 30 nm by pulsed laser deposition. Figure 4.2.1 shows the heterostructures of the four samples of BTO films grown on LAO(001) and Si(001) substrates used in this section. On LAO substrate, LNO was used as bottom electrode in Figure 4.2.1(a). When LSMO is used as bottom electrode in Figure 4.2.1(b), LNO works as buffer layer for epitaxial growth of LSMO. And the same purpose is for BTO on Si where YSZ/$CeO_2$ were sequentially deposited as buffer layers as shown in Figure 4.2.1(c) and (d). The LSMO electrode was grown at 700 ºC, 0.1 mbar at frequency 5 Hz. And the detailed growth conditions for other layers can be seen in Chapter 4.1.

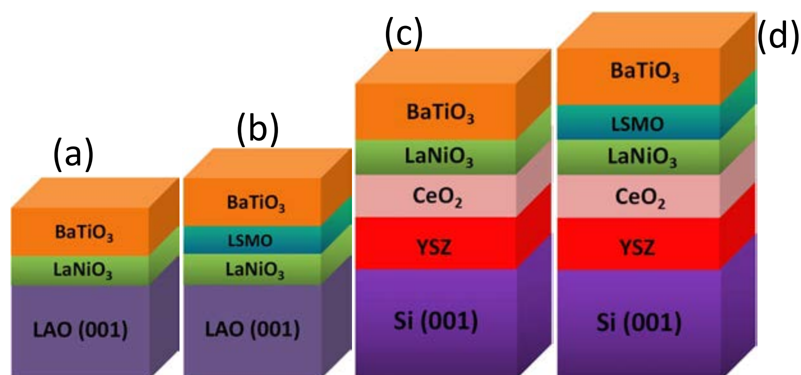


*Figure 4.2.1 (a)-(d) The sketch of the four heterostructures of $BaTiO_3$ films grown on LAO(001) and Si(001) substrates.*

For the deposition of symmetric top oxide electrodes, the top oxide electrodes were grown by PLD at same conditions with the bottom electrodes, and the thickness was between 20 nm - 30 nm. A TEM grid was used as mask to deposit the top perovskite oxide electrodes (LSMO and LNO) with eight different areas of 50 µm, 100 µm, 200 µm and 400 µm diameters of cycle and square in size. The representative images of LSMO and LNO top electrodes on Si(001) under optical microscopy are shown in Figure 4.2.2(a)-(d). The details about the deposition parameters of top Pt electrodes can be seen in chapter 3.

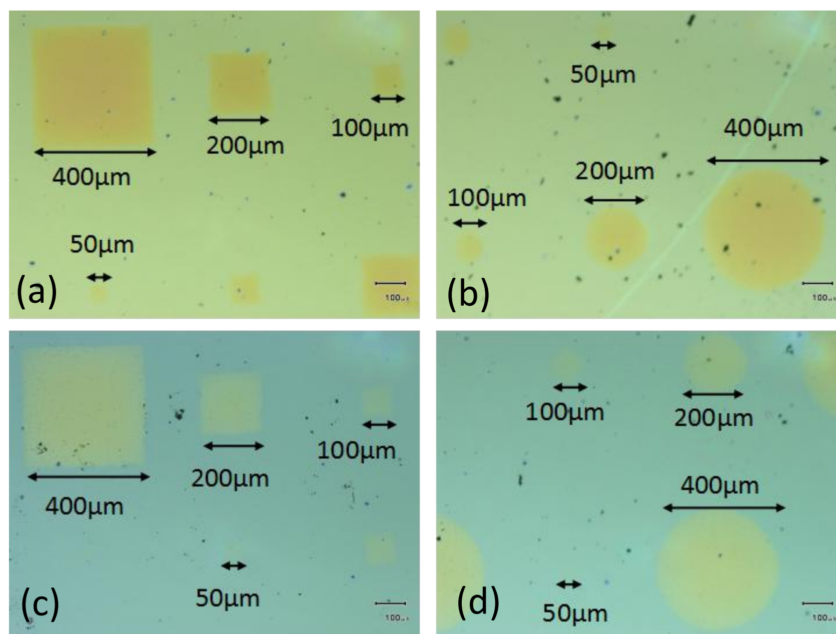


*Figure 4.2.2 The representative optical microscopic images of LSMO (a)-(b) and LNO (c)-(d) top electrodes of BTO films on Si(001) substrate with four sizes (50 µm, 100 µm, 200 µm and 400 µm) of in square and circle, respectively.*

Here we need to note that the top metallic oxides electrodes were grown under the same condition of bottom electrode by PLD. And steel masks were used. For instance, top and bottom LNO electrodes with same thicknesses were both grown at 700 ºC and 0.15 mbar. To check if the deposition process at high temperature has effects on the structure of BTO, the specular XRD $\theta$-$2\theta$ measurements were performed before and after the deposition of top electrodes for the two samples of BTO on LAO single crystal. The result is shown in Figure 4.2.3. There is a negligible variation between the peak positions of BTO(002), LNO(002) and LSMO(002) before and after the top electrode deposition. Therefore, the deposition process of top metallic electrodes has no significant influence on the BTO film.

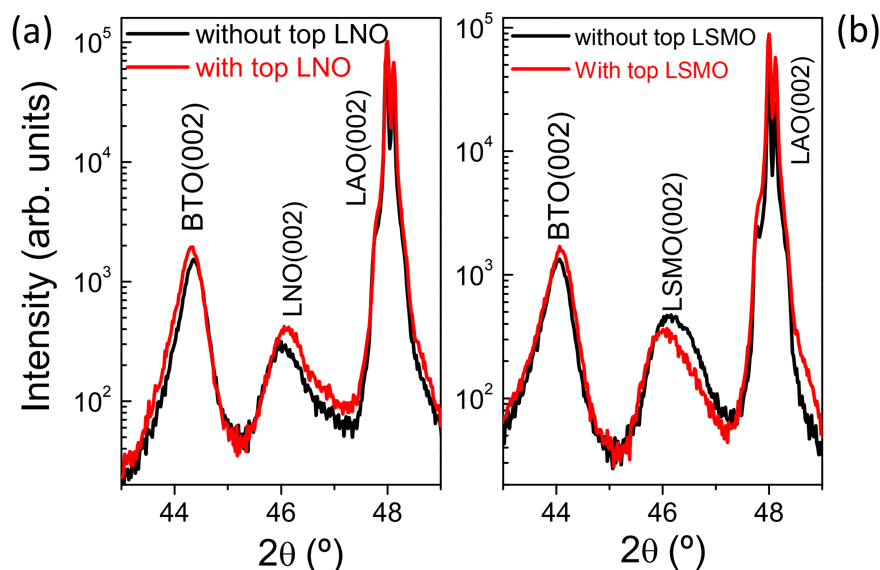


*Figure 4.2.3 The XRD θ-2θ patterns of BTO films on LAO(001) substrate before and after the deposition of top LNO (a) and LSMO (b) electrodes, respectively.*

## 4.2.2 Structural Study

The X-ray diffraction (XRD) $\theta$-$2\theta$ scans of the BTO thin film on LAO(001) and Si(001) after top electrodes (LNO and LSMO) deposited is shown in Figure 4.2.4(a). The XRD result reveals that all films on LAO(001) and Si(001) substrates are epitaxial and single phase. The right panel of Figure 4.2.4(a) shows the zoomed region of $\theta$-$2\theta$ around BTO(002) reflections. The dashed vertical lines mark the position of the (002) reflection of bulk BTO. All the films are *c*-oriented. The out-of-plane lattice parameter of BTO grown on LAO substrate, as shown in top panel of Figure 4.2.4(b), is significantly larger than on Si substrate. In addition, no matter on LAO or Si substrates, the BTO films using LSMO as bottom electrode show the larger out-of-plane lattice parameters with epitaxial strain of $\varepsilon$ = 1.54 % on LAO and 0.57 % on Si. The crystal quality of BTO was evaluated by rocking curves in bottom

panel of Figure 4.2.4(b). It was found that the crystallinity of BTO films is scarcely dependent on the bottom electrodes and better crystal quality of BTO film was obtained on LAO(100) single crystal ($\Delta\omega$ ~ 0.83°) than on Si(001) substrate ($\Delta\omega$ ~ 1.11°).

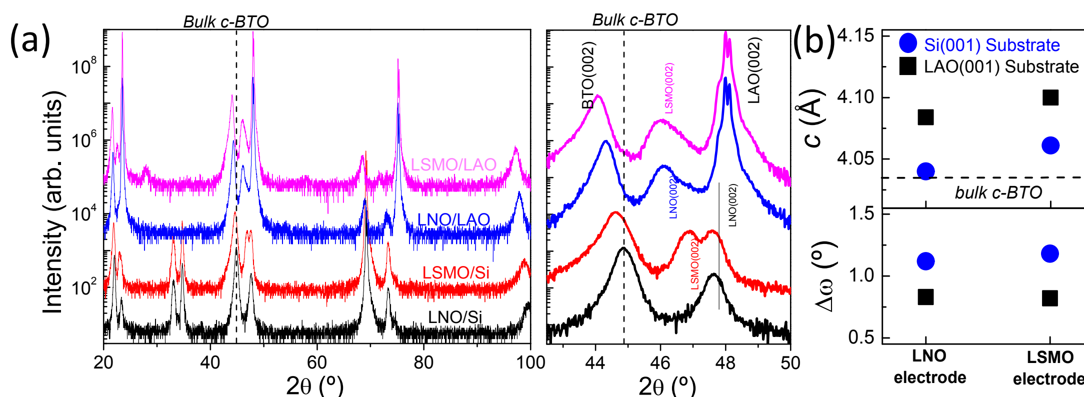


*Figure 4.2.4 (a) XRD θ-2θ scans of BTO films on LAO(001) and Si(001) substrates with LSMO or LNO electrodes. Right panel: Zoomed region of the θ-2θ scans around the (002) reflections of BTO and LNO (or LSMO). The vertical dashed lines mark the position of the (002) reflections in bulk BTO. (b) Dependence of c-axis strain (upper panel) and ω-scan (Δω) around BTO(002) (lower panel) on LNO and LSMO electrodes of BTO films on LAO and Si.*

Due to the similarity of structure and small lattice mismatch between BTO, LNO (LSMO) and LAO, BTO films and LNO (or LSMO) electrode will grow cube-on-cube on LAO(001) with the epitaxial relationships [100]BTO(001)/ [100]LNO(001)/[100]LAO(001). For epitaxial BTO films on Si(001), as discussed before in chapter 4.1, the epitaxial relationship between each layers will be [110]BTO(001)/[110]LNO(001)/[100]$CeO_2$(001)/[100]YSZ(001)/[100]Si(001).

In order to determine the in-plane lattice parameters and strain states, the reciprocal space maps (RSM) were measured around the (103) reflections of BTO, LNO and LAO for the sample of BTO on LAO(001) while around BTO(203) and Si(224) reflections on Si substrate in Figure 4.2.5(a) and (b). One can see a homogeneous strain in BTO films on LAO and Si substrates, respectively. The vertical dashed line indicates the value of the in-plane (3.994 Å) parameter of bulk BTO. On LAO substrate, the reference lattice parameter for bulk cubic LAO is 3.791 Å which means in principle there is a compressive in-plane strain in the BTO film imposed by the substrate. However, due to the high thickness (t > 100 nm) and lattice mismatch (around 5.3 %), BTO film on LAO substrate is relaxed close to the bulk value (slightly compressive strain of about 0.04 %), which can be seen from RSM in Figure 4.2.5(a), while on Si substrate, BTO present a tensile in-plane strain of about 0.95 % (Figure 4.2.5b). In addition, as indicate in Figure 4.2.5(c), BTO film on LAO presents a higher BTO tetragonality with the longer polar axis normal to the surface. While the

unit cell of BTO film on Si substrate is more expanded than on LAO(001) single crystal, which signals that higher defects were induced in BTO film on Si substrate resulting in more expanded crystal structure.

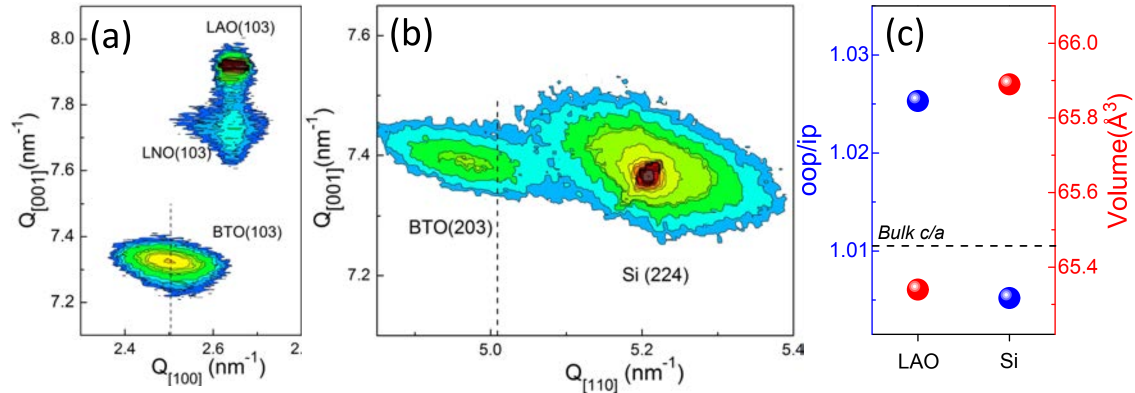


*Figure 4.2.5 (a) XRD reciprocal space maps around LAO(103) and BTO(103) asymmetrical reflections for BTO/LNO/LAO(001) sample. (b) XRD RSM around Si(224) and BTO(203) asymmetrical reflections for BTO/LNO/$CeO_2$/YSZ/Si(001) sample. (c) Tetragonality and unit cell volume of BTO on LAO and Si substrates using LNO electrode.*

AFM measurements of LSMO/BTO/LSMO/LNO/$CeO_2$/YSZ/Si(001) sample are shown in Figure 4.2.6. Despite the small islands on the top LSMO electrode, the bare BTO film and top LSMO electrode both present a flat surface. Remarkably, the root-mean-square (rms) roughness of top LSMO contacts is as low as 0.18 nm (1 μm x 1 μm region), implying a good epitaxial quality of top LSMO electrode grown on BTO. For the other samples, due to the low optical contrast, the top electrodes were not visible under the AFM microscopy, which made it not possible to check the surface morphology of top electrodes.

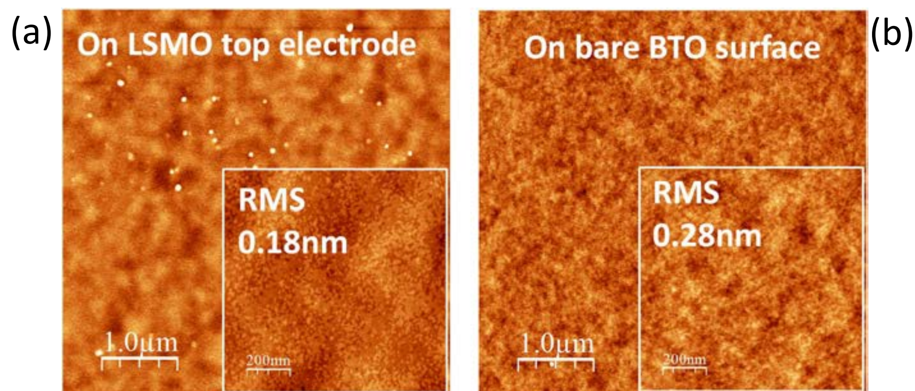


*Figure 4.2.6 Topographic AFM images, 5 μm x 5 μm in size (inset: 1 μm x 1 μm) on LSMO top electrode (a) and on bare BTO surface (b) for LSMO/BTO/LSMO/LNO/$CeO_2$/YSZ/Si(001) sample.*

### 4.2.3 Electrical comparison between metallic oxide electrodes

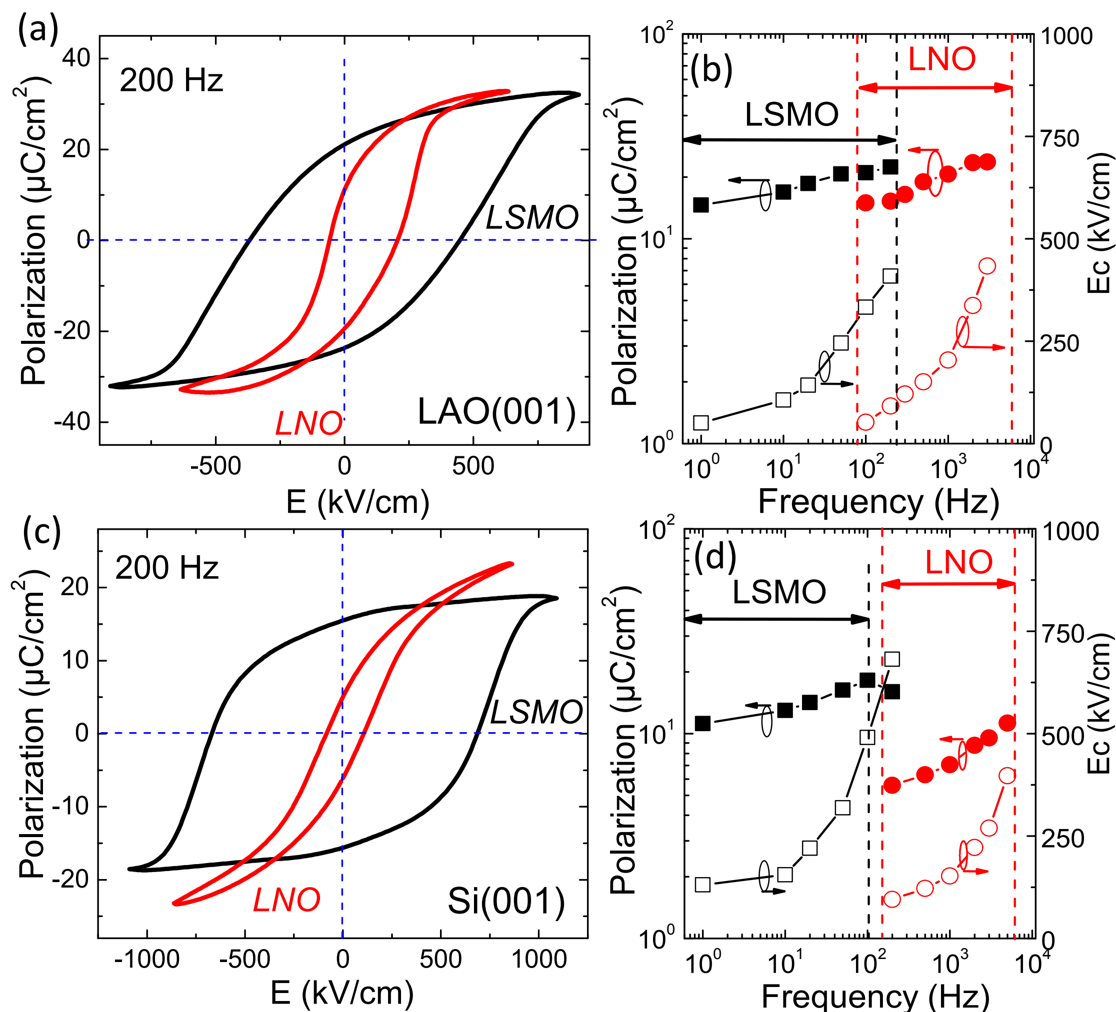


*Figure 4.2.7 Ferroelectric polarization loops of BTO films on LAO(001) (a) and Si(001) (c) using LSMO and LNO electrodes at 200 Hz. (b) and (d) are the corresponding remnant polarization and coercive field as a function of frequency.*

Ferroelectric meaurement was performed with top-bottom configuration for the samples with symmetric oxide electrodes. Figures 4.2.7(a) and (c) show ferroelectric polarization loops of the BTO films with LSMO and LNO electrodes on LAO(001) and Si(001) at 200 Hz, respectively. The different ferroelectric loops can be observed using LSMO and LAO electrodes. The polarization loop of BTO with LSMO electrode presents quite "broad" characteristic which is very different from the "slim" one with LNO electrodes. This diverse characteristics of hysteresis loops result from the distinct $P_r$ and coercive fields. On LAO(001) substrate (Figure 4.2.7a), the BTO film with LSMO electrode shows the larger $P_r \approx 22$ μC/cm$^2$ and $E_c \approx 410$ kV/cm while

for BTO using LNO electrode $P_r$ and $E_c$ are about 18 μC/cm$^2$ and 110 kV/cm, respectively. Despite the slightly larger $P_r$ obtained on LSMO electrode, the coercive field ($E_c$) of BTO film with LSMO electrode is over three times higher than that using LNO electrode. The detailed values for $P_r$ and $E_c$ at different frequencies with LSMO and LNO electrodes on LAO substrate are plotted in 4.2.7(b). It is clear to see that the equivalent $E_c$ around 400 kV/cm is obtained at 200 Hz for BTO with LSMO electrode while at 3 kHz for BTO with LNO electrodes. In principle, $E_c$ is dependent on the frequency.[1,2,5] With higher frequency applied, larger $E_c$ is required. Clearly, BTO films using LSMO electrode present larger coercive field than using LNO electrode. Similar conclusion is confirmed by the result of BTO film on Si with both electrodes as shown in Figure 4.2.7(c) and (d).

Here, we have to note that the $P_r$ and $E_c$ values are not extracted from the same frequencies in Figures 4.2.7(b) and (d). The reason is explained in Figure 4.2.8. For the BTO sample using LSMO (Figure 4.2.8a), with increasing the frequency to only 300 Hz, the normal FE loop cannot be obtained due to the large $E_c$. While the large leakage become evident for BTO film using LNO, which influences the precise determination of $P_r$ and $E_c$ (Figure 4.28b). This large leakage is evidenced by the leakage current measurement in Figure 4.2.8(c), over one order of magnitude higher than using LSMO electrode at 45 kV/cm and 225 kV/cm on both substrate. In addition, the leakage of BTO film on Si substrate is higher when using the same electrode than on LAO(001) single crystal.

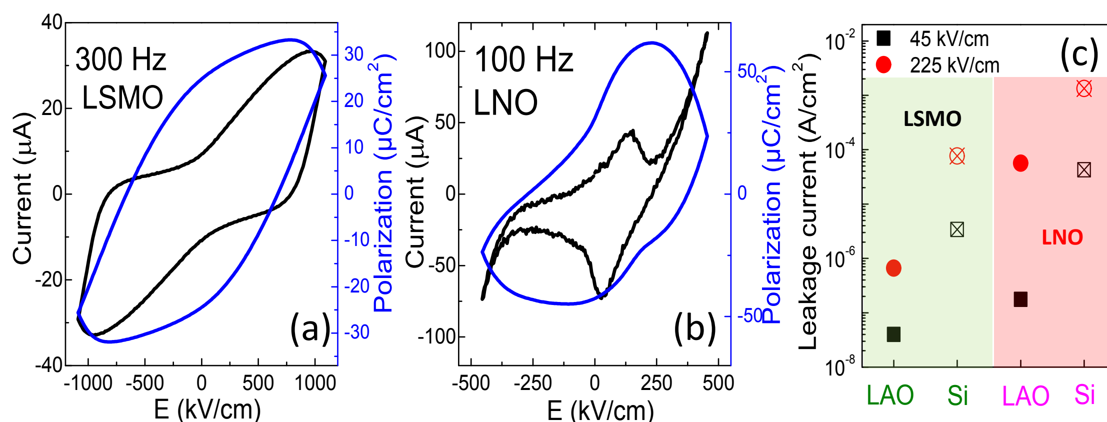


*Figure 4.2.8 Hysteresis loops of BTO films on LAO substrate (a) using LSMO electrode measured at frequency 300 Hz and (b) using LNO electrode measured at frequency 100 Hz. (c) Leakage current at 45 kV/cm and 225 kV/cm of BTO films on LAO and Si using LSMO and LNO electrodes.*

Respect the distinct coercive field between using LNO and LSMO electrodes, the reason may origin from the charge transport properties since the LSMO and LNO electrodes share the similar crystal structure and lattice constants with BTO. The conducting metallic oxides (LNO and LSMO) possess different electric resistivity. As

reported, the electrical resistivity of LSMO film at room temperature [199-201] is between 4 x $10^{-4}$ Ω cm ~ 2 x $10^{-3}$ Ω cm while the resistivity value ranges from around 9 x $10^{-5}$ Ω cm ~ 3 x $10^{-4}$ Ω cm for LNO film.[202-204] Thus, the electrical resistivity of LSMO film is close to one order of magnitude larger than that of LNO electrode at room temperature. The polarization screening of BTO with electrodes of high resistivity will be less effective. On the other hand, LSMO electrode can present a dead layer with degraded conductivity at interface. For these reasons, BTO film with LSMO electrodes has much larger coercive field. Indeed, as discussed in chapter 4.1.2, when the bottom electrode LNO is degraded at low oxygen pressure or ultra thin (around few nanometers), high frequency measurement for hysteresis loop become extremely difficult and BTO films present high coercive field even at low frequency.

Imprint describes a internal field driving ferroelectric polarization towards a preferential direction when external bias is removed. Imprint field ($E_{imp}$) is defined as: $E_{imp}$ = 0.5 x ($E_{c+}$+$E_{c-}$), expressing the electrical field shift in the hysteresis loop. The evident difference of ferroelectric loops between using LNO and LSMO electrodes for the imprint field can be seen in the ferroelectric loops in Figure 4.2.6. The summary of the imprint field of BTO films at different frequencies on LAO and Si substrates is presented in Figure 4.2.9. The imprint field is oriented from bottom electrode towards the top electrode and has low dependence on frequency. Two distinct features can be concluded: 1) The imprint fields of BTO films on Si substrate with LNO and LSMO electrodes are quite negligible below 20 kV/cm compared with the one of BTO on LAO substrate ranging between 40 kV/cm and 90 kV/cm; 2) Even on same LAO substrate, BTO film with LNO electrode has the imprint field around 90 kV/cm, much larger than using LSMO electrodes ($E_{imp}$ around 40 kV/cm). Damodaran reported that,[40] the epitaxial strain plays a crucial role in directing the out-of-plane alignment of the defect dipoles and the observation of built-in fields. They observed that BTO films grown on substrates ($DyScO_3$ and $GdScO_3$) that provide a compressive strain favored aligned defect dipoles and exhibited large imprint fields while films grown on substrate ($NdScO_3$) that provides a tensile strain showed negligible built-in fields, suggesting that the defect dipoles are not preferentially aligned in the out-of-plane direction. Besides BTO films,[40,205] similar in-plane strain effects on the imprint fields were also reported in PZT and BFO films.[206-208] The high imprint field of BTO on LAO substrate results from the compressive in-plane stress imposed by LAO substrate during the growth, even that due to lattice mismatch the BTO is relaxed. While on Si substrate, BTO film presents a large tensile in-plane strain, as revealed in RSM, which may cause the negligible imprint field. However, as concluded from this result, not only the in-plane strain state of BTO imposed by substrates can determine the imprint fields as reported but also the electrode can present an impact on the imprint field.

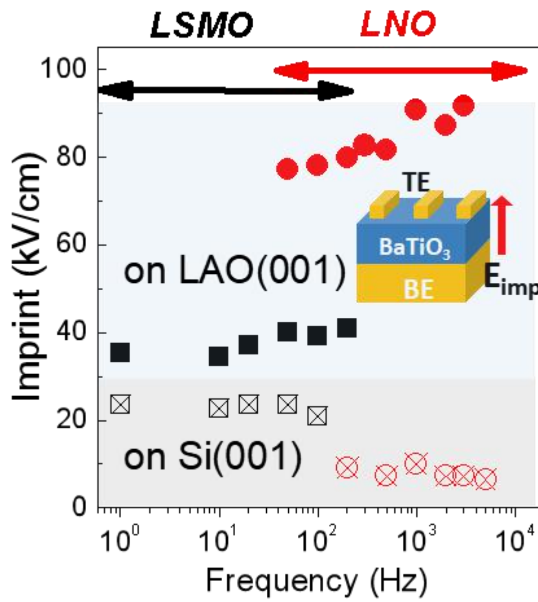


*Figure 4.2.9 Imprint field as a function of frequency for BTO films on LAO and Si using LSMO and LNO electrodes.*

On the other hand, it is of interest to check if the contact area has influence on the ferroelectric polarization since the different sizes of top electrode areas are used for perovskite oxide electrodes. The ferroelectric loops were measured for BTO films on LAO using LSMO and LNO symmetric electrodes as shown in Figure 4.2.10(a) and (b), respectively. It is clear to conclude that there is a low dependence of ferroelectric polarization on the electrode area. The smallest top contacts with circle and square in 50 µm were not be clearly seen using the camera in the probe station, thus these ferroelectric capacitors were not tested.

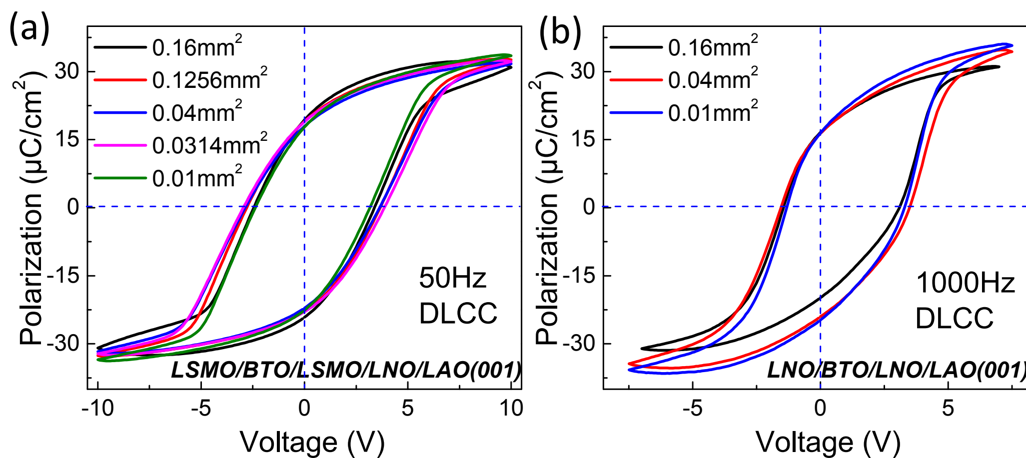


Figure *4.2.10 Ferroelectric polarization loops of BTO films on LAO(001) (a) using LSMO and (b) LNO electrodes with different electrode areas.*

### 4.2.4 Electrical comparison between metallic oxides and Pt electrodes

Top noble metal and oxide electrodes used here are Pt and LNO or LSMO, respectively. We first measured the samples with top-bottom configuration and strong effects of the type of top electrode is found. One example for the BTO/LNO/LAO(001) heterostructure with top Pt and LNO electrodes are shown in Figures 4.2.11(a) and (b), respectively. The hysteresis loops using asymmetric Pt/LNO electrodes were largely influenced by the leakage current as indicated in Figure 4.2.11(a), which makes it not possible to extract the polarization loops. This behaviour results from the asymmetry of the potential barriers at the electrode interfaces because of the two different ferroelectric-electrode contacts. In the following part, the top-top configuration was used since the interface asymmetry can be canceled with this configuration.[175]

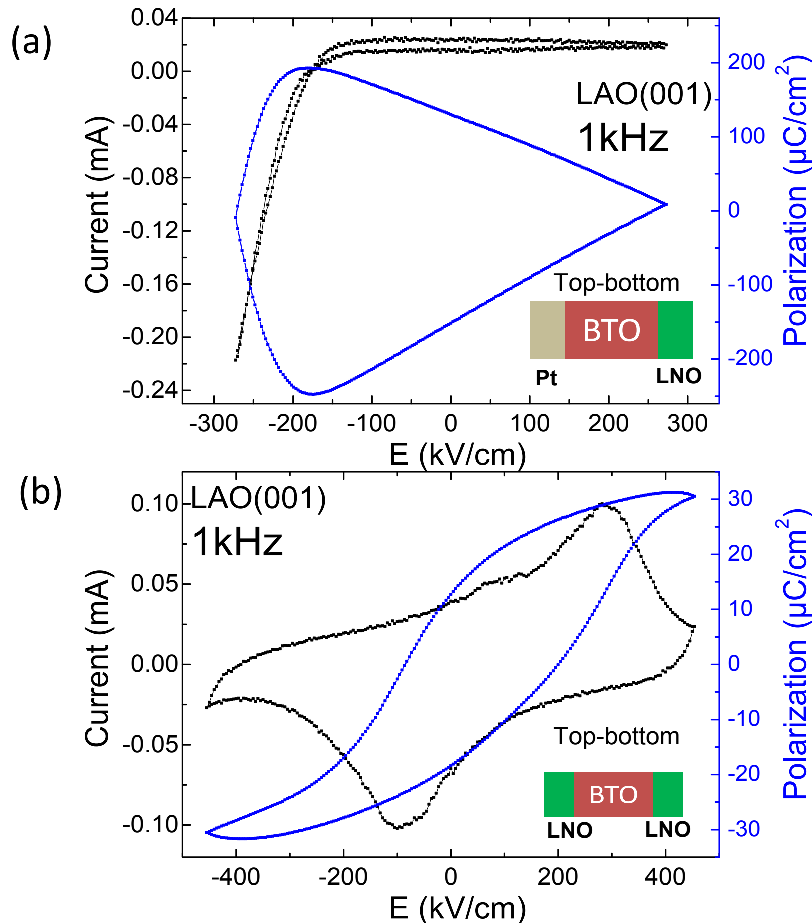


*Figure 4.2.11 Comparison of ferroelectric measurements of BTO capacitors on LAO substrate using symmetric LNO electrodes and asymmetric Pt/LNO electrodes measured in top-bottom configuration.*

The comparison of ferroelectric measurements using Pt electrode and perovskite

metallic oxide electrodes (LSMO and LNO) with top-top configuration are shown in Figure 4.2.12. A distinct feature of ferroelectric loops can be seen between using metallic perovskite oxides and Pt electrodes. The ferroelectric loops of BTO film grown on Si with top Pt electrodes is quite slim with largely decreased $E_c$ and $P_r$ compared with the one using top perovskite metallic oxide electrodes in top-top configuration. However, the maximum polarization with Pt electrodes or metallic oxide electrodes is similar. This apparent tilting of P-E hysteresis loops and large reduction in remnant polarization and $E_c$ are usually explained by the dominance of space charges over the intrinsic polarization in films.[209,210] When the space charge density is over $10^{19}$ $cm^{-3}$, the substantial shrinking and tilting of the P-V hysteresis loop appears for a ferroelectic film. Indeed, previous calculation about the space charge density for the Pt/BTO/LNO/$CeO_2$/YSZ/Si(001) heterostructure was about *Ne* = $10^{21}$ $cm^{-3}$,[44] which causes the large shrinking and tilting of the P-V hysteresis loop with Pt contacts. In the ferroelectric capacitors, it is well-known that a thin dielectric layer often forms between a metal electrode and a ferroelectric oxide layer, called passive layer or dead layer.[211] Pt contacts are deposited by sputtering at relatively low oxygen pressure (5 x $10^{-3}$ mbar), and the possibility of induction of defects in the ferroelectrics by the energetic plasma cannot be discard. This interfacial layer may suppress ferroelectricity at the interface and create a large space charge.

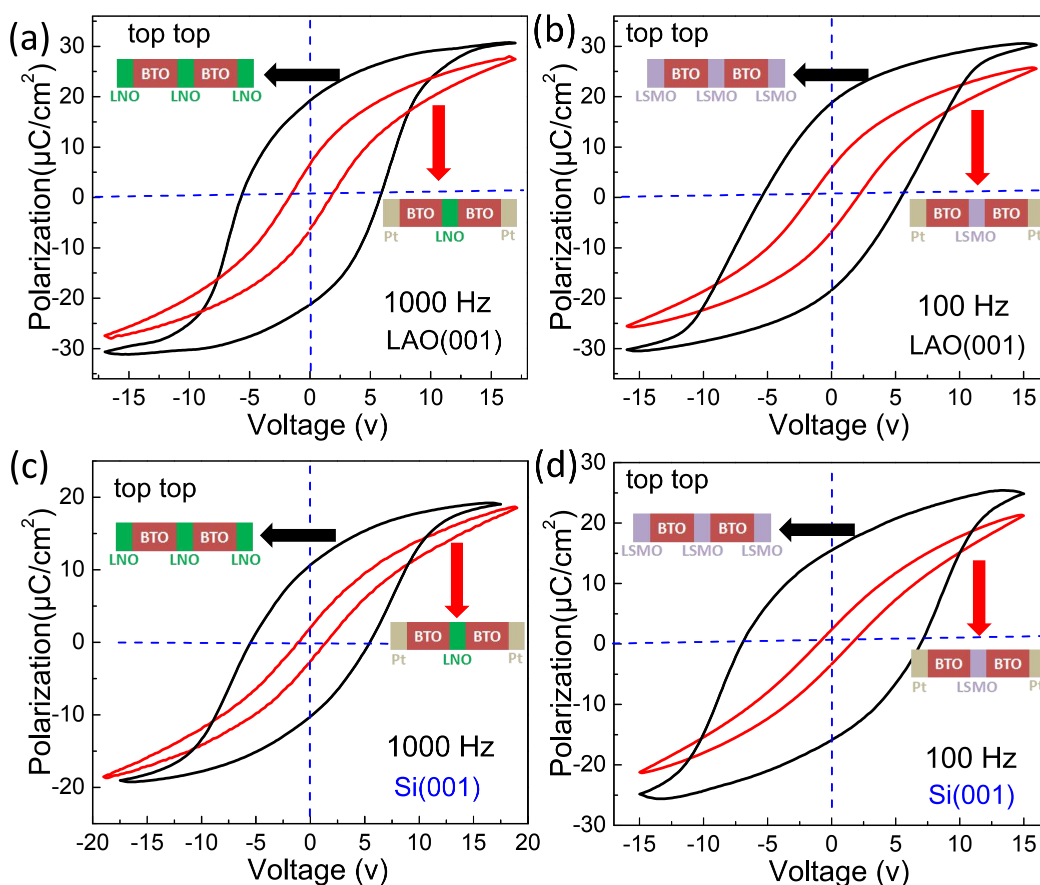


*Figure 4.2.12 Comparison of ferroelectric loops of BTO films on LAO(001) and Si(001) using symmetric oxide electrode or Pt/oxide asymmetric electrode in top-top measurement. The*

*capacitor structures are sketched in each figure.*

The leakage curves comparison of BTO films on LAO and Si with symmetric or asymmetric electrodes measured in top-top configuration are shown in Figure 4.2.13 (a)-(d). BTO films with Pt top electrode presents higher leakage than that with perovskite (LNO or LSMO) oxide electrodes. The detail leakage value extracted at 225 kV/cm can be seen in Figure 4.2.13(e). The relevance of the top electrode reflects the relevance of the interface is dominating the charge transport, with the metallic electrode giving better leakage rectifying characteristic than metallic oxide electrodes.

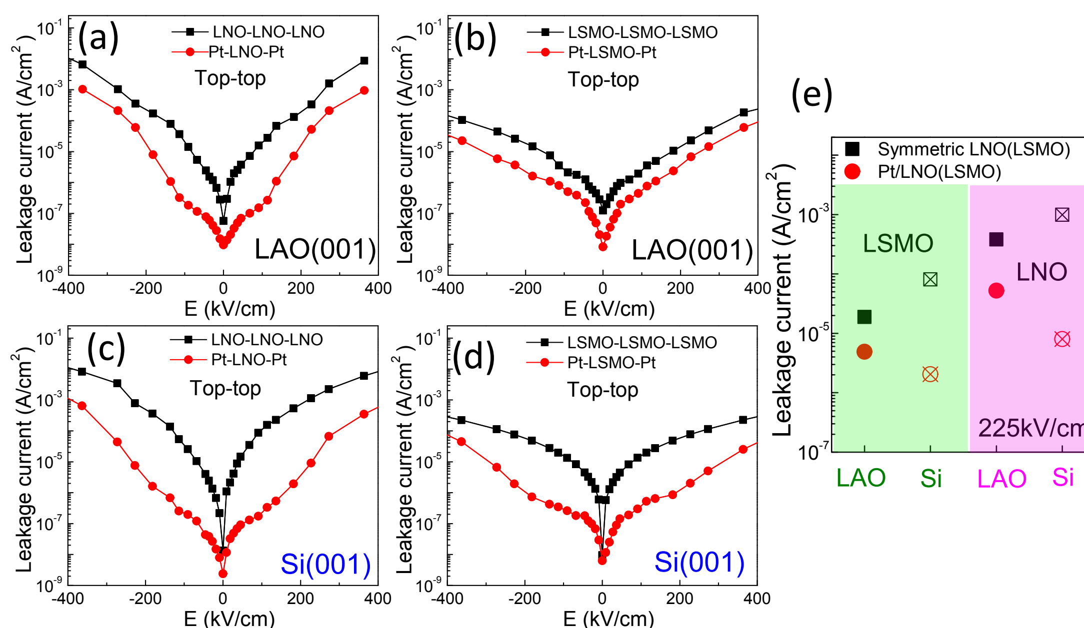


*Figure 4.2.13 (a)-(d) Leakage current curves of the BTO films with symmetric oxide electrodes or Pt/oxide asymmetric electrodes in top-top configuration. (e) Leakage current at 225 kV/cm.*

## Conclusion

In summary, the electrode materials have a strong impact on the properties of ferroelectric $BaTiO_3$ thin films. The perovskite conductive oxides $LaNiO_3$ and $La_{2/3}Sr_{1/3}MnO_3$ and noble metal Pt were used. Comparing the perovskite conducting oxide electrodes, ferroelectric $BaTiO_3$ films with $La_{2/3}Sr_{1/3}MnO_3$ electrode present higher remnant polarization and lower leakage than with $LaNiO_3$ electrode, either on $LaAlO_3$ or Si substrates. The larger coercive field are observed with $La_{2/3}Sr_{1/3}MnO_3$ electrode possibly related to higher $La_{2/3}Sr_{1/3}MnO_3$ resistivity. The epitaxial strain and selection of bottom electrodes together determines the internal field of $BaTiO_3$ films. With metal Pt electrode, $BaTiO_3$ films either grown on Si or $LaAlO_3$ present slim ferroelectric loops and lower leakage compared to perovskite oxide electrodes. As an hypothesis, we can speculate that the induced space charge close to the $BaTiO_3$/Pt interface could be a possible reason for these changes. It is concluded that selecting the electrode materials and controlling the electrode interface is of major importance in ferroelectric devices and can open effective way for better improving the performance of ferroelectric capacitors.

# Chapter 5. Epitaxial Ferroelectric $Hf_{0.5}Zr_{0.5}O_2$ Thin film

*The ferroelectric orthorhombic phase in doped $HfO_2$ films is usually stabilized in nanometric grains coexisting in polycrystalline films with non-ferroelectric phases, challenging the understanding of the intrinsic mechanisms of ferroelectricity in $HfO_2$ and prototyping devices. In this chapter, the epitaxial $Hf_{0.5}Zr_{0.5}O_2$ films have been grown on $SrTiO_3(001)$ substrate buffered with $La_{2/3}Sr_{1/3}MnO_3$ electrode and the growth window for epitaxial orthorhombic phase by pulsed laser deposition is determined. Further epitaxial growth of high quality $Hf_{0.5}Zr_{0.5}O_2$ films has been integrated on Si substrate in a capacitor heterostructure with different buffer layers. The epitaxial $Hf_{0.5}Zr_{0.5}O_2$ films present robust ferroelectricity (as high as over 30 $\mu C/cm^2$) with high retention (over 10 years) and fatigue (exceeding $10^{10}$ cycles). Such outstanding properties in the nascent research on epitaxial $HfO_2$-based ferroelectric films can pave the way for a better understanding of their intrinsic ferroelectricity and prototyping devices.*

## 5.1 Growth Window of Ferroelectric Epitaxial $Hf_{0.5}Zr_{0.5}O_2$ Thin Film

*Abstract*

*The metastable orthorhombic phase of hafnia is generally obtained in polycrystalline films, whereas in epitaxial films, its formation has been much less investigated. We have grown $Hf_{0.5}Zr_{0.5}O_2$ films by pulsed laser deposition, and the growth window (temperature and oxygen pressure during deposition and film thickness) for epitaxial stabilization of the ferroelectric phase is mapped. The remnant ferroelectric polarization, up to ~ 24 μC/cm$^2$, depends on the amount of orthorhombic phase and interplanar spacing, and increases with temperature and pressure for a fixed film thickness. The leakage current decreases with an increase in thickness or temperature, or when decreasing oxygen pressure. The coercive electric field ($E_c$) depends on thickness (t) according to the $E_c - t^{-2/3}$ scaling, which is observed for the first time in ferroelectric hafnia, and the scaling extends to thickness down to at least around 5 nm. The notable endurance (over $10^{10}$ cycles) and very long retention (over 10 years) are also reported in epitaxial o-HZO films. The proven ability to tailor the functional properties of high-quality epitaxial ferroelectric $Hf_{0.5}Zr_{0.5}O_2$ films paves the way toward understanding their ferroelectric properties and prototyping devices.*

Recently, several groups have reported that the ferroelectric orthorhombic phase can be stabilized in epitaxial doped $HfO_2$ films.[161-172] In epitaxial films, the orthorhombic phase is generally formed during deposition at high temperature, without need of annealing.[161-172] Epitaxial films with higher homogeneity with respect to polycrystalline films are definitely an advantage for better understanding of the effects of orientation, interfaces, strain, and defects on ferroelectricity in $HfO_2$. In spite of the evident interest, epitaxial ferroelectric hafnia is still in a nascent state. Up to now, the epitaxial films have been grown by pulsed laser deposition, and only the influence of thickness was discussed very recently.[168,220] The effect of deposition parameters on structural and ferroelectric properties, which is of pivotal importance for further development of epitaxial films of ferroelectric hafnia, is unreported. In this section, we present a detailed study of epitaxial growth of HZO on $SrTiO_3$ substrates. Three series of samples were prepared varying deposition temperature, oxygen pressure and thickness. The growth window of epitaxial ferroelectric hafnia films is mapped, permitting the control of the structural and functional properties by selection of deposition parameters and film thickness.

### 5.1.1 Growth conditions

Bilayers combining ferroelectric HZO film on $La_{2/3}Sr_{1/3}MnO_3$ (LSMO) bottom electrode were grown on STO(001) in a single process. The LSMO electrodes, 25 nm thick, were deposited at 5 Hz repetition rate, substrate temperature $T_s$ = 700 °C, and dynamic oxygen pressure $P_{O2}$ = 0.1 mbar. Three series of samples were prepared varying deposition conditions of HZO (see a schematic in Figure 5.1.1): $T_s$-series, $P_{O2}$-series, and thickness series. In $T_s$-series, HZO was deposited varying $T_s$ from 650 to 825 °C, under fixed conditions of $P_{O2}$ = 0.1 mbar and number of laser pulses (800 p, HZO thickness t = 9.2 nm). HZO was deposited in $P_{O2}$-series varying $P_{O2}$ in the 0.01 – 0.2 mbar range, at fixed $T_s$ = 800 °C and 800 laser pulses. In t-series HZO films of varied thickness were prepared at $T_s$ = 800 °C and $P_{O2}$ = 0.1 mbar, controlling the thickness (in the 2.3 – 37 nm range) with the number of laser pulses (from 200 to 3600). At the end of the deposition, samples were cooled down under 0.2 mbar oxygen pressure.

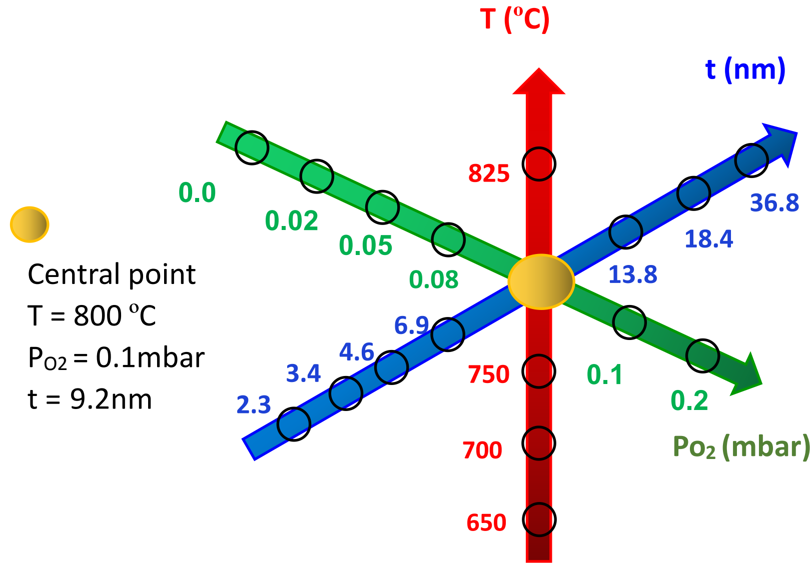


*Figure 5.1.1 Schematic of the three series for the deposition of HZO films on LSMO/STO(001).*

For accurate determination of thickness of HZO films, the simulations of the Laue interference peaks around the symmetrical orthorthombic HZO (111) reflection in the X-ray diffraction (XRD) patterns were done. The Laue interference fringes are shown in Figure 5.1.2(a)-(b), which can be simulated (red curve) according the dependence of equation (5-1) below [39]:

$$I(Q) = \left( \frac{\sin\left(\frac{QNc}{2}\right)}{\sin\left(\frac{Qc}{2}\right)} \right)^2 \tag{5-1}$$

where $Q = 4\pi\sin(\theta)/\lambda$ is the reciprocal space vector, $N$ the number of unit cells along the out-of-plane direction and $c$ the corresponding interplanar spacing. The simulation is fitted to the experimental curve. In the 800 laser pulses film, the fitting was done being the o-HZO(111) peak at $2\theta$ = 30.12° and the HZO thickness 92 Å. The respective values for the 1600 laser pulses film are $2\theta$ = 30.152° and 184 Å. Since the growth rate in pulsed laser deposition can depend on oxygen pressure, the simulations of the Laue interference peaks in XRD patterns at different oxygen pressures are also measured. The thickness of films in $P_{O2}$-series is in the 8 – 11 nm range with growth rates at each $P_{O2}$ shown in Figure 5.1.2(c).

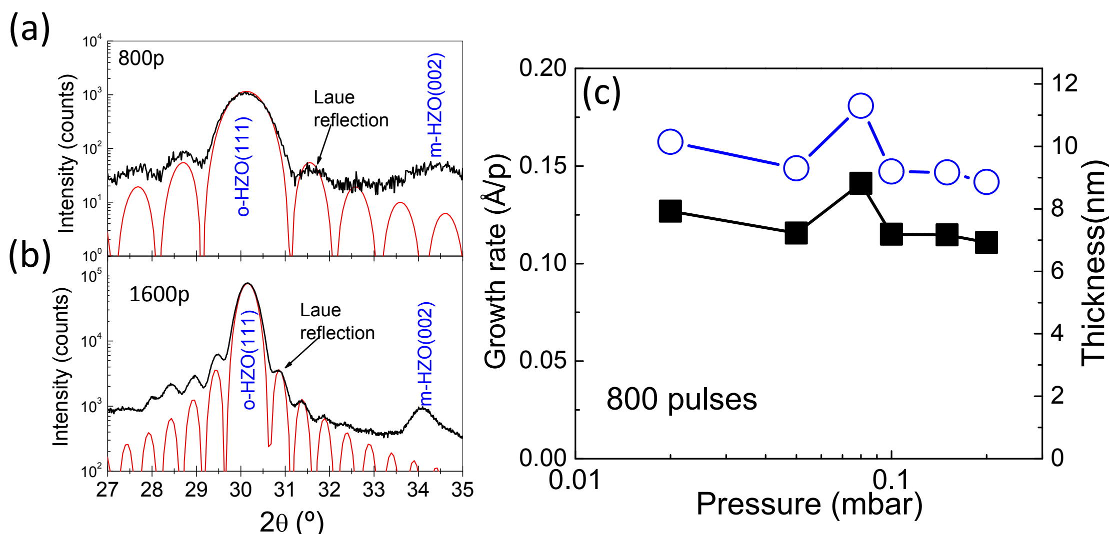


*Figure 5.1.2 XRD pattern of the films with 800 laser pulses with 2 seconds acquisition time (a) and 1600 laser pulses with 3 seconds acquisition time (D8-ADVANCE, Cu $K\alpha_1$) (b) deposited at $T_s$ = 800 °C and $P_{O2}$ = 0.1 mbar. Red lines are simulations of the Laue interference fringes. (c) HZO thickness (left axis, open blue circles) and growth rate (right axis, solid black squares).*

## 5.1.2 Structural Study

Firstly, the effect of the deposition temperature ($T_s$-series) on the crystallinity of the HZO films will be discussed. The XRD $\theta$-$2\theta$ scans in Figure 5.1.3(a) show (00$l$) reflections of STO and LSMO, and diffraction peaks in the $2\theta$ range of 27° – 35° corresponding to HZO. The highest intensity of HZO peak is the (111) reflection of orthorhombic HZO (o-HZO) at around 30°. Reflections of the monoclinic (m) phase, (-111) at $2\theta$ around = 28.5° and (002) at $2\theta$ around = 35°, usual in polycrystalline films[36] are not detected. Laue fringes (some of them marked with vertical arrows) can be observed around o-HZO(111), implying a good epitaxial quality. We have to note that the possible coexistence of minority tetragonal (t) phase cannot be discarded as t-HZO(101) and o-HZO(111) peaks would be overlapped. The intensity of the o-HZO(111) peak, normalized to that of the LSMO(002) peak, increases monotonously with $T_s$ (Figure 5.1.3b). Further XRD characterization was performed using a two-dimensional (2D) detector. The $2\theta$-$\chi$ frame around $\chi$ = 0° of the $T_s$ = 800 °C film is shown in Figure 5.1.3(c). The monoclinic HZO(002) reflection is present, with broad intensity distribution along $\chi$ that indicates the high mosaicity. The o-HZO(111) reflection is bright in spite of the low film thickness (t = 9 nm), and the narrow spot around $\chi$ = 0° is a signature of epitaxial ordering. The $\phi$-scans around asymmetrical o-HZO(-111) reflections (Figure 5.1.3d) confirms the epitaxy of o-HZO on LSMO/STO(001). Since the LSMO electrode grows cube-on-cube on STO,[221] the epitaxial relationships are [1-10]HZO(111)/[1-10]LSMO(001)/[1-10]STO(001). The four sets of three o-HZO(-111) peaks indicate that it presents four crystal

domains, 90° rotated in the in-plane direction. The epitaxial growth of o-HZO(111) on LSMO(001) is intriguing due to the symmetry discontinuity in the interface. The same intriguing epitaxial relationship and domain structure was observed in thicker o-HZO films. The substrate temperature has an impact on the out-of-plane lattice parameter of o-HZO. The vertical dashed line in Figure 5.1.3(a) marks the position of the o-HZO(111) peak in the $T_s$ = 825 °C film. The peak shifts moderately to higher angles with substrate temperature. The dependence of $d_{o\text{-}HZO(111)}$ on Ts (Figure 5.1.3e) shows that lattice spacing $d_{o\text{-}HZO(111)}$ decreases from 2.979 Å ($T_s$ = 650 °C) to 2.959 Å ($T_s$ = 825 °C), which corresponds to a contraction of 0.67 %.

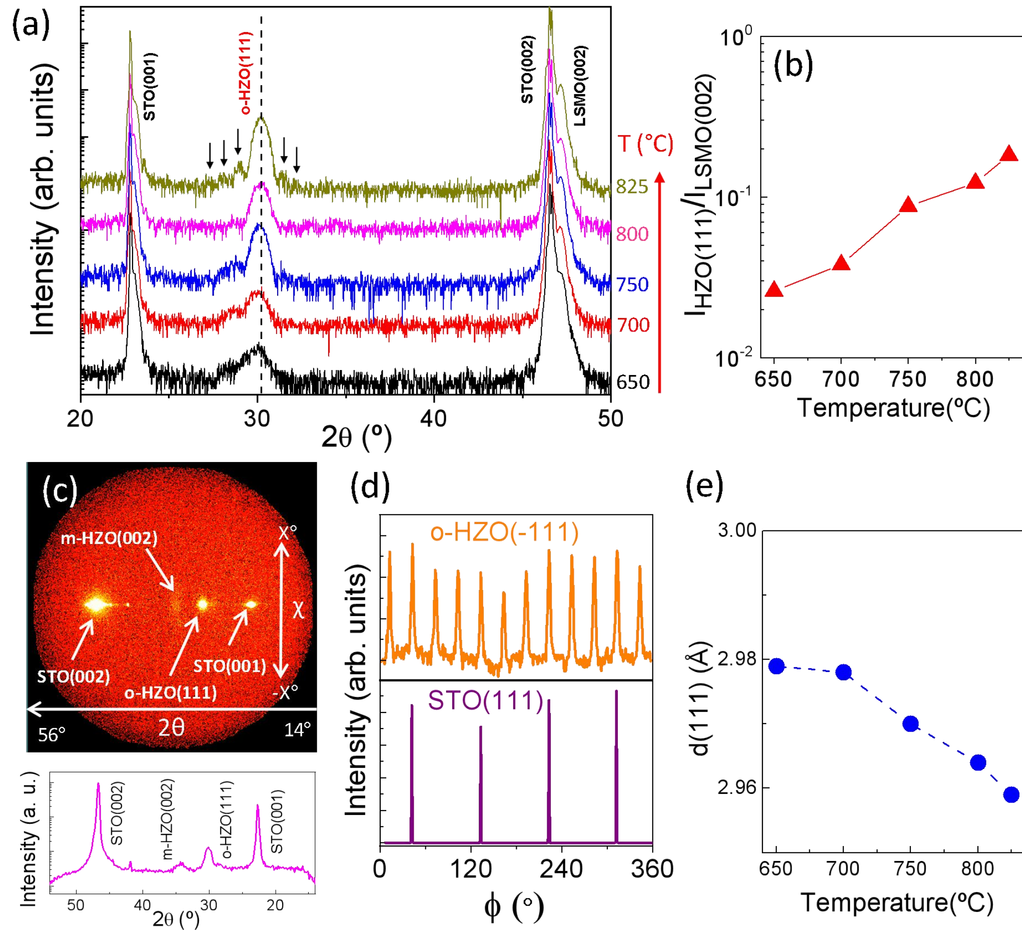


*Figure 5.1.3 (a) XRD θ-2θ scans of HZO films deposited from $T_s$ = 650 °C to 825 °C. The vertical dashed line marks the position of the o-HZO(111) reflection in the $T_s$ = 825 °C film, and vertical arrows mark Laue fringes. (b) Intensity of o-HZO(111) normalized to LSMO(002), plotted as a function of $T_s$. (c) XRD 2θ-χ frame of the $T_s$ = 800 °C film, and θ-2θ scan integrated ± 5° around χ = 0°. (d) XRD ϕ-scans around o-HZO(-111) and STO(111) reflections. (e) Dependence on $d_{o\text{-}HZO(111)}$ interplanar spacing with $T_s$.*

Figure 5.1.4 summarizes the influence of deposition oxygen pressure ($P_{O2}$-series) on the crystallinity of the films. There are no HZO diffraction peaks in the $P_{O2}$ = 0.01 mbar film (Figure 5.1.4a), whereas in the $P_{O2}$ = 0.02 mbar sample the o-HZO(111)

peak is weak. The intensity of this peak increases with deposition pressure (Figure 5.1.4b). The m-HZO(002) reflection, barely visible in Figure 5.1.4a, can be observed in $2\theta$-$\chi$ frames (Figures 5.1.4c and d). The intensity of the elongated m-HZO(002) spot is higher in the $P_{O2}$ = 0.02 mbar film than in the $P_{O2}$ = 0.2 mbar one. Thus, lowering pressure increases the monoclinic phase and reduces the orthorhombic phase. Oxygen pressure has also an important effect on the lattice strain of the orthorhombic phase. The o-HZO(111) peak (Figure 5.1.4a) shifts towards lower angles by reducing deposition pressure. The dependence of $d_{o\text{-}HZO(111)}$ with $P_{O2}$ (Figure 5.1.4e) shows that increasing deposition pressure from 0.02 mbar to 0.2 mbar the interplanar spacing decreases from 2.986 Å to 2.954 Å (1.07 % contraction).

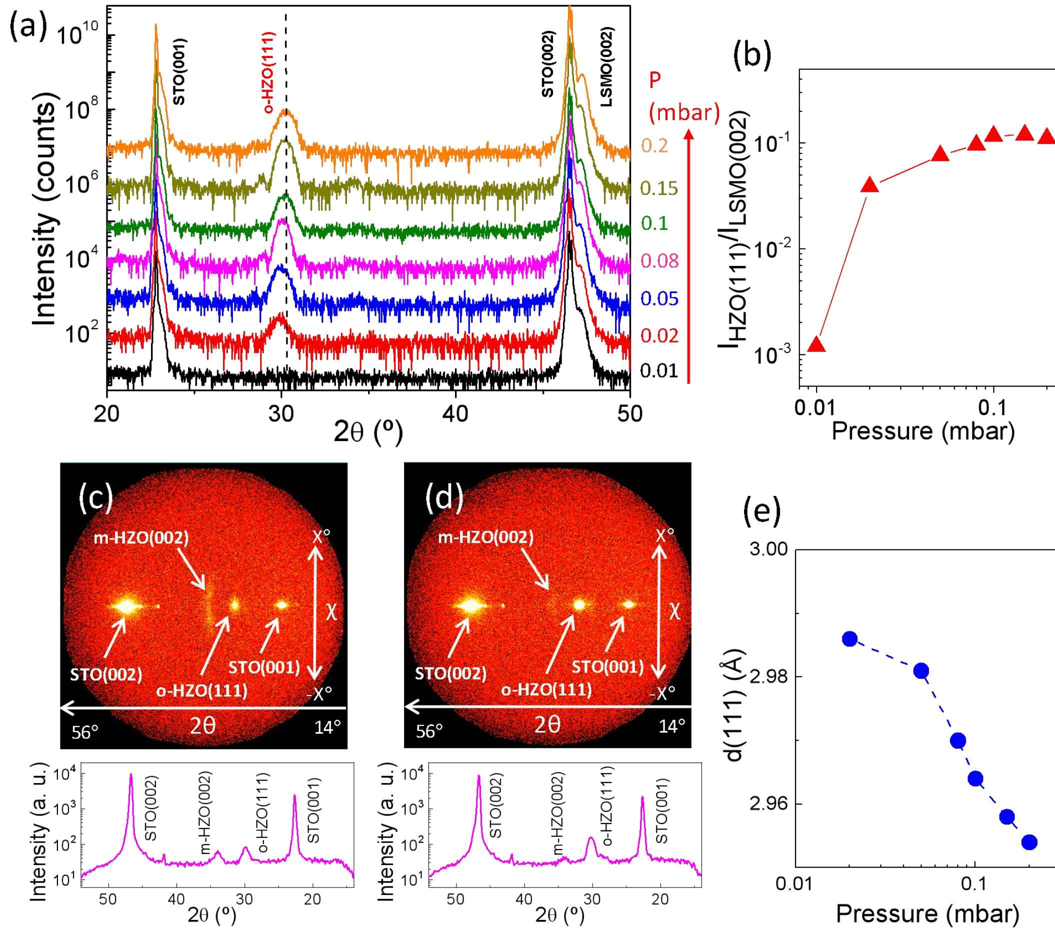


*Figure 5.1.4 (a) XRD $\theta$-$2\theta$ scans of HZO films deposited from $P_{O2}$ = 0.01 mbar to 0.2 mbar. The vertical dashed line marks the position of the o-HZO(111) reflection in the $P_{O2}$ = 0.2 mbar film. (b) Intensity of o-HZO(111) normalized to LSMO(002), plotted as a function of $P_{O2}$. XRD $2\theta$-$\chi$ frame of the $P_{O2}$ = 0.02 mbar (c) and 0.2 mbar (d) films, and corresponding $\theta$-$2\theta$ scans integrated ± 5° around $\chi$ = 0°. (e) Dependence on $d_{o\text{-}HZO(111)}$ interplanar spacing with $P_{O2}$.*

The XRD $\theta$-$2\theta$ scans of films of varying thickness (t-series) are presented in Figure 5.1.5(a). The o-HZO(111) peak becomes narrower and more intense when increasing thickness (Figure 5.1.5b). The inset shows the linear scaling of the width of this XRD

reflection with the reciprocal of the thickness. It signals, according to the Scherrer equation,[222] that epitaxial o-HZO (111) crystals grow across the entire film thickness. The m-HZO (002) peak is seen in films thicker than 10 nm, and the $2\theta$-$\chi$ frames corresponding to the t = 4.6 nm (Figure 5.1.5c) and 36.6 nm (Figure 5.1.5d) films evidence an increasing fraction of the monoclinic phase respect the orthorhombic with thickness. Whereas the monoclinic phase is not detected in the t = 4.6 nm, the thickest film shows a high intensity m-HZO(002) spot elongated along $\chi$ and a weaker m-HZO(-111) spot at $2\theta$ around 28.5°. On the other hand, the orthorhombic phase shows important reduction of the out-of-plane lattice parameter with thickness (Figure 5.1.5e), decreasing the interplanar spacing $d_{o\text{-}HZO(111)}$ from 3.035 Å to 2.964 Å (2.3 % contraction) as thickness increases from 2.3 to 9.2 nm, and presenting little variation in thicker films.

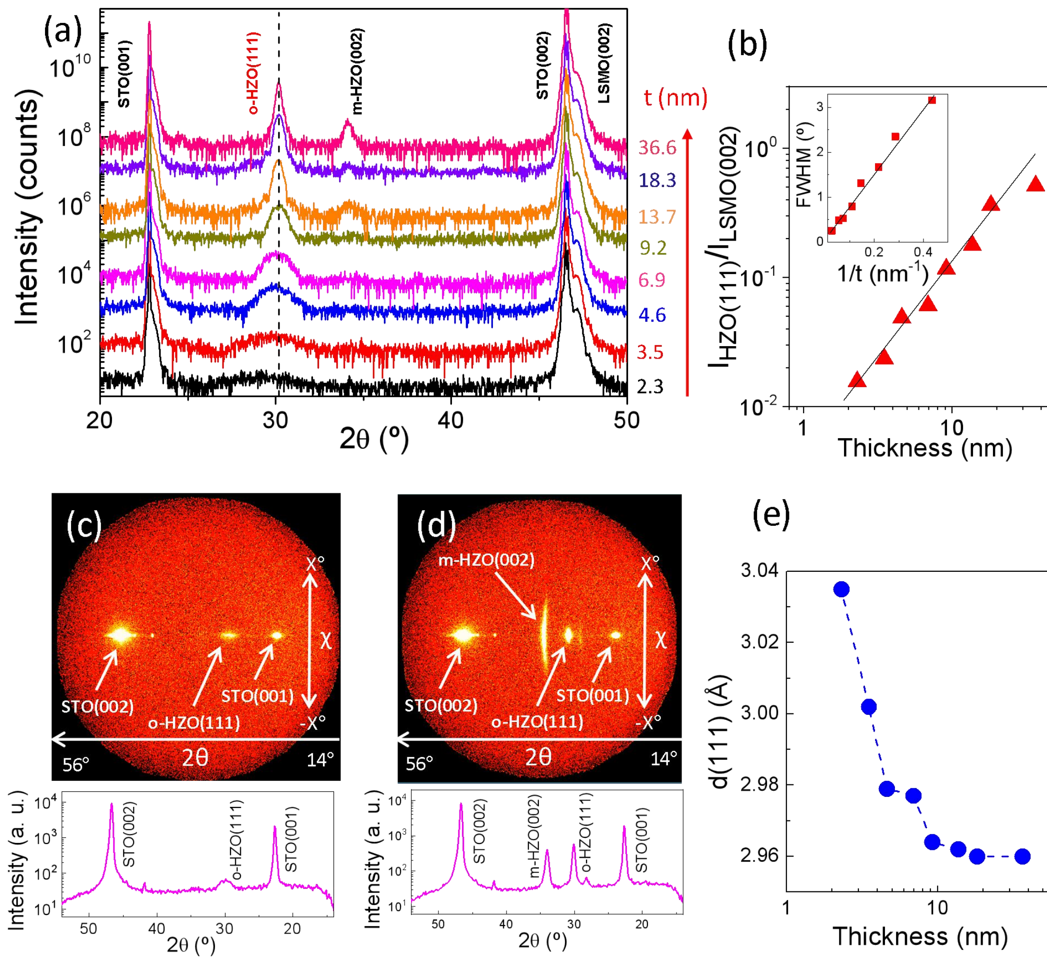


*Figure 5.1.5 (a) XRD $\theta$-$2\theta$ scans of HZO films of varying thickness from t = 2.3 nm to 36.6 nm. The vertical dashed line marks the position of the o-HZO(111) reflection in the t = 36.6 nm film. (b) Intensity of o-HZO(111) normalized to LSMO(002), plotted as a function of thickness. Inset: full-width at half-maximum (FWHM) of the o-HZO(111) peak as a function of the reciprocal of film thickness. XRD $2\theta$-$\chi$ frame of the t = 4.6 nm (c) and t = 36.6 nm (d) films, and corresponding $\theta$-$2\theta$ scans integrated ± 5 ° around $\chi$ = 0 °. (e) Dependence on $d_{o\text{-}HZO(111)}$ interplanar spacing with*

*film thickness.*

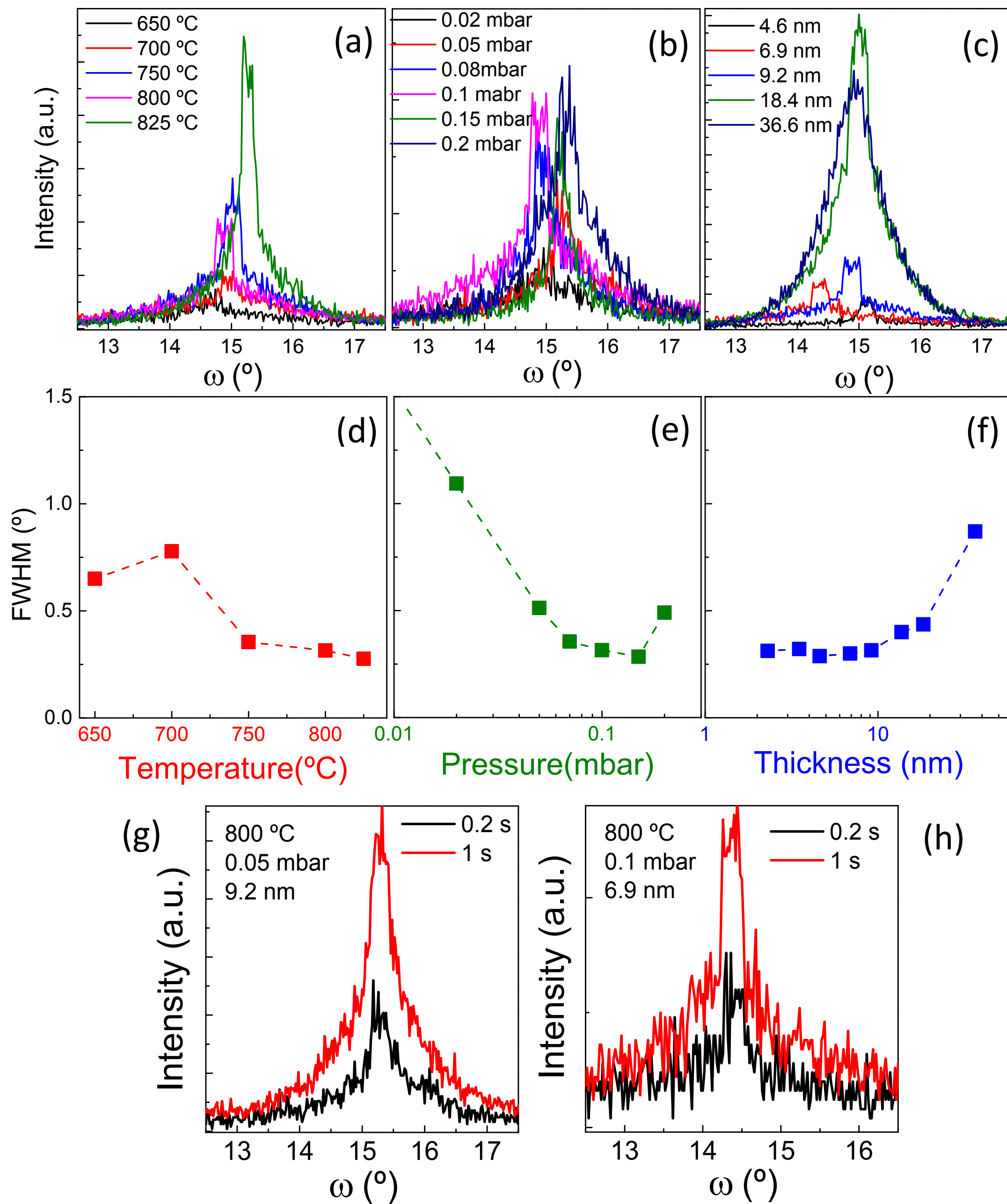


*Figure 5.1.6 The rocking curve for HZO films on STO(001) grown at different temperatures (a), oxygen pressures (b), and film thicknesses (c) with steptime 0.2 s. Dependence of FWHM with temperature (d), oxygen pressure (e) and film thickness (f). Inset: rocking curve of 18.4 nm thick sample. (g) and (h) Two examples of rocking curve measured with step time 0.2 s and 1 s.*

The rocking curves of HZO films on STO(001) substrate (measured at step time 0.2 s) varying the different growth temperatures, pressures and thicknesses are shown in Figure 5.1.6(a)-(f). Rocking curve of some films (for examples those of the thinnest films) were difficult to be measured due to the narrowness (confirmed with high

resolution diffractometer, not shown here) and low intensity. Despite the experimental difficulties, it was found that crystal quality of HZO films has dependence on the growth parameters and thickness. The HZO films grown at higher temperature, oxygen pressure and lower thickness present the lower mosaicity in the film. Rocking curve of some of the films present sharp peak and broad shoulder in Figure 5.1.16(a)-(c). To confirm that this observation is not measurement artifact, the rocking curves were remeasured at step time 0.2 s and longer 1 s as shown in Figure 5.1.16(g) and (h). The rocking curve does not show a big changes at two different acquisition time, both presenting the similar sharp peak and broad shoulder. The reason might origin from the formation of other minor phases (such as t-phase or c-phase) of HZO on STO substrate. The detail reason needs further study.

The dependence of surface morphology with deposition temperature is shown in Figure 5.1.7. All the films in $T_s$-series have very flat surfaces. The $T_s$ = 650 °C film is particularly flat, with root mean square (rms) roughness of 0.21 nm. The $T_s$ = 825 °C film is slightly rougher, but the rms roughness being as low as 0.36 nm. The terraces and steps[223] can be observed on the films grown at 750 °C and 800 °C. The dependence of the rms roughness on $T_s$ is shown in the right bottom corner of Figure 5.1.7 with rms in the 0.21 - 0.36 nm range.

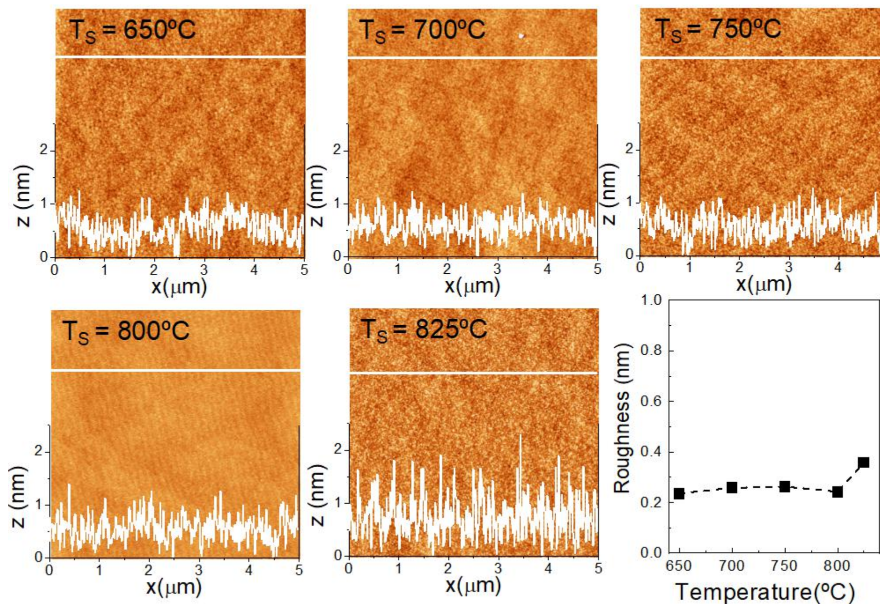


*Figure 5.1.7 AFM topographic 5 μm x 5 μm images of HZO films in $T_s$-series. A height profile along the horizontal marked line is shown in the bottom of each image. The dependence of root-mean-square (rms) in $T_s$-series is shown in the right bottom corner.*

Figures 5.1.8 shows the influence of the deposition pressure on surface morphology. The 0.01 mbar film presents terraces around 100 nm wide, and similar terraces and steps morphology is observed in most of the samples in this series. This is not the case

of the film deposited at the highest pressure of 0.2 mbar, where high density of islands increases the roughness to about 0.6 nm. The dependence of the rms roughness on pressure reflects the surface roughening with deposition pressure.

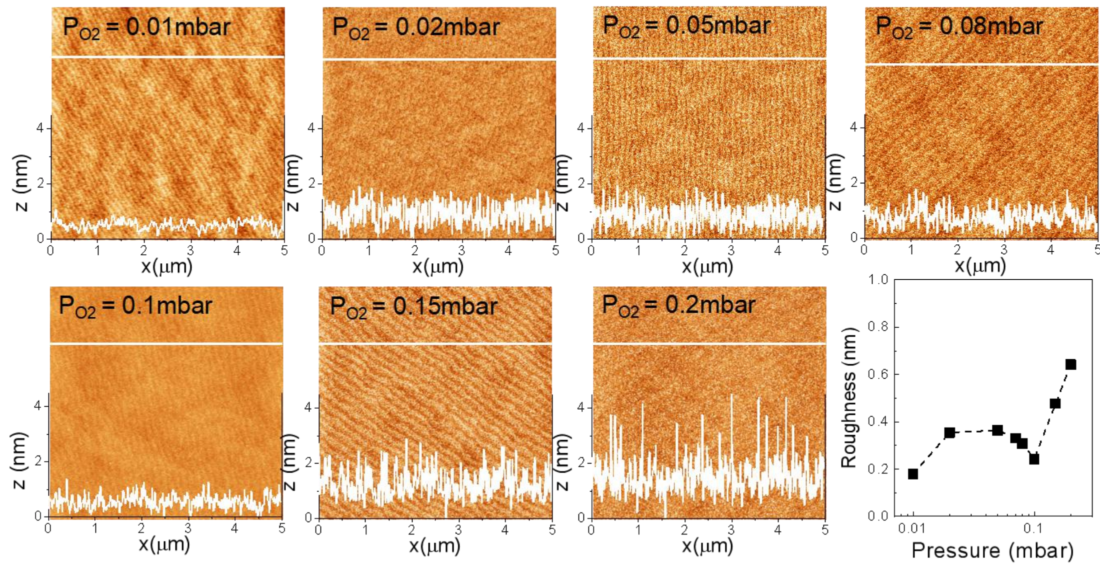


*Figure 5.1.8 AFM topographic 5 μm x 5 μm images of HZO films in $P_{O2}$ series. A height profile along the horizontal marked line is shown in the bottom of each image. The dependence of root-mean-square (rms) in $P_{O2}$ series is shown in the right bottom corner.*

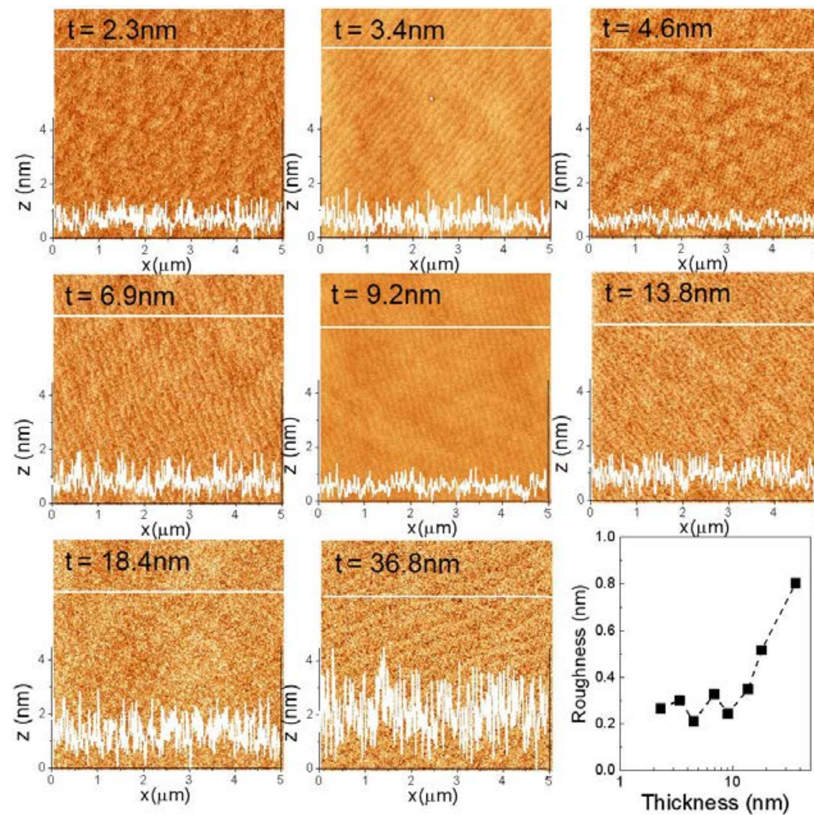


*Figure 5.1.9 AFM topographic 5 μm x 5 μm images of HZO films in thickness series. A height*

*profile along the horizontal marked line is shown in the bottom of each image. The dependence of root-mean-square (rms) in thickness series is shown in the right bottom corner.*

The dependence of the surface morphology on thickness of all films is summarized in Figures 5.1.9. The morphology of the thinnest film, t = 2.3 nm, shows terraces and steps, with low rms surface roughness of 0.26 nm. Roughness increases with thickness in films thicker than 10 nm, up to rms = 0.8 nm in the t = 36.6 nm film. In spite of the higher roughness of this film, morphology of terraces and steps is observed.

### 5.1.3 Electric characterization

**Ferroelectric polarization**

Ferroelectric polarization loops for samples of $T_s$-series and $P_{O2}$-series are presented in Figure 5.1.10(a)-(b), respectively. All the samples are ferroelectric. At the maximum measured voltage (5.5 V), the polarization is fully saturated. Larger applied voltages (≥ about 6 V) causes device breakdown. Remarkably, the high polarization is present in the pristine film, without the need of a wake-up process (inset of Figure 5.1.10a) as generally occurs in polycrystalline samples.[36,37,139,144,145,150-153] The remnant polarization $P_r$ and the coercive voltage ($V_c$) as a function of $T_s$ and $P_{O2}$ are plotted in Figures 5.1.10(c)-(d), respectively. $P_r$ increases with $T_s$ up to around 23 μC/cm$^2$ at $T_s$ = 825 °C, and it increases with $P_{O2}$, strongly for low pressures, from very low polarization up to around 20 μC/cm$^2$ for deposition pressure around 0.1 mbar. $V_c$ shows similar trends to $P_r$ with values always below around 3 V. In both series of samples, imprint electric field favoring downwards polarization (towards LSMO layer) is present, which produces a shift towards positive voltage, always smaller than 0.4 V (around 400 kV/cm). The detailed dependence of imprint field on the deposition conditions will be discussed later. Here, we need to note that the polarization is well below the saturation polarization of 53 μC/cm$^2$ theoretically predicted for this compound.[146] A reason for the smaller value is that the polar axis of orthorhombic hafnia is [010], whereas the epitaxial films are [111] oriented along the out-of-plane direction. Moreover, the lattice strain in epitaxial films (in particular they show expanded (111) interplanar spacing compared to polycrystalline films) can influence the polarization. Also, paraelectric monoclinic crystallites could be present in the film as secondary phase, as found in similar HZO films on LSMO/$SrTiO_3$(001). Finally, some domains could be non-switchable due to the pinning by defects.

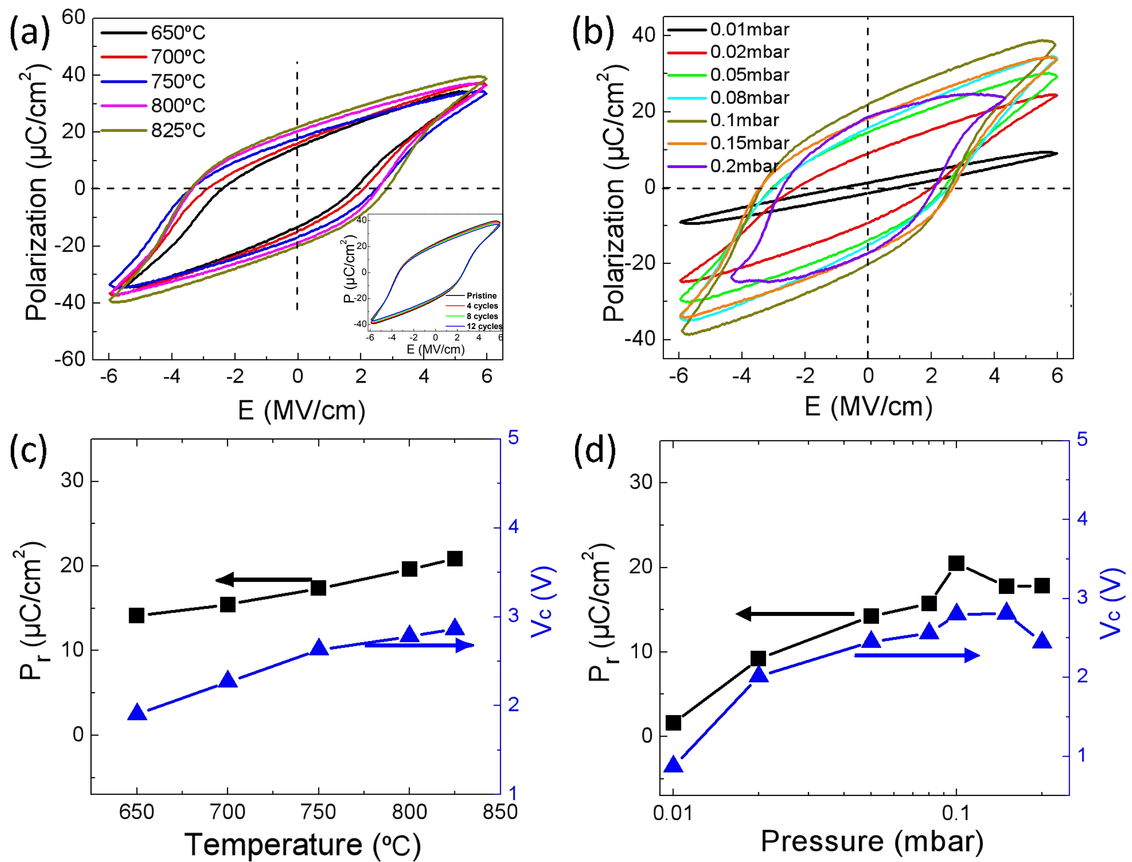


*Figure 5.1.10 (a) and (b) Polarization —electric field loops for the $T_s$ and $P_{O2}$ series, respectively. The inset records the ferroelectric hysteresis loops (t = 9 nm film) for the pristine state and subsequently measured cycles. (c) and (d) Dependence of $P_r$ and $V_c$ on $T_s$ and $P_{O2}$ for the $T_s$ and $P_{O2}$ series, respectively.*

Ferroelectric P-E hysteresis loops for the samples of t-series are presented in Figure 5.1.11(a). Films thicker than 4 nm show ferroelectric hysteresis. In the thinnest films (t = 2.3 and 3.4 nm), reliable polarization value was not extracted due to the high leakage current contribution. The dependence of remnant polarization on thickness shows that the t = 6.8 nm film has the largest $P_r$, and decreasing the polarization with increasing thickness as shown in Figure 5.1.11(b).

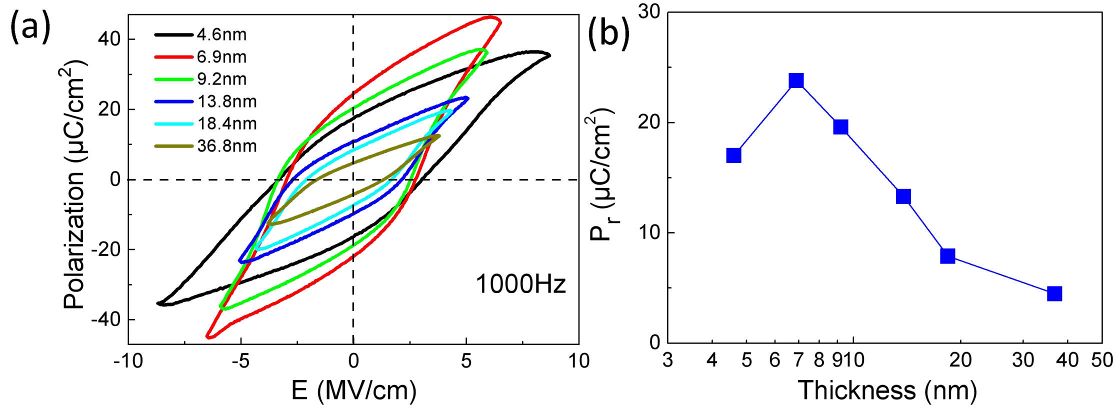


*Figure 5.1.11 (a) Polarization — electric field loops for the samples of the thickness series. (b) Dependence of $P_r$ on thickness.*

The coercive voltage $V_c$ increases with thickness as shown in Figure 5.1.12(a) (right axis). The corresponding electric field is plotted as a function of the thickness in the left-axis of Figure 5.1.12(a) (log scale). The slope of linear fit (red dashed line) to log ($E_c$) versus thickness is -0.61, which is in agreement with the scaling value of -2/3.[224] As this $V_c$ data was extracted from the P-E loops in Figure 5.1.12(a), which includes the electric susceptibility contribution as can be seen from the large slope, we make another fitting after removing the susceptibility contribution. The dielectric contribution of the loops can be removed by subtraction of the constant slope at high field. Figure 5.1.12(b) shows one example of ferroelectric loop of the t = 9.2 nm sample ($T_s$ = 800 °C, $P_{O2}$ = 0.1 mbar) before and after dielectric compensation. Similar dependence of coercive electric field and coercive voltage with thickness from dielectric compensated loops with the slope ($k$ = - 0.59) is also compatible with $E_c - t^{-2/3}$ scaling. This scaling is usually observed in the ferroelectric perovskite films.[34,225] It requires good screening of polarization charges by the electrodes, particularly for very thin ferroelectric films.[37] However, this scaling behavior has been not observed in polycrystalline ferroelectric hafnia[227] or even in epitaxial hafnia obtained by annealing of room temperature deposited films.[220] Depolarizing effects due to imperfect screening,[226] dispersion of ferroelectric domains in a dielectric matrix[227] or effects of small domain size even in thick films[220] have been proposed as responsible for the up to now elusive observation of $E_c - t^{-2/3}$ scaling in hafnia. Therefore, the $E_c - t^{-2/3}$ scaling in our films, deposited epitaxially at high temperature, signals the importance of the electrodes and film microstructure, and thus high quality samples are required for accurate control of ferroelectricity.

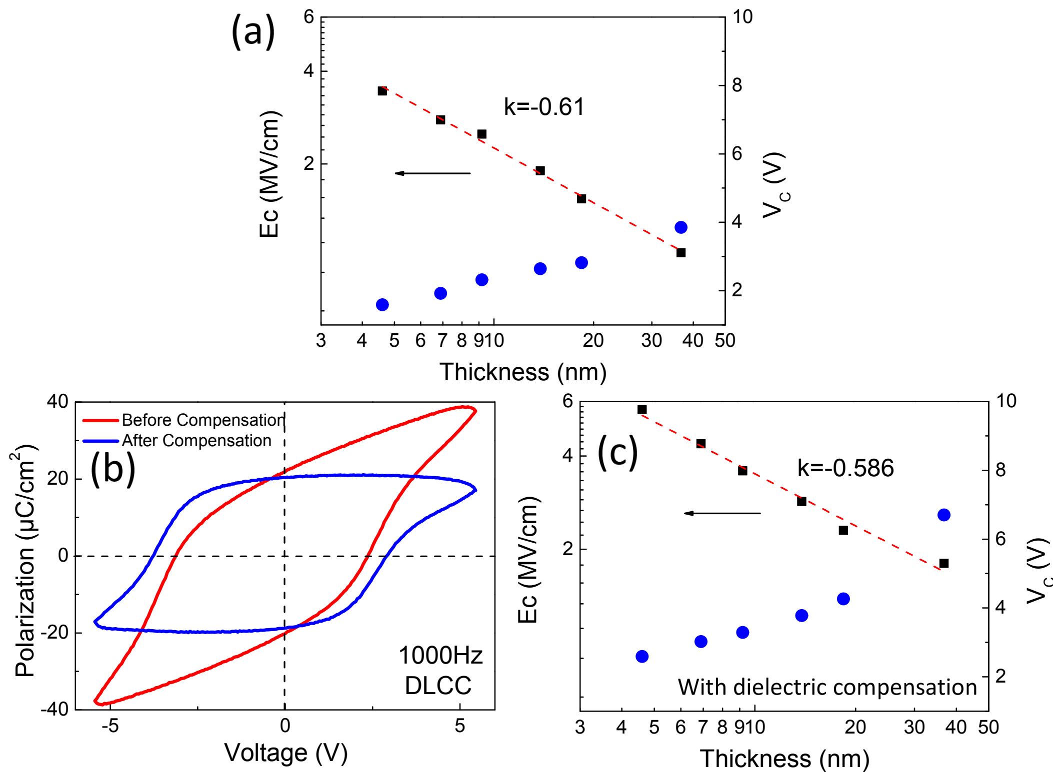


*Figure 5.1.12 (a) Dependences of $E_c$ (black squares) and $V_c$ (blue circles) on thickness with dielectric contribution. Data was extracted from Figure 5.1.10(a). The red dashed line is a linear fit with a slope of -0.61, compatible with $E_c$ - $t^{-2/3}$ scaling. (b) Polarization – voltage loops of the t = 9.2 nm sample without (red curve) and after (blue curve) compensation of the dielectric contribution. (c) Equivalent plot (Figure d) determined from compensated loops with a slope of -0.59.*

Here, we need to note that the measurement of saturated loops is challenging due to the huge coercive electric field of ferroelectric hafnia[139] and coercive field typically depends on the maximum electric field.[117] The polarization loops for epitaxial HZO films in the thesis were measured using electric field amplitudes as high as possible in order to obtain saturated loops. Figure 5.1.13 shows loops of the t = 6.9 nm (a) and t = 36.6 nm (b) films measured at varying applied field. Breakdown field decreases with thickness, being around 6.8 and 4.1 MV/cm for the t = 6.9 nm (c) and t = 36.6 nm (d) samples. Figures 5.1.13(e) and (f) show the dependence of coercive field with maximum applied field for the t = 6.9 nm (e) and t = 36.6 nm (f) samples. For both samples, the coercive field does not show significant increase at high electric field, indicating the saturated ferroelectric behavior.

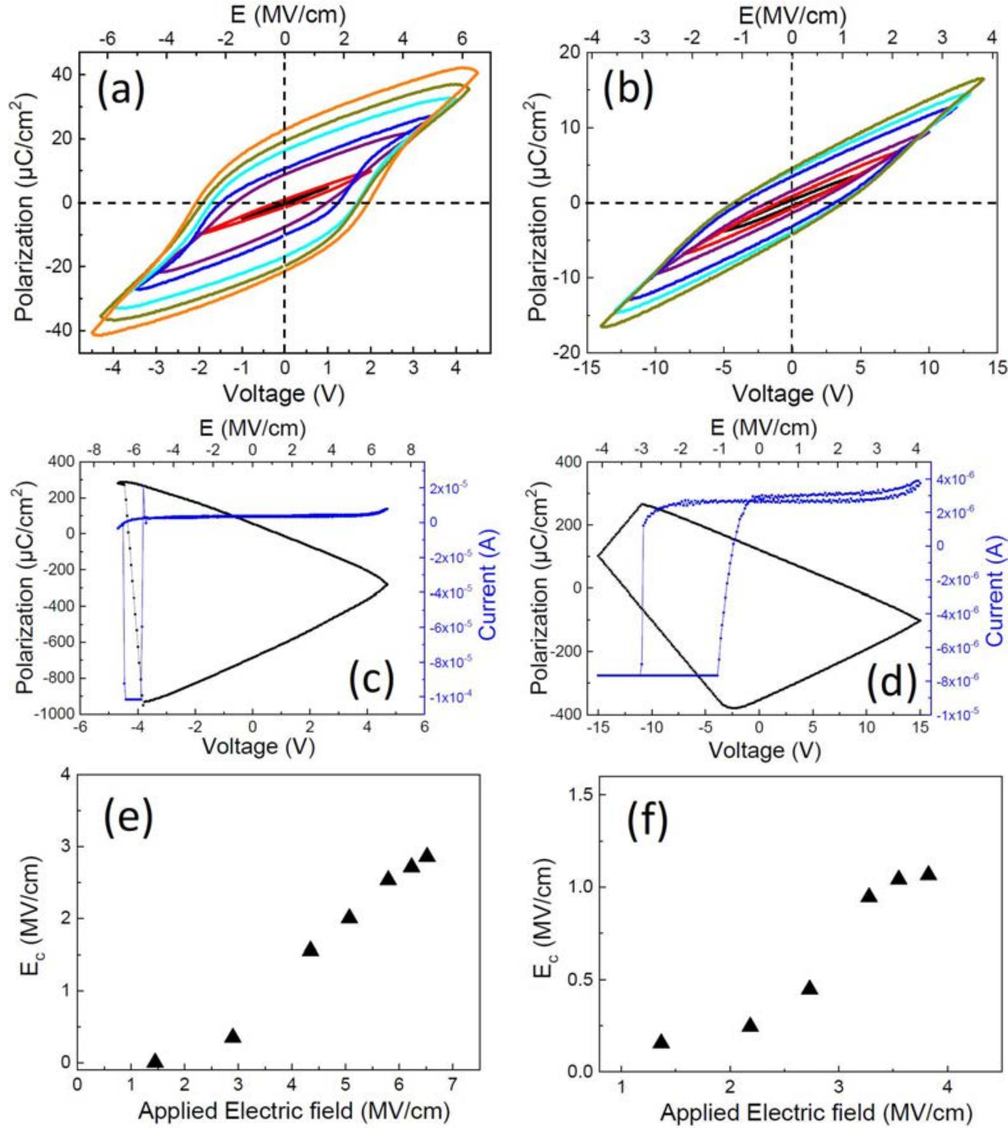


*Figure 5.1.13 Polarization loops of the t = 6.9 nm (a) and t = 36.6 nm (b) films. Breakdown of a capacitor in the t = 6.9 nm (c) and t = 36.6 nm (d) samples at applied fields of E = 6.8 MV/cm and E = 4.1 MV/cm, respectively. Coercive field $E_C$ as a function of the amplitude of the applied field for the t = 6.9 nm (e) and t = 36.6 nm (f) films.*

We have presented the growth window of epitaxial HZO films, which permits tailoring structural and ferroelectric properties of the films. In order to elucidate if there is direct effect of structure (relative orthorhombic phase amount and strain), the remnant polarization has been plotted as a function of the normalized intensity of the o-HZO(111) reflection (Figure 5.1.14a) and as a function of the $d_{o\text{-}HZO(111)}$ interplanar spacing (Figure 5.1.14b). The polarization scales with the amount of the relative orthorhombic phase excluding films thicker than 10 nm as shown in Figure 5.1.14(a). Similar correlation between the orthorhombic phase content and ferroelectric polarization was observed for polycrystalline hafnia.[38] On the other hand, the polarization appears to increase as rising the out-of-plane lattice parameter (Figure

5.1.14b). The thicker films of the thickness series deviate from this dependence, but the strong influence of film thickness on the amount of paraelectric monoclinic phase can hide strain effects. Thus, our results demonstrate flexible engineering of the ferroelectric properties of epitaxial films deposited on a particular substrate by proper selection of deposition parameters.

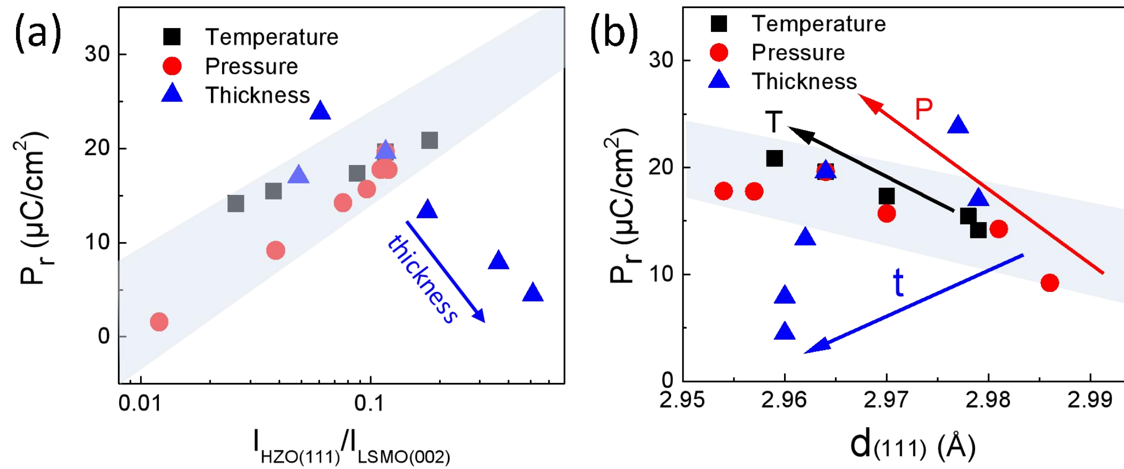


*Figure 5.1.14 $P_r$ plotted vs (a) the intensity of the HZO(111) peak normalized to LSMO(002) and (b) the out-of-plane lattice parameter of o-HZO, $d_{(111)}$. Black squares, red circles, and blue triangles correspond to samples of the $T_s$, $P_{O2}$, and thickness series, respectively.*

**Leakage current**

The leakage curves of all HZO films in the $T_s$, $P_{O2}$ and thickness series are presented in Figure 5.1.15. Leakage depends on the substrate temperature and films thickness, and particularly on the oxygen pressure as can be observed in Figure 5.1.15(a)-(c). The detailed leakage current at several electric fields for all the samples of Ts- and $P_{O2}$-series is shown in Figures 5.1.15(d)-(e), respectively. The leakage current decreases more than one order of magnitude with $T_s$, and it increases more than three orders of magnitudes with $P_{O2}$. The leakage of the $P_{O2}$ = 0.02 mbar film is around 2x10$^{-7}$ A/cm$^2$ at 1 MV/cm (whereas the 0.01 mbar sample was too insulating for a reliable measurement). The dependence shown in Figure 5.1.15(e) suggests that leakage in this range of $P_{O2}$ is not dominated by oxygen vacancies. Boundaries between monoclinic and orthorhombic grains and/or crystal domains can present high electrical conductivity. The orthorhombic phase increases with $P_{O2}$, and an eventual increase in boundaries density could cause larger leakage. Beyond the leakage mechanisms, from the experimental dependences of both polarization and leakage on $T_s$ and $P_{O2}$, it is concluded that high $T_s$ is convenient for high polarization and low leakage, whereas $P_{O2}$ in the 0.05－0.1 mbar range is optimal for good combination of large polarization and low leakage.

The leakage current as a function of thickness can be seen in Figure 5.1.15(f). It is

seen that the leakage increases by around two orders of magnitude with reducing thickness, presenting the thicker film (36.6 nm) remarkably low leakage of around $1x10^{-7}$ $A/cm^2$ at 1 MV/cm. It has to be noted that some polycrystalline ferroelectric $HfO_2$ films have been reported having smaller leakage[140] in spite of the presence of grain boundaries. Epitaxial films are not necessarily monocrystalline and they can present grain boundaries too. In particular, the presence of four o-HZO(111) crystal variants implies domain walls. Further studies are needed to determine the origin of the leakage in epitaxial films.

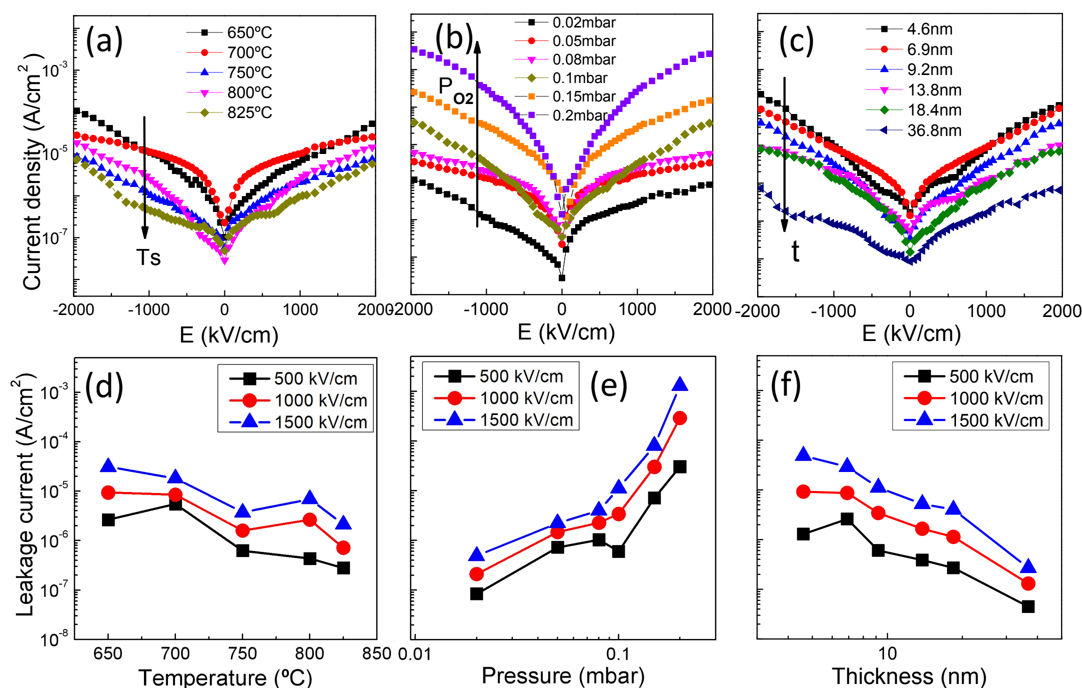


*Figure 5.1.15 Current density – electric field characteristics for the HZO films in the substrate temperature series (a), oxygen pressure series (b), and thickness series (c) along with the leakage currents at the indicated electric fields as a function of (d) $T_s$, (e) $P_{O2}$ and (f) thickness.*

**Dielectric measurement**

The dielectric measurements for the HZO/LSMO/STO(001) samples grown at different substrate temperatures, oxygen pressures and thicknesses are shown in Figure 5.1.16(a)-(c), respectively. For all the samples, the permittivity $\varepsilon_r$ ranges from below 20 to around 36. Specifically, with rising the growth temperature in Figure 5.1.16(a), the permittivity $\varepsilon_r$ decreases from almost 35 at 650 °C to about 30 at 825 °C. At 0.01 mbar, the sample without showing any reflection of HZO as observed in XRD $\theta$-$2\theta$ scans presents the smallest $\varepsilon_r$ about 16. Increasing oxygen pressure, the permittivity is hugely getting larger to around 30 at 0.1 mbar where it reaches a plateau state when continuously increasing the oxygen pressure (Figure 5.1.16b). For

the thickness series, the permittivity $\varepsilon_r$ drops monotonically from close to 36 at 4.6 nm to only 20 at 36.6 nm when the film thickness increases (Figure 5.1.16c).

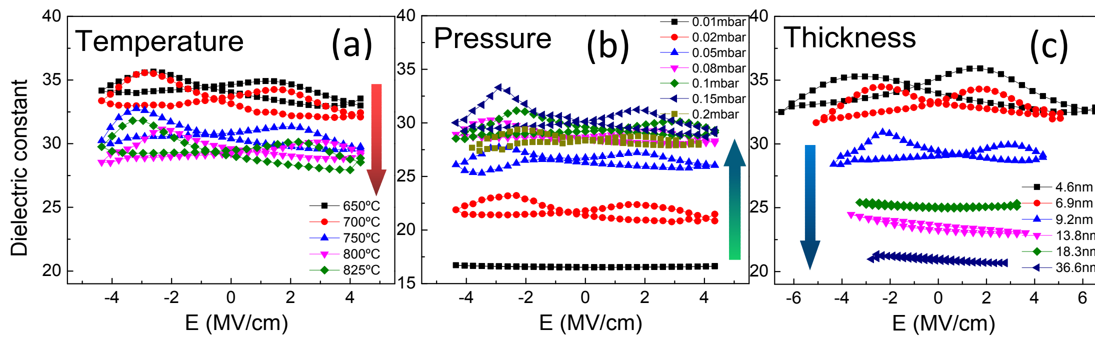


*Figure 5.1.16 Dielectric permittivity versus applied voltage loops for the HZO/LSMO/STO(001) samples measured at 50 kHz with varying the growth temperature (a), oxygen pressure (b) and thickness of HZO film (c).*

Figure 5.1.17(a) shows the dielectric permittivity of the epitaxial HZO films on STO(001) as a function of deposition temperature, oxygen pressure and thickness. These $\varepsilon_r$ values were extracted from the maximum electric field region, avoiding the influence from the domain wall motions. In the investigated range of growth window, the dielectric constant in oxygen pressure and thickness series presents a larger variation than in temperature series. Figure 5.1.17(b) shows the relative dielectric constant of competing crystalline phases in doped $HfO_2$ films (cubic, tetragonal, orthorhombic and monoclinic) from literature.[78-82,134,138,244-246] Tetragonal phase usually presents largest permittivity while the monoclinic phase has the lowest. The ferroelectric orthorhombic phase has the medium permittivity ranging from below 20 to almost 40 among these possible phases. In $T_s$ series, as $\varepsilon_r$ is increasing when lowering the temperature, one possible assumption is the coexistence of tetragonal phase with higher permitivity. The presence of tetragonal phase cannot be easily appreciated in XRD $\theta$-$2\theta$ scans due to the similar structure between o-phase and t-phase. In the $P_{O2}$ series, the sample in 0.01mbar has small permitivity of 16, implying the monoclinic phase or even coexisting amorphous phase in the film. When increasing the pressure, the increased o-phase formed causes the huge increase of dielectric constant $\varepsilon_r$. Similar high increase of polarization with pressure was observed (Figure 5.1.10b). On the other hand, as increasing the thickness, the permittivity is decreasing, which signals the formation of m-phase with low $\varepsilon_r$. This is confirmed by the XRD $\theta$-$2\theta$ scans and XRD $2\theta$-$\chi$ frames (discussed later) and it was also reflected at the strong reduction of ferroelectric polarization with thickness (Figure 5.1.11).

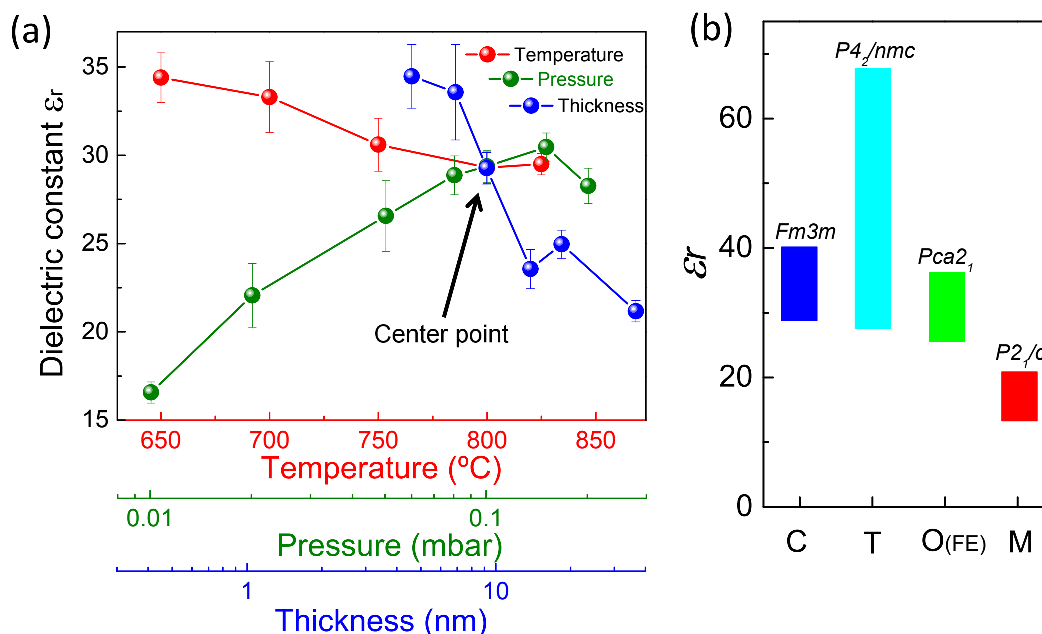


*Figure 5.1.17 (a) The dielectric permittivity as a function of deposition temperature, oxygen pressure and thickness. (b) The dielectric permittivity of competing crystalline phases (cubic, tetragonal, orthorhombic and monoclinic) in doped $HfO_2$ films.[78-82,134,138,244-246]*

**Endurance**

The characterization of the endurance for the sample grown at center parameters ($T_s$ = 800 °C, $P_{O2}$ = 0.1 mbar and t = 9.2 nm) is summarized in Figure 5.1.18. Polarization loops collected after cycling the sample for $10^2$, $10^5$, and $10^8$ times, for applied voltage up to 4.5 and 4.1 V, are presented in Figure 5.1.18(a)-(b), respectively. After $10^8$ cycles at 4.5 V (E = 5 MV/cm), the polarization window decreases up to 36 % of the initial value due to ferroelectric fatigue. The memory window as a function of the number of cycles is shown in Figure 5.1.18(c). Remarkably, after the large number of cycles at a high field of E = 5 MV/cm, a polarization window of 9 μC/cm$^2$ remains. When the sample was cycled at a smaller voltage (4.1 V), the initially smaller polarization decreased to a polarization of about 2.2 μC/cm$^2$ after $10^8$ cycles (around 24 % of the initial value). A similar gradual decrease to that of $P_r$ is shown by $\varepsilon_r$ extracted from the P-V loops around 0 V in Figure 5.1.18(c) inset. We need to note the initial $\varepsilon_r$ value is over 40, higher than the $\varepsilon_r$ value around 30 shown in 5.1.17(a). The reason is probably because the P-V loops were measured at 1 kHZ and the C-V loop were at 50 kHz. And the different devices used for measuring the P-V and C-V loops is another possible reason. The leakage currents have been observed to increase with the cycling number as shown in Figure 5.1.18(d)-(e), where an increase of leakage current is observed from $10^4$ cycles. Note that due to the leakage compensation performed, the relative leakage contribution to $P_r$ is constantly small. On the other

hand, we note that the endurance properties of the epitaxial film here reported do not achieve yet the record stability against fatigue after above $10^{10}$ cycles reported in polycrystalline La-doped[151] or high-pressure $N_2$ annealed[228] HZO films. However, it is worth noticing that endurance of polycrystalline films has been generally determined using capacitors with symmetric TiN electrodes. The different electrodes we have used in our capacitors (Pt and LSMO) cause an internal field that can favor fatigue. La-doping and symmetric electrode strategies for fatigue optimization could be also attempted in our epitaxial films.

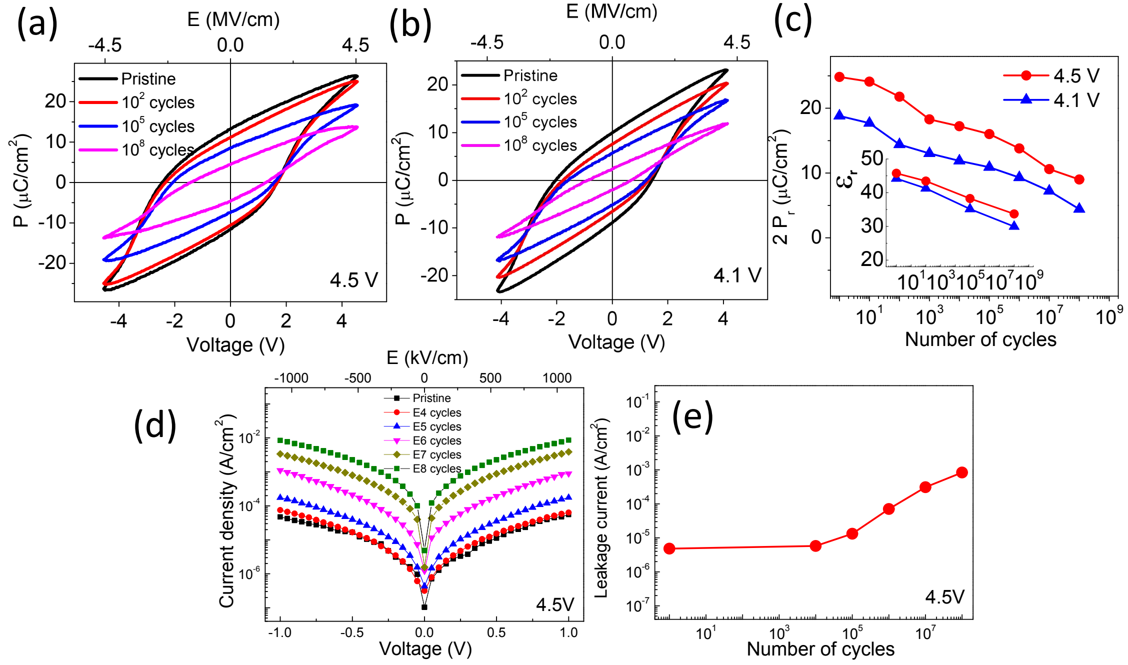


*Figure 5.1.18 Ferroelectric hysteresis loops ($T_s$ = 800 °C, $P_{O2}$ = 0.1 mbar and t = 9.2 nm film) recorded at 1 kHz, for the pristine state and after indicated number of electric cycles at 10 kHz at 4.5 V (a) and 4.1 V (b). (c) Remnant polarization versus number of cycles at 4.5 and 4.1 V. Inset: Dielectric permittivity versus number of cycles at 4.5 and 4.1 V. (d) Leakage current versus electric field in the pristine state and after the indicated number of bipolar cycles at 4.5 V. (e) Leakage current evaluated at 0.2 V (300 kV/cm) versus the number of bipolar cycles at 4.5 V.*

The growth parameters (deposition temperature and oxygen pressure) and film thickness are also investigated to evaluate their influence on the fatigue property of HZO films:

*Deposition temperature and oxygen pressure.* The influence of deposition temperature and oxygen pressure are shown in Figure 5.1.19. The applied cycling voltage is 4.5 V for all the measures. As decreasing the deposition temperature from 825 °C to 650 °C, the degradation rate of $P_r$ is gradually decreased. Similarly, when reducing the oxygen pressure from 0.2 mbar to 0.02 mbar, the endurance against fatigue is getting better. For the sample at 0.2 mbar, the endurance at 4 V can only last to 1000 cycles due to

the large leakage causing the capacitor breakdown. Therefore, we can conclude that low deposition and oxygen pressure can favor the endurance of epitaxial HZO films despite the limited improvement of endurance.

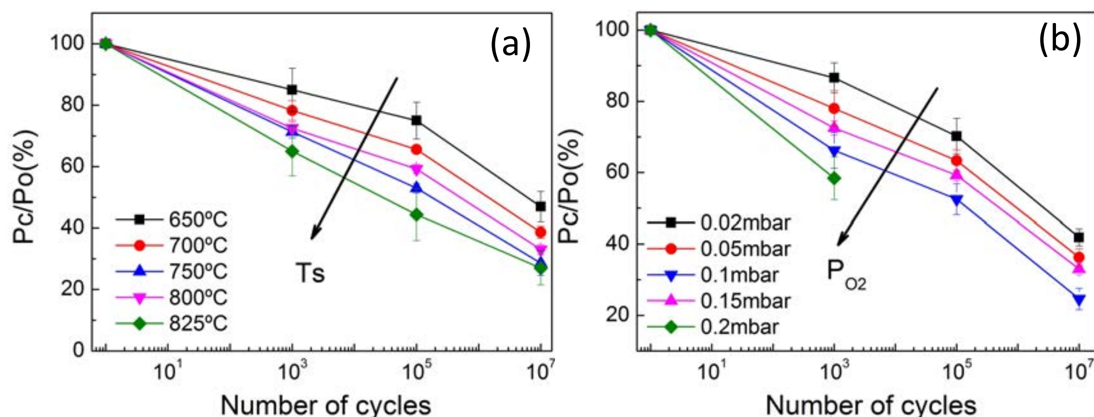


*Figure 5.1.19 Summary of the remnant polarization (positive and negative average values) normalized to its initial value ($P_0$) for samples with (a) deposition temperature and (b) oxygen pressure obtained at $10^3$ cyles, $10^5$ cycles and $10^7$ cycles at 10 kHz.*

*Film Thickness.* Remarkably, film thickness presents a huge influence on the endurance. Figure 5.1.20(a) and (b) shows the endurance properties of HZO films with thickness 4.6 nm and 18.4 nm under fatigue frequency 100 kHz, respectively. For 4.6 nm film, the endurance of $10^7$ and 3 x $10^8$ cycles at 3.5 V (7.61 MV/cm) and 3.0 V (6.52 MV/cm) can be achieved with memory window of the $2P_r$ around 20 μC/cm$^2$ and 10 μC/cm$^2$ remained before breakdown, respectively. Also, it shows a robust endurance at 2.5 V (5.43 MV/cm) cycles which can last up to 3 x $10^{10}$ cycles without breakdown, keeping significantly large memory window of $2P_r$ around 4 μC/cm$^2$. However, in Figure 5.1.20(b), the endurance for the 18.4 nm sample is only $10^6$ cycles with $2P_r$ less than 2 μC/cm$^2$ under 7 V (3.8 MV/cm) switching voltage. Under 6 V (3.26 MV/cm) cycles, only $10^5$ cycles can be obtained before reaching $2P_r$ at around 2 μC/cm$^2$. The maximum endurance at various cycling fields for different thicknesses is summarized in Figure 5.1.20(c). One can clear see that the thinner film can undertake higher electric field with better endurance while the thicker one cannot suffer from a equivalent or even lower cycling field and breakdown at shorter cycles. The endurance is thus much more improved with lowering the thickness. To further quantify the endurance difference with thickness, the dependence of $P_r$ value normalized to its initial value ($P_0$) with cycles at different thicknesses are shown in Figure 5.1.20(d). For the different thicknesses, cycling voltage was 3 V (4.6 nm), 3 V (5.75 nm), 3.5 V (6.9 nm) 4.5 V (9.2 nm), 5 V (13.8 nm) and 6 V (18.4 nm). It is clear that polarization of thicker HZO films degrades faster with increasing number of field cycles compared to that of thinner HZO films.

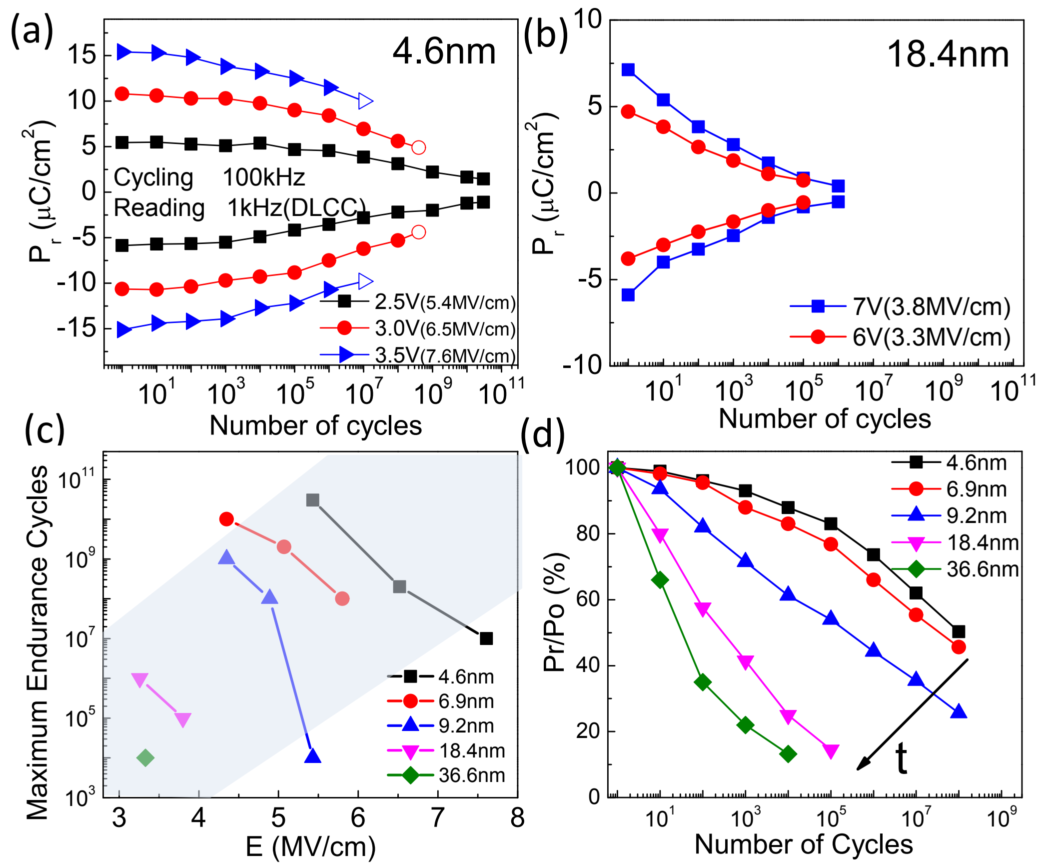


*Figure 5.1.20 Endurance characteristics of HZO films on STO with thickness (a) 4.6 nm and (b) 18.4 nm under different electric cycling field. (The open shape means dielectric breakdown at corresponding cycles; The solid shape means the capacitor does not breakdown; the measurement was stopped due to either the longer measurement time or the $2P_r$ below 2 μC/cm²). (c) Maximum endurance as a function of the electric field for sample with each thickness. (d) Summary of the remnant polarization (positive and negative average values) normalized to its initial value ($P_0$) for samples with each thickness.*

The fatigue degradation of each sample until breakdown is independent of the applied field. As shown in Figure 5.1.21 for each sample with t = 4.6 nm, 6.9 nm, 9.2 nm and 18.4 nm samples, the applied field does not influence the polarization degradation but only determines the maximum endurance.

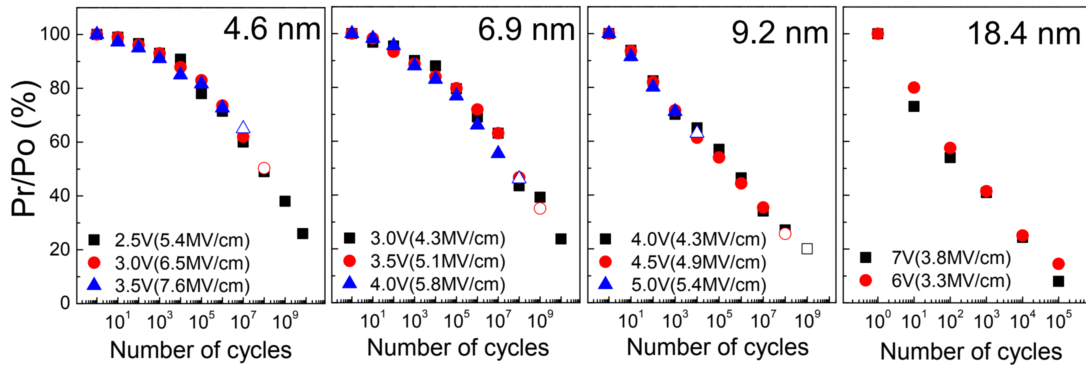


*Figure 5.1.21 The remnant polarization degradation (averaged $P_r$ normalized to its initial value ($P_0$)) vs cycling number at the different maximum applied voltages for HZO films with different thicknesses on STO.*

As reported, the monoclinic phase in doped-$HfO_2$ films degrade the ferroelectric polarization and endurance of HZO capacitors.[36,37,129] Herein, the direct evidence for m-phase increasing with t can be confirmed by XRD $2\theta$-$\chi$ frames in Figure 5.1.22. In the t = 4.6 nm film, the monoclinic phase is difficult to be detected. When the *t* increases, the monoclinic phase in film is getting increasing as indicated from the growing and elongated intensity of the (002) and (-111) reflections of m-phase. Indeed, the progressive increase of monoclinic phase respect to the orthorhombic one with thickness is shown in Figure 5.1.22. For the endurance of epitaxial HZO films, as paraelectric monoclinic secondary phase, the effects appear to be severe. TEM characterization shows columnar grains for both phases in films around 9 nm thick.[168] The study of the microstructure with thickness, which is not reported, could help understanding the apparently high impact of the monoclinic phase on the endurance. Also, suppressing the formation of the monoclinic phase in epitaxial HZO films could be an effective way to improve the endurance.

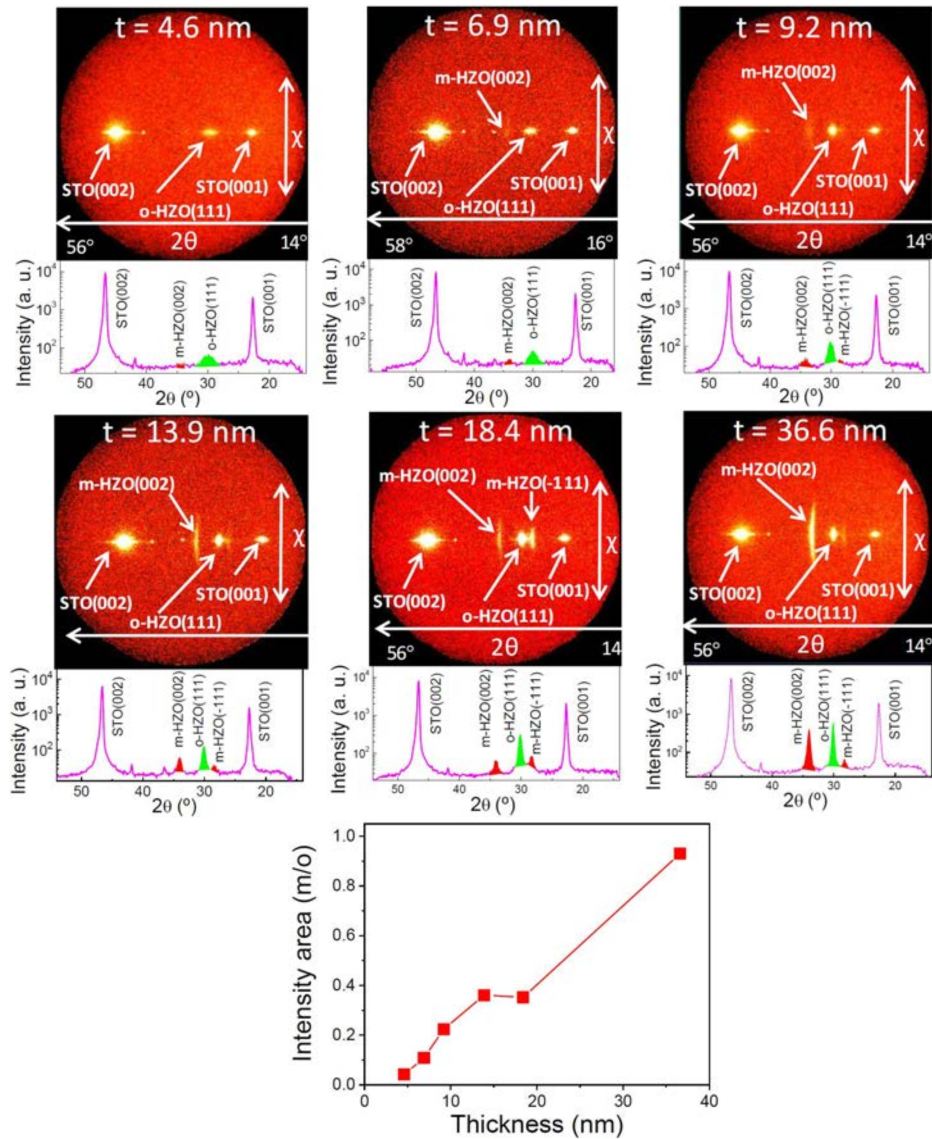


*Figure 5.1.22 XRD 2θ-χ frames of films of varying thickness (indicated in the top of each frame). The 2θ scan below each frame has been obtained by integration in XRD 2θ-χ frames from -5° to +5°. The area of m-HZO(1-111) and m-HZO(002) peaks is colored in red, and the area of o-HZO(111) peak in green. Bottom panel: ratio between intensity area of monoclinic HZO (sum of m-HZO(-111) and m-HZO(002) areas) and orthorhombic HZO (o-HZO(111) area) plotted against thickness.*

Another important improvement for endurance with thickness is the leakage state with cycles. Since the leakage is an important factor which can accelerate breakdown due to the possible impact of thermal effects generation by Joule heating, a stable low leakage current is critical to suppress breakdown and improve endurance. It is noted that thicker films have lower leakage in pristine state (Figure 5.1.15), but the leakage of the thinner film is more stable during cycling. Figure 5.1.23(a) shows the leakage comparison with cycles for 4.6 nm and 9.2 nm films under same electric field (5.43 MV/cm). A slight increase of leakage for 9.2 nm film happened in $10^3$ cycles,

followed by a huge increase by two orders of magnitude occurring at $10^4$ cycles and further measurement causes a hard dielectric breakdown. For the thicker films, not shown in Figure 5.1.23(a), dielectric breakdown occurs before reaching the same electric field (5.43 MV/cm). However, it is remarkable that the leakage in 4.6 nm HZO film presents a constant level (slight decrease) with increasing field cycles despite the initial high leakage. The low constant leakage current during cycles makes the longer endurance possible. Figure 5.1.23(b) shows the threshold cycles before leakage increases sharply by over one order of magnitude with applied field for different thicknesses. The leakage increase which further causes the capacitor breakdown often occurs at shorter number of cycles for thicker films than the thinner HZO films, which is more stable leakage current. The specific reason of the leakage current increasing with field cycles is still not clear. In the polycrystalline HZO films, the leakage increase is generally attributed to the formation of new oxygen vacancies favored by the TiN electrode usually employed, which leads to the fast growth of leakage currents.[229] The specific mechanisms in epitaxial films are unknown, which requires deeper study.

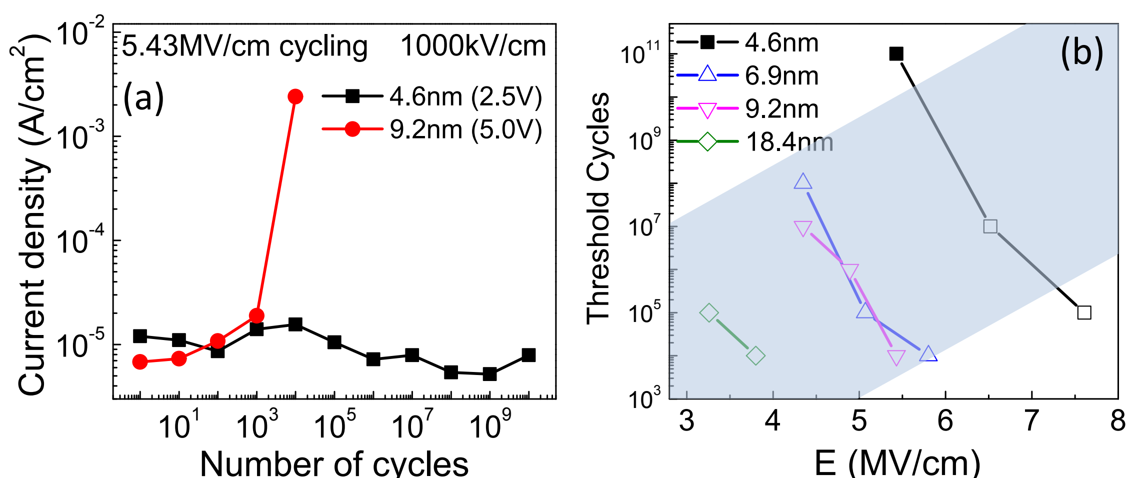


*Figure 5.1.23 (a) Leakage current at 1000 kV/cm as a function of the number of applied cycles of 5.43 MV/cm for the HZO/LSMO/STO(001) samples with 4.6 nm and 9.2 nm film thickness. (b) Threshold of number of cycles before leakage increasing sharply as a function of electric field for each thickness. (Solid symbol indicates the leakage does not increase within the applied field cycles.)*

**Retention**

As retention is a major property for applications in memory devices, detailed ferroelectric retention characterization of positive and negative polarization has been performed. The retention of positive (negative) polarization describes poling a sample into a positive (negative) state and reading out the remaining remnant polarization

after a defined period. Figure 5.1.24(a) shows the retention behaviour of the HZO sample with $T_s$ = 800 °C, $P_{O2}$ = 0.1 mbar and t = 9.2 nm film with poling field around 6 MV/cm (5.5 V). This ultrathin film presents very long polarization retention. The difference between positive and negative polarization decreases to about 74 % of the initial value for the maximum measurement time of $10^4$ s, and the polarization window extrapolated to 10 years is around 41 % ($2P_r$ > 15 μC/cm$^2$ ) of the initial value. The corresponding normalized retention degradation of positive and negative polarization is shown in Figure 5.1.24(b). Retention is calculated by the ratio of the remnant polarization $P_r$ (positive and negative) after a delay time versus its initial value. It can be observed that positive $P_r$ has a longer retention while the negative $P_r$ degrades faster.

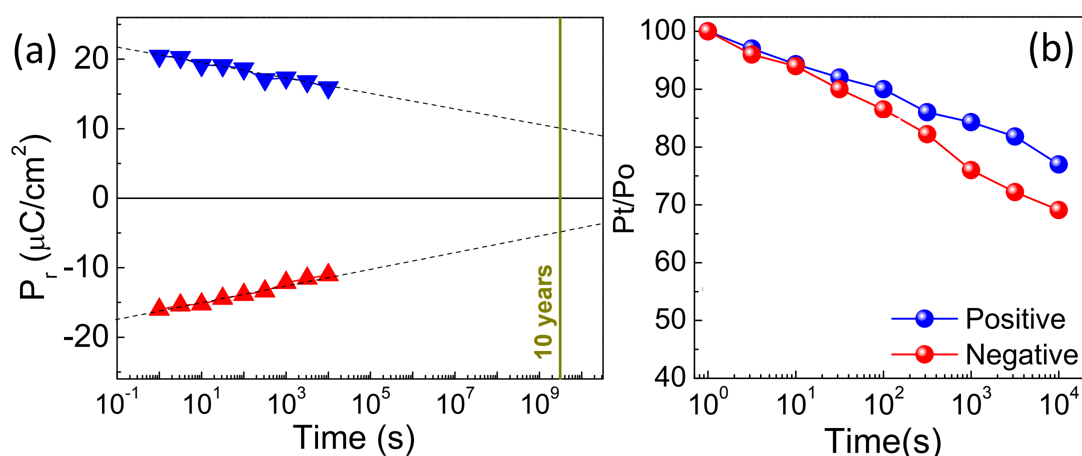


*Figure 5.1.24 (a) Ferroelectric retention (t = 9 nm) after poling the sample with "positive" (blue down triangles) or "negative" (red up triangles) voltage pulsed in the given direction and measuring the switchable charge after a delay time. Writing and reading voltages were 5.5 V. (b) retention degradation of positive and negative polarization for 9 nm HZO films on $SrTiO_3$.*

The deposition temperature, oxygen pressure and film thickness are also investigated to evaluate their influence on the retention property of HZO films:

*Deposition Temperature.* Figure 5.1.25(a)-(e) summarizes the retention degradation of positive and negative $P_r$ within 1000 s time for all the samples in $T_s$ series. Each retention results for samples at different temperatures were obtained from at least five capacitors with poling field around 5.5 V. For all the samples in the $T_s$ window, the positive $P_r$ has a longer retention. The anisotropy in the retention for positive and negative side depends strongly on the HZO deposition temperature. The polarization lost rate of all the $T_s$ samples was characterized by linear fitting and the slope values are shown in Figure 5.1.25(f). Above 750 °C, the retention of both sides is not very different and similar in the three samples. However, when the $T_s$ was below 750 °C, the retention of negative polarization is severely degraded while the positive $P_r$ presents high retention.

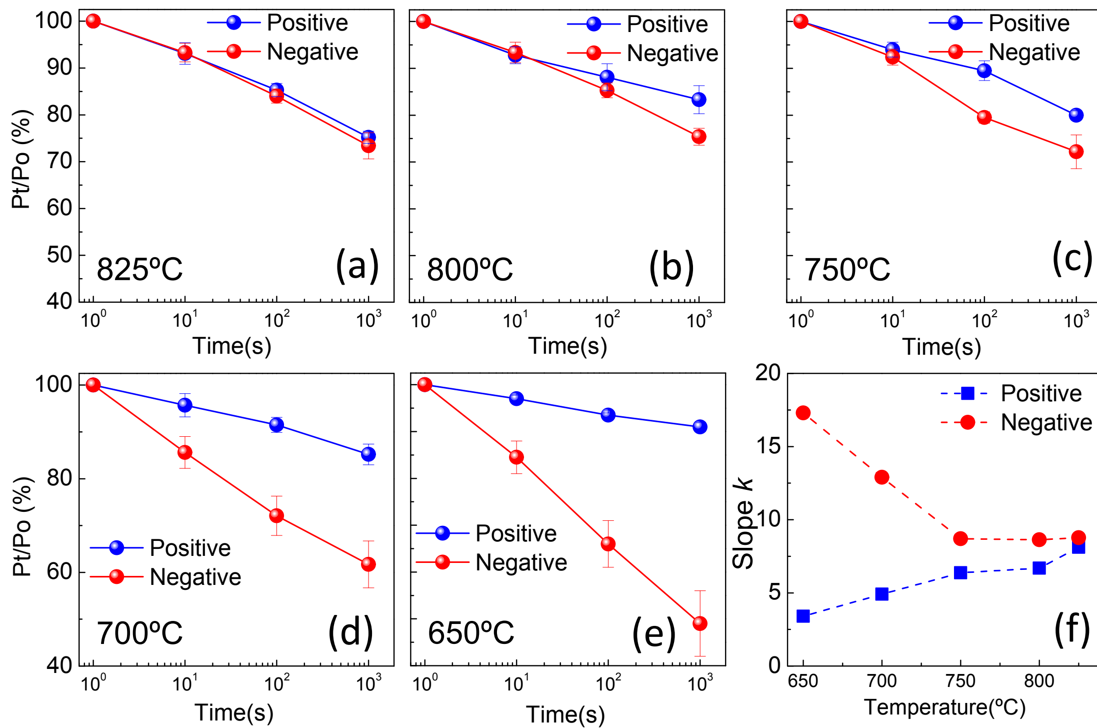


*Figure 5.1.25 (a)-(e) Retention of ferroelectric polarization of the epitaxial HZO film on STO (001) substrate poled positively and negatively for film thickness at different deposition temperatures. Inset of (a): the sketch indicating the imprint direction. (f) Retention degradation slope value k as a function of deposition temperatures of HZO on STO.*

*Oxygen Pressure.* The retention degradation of samples in $P_{O2}$ series are shown in Figure 5.1.26(a)-(e). All the retention data was also obtained at 5.5 V poling voltage. The one under $P_{O2}$ = 0.2 mbar was not shown here because of the large leakage and breakdown at high voltage (≥ 4.5V). And for the sample at $P_{O2}$ = 0.01 mbar, the polarization is quite small ($P_r$ below 1 μC/cm$^2$) which does not support a reliable measurement. The better retention ability of positive polarization can also be observed in $P_{O2}$ series due to the downward imprint field. Unlike in $T_s$ series, the retention does not show an evident variation neither for positive or negative polarization with the oxygen pressure window (Figure 5.1.26f).

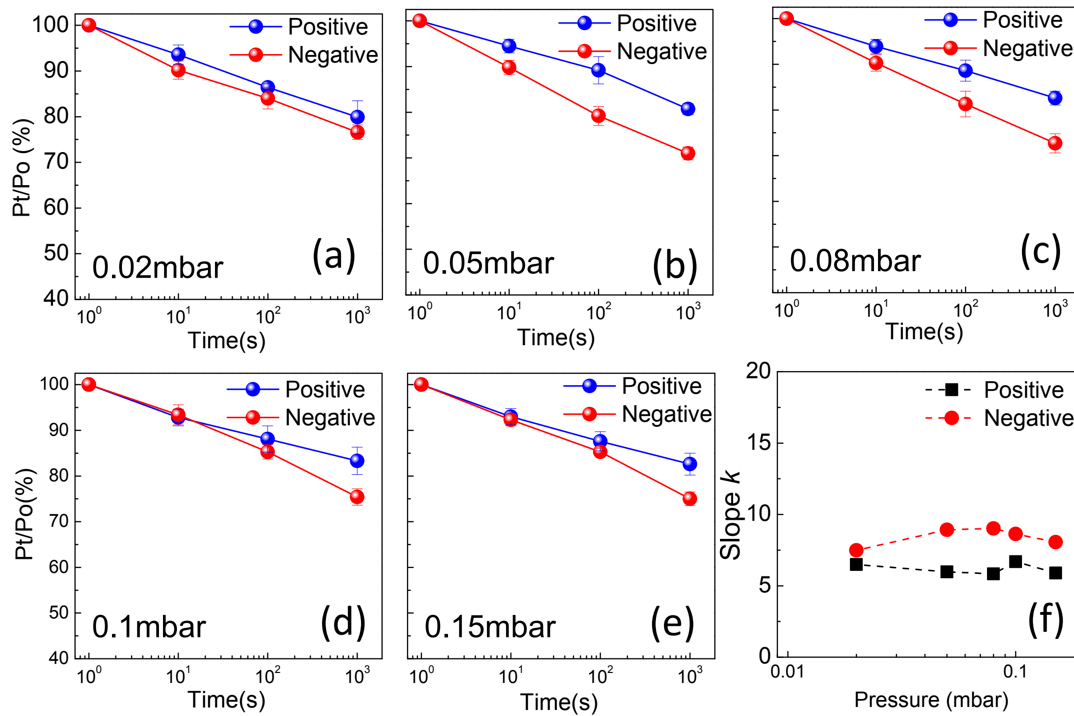


*Figure 5.1.26 (a)-(e) Retention of ferroelectric polarization of the epitaxial HZO film on STO (001) substrate at different oxygen pressures. (f) Retention degradation slope value k as a function of oxygen pressure of HZO on STO.*

*Film Thickness.* For the t series, the retention degradation of samples is shown in Figure 5.1.27(a)-(d). One difference from the $T_s$ and $P_{O2}$ series is that the retention of negative $P_r$ can be much more favored while the positive $P_r$ severely suffers in the thinnest 4.6 nm sample. As shown in Figure 5.1.27(d), when the thickness of HZO film increases to 18.4 nm, the slope value is much increasing, indicating the decreased retention ability. It should be noted that during the retention measurement (described in chapter 3), several pulses has to be applied to the sample to extract the polarization values. As presented before, when t increases, the fatigue problem is getting more obvious. And thicker samples such as 18.4 nm and 36.8 nm ones present fast polarization drop at initial cycles. Thus, the high fatigue of the sample contributes to the low retention.

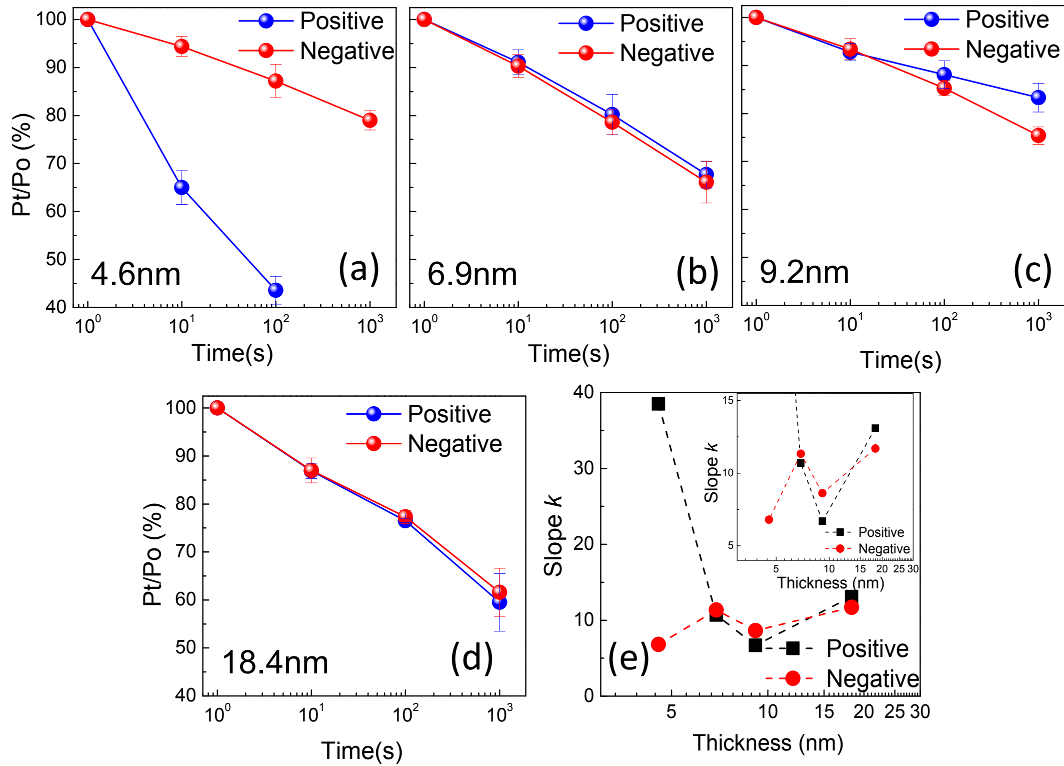


*Figure 5.1.27 (a)-(d) Retention of ferroelectric polarization of the epitaxial HZO film on STO (001) substrate poled positively and negatively for different film thicknesses. Note: the poling field used for retention of samples with different thickness is as same as the electric field for P-E loops recorded in Figure 5.1.11(a). (e) Retention degradation slope value k as a function of film thickness of HZO on STO with zoomed region (inset).*

The internal electric fields usually play a important role in determining the memory retention of ferroelectrics.[175,230] It includes two types of internal electric fields: one is the depolarization field ($E_{dep}$) and another the imprint field ($E_{imp}$). $E_{dep}$ is opposite to the direction of the polarization, responsible for the loss of polarization. The formation of a depolarization field is usually caused by the incomplete compensation of polarization-induced bound charges and its effects can be more pronounced if the ferroelectric film has large leakage. While low permittivity and high coercive voltage of ferroelectric film can mitigate the depolarization effects.[98,231] Depolarization filed is not the only internal field, coexisting with imprint field which is manifested by the shift of the polarization loop towards positive or negative voltage. The imprint field describes a internal field driving ferroelectric polarization towards a preferential direction when external bias is removed. $E_{imp}$ is defined as: $E_{imp} = 0.5 \times (E_{c+}+E_{c-})$, expressing the electrical field shift in the hysteresis loop. Imprint fields can have different origins such as asymmetric interfaces, giving rise to unequal Schottky barriers, or defects.[40,98] Both internal electric fields can have important influence on the ferroelectric retention.

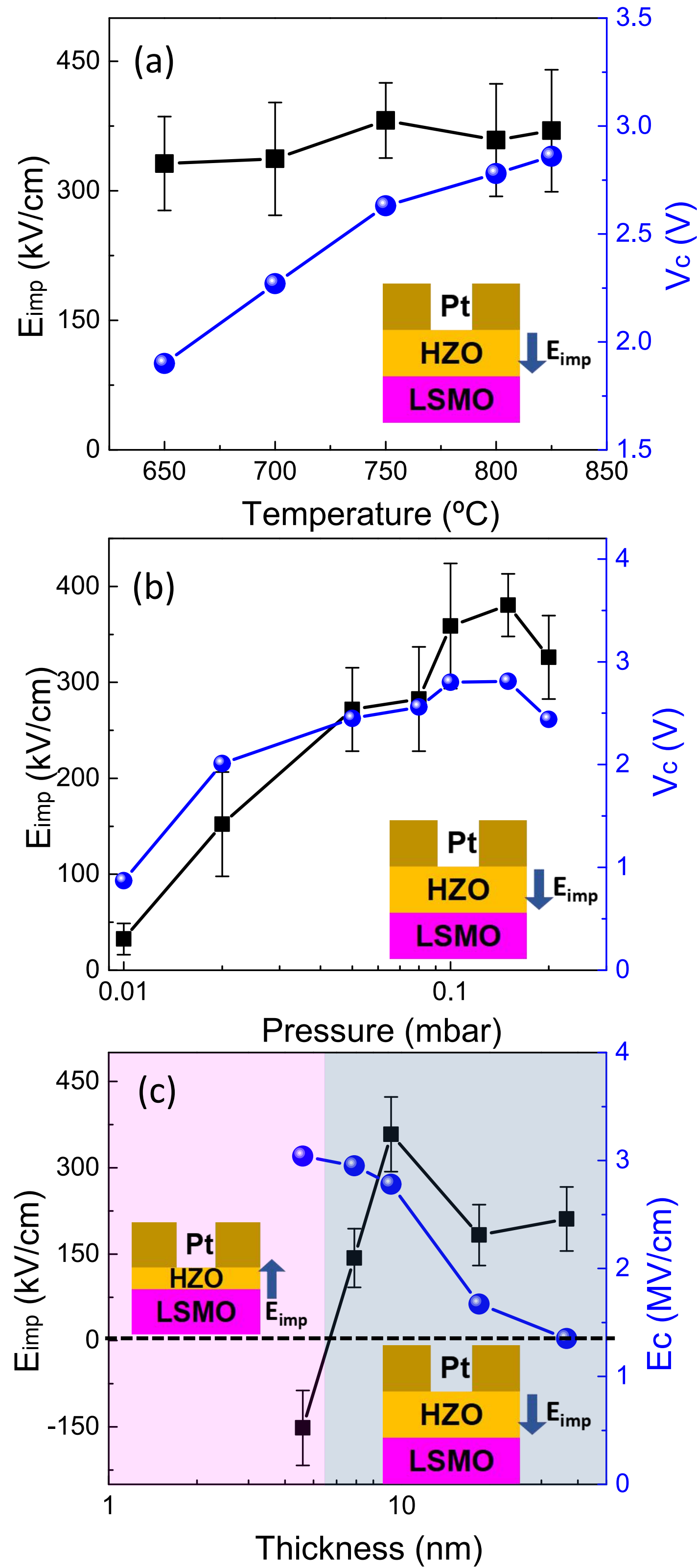


*Figure 5.1.28 The dependence of imprint field and coercive field on the deposition temperature (a), oxygen pressure (b) and film thickness (c) for the HZO films on STO(001) with the sketch indicating the imprint field direction.*

The dependence of imprint field and coercive voltage (field) on the deposition temperature, oxygen pressure and film thickness is shown in Figure 5.1.28. The imprint field and coercive voltage of all the samples are obtained from the P-V loops. With similar thickness, $E_{imp}$ depends strongly on $P_{O2}$, increasing from negligible value at 0.01 mbar to about 400 kV/cm at 0.1 mbar, likely due to the defects. And the $E_{imp}$ during the temperature window is almost constant for all the samples around 400 kV/cm. The direction of $E_{imp}$ is from the top electrode towards the bottom electrode (as sketch in the inset of Figure 5.1.28) favoring the positive polarization and degrading the negative side except in the thinnest one t = 4.6 nm. For the thinnest sample of t = 4.6 nm, $E_{imp}$ direction present opposite direction pointing from bottom electrode to top electrode (Figure 5.1.28c), causing the shorter retention of positive polarization. Thus, $E_{imp}$ direction appears to determines the observed anisotropy in the loss of polarization (retention). A second point is what determines the magnitude of the polarization loss. However, there is no clear correlation between magnitude of the polarization loss and $E_{imp}$. Another internal field is related to the depolarization field that is influenced by the leakage, coercive voltage (field) and dielectric permittivity $\varepsilon_r$. 1) Leakage current, as described in Figure 5.1.15, depends strongly on the oxygen pressure, whereas the evident variation in retention is not observed. 2) Coercive voltage $V_c$ show similar variation in $T_s$ and $P_{O2}$ series, increasing from 1.9 V to 2.9 V with temperature and from 2 V to 2.8 V between 0.02 mbar to 0.2 mbar. However, the retention are almost similar in the pressure window and retention of positive side is shorter as temperature increases. In the thickness series, the leakage decrease with thickness increasing. And the retention is worse in thicker film due to the fatigue problem as discussed before. 3) The dielectric permittivity $\varepsilon_r$ ranges from 22 to around 30 increasing the pressure from 0.02 mbar to 0.2 mbar with direct correlation with retention data. And the dielectric permittivity $\varepsilon_r$ does not show an evident variation with temperature. The permittivity of HZO film is getting higher as decreasing the thickness causing the larger depolarization field formed in thinner films, together with larger leakage which degrades the ferroelectric retention in thinner film. As can be observed in Figure 5.1.27(e), the sample at t = 6.9 nm has a decreased (positive and negative) retention ability than 9.2 nm sample despite the smaller imprint field and higher $V_c$ in 6.9 nm sample.

Thus, 1) the direction of $E_{imp}$ is an important factor in the retention and a particular direction of bias would be clearly preferable in memory device. 2) the magnitude of the retention does not depend apparently on a single property and it is the result of competition between the leakage current, coercive voltage (field) and dielectric permittivity $\varepsilon_r$ in the film.

## Conclusion

The growth window of epitaxial stabilization of $Hf_{0.5}Zr_{0.5}O_2$ films on $La_{2/3}Sr_{1/3}MnO_3$/$SrTiO_3$(001) has been determined. The deposition parameters and thickness have great impact on the orthorhombic phase amount, and the lattice strain can be varied within a range wider than 3 %. The ferroelectric polarization increases with the amount of orthorhombic phase and is found to increase as the out-of-plane lattice parameter decreases, and thus it can be controlled by deposition parameters. The leakage current is also conditioned by the deposition parameters, being lower for higher temperature and particularly for lower oxygen pressure. Remarkably, the $E_c - t^{-2/3}$ scaling of electric coercive field and thickness is found by the first time for ferroelectric hafnium oxide, even for films thinner than 5 nm. In addition, the epitaxial $Hf_{0.5}Zr_{0.5}O_2$ films present a good endurance over $10^{10}$ cycles, and an extremely long retention extending well beyond 10 years. The growth window map is an important tool for further studies on epitaxial films, for example to unravel the individual contributions of relative amount of the orthorhombic phase and elastic strain effects on ferroelectric properties.

## 5.2 Epitaxial Integration on Si(001) of Ferroelectric $Hf_{0.5}Zr_{0.5}O_2$ Capacitors

### *Abstract*

*Epitaxial ferroelectric $Hf_{0.5}Zr_{0.5}O_2$ films have been successfully integrated in a capacitor heterostructure on Si(001). The orthorhombic $Hf_{0.5}Zr_{0.5}O_2$ phase, [111] out-of-plane oriented, is stabilized in the films. In this part, two different buffer layers are employed, $LaNiO_3/CeO_2$/YSZ and simpler $SrTiO_3$ buffer layers, for achieving the epitaxial growth of $Hf_{0.5}Zr_{0.5}O_2$ films on Si(001).*

***In section 5.2.1**, the bottom $La_{2/3}Sr_{1/3}MnO_3$ electrode and $LaNiO_3/CeO_2$/YSZ buffering structure was used for epitaxial growth of $Hf_{0.5}Zr_{0.5}O_2$ film on Si with varying $Hf_{0.5}Zr_{0.5}O_2$ film thickness from 2.3 nm to 18.4 nm. The films at t = 4.6 nm present high remnant polarization $P_r$ around 33 µC/cm$^2$. Retention time is longer than 10 years for a writing field of around 5 MV/cm, and the capacitors show endurance up to over $10^{11}$ cycles for a writing voltage of 2.5 V in 4.6 nm $Hf_{0.5}Zr_{0.5}O_2$ film. It is also found that the formation of the orthorhombic ferroelectric phase depends critically on the bottom electrode, being achieved on $La_{2/3}Sr_{1/3}MnO_3$ but not on $LaNiO_3$.*

***In section 5.2.2**, $SrTiO_3$ templates have been used to integrate epitaxial bilayers of ferroelectric $Hf_{0.5}Zr_{0.5}O_2$ and $La_{2/3}Sr_{1/3}MnO_3$ bottom electrode on Si(001). The $Hf_{0.5}Zr_{0.5}O_2$ films show very high remnant polarization $P_r$ of 34 µC/cm$^2$ and present long retention time well beyond 10 years and high endurance against fatigue up to $10^9$ cycles at operating voltage of 4 V.*

For device applications in CMOS technology, ferroelectric films has to be integrated with Si substrate. However, the integration on Si(001) of epitaxial FE $HfO_2$ in a capacitor structure with top and bottom electrodes is still elusive. The epitaxial stabilization of a metastable phase depends critically on the substrate and buffer layers. For instance, the epitaxial stress can be responsible for the reported impact of the thickness on the amount of the orthorhombic phase in epitaxial $HfO_2$ films.[168,231] In the particular case of epitaxy on Si(001) substrates, thermal expansion mismatch can induce additional strain. In this chapter, We have investigated the stabilization of orthorhombic $HfO_2$ on epitaxial oxide electrodes deposited on Si(001) with two different heterostructures: LSMO/LNO/$CeO_2$/YSZ/Si(001) and LSMO/STO/Si(001). Epitaxial HZO films with high quality can be stabilized on Si(001) with both heterostructures. And the excellent ferrolectric properties are also achieved in both cases.

### 5.2.1 Ferroelectric $Hf_{0.5}Zr_{0.5}O_2$ capacitor epitaxially integrated on $La_{2/3}Sr_{1/3}MnO_3$/$LaNiO_3$/$CeO_2$/YSZ/Si(001) structure

#### Growth conditions

The HZO/LSMO/LNO/$CeO_2$/YSZ/Si(001) and HZO/LNO/$CeO_2$/YSZ/Si(001) heterostructures as sketched in Figure 5.2.1(a) were fabricated in a single process by pulsed laser deposition. HZO, $CeO_2$, and YSZ were grown at the substrate temperature of 800 °C and LSMO and LNO at 700 °C. The oxygen pressure was 0.1 mbar for the deposition of HZO and LSMO, 0.15 mbar for LNO, and 4 $\times10^{-4}$ mbar for $CeO_2$ and YSZ at a laser frequency of 5 Hz. The heterostructures were cooled to room temperature under an oxygen pressure of 0.2 mbar. The HZO films were prepared at 800 laser pulses in both cases. The thickness of HZO films was confirmed by simulating the Laue reflections of HZO(111) peak of the HZO/LSMO/LNO/$CeO_2$/YSZ/Si(001) sample according to the equation (5-1) as shown in Figure 5.2.1(b). The simulation around HZO(111) (red curve) has been fitted supposing a thickness of 97.3 Å ($N$ = 33 and $c$ = 2.948 Å), being the corresponding Bragg reflection located at $2\theta$ = 30.319°. For the blue curve, corresponding to $CeO_2$(002), thickness was 168 Å ($N$ = 31 and $c$ = 5.41 Å), being the corresponding Bragg reflection located at $2\theta$ = 33.117°.

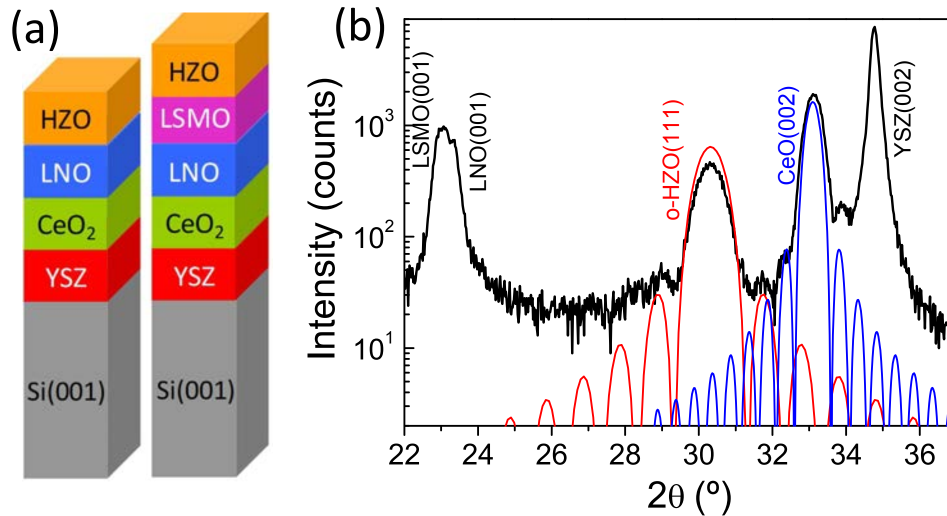


*Figure 5.2.1 (a) Sketch of the two epitaxial heterostructures; (b) XRD θ-2θ scan of the HZO/LSMO/LNO/CeO$_2$/YSZ/Si(001) sample measured with long acquisition time.*

In addition, a series of samples by varying the HZO thickness was also prepared. The specific thicknesses for HZO films are 2.3 nm, 3.4 nm, 4.6 nm, 5.8 nm, 6.9 nm, 9.7nm, 13.8 nm and 18.4 nm.

## Structural Study

### Role of LSMO bottom electrode

Figure 5.2.2(a) shows XRD $\theta$-2$\theta$ scans of the HZO/LSMO/LNO/$CeO_2$/YSZ/Si(001) (upper scan) and HZO/LNO/$CeO_2$/YSZ/Si(001) (lower scan). The pattern of the HZO/LSMO/LNO/$CeO_2$/YSZ/Si(001) sample shows (00$l$) reflections corresponding to the Si wafer and the LSMO, LNO, $CeO_2$ and YSZ layers. There is also a peak at the position (2$\theta$ ~ 30°, see the zoom in the right panel) of the (111) reflection of the orthorhombic phase of HZO. It can be appreciated that the HZO(111) peak is slightly shifted towards lower angles in comparison with the corresponding position (marked with a vertical dashed line) of polycrystalline films.[152,233,234] It is clear to see that LSMO is critical in stabilizing the orthorhombic phase of HZO. The XRD $\theta$-2$\theta$ scan of the sample without this layer, HZO/LNO/$CeO_2$/YSZ/Si(001), does not show diffraction peaks of HZO. HZO reflections in HZO/LNO/$CeO_2$/YSZ/Si(001) neither were detected in XRD 2$\theta$-$\chi$ frames measured using a 2D detector in left panel of Figure 5.2.2(b). Very low intensity peaks corresponding to o-HZO(111), and (-111) and (002) of m-HZO were only observed in grazing incidence XRD (Figure 5.2.2c). This indicates a small amount of crystalline phases or very small crystal size when HZO is grown on LNO, in comparison to polycrystalline films obtained by annealing.[36] A set of HZO/LNO films was deposited on $SrTiO_3$(001) substrates to

confirm the critical role of the electrode on the epitaxial stabilization of o-HZO. In agreement with the samples on Si(001), equivalent HZO films on LNO/$SrTiO_3$(001), not shown here, did not present orthorhombic phase. The XRD $2\theta$-$\chi$ frame measured using a 2D detector HZO/LSMO/LNO/$CeO_2$/YSZ/Si(001) sample in right panel of Figure 5.2.2(b) shows a HZO(111) spot, which sharpness around $\chi$ = 0° points to epitaxial ordering. The $2\theta$-$\chi$ frame shows a low-intensity m-HZO(002) spot, elongated along $\chi$ and located between the YSZ(002) and $CeO_2$(002) spots. Thus, a minority monoclinic phase is present in HZO films that are predominantly orthorhombic and present a (111) texture. Epitaxy of HZO and buffer layers was confirmed by XRD $\phi$-scans (Figure 5.2.2d). The $\phi$-scans around (111) reflections of Si, $CeO_2$, and YSZ show four peaks at the same $\phi$ angles, whereas the corresponding four peaks of LNO and LSMO are 45° apart of the former. The $\phi$-scan around HZO(-111) presents four sets of three peaks, confirming the presence and crystal orientation of o-HZO, and indicating the presence of four crystal domains in o-HZO. The epitaxial relationships are[1-10]HZO(111)/[1-10]LSMO(001)/[1-10]LNO(001)/[100]$CeO_2$(001)/[100]YSZ(001)/[100]Si(001). This epitaxial relationship is same for HZO films on LSMO/$SrTiO_3$(001).[168,223]

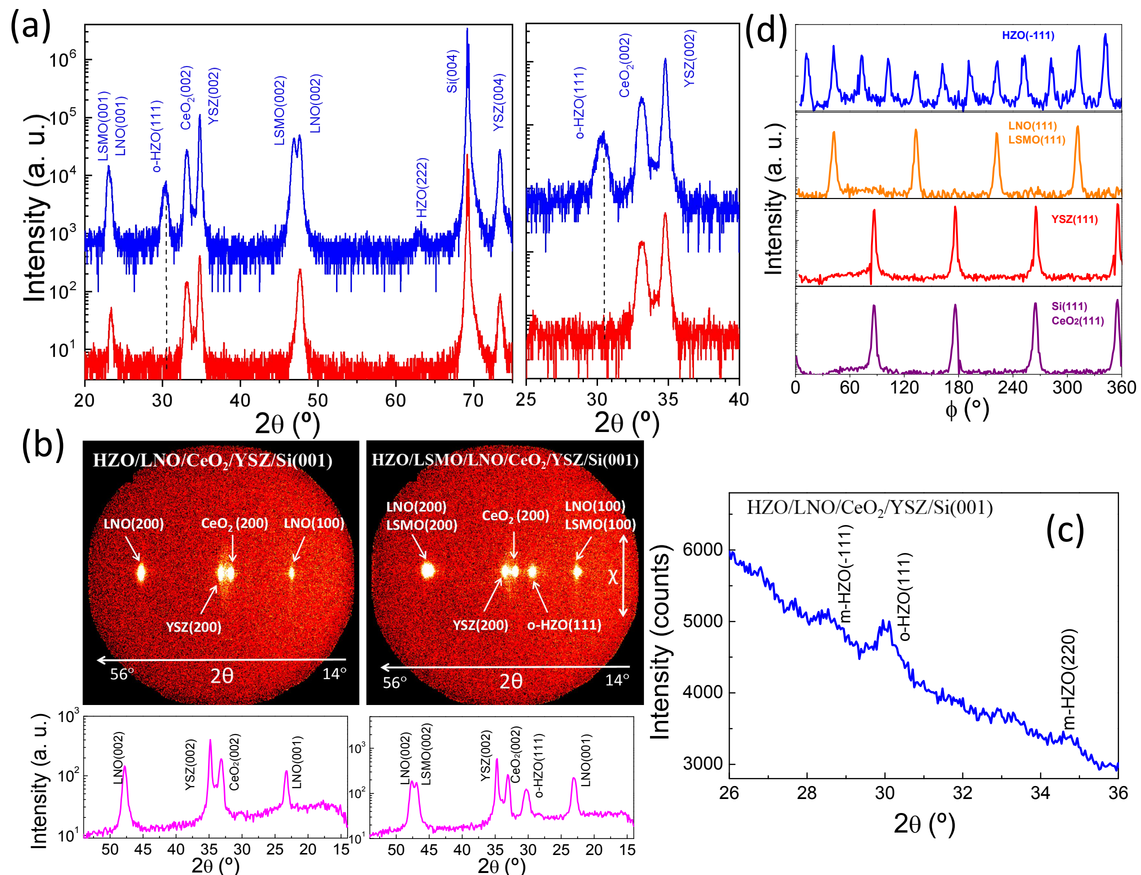


*Figure 5.2.2 (a) XRD θ-2θ scans of HZO/LSMO/LNO/$CeO_2$/YSZ/Si(001) (upper scan) and HZO/LNO/$CeO_2$/YSZ/Si(001) (lower scan). A zoomed region around the HZO(111) reflection is shown in the right panel. (b) XRD 2θ- χ frame with a 2D detector, corresponding to*

*HZO/LNO/$CeO_2$/YSZ/Si(001)(left panel) and HZO/LSMO/LNO/$CeO_2$/YSZ/Si(001)(right panel). The corresponding $\theta$-$2\theta$ scans were obtained by integrating ± 5° around $\chi$ = 0°. (c) Grazing incidence XRD corresponding to the HZO/LNO/$CeO_2$/YSZ/Si(001) sample. (d) XRD $\phi$-scans around the o-HZO(-111) and (111) reflections of LSMO, LNO, $CeO_2$, YSZ, and Si corresponding to the HZO/LSMO/LNO/$CeO_2$/YSZ/Si(001) sample.*

**Dependence with thickness**

X-ray diffraction (XRD) $\theta$-$2\theta$ scans of HZO/LSMO/LNO/$CeO_2$/YSZ/Si(001) samples with varying the thicknesses are shown in Figure 5.2.3(a). When increasing the thickness, the o-HZO(111) reflections become narrower and more intense (Figure 5.2.3b). The weak peak of (-111) m-phase can observed in 18.4 nm HZO film while the peak of (-111) m-phase is quite subtle for thinner ones. The peak of (002) m-phase which is evident for thicker HZO film on STO(001) is overlapped by the (002) peaks of YSZ and $CeO_2$ as they share the similar peak position around 35º. In the inset of Figure 5.2.3(b), the linear fitting of the reciprocal of the thickness with the half width of o-HZO(111) peak indicates the epitaxial o-HZO (111) crystals grow across the entire film thickness according to the Scherrer equation.[222] The out-of-plane lattice parameter of orthorhombic phase decreases with thickness (Figure 5.2.3c), from 2.988 Å to 2.942 Å (1.56 % contraction) as thickness increases from 2.3 nm to 18.4 nm. The inter-planar spacing $d_{o\text{-}HZO(111)}$ of HZO films on Si is smaller than on STO(001), but similar to that of HZO on Si with STO template, which is probably caused by the strain state of LSMO induced by substrates and the thermal expansion coefficient between buffer layers and substrates. As shown in Figure 5.2.3(d), the rocking curve signals the lower mosaicity in thinner HZO films with value from 1.0 to 1.6 as increasing the thickness from 4.6 nm to around 19 nm.

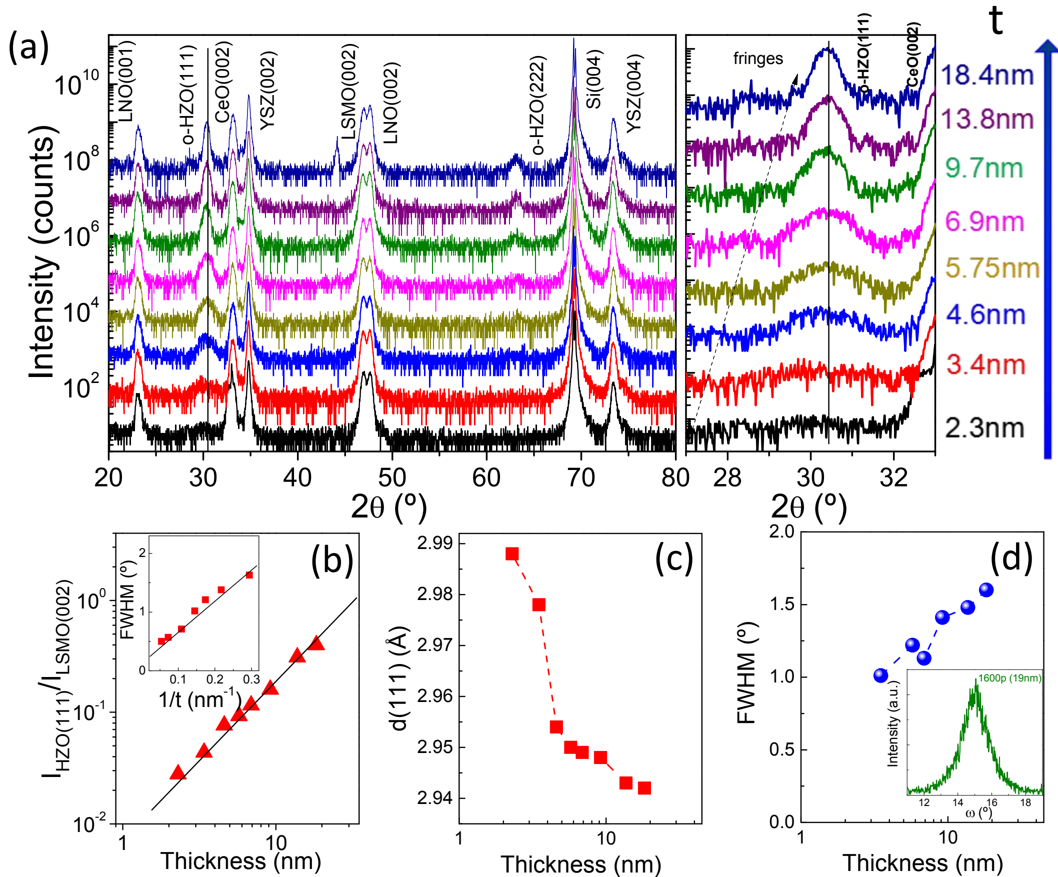


*Figure 5.2.3 (a) XRD θ-2θ scans of HZO/LSMO/LNO/$CeO_2$/YSZ/Si(001) of varying thickness from t = 2.3 nm to 18.4 nm. A zoomed region around the HZO(111) reflection is shown in the right panel. (b) Intensity of o-HZO(111) normalized to LSMO(002), plotted as a function of thickness. Inset: full-width at half-maximum (FWHM) of the o-HZO(111) peak as a function of the reciprocal of film thickness. (c) Dependence on $d_{o\text{-}HZO(111)}$ interplanar spacing with film thickness. (d) Dependence of FWHM with film thickness. Inset: rocking curve of 18.4 nm thick sample.*

As shown in Figure 5.2.4, all the films have very flat surfaces with a root-means-square (rms) roughness below 0.5 nm at all thicknesses. The morphology of the thinnest film at 4.6 nm presents lowest roughness around 0.26 nm. Then roughness increases with thickness. Even though for the thickest 18.4 nm film, the roughness is still as low as 0.47 nm.

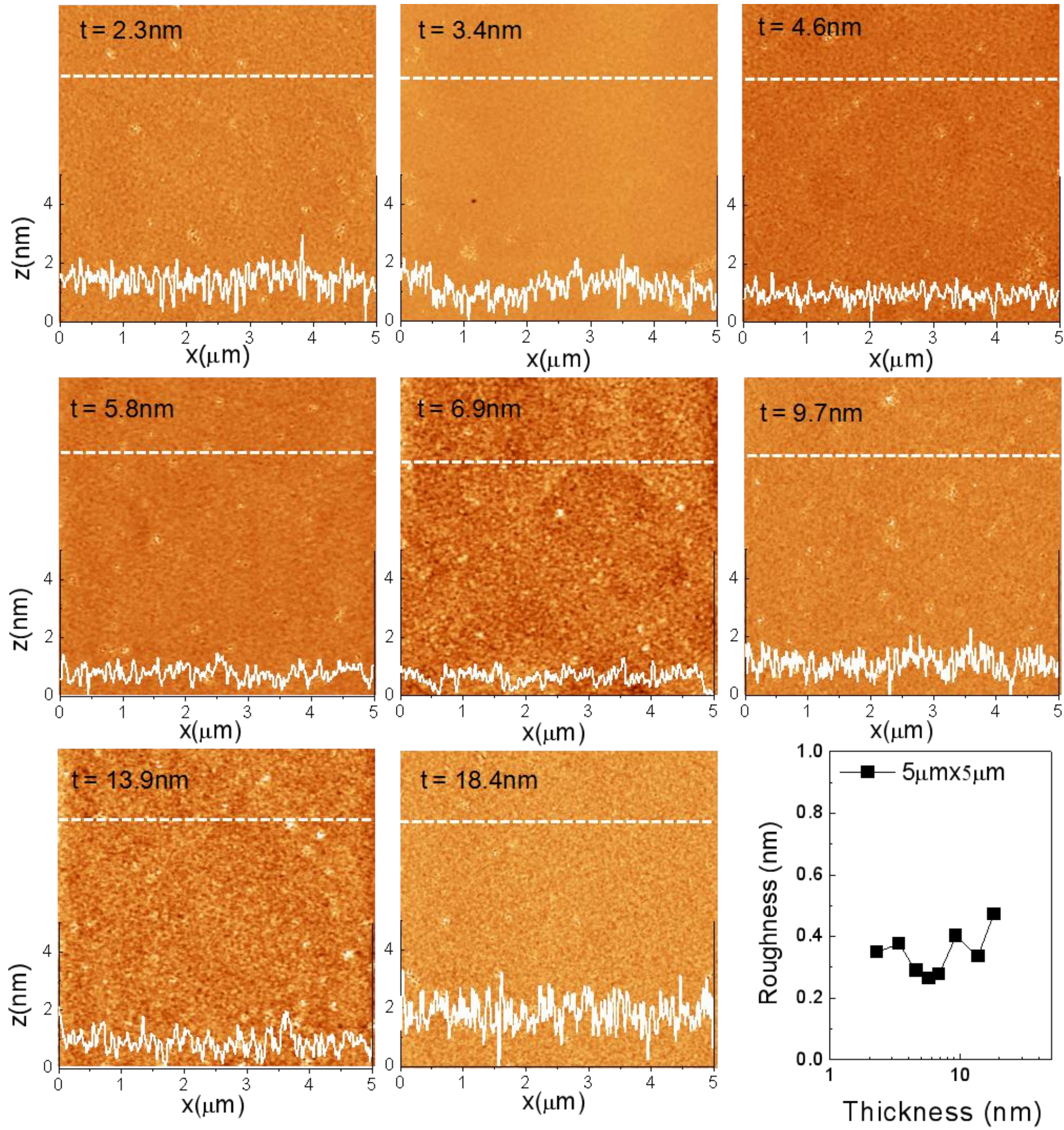


*Figure 5.2.4 AFM topographic 5 μm x 5 μm images of HZO films of varying the thickness (indicated in the top left of the corresponding image). A height profile along the marked horizontal line is shown in the bottom of each image. The dependence of root-mean-square (rms) on thickness is shown in the right bottom corner.*

## Electric characterization

### Ferroelectric polarization and leakage

Firstly, we note that when HZO is grown directly on the LNO electrode for the HZO/LNO/$CeO_2$/YSZ/Si(001) sample which does not present the orthorhombic (111) reflection in XRD $\theta$-$2\theta$ scans, the polarization versus voltage measurement does not show any signature of ferroelectricity as confirmed by the loops in Figure 5.2.5.

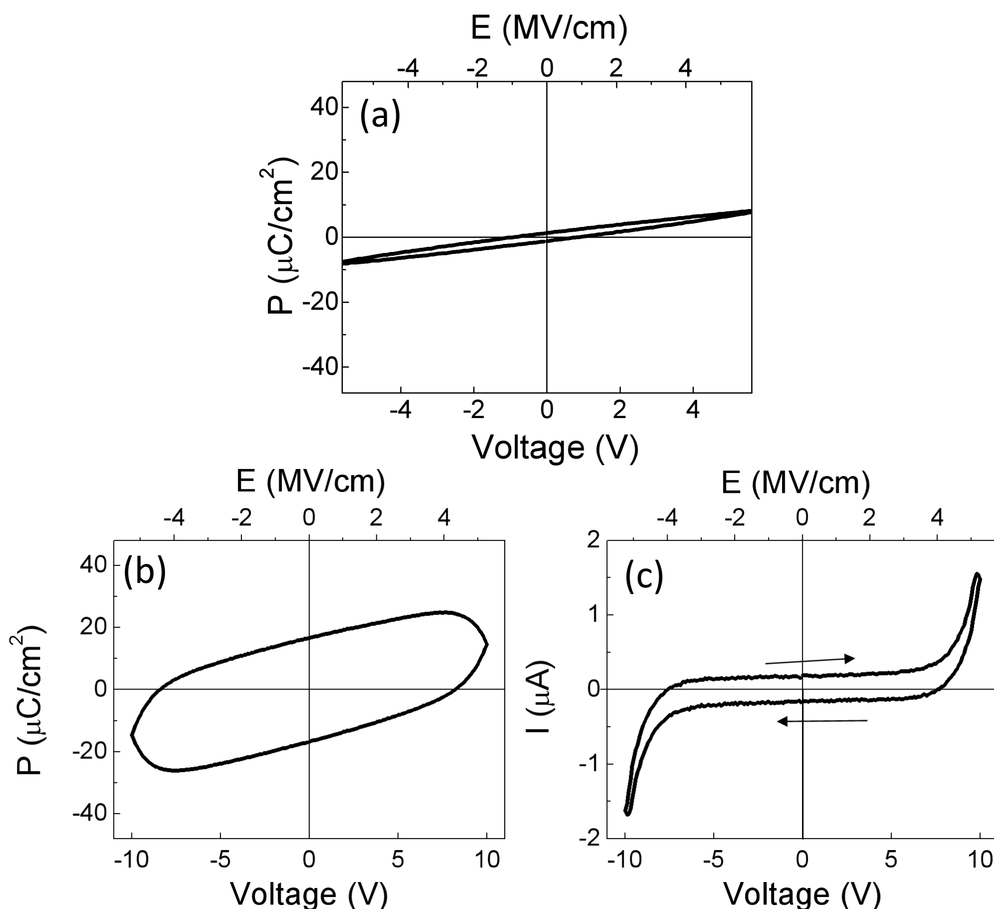


*Figure 5.2.5 (a) Polarization-voltage loop, obtained at 1 kHz without using the DLCC method, for the HZO/LNO/$CeO_2$/YSZ/Si(001) sample in top-bottom configuration. (b) and (c) P-V loop and corresponding I-V loop recorded at 1kHz in top-top configuration, respectively. Cigar-shape like P-V loop is observed without signature of ferroelectricity. Non-zero current in I-V loop at low voltage range corresponds to displacive current due to the dielectric nature of the film. Current increase near the maximum applied voltage is due to leakage.*

Ferroelectric characterization of the HZO/LSMO/LNO/$CeO_2$/YSZ/Si(001) samples at 9.7 nm thickness is shown in Figure 5.2.6. The polarization versus voltage loop recorded for the HZO film on LSMO (Figure 5.2.6a) shows a clear ferroelectric hysteresis loop. The remnant polarization is 18 μC/cm$^2$, and the average coercive voltage 3.2 V (3.3 MV/cm) with an imprint voltage displacing the loop by around 0.48 V (490 kV/cm) towards negative voltage. It signals the presence of an internal field pointing from top Pt towards bottom LSMO electrode. There is no need of wake-up electric cycling in pristine devices as observed in epitaxial HZO film on perovskite STO(001).[168] On the other hand, the presence of a large dielectric contribution is manifested by the substantial slope of the loop.[152,168,232,233] In Figure 5.2.6(a) we show (red curve) the compensated loop after removing the electric susceptibility contribution by linear subtraction of the constant slope (corresponding to $\varepsilon_r$ = 33) in the pristine loop. Even though the *DLCC* mode is applied during the

measurement, the pristine sample still show a small aperture at high electric field due to the leakage current.[236,237] The leakage compensation by exponential fitting at high voltage indicates an overestimation of $P_r$ about 1 μC/cm$^2$ as shown in Figure 5.2.6(b). The remnant polarization of 18 μC/cm$^2$ is comparable to the highest values for polycrystalline HZO films,[36,139] and is similar to that of epitaxial films on perovskite $SrTiO_3$(001) substrates of same thickness.

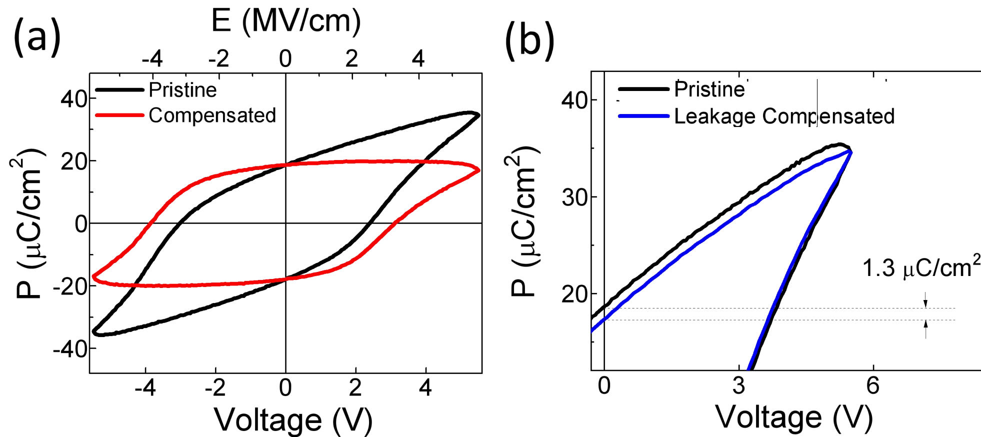


*Figure 5.2.6 (a) Ferroelectric hysteresis loop (black curve) at 1 kHz for the HZO (9.7 nm)/LSMO/LNO/$CeO_2$/YSZ/Si(001) sample and compensated loop (removing the electric susceptibility contribution of HZO) by subtraction of the linear slope. (b) Positive voltage side of leakage contribution compensation for the pristine loop. It can be inferred that the leakage contribution produces an overestimation of P of near 1.3 μC/cm$^2$.*

We clarify that the ferroelectric loops presented are saturated. As shown in Figure 5.2.7(a) and (b), the ferroelectric loops for 9.7 nm sample are measured by gradually increasing the voltage. It can be inferred that the loops measured at 5.3 and 5.5 V are very similar revealing that at 5.5 V the polarization is almost saturation. In Figure 5.2.7(c), it can be observed that the $P_r$ value is gradually increasing until saturation. Measurements performed at larger applied voltage result in dielectric breakdown.

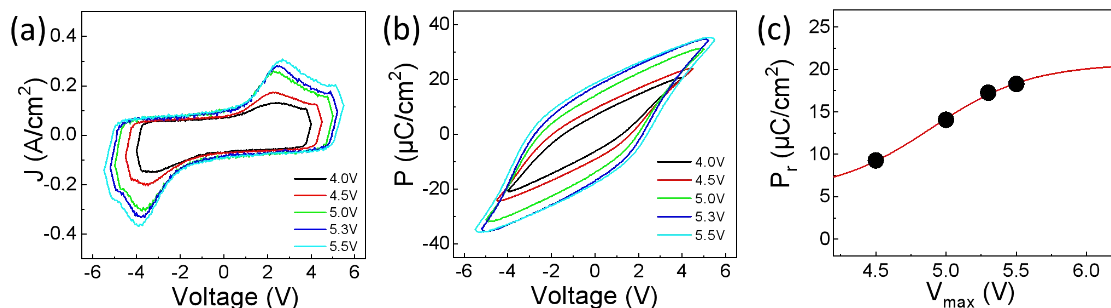


*Figure 5.2.7 (a) Current versus voltage hysteresis loops recorded at 1 kHz for increasing voltage*

*in the HZO(9.7 nm)/LSMO/LNO/$CeO_2$/YSZ/Si(001) sample. (b) Ferroelectric polarization versus voltage hysteresis loop recorded at 1 kHz measured for increasing voltage. (c) $P_r$ versus maximum applied voltage.*

With varying the thickness for the HZO/LSMO/LNO/$CeO_2$/YSZ/Si(001) samples, the films thicker than 4 nm are ferroelectric. The reliable polarization value was not extracted for thinner films (below 4 nm) due to the large leakage current contribution. And the hysteresis loops were measured with applying electric fields as large as possible, close to the breakdown fields. As shown in Figure 5.2.8(a)-(b), HZO film with t = 4.6 nm presents the largest $P_r$ around 33 μC/cm$^2$, and the polarization decreases as increasing the thickness. The coercive voltage $V_c$ increases with thickness as shown in 5.2.8(c) right axis. And the linear fitting of logarithmic relationship between the corresponding electric field and thickness is in the left axis. The slope $k$ is -0.64, which is in agreement with the scaling value of -2/3.[224] And this result is consistent with the one of epitaxial HZO films on STO(001).

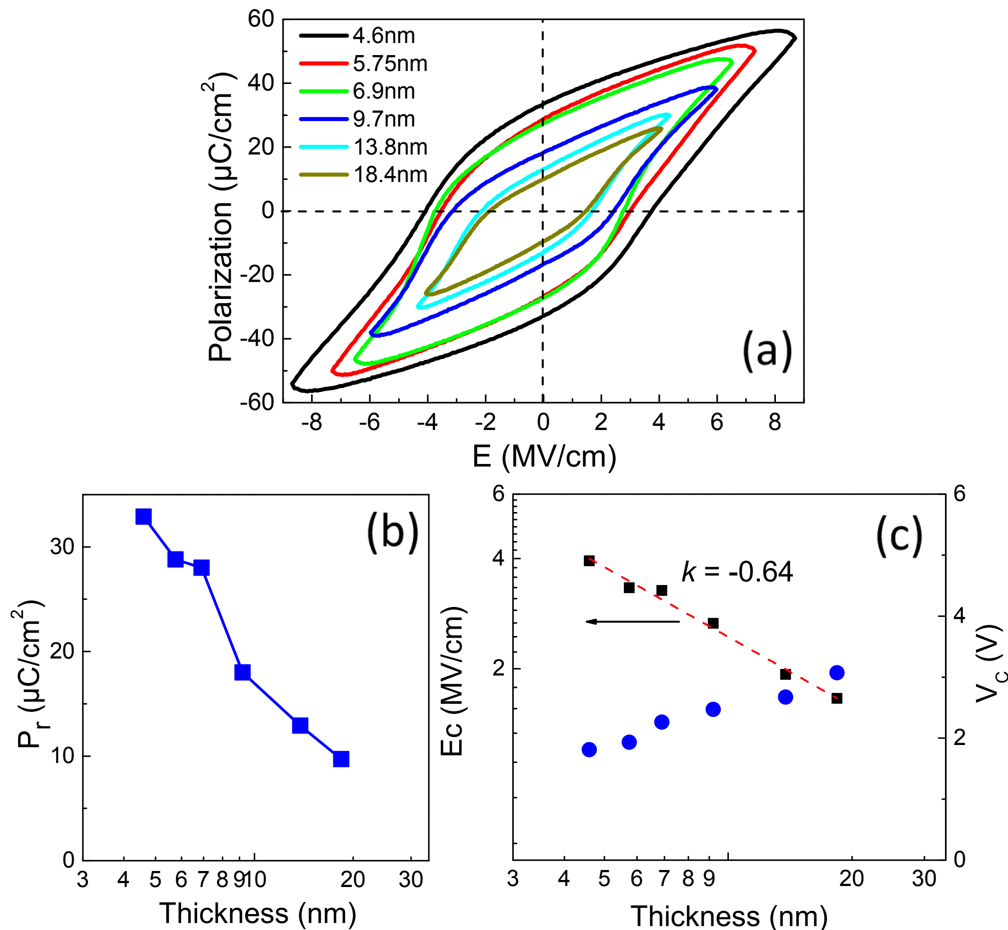


*Figure 5.2.8 (a) Polarization — electric field loops for the samples with each thickness. (b) Dependence of $P_r$ on thickness. (c) Dependences of $E_c$ (black squares) and $V_c$ (blue circles) on thickness. The red dashed line is a linear fit with a slope of -0.64, compatible with $E_c$ - $t^{-2/3}$ scaling.*

The leakage curves of HZO films on Si with different thicknesses are shown in Figure 5.2.9(a). Leakage is decreasing as the film thickness increases. Figures 5.2.9(b) shows the leakage current at several electric fields plotted as a function of thickness. Here, with reducing thickness from 18.4 nm to 4.6 nm, the leakage increases around one order of magnitude.

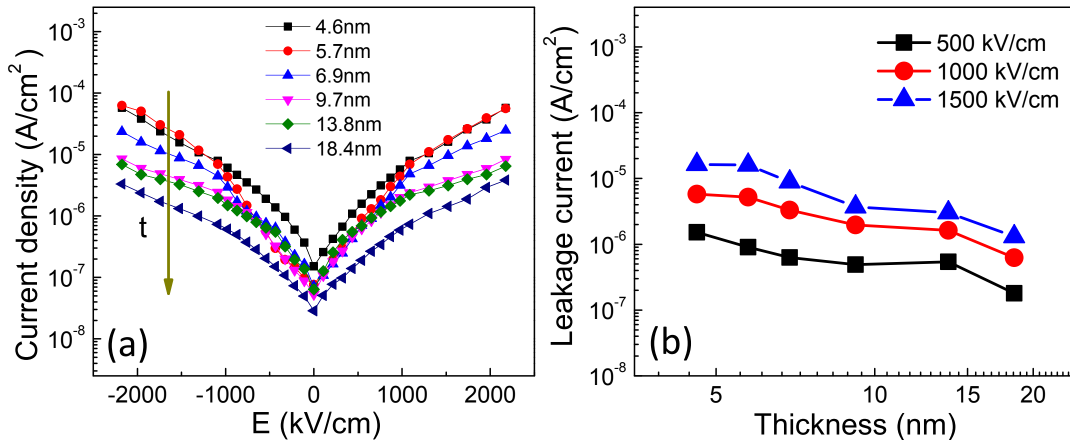


*Figure 5.2.9 (a) Current leakage density vs electric field characteristics for the HZO/LSMO/LNO/$CeO_2$/YSZ/Si(001) sample with thickness ranging from 4.6 nm to 18.4 nm. (d) Leakage current at the indicated electric fields as a function of thickness. The inset is a sketch for the crystal boundaries created by the in-plane variations.*

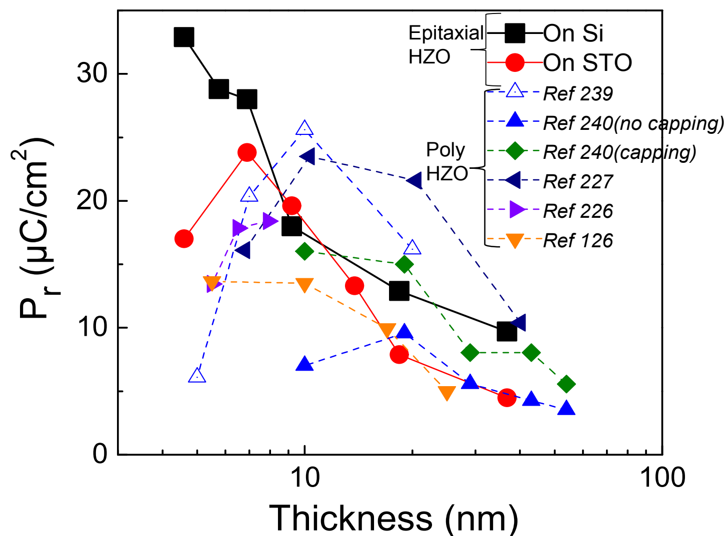


*Figure 5.2.10 Remnant polarization of $Hr_{0.5}Zr_{0.5}O_2$ films as a function of thickness. Black solid squares correspond to the epitaxial films reported here (thickness series). Other symbols (see label in Figure) correspond to polycrystalline $Hr_{0.5}Zr_{0.5}O_2$ films reported in the indicated references.*

The thickness dependence of remnant polarization reported for polycrystalline $Hf_{0.5}Zr_{0.5}O_2$ films is compared to the dependence of our epitaxial HZO films on

Si(001) and STO(001) substrates in Figure 5.2.10. Remarkably, the thickness for the largest $P_r$ is shifted from above 10 nm in polycrystalline HZO films to around 7 nm on STO(001) and below 5 nm on Si(001) in epitaxial films. Particularly, the 4.6 nm-thick epitaxial HZO film on Si(001) shows a larger maximum of polarization than the polycrystalline HZO ones with similar thickness. This progress provides the potential for memory devices requiring ultrathin layers such as ferroelectric tunnel junctions.

**Dielectric measurement**

The dielectric measurement for the HZO/LSMO/LNO/$CeO_2$/YSZ/Si(001) samples with different thicknesses was performed as shown in Figure 5.2.11. Dielectric permittivity versus voltage loops show butterfly-like shape in all the thickness films, indicating the ferroelectric nature of HZO film. The permittivity value $\varepsilon_r$ is decreasing from around 36 to below 28 with the thickness increasing, presenting the similar dependence of dielectric constant with thickness of epitaxial HZO films on STO(001) as discussed before.

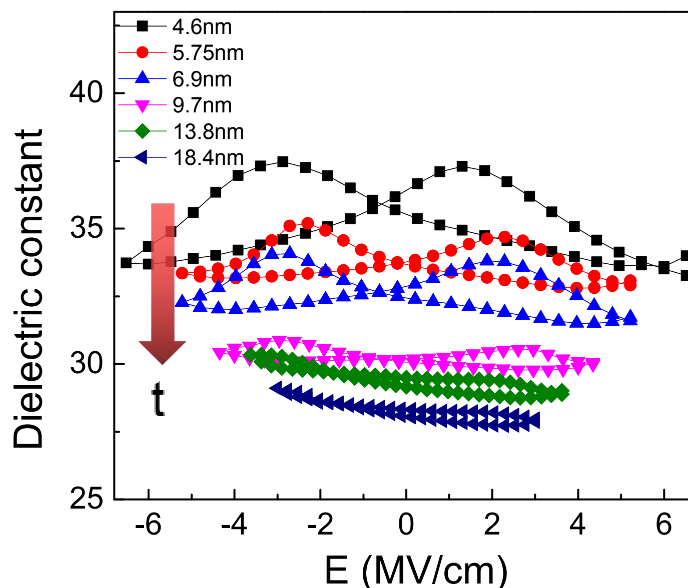


*Figure 5.2.11 Dielectric permittivity versus applied voltage loops for the HZO/LSMO/LNO/$CeO_2$/YSZ/Si(001) samples with each thickness measured at 50 kHz.*

**Endurance**

Endurance characterization of the 9.7 nm-thick sample is summarized in Figure 5.2.12. Polarization loops collected either in the pristine state and after cycling the sample for $10^3$ and $10^5$ times using an applied voltage of 5.0 V are shown in Figure 5.2.12(a). When the cycling number exceeds $10^5$ cycles at 5.0 V, dielectric rupture occurs. The

dielectric rupture is delayed up to $10^8$ cycles when reducing the switching voltage (4.5 V) is used as shown in Figure 5.2.12(b). If switching voltage is further decreased (4.0 V) ruptures does not occur in the explored cycling range (Figure 5.2.12c); however remnant polarization is smaller and the polarization window is reduced to $2P_r$ = 3 μC/cm$^2$ after $10^9$ cycles. Figure 5.2.12(d) summarizes the effect of electric cycling on the remnant polarization normalized to its initial value ($P_0$) with the $2P_r$ value at different cycles in the inset. These data show that the polarization fatigue effect is independent of the maximum applied voltage and thus only caused by ferroelectric switching. Therefore, the maximum applied voltage determines the dielectric rupture but not the polarization reduction, which is similar to the behavior observed in HZO films on STO(001).

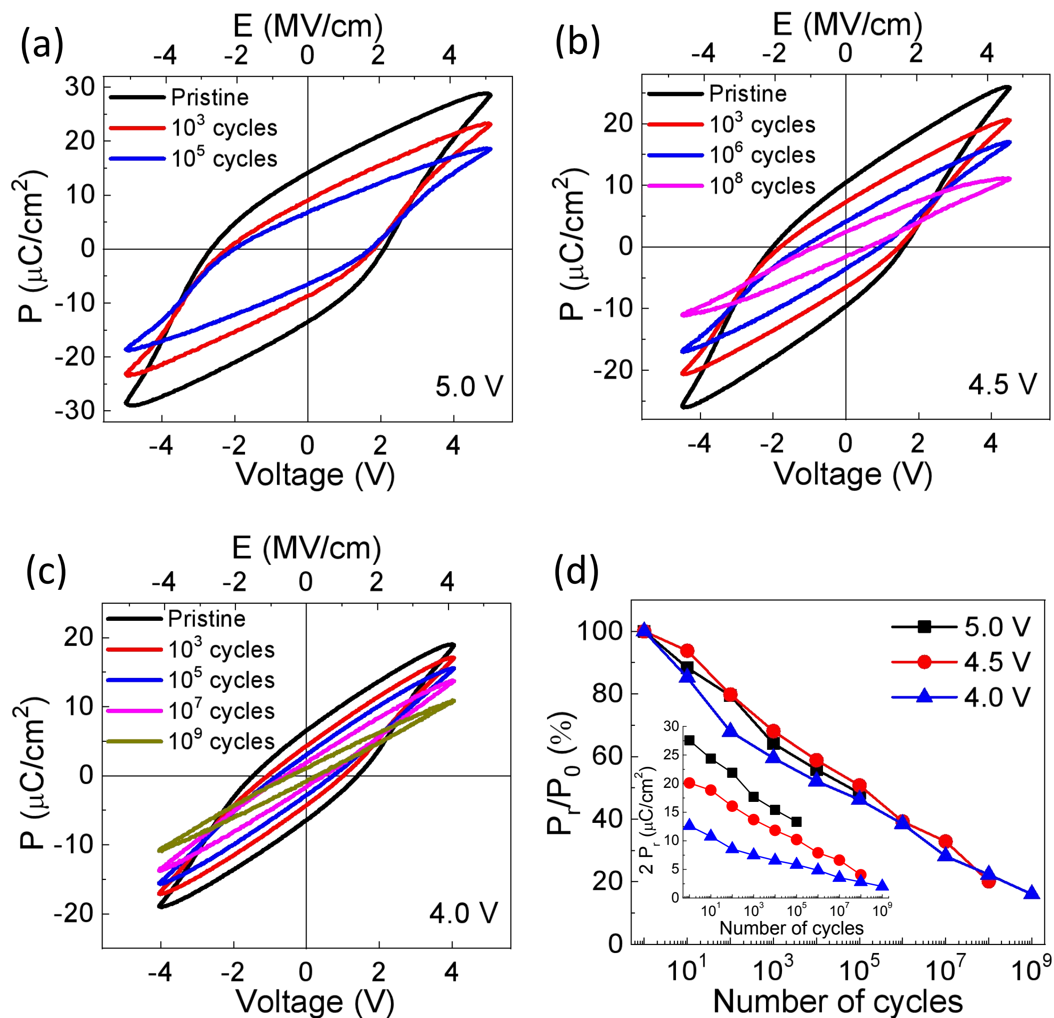


*Figure 5.2.12 (a-c) Polarization vs voltage loops measured for the pristine state and after the indicated number of electrical cycles of 5.0, 4.5, and 4.0 V at 10 kHz, respectively. (d) Summary of the remnant polarization (positive and negative average values) normalized to its initial value ($P_0$) obtained in (a-c) vs cycling number for the different maximum applied voltage. Inset: $2P_r$ value vs cycling number at three different voltage.*

Leakage current curves with cycles for 9.7 nm sample are shown in Figure 5.2.13. The leakage can be an important factor causing fatigue, so to further investigate the endurance, leakage current density measurements were performed after different cycling number as shown in Figures 5.2.13(a)-(c) for maximum applied voltage of 5.0, 4.5 and 4.0 V, respectively. It can be observed that leakage current remains almost constant up to $10^4$, $10^6$, $10^6$ cycles for maximum applied voltage of 5.0, 4.5 and 4.0 V, respectively. Afterwards, the leakage current suddenly increases (marked by an arrow). This effect can be clearly inferred in Figure 5.2.13(d), where the leakage current at 300 kV/cm is plotted as a function of cycling number. It is observed that the leakage increases significantly after $10^4$ cycles at 5.0 V and after $10^7$ cycles at 4.5 or 4.0 V.

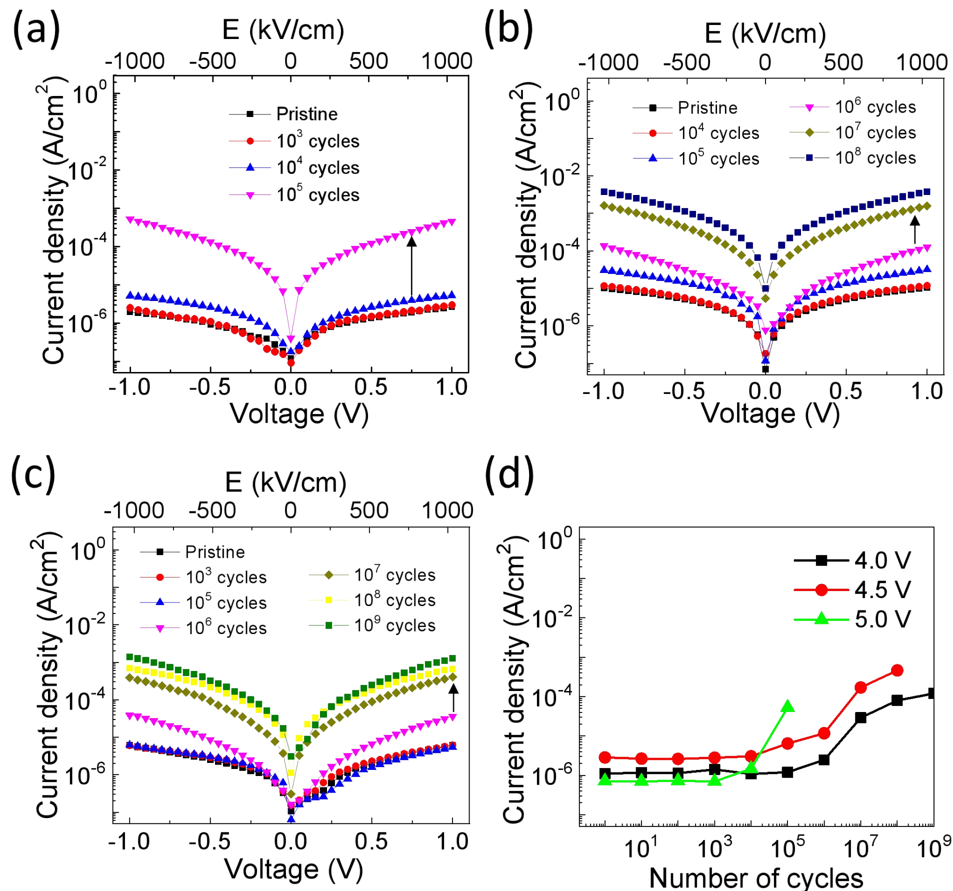


*Figure 5.2.13 (a)-(c) Current leakage density vs electric field characteristics of the pristine state and after the indicated number of bipolar cycles at 5.0, 4.5, and 4.0 V, respectively. (d) Current leakage density evaluated at 300 kV/cm vs the number of bipolar cycles of indicated amplitude.*

The film thickness also has a critical influence on the endurance for the HZO/LSMO/LNO/$CeO_2$/YSZ/Si(001) samples. Figure 5.2.14 shows the switching endurance properties of HZO films with thickness 4.6 nm, 9.7 nm and 18.4 nm. The 4.6 nm film shows a robust endurance up to $10^9$ and $10^{10}$ cycles at 3.5 V (7.61 MV/cm) and 3.0 V (6.52 MV/cm) and large memory window of the $2P_r$ around 21 $\mu C/cm^2$ and

11 μC/cm$^2$ remained before breakdown, respectively. Also, it is remarkable that the 4.6 nm sample measured at 2.5 V (5.43 MV/cm) cycles can last to until $10^{11}$ cycles without breakdown, keeping large memory window of $2P_r$ around 6 μC/cm$^2$. The dielectric breaks down for 9.7 nm HZO capacitor happens at $10^5$ cycles and 5 x $10^8$ cycles under 5.0 V (5.43 MV/cm) and 4.5 V (4.9 MV/cm) cycling voltage, which shows the earlier breakdown and degraded endurance compared with the one of 4.6 nm as shown in Figure 5.2.14(b). At 4 V cycling voltage, the endurance can last to 5 x $10^9$ cycles with memory window $2P_r$ around 2 μC/cm$^2$ without dielectric breakdown. This value is too small to apply an accurate measurement for the device. The 18.4 nm HZO film (Figure 5.2.14c) shows much more deteriorated endurance. Under 6 V (3.26 MV/cm) switching voltage, $2P_r$ drops from initial 13 μC/cm$^2$ to below 2 μC/cm$^2$ within only $10^6$ cycles despite the fact of no dielectric breakdown. Figure 5.2.14(d) shows the representative P-V loops and corresponding permittivity measurement after different number of cycles under 3 V for the 4.6 nm HZO film. The pristine film has the largest polarization and permittivity (no wake up effects observed). The memory window decrease with cycles from $2P_r$ about 35 μC/cm$^2$ at beginning to around 18 μC/cm$^2$ after $10^8$ cycles along with progressive decreasing of the permittivity.

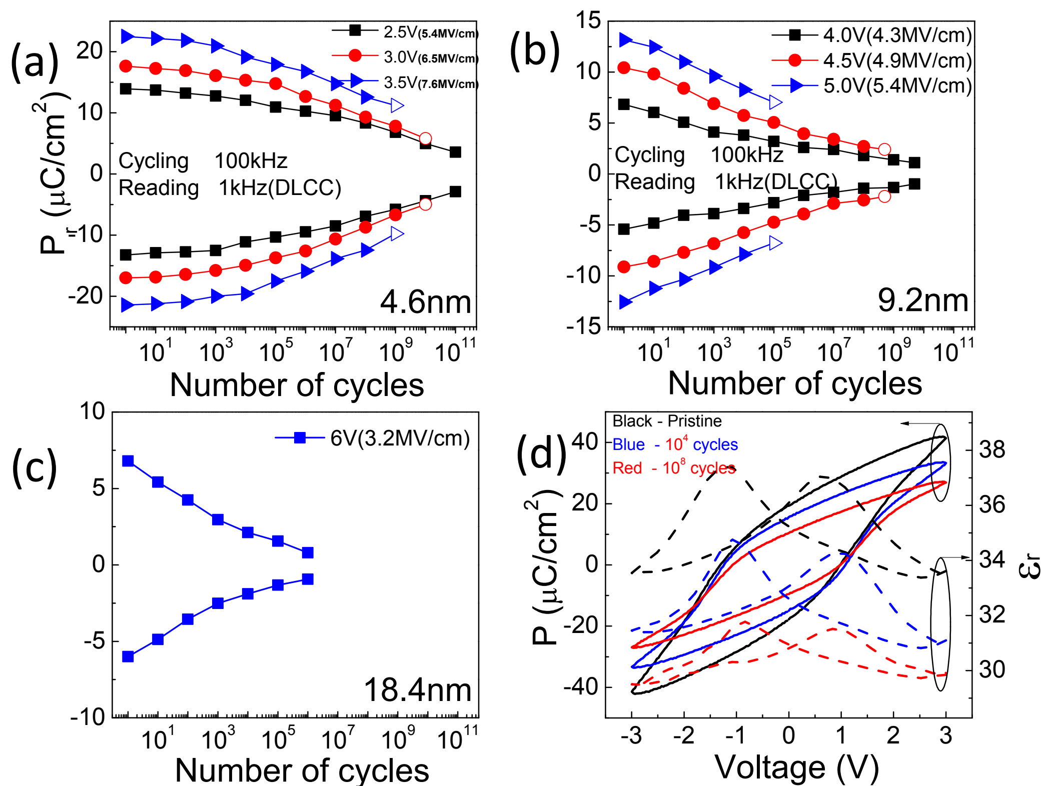


*Figure 5.2.14 Endurance characteristics of HZO films on Si with thickness (a) 4.6 nm (b) 9.7 nm and (c) 18.4 nm. (Open shape symbols indicate that dielectric breakdown occurred at corresponding number of cycles; Solid shape symbols mean that the capacitor did not break. In these cases, the measurement was stopped due to either the longer measurement time or the low polarization ($2P_r$ below 2 μC/cm$^2$). (d) Polarization —voltage loops (solid line) and corresponding*

*relative permitivity $\varepsilon_r$ loops (dashed line) for 4.6 nm thick sample at pristine state and after $10^4$ cycles and $10^8$ cycles.*

The impact of the thickness on the endurance－applied field dependence is presented in Figure 5.2.15(a). As it was observed in HZO films on STO (001), thinner films present better endurance with higher electric field while the thicker one last lower number of cycles and breakdown at lower fields. Further quantification of the endurance difference with thickness are shown in Figure 5.2.15(b). For the different thickness, $P_r$ of thinner HZO films degrade much slower with increasing number of applied cycles than that of thicker films.

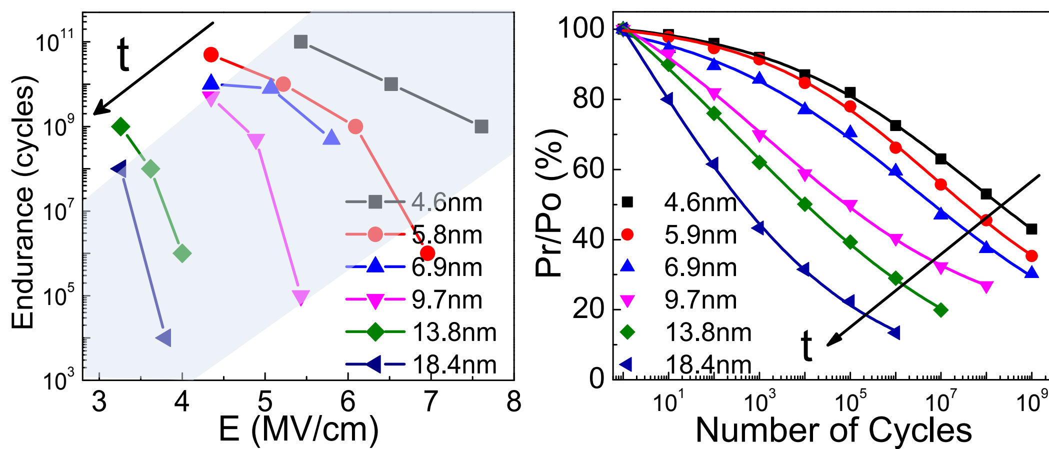


*Figure 5.2.15 (a) Endurance as a function of the applied electric field for the series of samples with varied HZO thicknesses. (b) Remnant polarization (positive and negative average values) normalized to its initial value ($P_0$) for the series of samples.*

The pole figure with 2D detector for films with t = 6.9 nm, 13.9 nm and 18.4 nm are shown in Figure 5.2.16. In the t = 6.9 nm film, the monoclinic phase is difficult to be detected. When the t increases to 13.9 nm and 18.4 nm, the monoclinic phase in film is getting increasing as indicated from the growing and elongated intensity of the (002) and (-111) reflections of m-phase. The increased amount of m-phase with thickness can be responsible for the degraded endurance of HZO films.

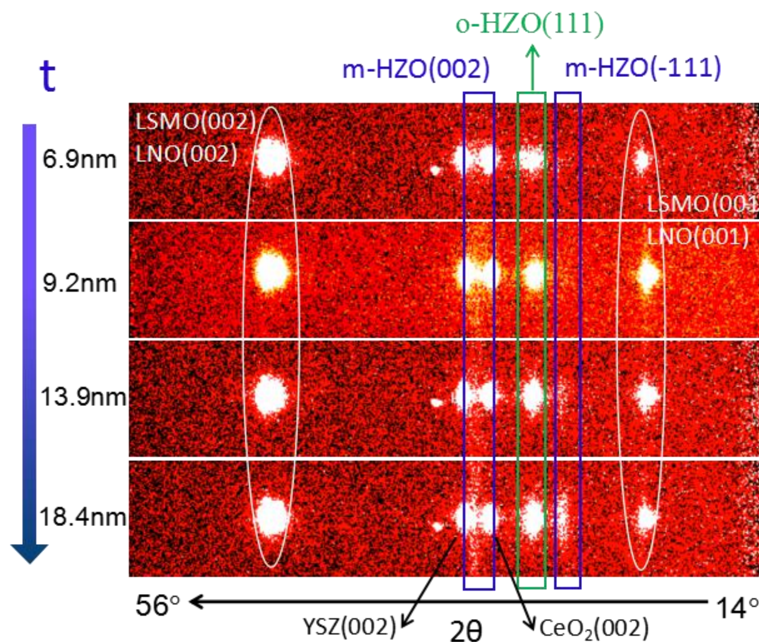


*Figure 5.2.16 XRD 2θ-χ frames with χ ranging about ± 5° of t = 6.9 nm, 9.2 nm, 13.9 nm and 18.4 nm films.*

The excellent endurance property of the thinner films is accompanied by stable leakage, without increasing with field cycles (Figure 5.2.17). Since increased leakage is the reason of capacitor degradation causing breakdown, the stable leakage in the t = 4.6 nm film is responsible for its huge endurance.

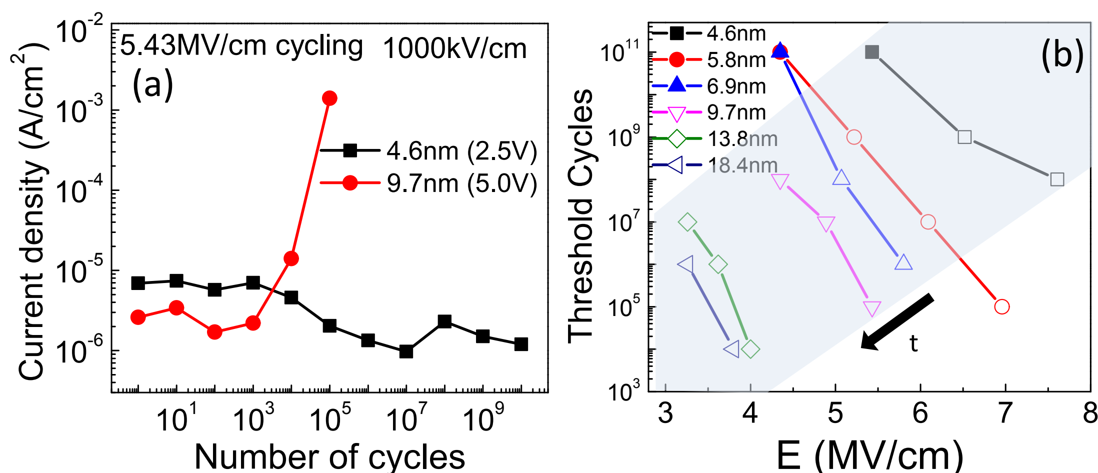


*Figure 5.2.17 (a) Leakage current at 1000 kV/cm as a function of the number of applied field cycles of 5.43 MV/cm for t = 4.6 nm and t = 9.7 nm samples. (b) Threshold of number of cycles before leakage increasing sharply as a function of electric field for each thickness. (Solid symbols indicate the leakage increase was not observed.)*

The thickness-dependent endurance behaviour was similar in HZO/LSMO/STO(001) samples. Here, both series of epitaxial HZO films on Si(001) and STO(001) substrate will be compared. Endurance of HZO on Si is larger than on STO with identical thickness at same electric field as shown in Figure 5.2.18 (a). As shown in Figure 5.2.18 (b), at 4.0 V and 3.5 V cycling voltage, the 6.9 nm-thick HZO film on Si(001) can last to around $10^9$ and $10^{10}$ cycles before breakdown, respectively. While for HZO on STO, the endurance is about $10^8$ and $10^9$ cycles at corresponding cycling voltages, by almost one order of magnitude lower than on Si substrate. The reason can be attributed to the earlier leakage increase with cycling. At 4.0 V and 3.5 V cycling voltage, leakage increase of HZO films happened in $10^6$ and $10^9$ cycles on Si substrate while at $10^4$ and $10^5$ cycles on STO(001), respectively. On the other hand, at 3.0 V cycling voltage, both films do not show breakdown under the measured $10^{10}$ cycles. However, the leakage value of HZO on Si(001) keeps constant at the measured $10^{10}$ cycles, while the leakage started rising at $10^9$ cycles on STO(001). The underlying reason for the leakage rising at different cycles on Si and STO substrates may be related to a large amount of the defects in the films on STO(001).

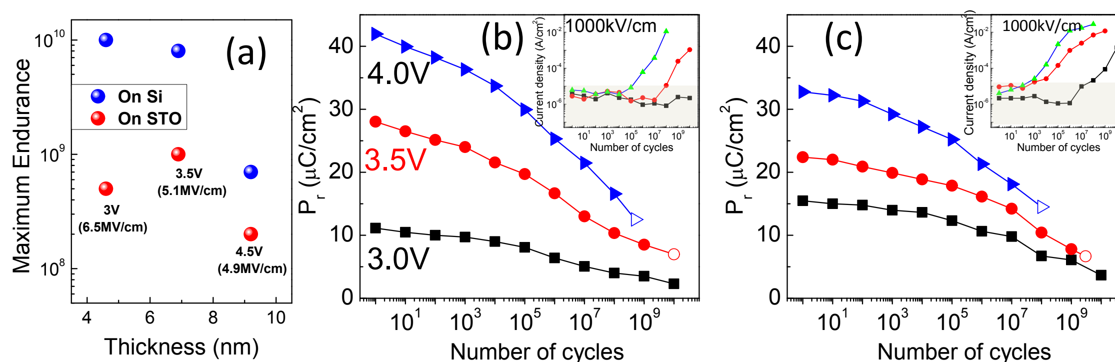


*Figure 5.2.18 (a) Endurance as a function of thickness for 4.6 nm, 6.9 nm and 9.7 nm HZO films on STO(001) and Si(001) under the corresponding same voltage (electric field). Remnant polarization versus number of cycles for 6.9 nm samples (b) on Si(001) and (c) STO(001) at 4.0 V, 3.5 V and 3.0 V. Inset: Evolution of leakage current, at 1000 kV/cm, with number of applied cycles.*

## Retention

Retention experiments for the 9.7 nm sample are shown in Figure 5.2.19 for several applied poling voltages. It can be observed that if polarization is settled by voltage pulses of 5.0 and 5.5 V, extrapolated data safely overpasses 10 years retention. A high polarization window of $2P_r$ around 14 μC/cm$^2$ is extrapolated 10 years after 5.5 V poling. The experiments performed at 4.5 V and 4.0 V show that retention reaches 10 and 1 year, respectively.

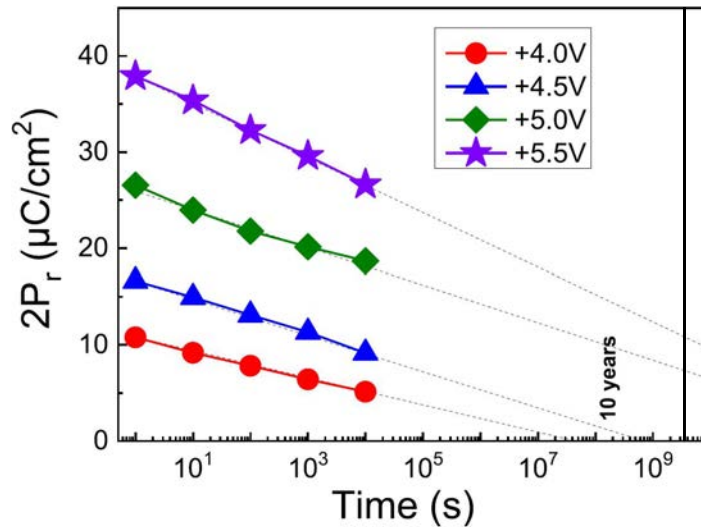


*Figure 5.2.19 Ferroelectric retention ($2P_r$) after poling the film (9.7nm) with voltage pulses of the indicated amplitude. Reading voltage was the same as that used for writing. Dashed lines are guides to the eye. Vertical solid line indicates time of 10 years.*

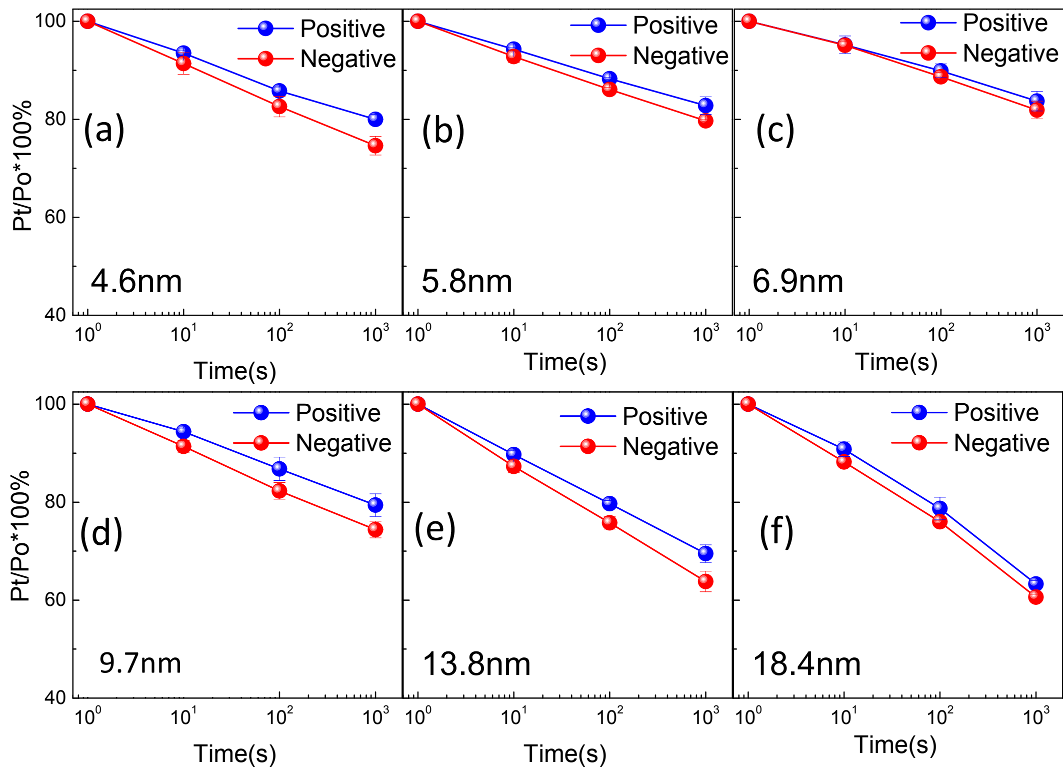


*Figure 5.2.20 (a)-(f) Retention of ferroelectric polarization of the epitaxial HZO film on Si (001) substrate poled positively and negatively for film thickness at 4.6 nm, 5.8 nm, 6.9 nm, 9.7 nm, 13.8 nm and 18.4 nm, respectively. Note: the poling field used for retention of samples with different thicknesses is as same as the electric field for P-E loops recorded in Figure 5.2.8 (a).*

The normalized retention of HZO films on Si(001) with varying the thickness is shown in Figure 5.2.20. The retention values for all the thickness within 1000 seconds are obtained at writing and reading electric fields used in hysteresis loops measurements as in Figure 5.2.8(a). Different from the HZO films on STO with varying the thickness, the retention of positive polarization is favored in all the thickness range for HZO films on Si(001). This difference may be caused by the defects in the sample on Si.

The retention degradation rates by linear fitting in all thickness samples are shown in Figure 5.2.21. Due to the downward imprint field as sketched inset of Figure 5.2.21, the positive $P_r$ has better retention than the negative $P_r$ for all the samples. The smallest slope value happens at 6.9 nm thick sample, signaling the longer retention in this sample. The reason is likely the increasing depolarization field as thickness is reduced due to the increased dielectric dielectric permittivity $\varepsilon_r$ and leakage current in thinner film. As thickness increases, the imprint field does not present large deviation (Figure 5.2.21b). On the other hand, comparing with the retention of samples on STO(001), the sample at similar thickness on Si(001) presents better retention. For instance, retention degradation value *k* for sample at 6.9 nm thick on Si is around 5, lower than that of 6.9 nm sample on STO with value around 11, which indicates a better retention of films on Si. Therefore, the optimized sample can be the HZO film on Si(001) with 6.9 nm showing good endurance (over $10^{10}$ cycles with stable low leakage) and long retention time (over 10 years). The films, epitaxially grown on oxide LSMO electrodes, offer opportunities to develop devices like ferroelectric tunnel junctions requiring high homogeneity and accurate control of the interfaces.

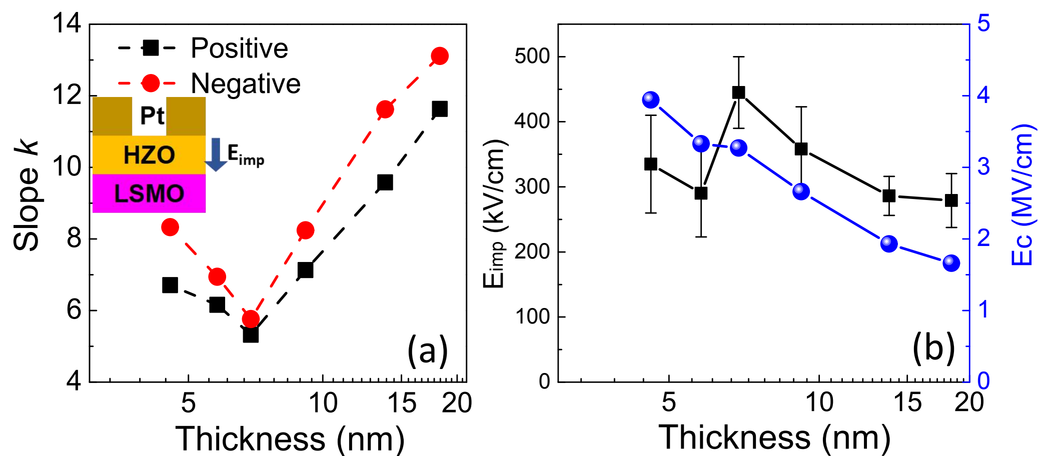


*Figure 5.2.21 (a) Retention degradation value k as a function of film thickness of HZO on Si. Inset: the sketch indicating the imprint direction. (b) The dependence of imprint field and coercive field on the HZO film thickness.*

### 5.2.2 Ferroelectric $Hf_{0.5}Zr_{0.5}O_2$ capacitor epitaxially integrated on $La_{2/3}Sr_{1/3}MnO_3/SrTiO_3/Si(001)$ structure

#### Growth conditions

The epitaxial $SrTiO_3$ template of thickness t = 26 nm thick was deposited by solid-source molecular beam epitaxy (MBE) on a Si(001) wafer[3]. Bottom LSMO electrodes (t = 25 nm) and HZO films were grown on the $SrTiO_3$ template by PLD. The sketch of the sample is shown in Figure 5.2.22. The LSMO bottom electrode was deposited at 5 Hz repetition rate, substrate temperature $T_s$ = 675 °C, and dynamic oxygen pressure $P_{O2}$ = 0.1 mbar. HZO was deposited at 2 Hz laser frequency, $T_s$ = 800 °C, and $P_{O2}$ = 0.1 mbar. The films were cooled down under $P_{O2}$ = 0.2 mbar.

*Figure 5.2.22 The sketch of heterostructure for HZO films on Si(001) using $SrTiO_3$ templates.*

#### Structural study

The XRD $\theta$-$2\theta$ scan in Figure 5.2.23(a) shows (00*l*) reflections corresponding to the Si wafer, the STO buffer layer and the LSMO electrode. The (111) reflection of orthorhombic HZO (o-HZO), at 2θ around 30°, is accompanied by the small o-HZO(222) peak at around 63°, and no other orientation or phase is observed. The zoomed region in the inset shows the o-HZO(111) peak at 2θ = 30.4° and low intensity Laue interference fringes indicating rather good crystalline and flat interface quality. The thickness of HZO film was determined by fitting the Laue fringes according to the equation (5-1). The red curve has been simulated considering a thickness of 76.5 Å (N = 26 and $c$ = 2.942 Å), being the corresponding Bragg reflection located at $2\theta$ = 30.382°.

[3] Deposition and structural characterization of $SrTiO_3$ template on Si wafer by solid-source molecular beam epitaxy (MBE) were done by Romain Bachelet and Guillaume Saint-Girons at Institut des Nanotechnologies de Lyon (INL-CNRS). Details are reported elsewhere [*Applied Physics Letter, 114, 222901*].

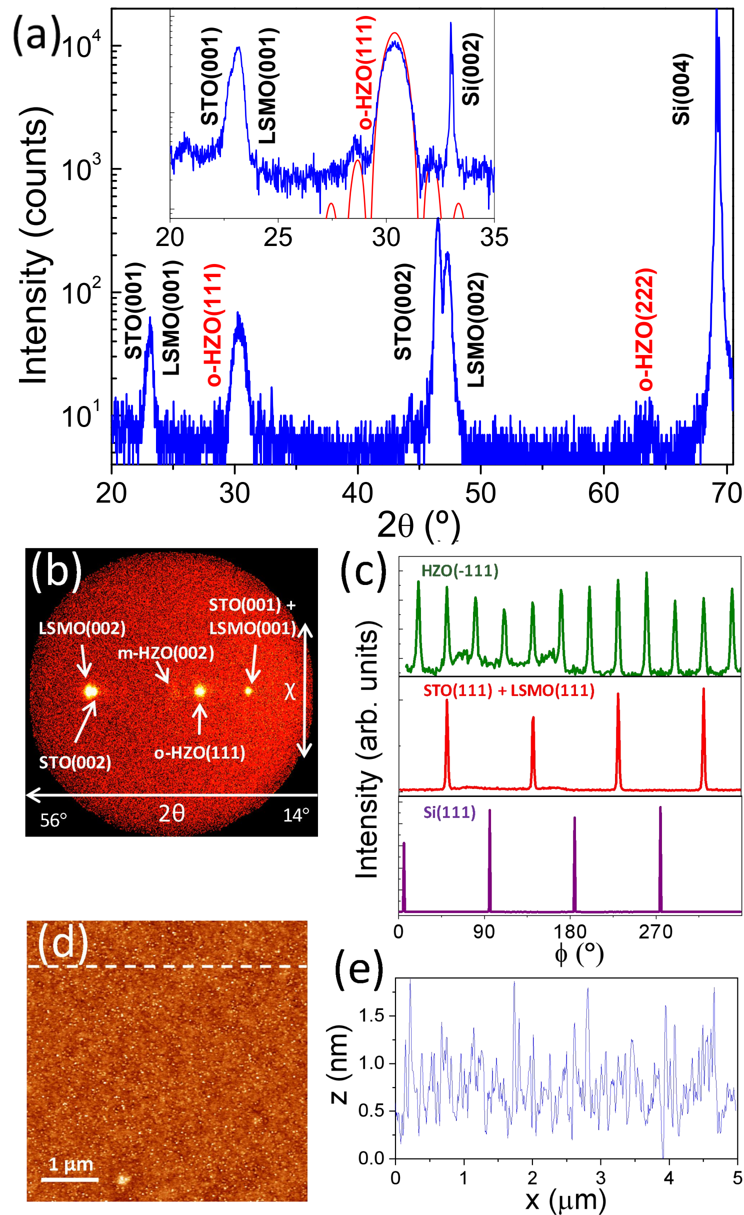


*Figure 5.2.23 (a) XRD θ-2θ scan of the HZO/LSMO/STO/Si(001) sample. Inset: zoom in the 2θ = 20 - 35° range with 2 seconds acquisition time. The red line is the simulation of Laue fringes around the o-HZO(111) peak. (b) XRD 2θ-χ frame around χ = 0°. (c) XRD ϕ-scans around asymmetrical o-HZO(-111), LSMO and STO (111), and Si(111) reflections. (d) AFM topographic 5 µm x 5 µm images and (e) a height profile along the horizontal marked line in (d).*

The out-of-plane interplanar spacing, $d_{o\text{-}HZO(111)}$ = 2.942 Å, is smaller to that of equivalent HZO films on LSMO/STO(001) ($d$ = 2.963 Å), but similar to the one on Si with YSZ as template ($d$ = 2.948 Å) at similar thickness. On the other hand, the XRD $2\theta$-$\chi$ frame (Figure 5.2.23b) shows (001) and (002) reflections of the LSMO and STO layers, and a bright spot corresponding to the o-HZO(111) reflection, whereas the

(002) reflection of the monoclinic HZO (m-HZO) phase is barely visible at $2\theta$ around 35°. The narrow intensity distribution of the o-HZO(111) spot along $\chi$ is a signature of highly oriented growth, suggesting that the film is epitaxial. This was confirmed by $\phi$-scans around asymmetrical reflections (Figure 5.2.23c). The four (111) reflections of LSMO and STO at 45° of the Si(111) ones signal in-plane rotation of 45° of both layers respect to the Si(001) wafer. The $\phi$-scan around o-HZO(-111) shows four set of three peaks, the 12 peaks being 30° apart. The $\phi$-scans indicate [1-10]HZO(111) /[1-10]LSMO(001)/[1-10]STO(001)/[100]Si(001) epitaxial relationship and the presence of four HZO crystal domain with in-plane rotation of 90°, the same type domains as it was observed in HZO films on $SrTiO_3$(001) single crystalline substrates and Si substrate with YSZ as template. The topographic AFM image of this sample is shown in Figure 5.2.23(d) with a height profile along the marked horizontal line in Figure 5.2.23(e). The surface is flat, with root mean square (rms) roughness of 0.35 nm in the 5 µm x 5 µm scanned area. There are some small islands with height up to a few nm, but in most of the topographic image height variations are below 1 nm.

## Electrical characterization

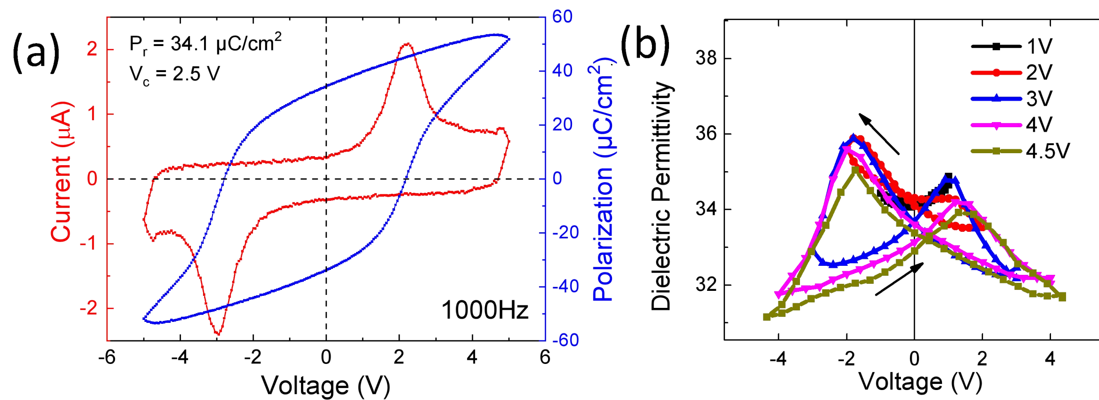


*Figure 5.2.24 (a) Ferroelectric polarization loop (in blue, right-axis) and current-voltage (in red, left-axis) curve. (b) Dielectric permittivity versus applied voltage loops performed at different maximum applied voltages.*

The ferroelectric polarization loop of a Pt/HZO/LSMO/STO/Si(001) capacitor with current-voltage curve in Figure 5.2.24(a) shows a large remnant polarization around 34 µC/cm² with high amplitude ferroelectric switching current peaks. It is significantly larger than the $P_r$ value of around 20 - 24 µC/cm² reached in epitaxial HZO(111) films of similar thickness on LSMO/STO(001) and also higher than the $P_r$ value of 20 - 28 µC/cm² for HZO films on Si with YSZ as template. The polarization loop also evidences an imprint voltage towards the negative axis. The imprint voltage of around 0.4 V corresponds to an internal field of around 430 kV/cm pointing

towards the bottom LSMO electrode. Dielectric permittivity versus voltage loops in Figure 5.2.24(b) show the butterfly-like shape associated with the ferroelectric nature of the material. The $\varepsilon_r$ value of HZO film with about 8 nm thick on STO buffered Si(001) is 32, extracted from the maximum electric field region. This value is comparable to the $\varepsilon_r$ value of 30.2 - 32.5 for films on YSZ buffered Si or the one of 29.3 - 31 for films on single crystal STO(001) as achieved before. Also, comparable permittivity values and shape have been reported on polycrystalline films.[242,243]

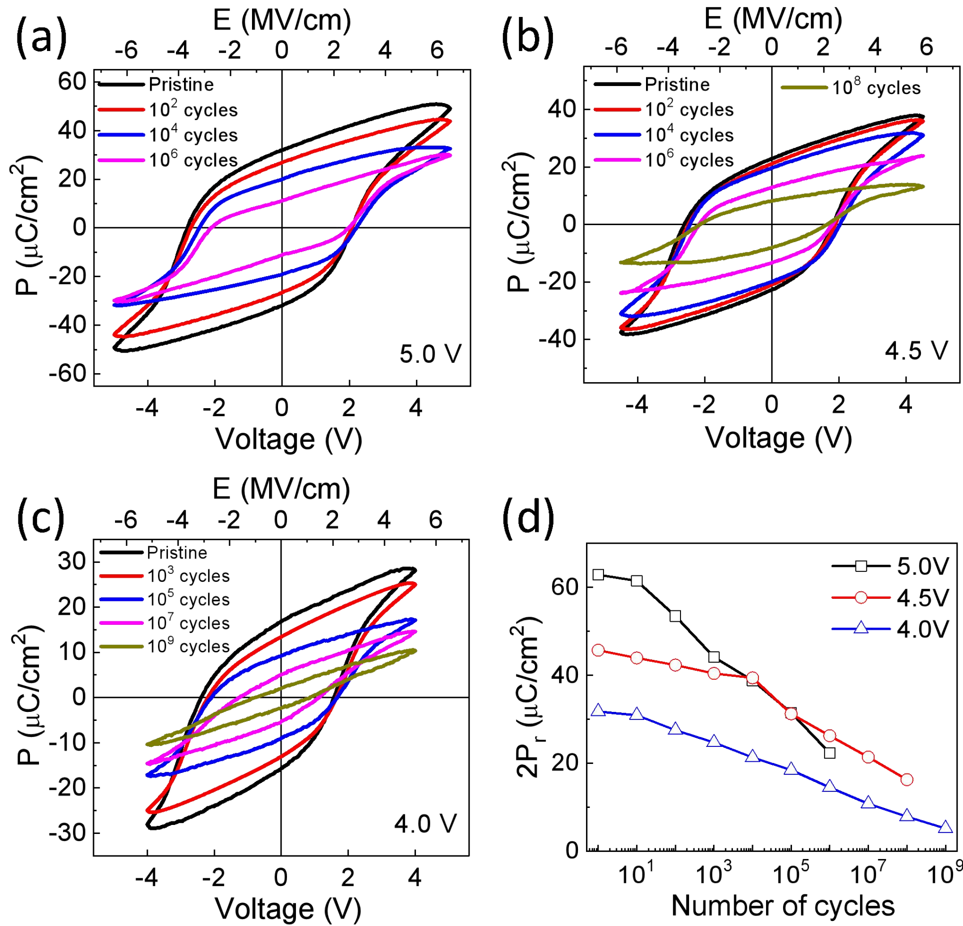


*Figure 5.2.25 Ferroelectric polarization loops measured at maximum voltage of (a) 5 V, (b) 4.5 V, and (c) 5 V in pristine state and after bipolar switching with the number of cycles indicated in each label. (d) Ferroelectric memory window ($2P_r$) as a function of applied number of cycles at 5 V, 4.5 V and 4 V.*

The evolution of the polarization loops when applying high number of bipolar square pulses was investigated. Figure 5.2.25(a) shows representative loops after different numbers of cycles of amplitude 5 V. There are not wake-up effects observed. The memory window reduces with cycling from more than $2P_r = 60$ μC/cm$^2$ up to around 26 μC/cm$^2$ after $10^6$ cycles, and further cycling causes capacitor breakdown. When the sample is cycled with 4.5 V pulses (Figure 5.2.25b) the initial polarization is

smaller, but fatigue is less severe and the capacitor preserves memory window larger than $2P_r$ = 16 μC/cm$^2$ after $10^8$ cycles, before breakdown. Reducing the pulses amplitude to 4 V, the capacitor maintains a significant memory window of $2P_r$ = 4.5 μC/cm$^2$ after $10^9$ cycles (Figure 5.2.25c) without breakdown. The evolution of the memory window with the number of cycles at 4, 4.5 and 5 V is shown in Figure 5.2.25(d). It is remarkable that both endurance and remnant polarization are improved with respect to epitaxial films of 9.2 nm HZO on perovskite STO(001) substrate and films of 9.7 nm HZO on YSZ buffered Si substrate. The slightly smaller thickness of HZO films on STO buffered Si is one possible reason.

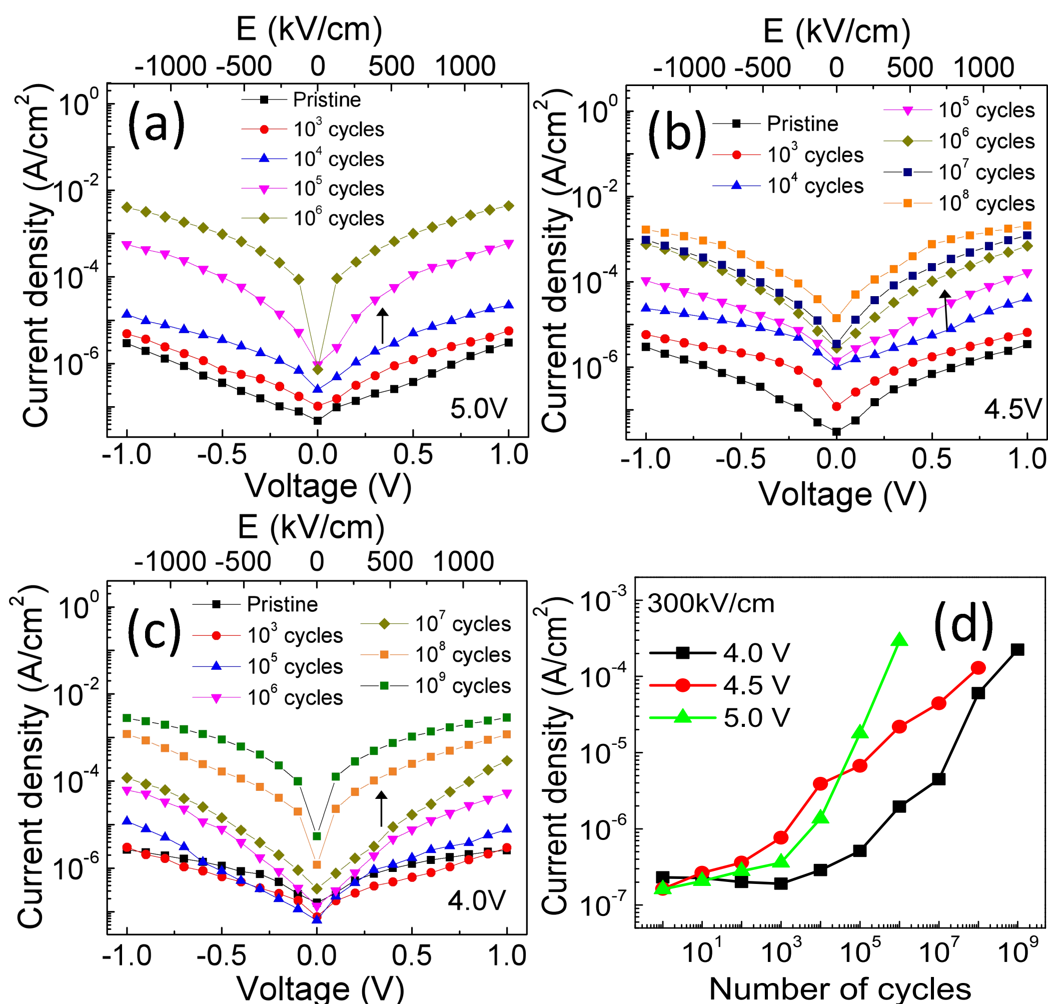


*Figure 5.2.26 Leakage current versus applied voltage curves measured after cycling the capacitors with bipolar pulses of amplitude (a) 5 V, (b) 4.5 V, and (c) 4 V. The number of cycles indicated in each label. (d) Current leakage at 300 kV/cm as a function of the number of applied cycles of 4 V, 4.5 V, and 5 V.*

The current leakage measurements after each decade of switching cycles equal to those applied in the polarization fatigue measurements of Figure 5.2.25 were also

performed. Representative leakage current versus voltage curves are shown in Figure 5.2.6 (a)-(c). The current leakage at given electric field (300 kV/cm) is plotted against number of switching cycles of different amplitude in Figure 5.2.26(c). Leakage is below $10^{-6}$ A/cm$^2$ up to around $10^3$ cycles for 4 V, 4.5 V or 5 V cycling voltage. Above the threshold, leakage increases progressively with additional cycles, and dielectric breakdown occurs when leakage approaches around $10^{-3}$ A/cm$^2$. It can be seen that for 4 V cycling voltage, the leakage remains low until around $10^7$ bipolar pulses, and dielectric breakdown does not occur until $10^9$ cycles.

Ferroelectric retention measurements were performed after poling a capacitor with 5 V, 4.5 V and 4 V as shown in Figure 5.2.27. The reduction of the remnant polarization is small after $10^4$ seconds and the extrapolated retention is very high for the three poling voltages. In similar epitaxial HZO films deposited on STO(001) single crystalline and Si substrate with YSZ template retention was also long, but only for large poling fields. In contrast, here the retention of Pt/HZO/LSMO capacitor on STO/Si(001) after applying a 4 V pulse is very high. To estimate the polarization after longer times, the experimental data are fitted to the power-law decay usually observed[248,249] in ferroelectric oxide films (red dashed curves in Figure 5.2.27). After 10 years (marked with a vertical solid line) the memory window is reduced by only around 17% of the original value. Therefore, same poling condition permits good endurance and extraordinarily long retention. Remarkably, these outstanding properties are obtained with pure (undoped) HZO films integrated epitaxially on Si(001) buffered with STO templates, and the properties are also improved in comparison to films grown on STO(001) oxide single-crystalline substrates.

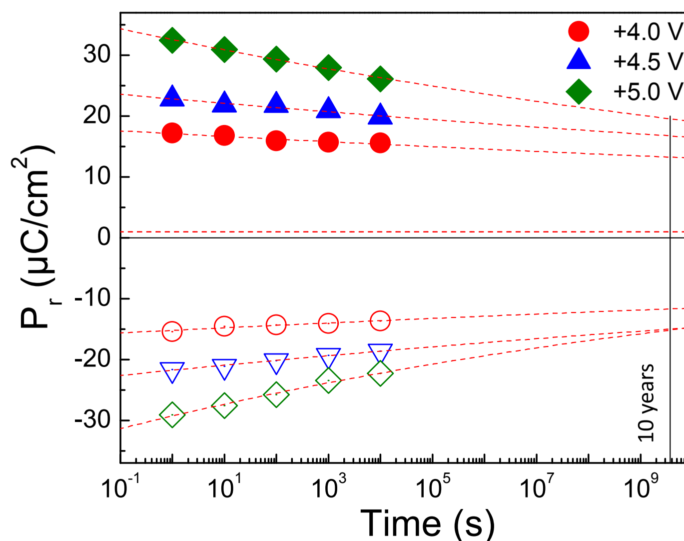


*Figure 5.2.27 Remnant polarization as a function of the time after poling with a pulse of 5, 4.5 and 4 V. Dashed lines are guides for the eye. Dashed lines correspond to $P_r \propto t^{-n}$ equation data fitting,32,33 where t refers to the time after poling. The vertical line marks a time of 10 years.*

## Conclusion

In conclusion, ferroelectric capacitors with epitaxial $Hf_{0.5}Zr_{0.5}O_2$ have been successfully integrated on Si(001) by the first time. The epitaxial integration can be achieved on a buffer heterostructure that includes YSZ or $SrTiO_3$ as epitaxial templates. The ferroelectric properties of epitaxial $Hf_{0.5}Zr_{0.5}O_2$ films on Si(001) present enhanced ferroelectric properties of $P_r$ over 30 μC/cm$^2$ respect to those of epitaxial films of similar thickness on single oxide crystalline substrates. Epitaxial $Hf_{0.5}Zr_{0.5}O_2$ films on both heterostructures present long retention time extrapolated over 10 years. The robust endurance up over to $10^{11}$ cycles can be achieved in films when reducing the thickness to 4.6 nm. The epitaxial $Hf_{0.5}Zr_{0.5}O_2$ capacitors integrated with Si platforms can be very valuable to study its intrinsic ferroelectric-based properties and to develop devices with ultra-small dimensions on semiconductor platforms.

# Chapter 6. General conclusions

In this thesis, epitaxial growth by pulsed laser deposition and properties of ferroelectric barium titanate ($BaTiO_3$) and doped hafnium oxide ($Hf_{0.5}Zr_{0.5}O_2$) have been widely studied and investigated. Both oxides have been successfully epitaxially integrated with silicon, presenting excellent ferroelectric properties with high improvement respect to previous strategies.

(i) A new strain engineering has been developed for ferroelectric $BaTiO_3$ on Si with tunable lattice strain and ferroelectric properties in contrast to the conventional substrate-based strain engineering. High quality epitaxial $BaTiO_3$ films with flat surface are integrated on Si(001) substrate with $LaNiO_3/CeO_2$/YSZ heterostructure. The deposition parameters have a huge impact on the $BaTiO_3$ tetragonality and ferroelectric polarization. In particular, *c*-oriented epitaxial $BaTiO_3$ films are grown at temperature even as low as 450 °C. The deposition temperature window for epitaxial *c*-oriented films is about 300 °C wide, permitting a tailored strain from 0 to above 2%, with the remnant polarization scaling with strain. Oxygen pressure during pulsed laser deposition can also be used as a tuning knob to control lattice strain of epitaxial $BaTiO_3$ over a broad range, and also permits selecting the polar axis to be in-plane or out-of-plane of $BaTiO_3$ films. Lastly, the lattice strain of epitaxial *c*-oriented $BaTiO_3$ films can be tuned by growth rate and the remanent polarization can be up to 14 $\mu C/cm^2$ even though there is no simple correlation between lattice strain and polarization. This methodology of strain engineering for epitaxial $BaTiO_3$ films is valid either on Si(001) or on perovkite oxide single crystals and is not limited to very thin ferroelectric films. Important limitations of conventional strain methodology are thus overcome, opening new avenues for better control of strain and polar orientation in ferroelectric oxides and particularly for its integration on semiconducting substrates. In addition, the role of the electrode interface between perovskite metallic oxide electrode and Pt on $BaTiO_3$ films was determined. The ferroelectric polarization, coercive field, imprint field and leakage of epitaxial $BaTiO_3$ films are largely dominated by the electrode materials.

(ii) The growth conditions for stabilizing the ferroelectric orthorhombic phase in epitaxial $Hf_{0.5}Zr_{0.5}O_2$ thin films on $La_{2/3}Sr_{1/3}MnO_3/SrTiO_3(001)$ have been mapped. The selection of deposition parameters (deposition temperature and oxygen pressure) and film thickness can permit the control of the structural and functional properties of the epitaxial ferroelectric $Hf_{0.5}Zr_{0.5}O_2$ films. In particular, the deposition parameters and thickness determine the relative amount of orthorhombic phase, and the lattice strain of orthorhombic $Hf_{0.5}Zr_{0.5}O_2$ phase in a range wider than 3 %, having the films extremely flat surface. The ferroelectric polarization up to 24 $\mu C/cm^2$ is mostly conditioned by the amount of orthorhombic phase, with possible additional influence of the out-of-plane lattice parameter. The leakage current is also conditioned by the

deposition parameters, being lower for higher temperature and particularly for lower oxygen pressure. The remarkable $E_C - t^{-2/3}$ scaling of electric coercive field and thickness is reported by the first time for ferroelectric hafnium oxide. Long retention (over 10 years) and high endurance (over $10^{10}$ cycles) are also achieved. The growth window map will provide an useful tool for further studies on epitaxial films. Using the determined optimal conditions, $Hf_{0.5}Zr_{0.5}O_2$ films are successfully integrated on Si substrate in capacitor heterostructures with $La_{2/3}Sr_{1/3}MnO_3$/$LaNiO_3$/$CeO_2$/YSZ and $La_{2/3}Sr_{1/3}MnO_3$/$SrTiO_3$ as buffer layes. High quality of epitaxial $Hf_{0.5}Zr_{0.5}O_2$ film with flat surface is obtained on Si(001) in both cases for the first time. The epitaxial $Hf_{0.5}Zr_{0.5}O_2$ films present enhanced ferroelectric properties compared with those of epitaxial films of equivalent thickness on single oxide crystalline substrates and over 10 year retention is achieved in both cases. The robust endurance up over to $10^{11}$ cycles can be achieved in films with YSZ as buffer layer when reducing the film thickness. The epitaxial $Hf_{0.5}Zr_{0.5}O_2$ capacitors integrated with Si platforms with structure homogeneity can can make prototyping tunnel devices and investigating intrinsic ferroelectric properties easier.

# Appendix

## Texture control of epitaxial $BaTiO_3$ films on silicon

Ferroelectric oxides are strongly anisotropic, and the in-plane and out-of-plane polarization of epitaxial ferroelectric thin films can depend critically on the film orientation. Similarly, piezoelectric and electro-optical coefficients are highly anisotropic. Epitaxial ferroelectric films are usually deposited on (001) oriented cubic (or pseudocubic) substrates. The polar *c*-axis of $BaTiO_3$ or $PbZr_xTi_{1-x}O_3$ films on these substrates is generally aligned either along the out-of-plane direction (named *c*-oriented, or (001)-oriented films) or along the in-plane direction (named *a*-oriented, or (100)-oriented films). Epitaxial growth of tetragonal ferroelectrics with an orientation different to (001) or (100) has been much less investigated even though their anisotropic properties offer opportunities for new technological developments. As an example of genuine properties derived from uncommon textures, peculiar patterns of crystal variants and domain walls were observed in PZT(101) films.[250,251] Typically, (110)-oriented perovskite substrates instead of the usual (001) ones are used to obtain epitaxial PZT(101) films.

Epitaxial ferroelectric oxides on Si(001) are generally (001) or (100) oriented and rarely present different textures. Exceptions include (110)-oriented PZT[29] on $SRuO_3/CeO_2$/YSZ/Si(001), and $PbSc_{0.5}Ta_{0.5}O_3$[252] and BTO[247] films on $SRuO_3$/YSZ/Si(001). Integration of high-quality BTO(110) films with silicon is particularly elusive, with the films having a large roughness and their electrical properties remain undisclosed. In contrast, flat BTO(001) epitaxial films with large polarization have been obtained on Si(001) buffered with either $LaNiO_3/SrTiO_3$[253] or LNO/$CeO_2$/YSZ (discussed in the main thesis). Aiming to obtain flat epitaxial BTO(110) films on silicon, we have investigated two alternative routes to the usual LNO/$CeO_2$/YSZ buffer layer and the usual Si(001) orientation. The first route involves the use of the alternative LNO/$CaTiO_3$ (CTO)/YSZ buffer layer on Si(001). In the second route, we use the conventional LNO/$CeO_2$/YSZ buffer but replacing the Si(001) substrate by Si(111). We show that very flat epitaxial BTO films are obtained in both cases, with the films being (l0l) oriented on LNO/CTO/YSZ/Si(001) and presenting the coexistence of (l0l) and (l00) out-of-plane oriented epitaxial crystal variants on LNO/$CeO_2$/YSZ buffered Si(111). The BTO films have low leakage current and are ferroelectric with remnant polarization in the 1.9 – 4.5 μC $cm^{-2}$ range.

## Samples preparation

BTO films (thickness t = 110 nm) were deposited on LNO (t = 30 nm)/$CeO_2$ (t = 20 nm)/YSZ (t = 60 nm) buffered Si(001) and Si(111), and LNO (t = 30 nm)/$CaTiO_3$ (t = 50 nm)/YSZ (t = 2.5 nm) buffered Si(001) at 700 °C with 0.02 mbar dynamic oxygen pressure. Figure A.1 shows the sketch of the heterostructures for the three samples. The $CaTiO_3$ buffer layer was deposited at 750 °C, 0.02 mbar of molecular oxygen and a laser frequency of 5 Hz. The growth conditions for other buffer layers can be seen in Chapter 4 of the main thesis.

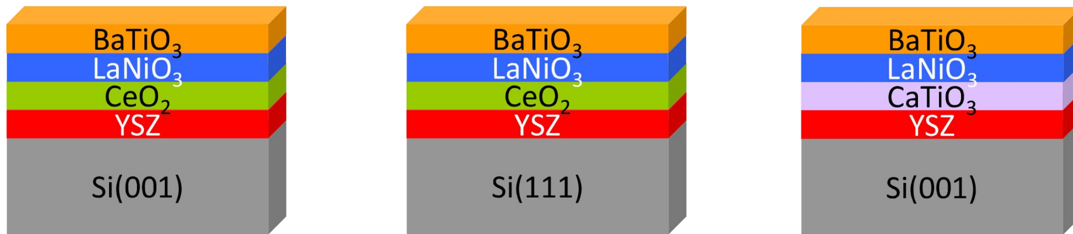


*Figure A.1 Sketches of the heterostructures for the three samples.*

## Structural characterization

The XRD specular $\theta$-$2\theta$ scans of all the samples are presented in Figure A.2(a). Vertical dashed lines at $2\theta$ = 22.039°, 31.498°, 44.856°, and 65.755 °C mark the position of the (001), (101), (002) and (202) reflections in bulk BTO, respectively. The upper scan in Figure A.2(a), corresponding to the BTO/LNO/$CeO_2$/YSZ/Si(001) sample which is the structure described in detail in chapter 4 of the main thesis, shows (00*l*) reflections of the Si substrate and films, without peaks corresponding to other phases or orientations. The BTO(00*l*) reflections (see a zoom in Figure A.2b) are at slightly lower angles than in bulk BTO, signaling an expanded out-of-plane parameter. The corresponding XRD measurement using a 2D detector around $\chi$ = 0° in Figure A.2(c) shows a bright and narrow spot of all the layers (YSZ, $CeO_2$, $LaNiO_3$ and $BaTiO_3$), which indicates good epitaxial quality.

The XRD specular $\theta$-$2\theta$ scan of BTO/LNO/$CeO_2$/YSZ/Si(111) sample (Figure A.2a, middle scans) shows that YSZ is (111) oriented although with presence of minority (001) domains. The (*lll*) reflections of $CeO_2$ are overlapped with Si(*lll*) ones. LNO and BTO are preferentially (*l*0*l*)-oriented, with minority (*l*00) domains. The formation of (*l*0*l*) and (*l*00) out-of-plane oriented domains of LNO on the $CeO_2$(*lll*) surface is caused by the large lattice mismatch between both oxides, being the corresponding lattice parameters 3.84 Å and 5.41 Å, respectively. The measurement of $2\theta$-$\chi$ frames

is shown in Figure A.2(d). The BTO film are (101) and (001) epitaxially oriented with a little fraction of other domains and mosaicity reflected by the elongated distribution of BTO(101) and BTO(001) spots along $\chi$ direction.

The XRD $\theta$-$2\theta$ scan of the third sample BTO/LNO/CTO/YSZ/Si(001) (Figure A.2a, lower scan) shows diffraction peaks corresponding to BTO ($l0l$), LNO ($ll0$) and Si ($00l$) reflections. The lattice parameters of CTO ($a$ = 3.83 Å) and LNO ($a$ = 3.86 Å) are very close and their XRD reflections are at the same $2\theta$ positions. The YSZ layer in this sample is 2.5 nm thick, permitting epitaxial crystallization of YSZ($00l$) on $SiO_x$/Si(001). Thus, the texture relationship is BTO(101)/LNO(110)/CTO(110) /YSZ(001)/Si(001). The bright spot of BTO(101) reflection in XRD 2D measurement as shown in Figure A.2(e) signals the good epitaxial ordering of (101) oriented BTO film.

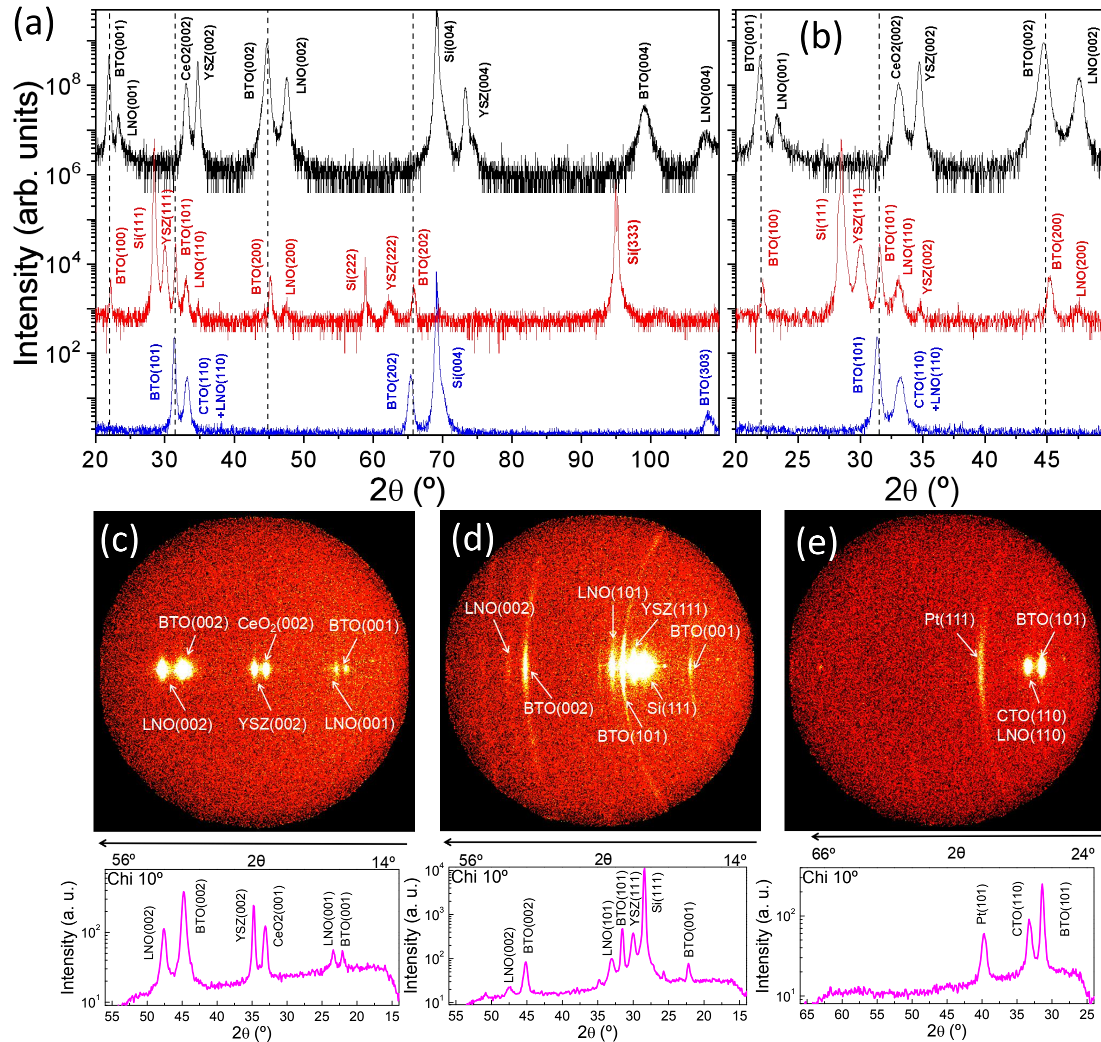


*Figure A.2 (a) XRD symmetrical θ-2θ scans of BTO/LNO/$CeO_2$/YSZ/Si(001) (top),*

*BTO/LNO/$CeO_2$/YSZ/Si(111) (middle) and BTO/LNO/CTO/YSZ/Si(001) (bottom) samples. Vertical dashed lines at 2θ = 22.039°, 31.498°, 44.856°, and 65.755° mark the positions of (001), (101), (002), and (202) reflections in bulk BTO, respectively. (b) Zoom of the diffractograms in the 20 - 50° 2θ range. (c) XRD 2θ-χ frame of BTO(00l) film, and θ-2θ scan integrated ± 10° around χ = 0°. (e) XRD 2θ-χ frame of BTO(l0l)/(l00) film, and θ-2θ scan integrated ± 10° around χ = 0°. (e) XRD 2θ-χ frame of BTO(l0l) film, and θ-2θ scan integrated ± 10° around χ = 0°.*

XRD $\phi$-scans around asymmetrical reflections are shown in Figure A.3 to determine the epitaxial relationships in all the samples. The first sample with BTO/LNO/$CeO_2$/YSZ/Si(001) structure (Figure A.3a) is already discussed in the main thesis. BTO (110) and LNO (110) peaks shifted 45° with respect to the other sets of peaks, which confirms cube-on-cube growth with a 45° in-plane rotation of BTO and LNO with respect to the other layers.

The $\phi$-scans of BTO/LNO/$CeO_2$/YSZ/Si(111) sample are presented in Figure A.3(b). The scan around the Si (220) reflection displays three high intensity peaks, whereas there are six YSZ (220) reflections indicating the presence of two YSZ crystal in-plane variants, one of them more abundant than the other. These $\Sigma 3$ twinning domains, one rotated by 180° in-plane with respect to the other, are usual in epitaxial films with a (111) out-of-plane orientation.[77-79] On the other hand, the observation of six reflections associated with $CeO_2$ (220) planes (see a Gaussian fit in the lower panel) indicates the presence of a domain distribution similar to that of the YSZ described earlier. As indicated by $\phi$-scan measurements of BTO asymmetrical reflections, we confirm that the two domains in BTO, (*l*0*l*) and (*l*00) oriented, are epitaxial. In the case of BTO(*l*0*l*) texture, the $\phi$-scans around the BTO(002) asymmetrical reflections show two sets (60° apart) of three peaks corresponding to two BTO crystal variants. On the other hand, in the case of the BTO crystal variant with the (100) texture, the asymmetrical BTO (101) reflections show 24 peaks, 15° apart. In this $\phi$-scan, two sets of three peaks have higher intensity, which corresponds to [010]BTO(100) domains rotated by ± 15° in-plane with respect to [11-2]Si(111).

Figure A.3(c) shows the XRD $\phi$-scans of BTO/LNO/CTO/YSZ/Si(001) sample. Narrow peaks corresponding to Si(220) reflections overlap with CTO (200) and LNO (200) reflections (see a Gaussian fit in the lower panel). The $\phi$-scan around BTO (111) reflections shows four broad peaks signaling the presence of in-plane [010]BTO(101) domains around [100]Si(001). This type of domain is usually observed in epitaxial oxide heterostructures with a high lattice mismatch.[80,81]

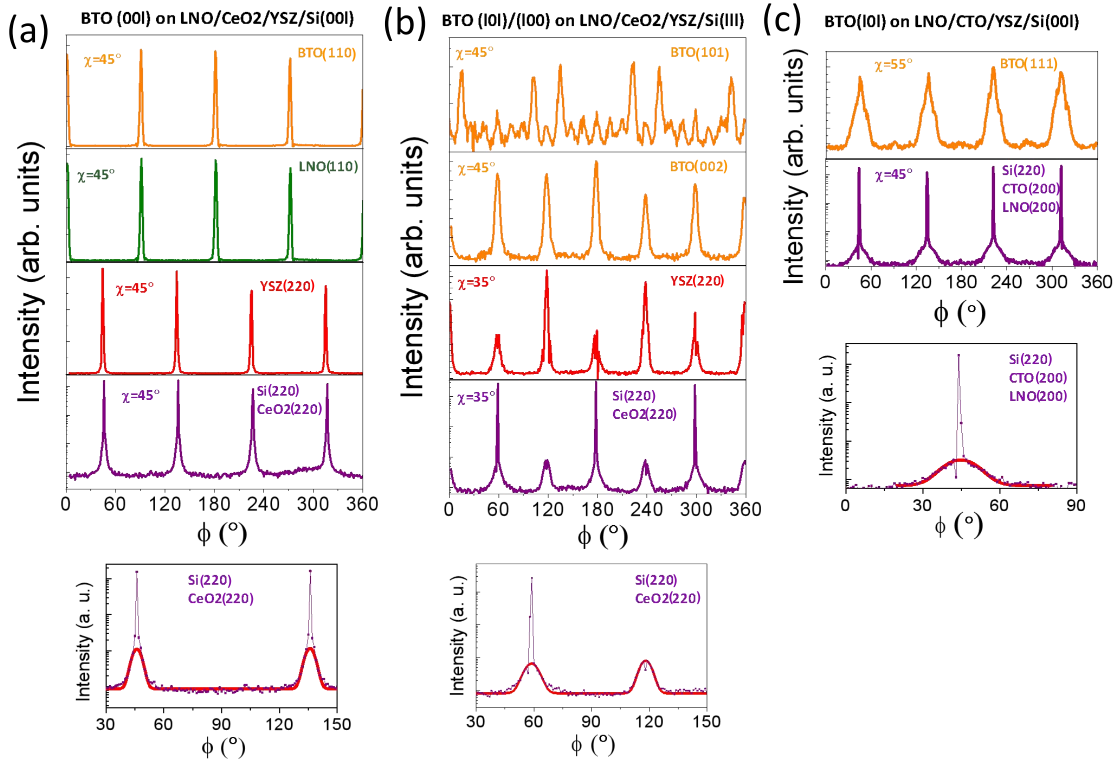


*Figure A.3 XRD $\phi$-scans (a) around BTO (110), LNO (110), YSZ (220) and $CeO_2$ and Si (220) asymmetrical reflections of the BTO(001)/LNO/$CeO_2$/YSZ/Si(001) sample. Lower panel: zoom of the Si and $CeO_2$ (220) reflections. The red curve is a Gaussian fit of the latter. (b) BTO (101) and (002), YSZ (220) and $CeO_2$ and Si (220) asymmetrical reflections of the BTO(101)/(100)/ LNO/$CeO_2$/YSZ/Si(111) sample. Lower panel: zoom of the Si and $CeO_2$ 220 reflections. The red curve is a Gaussian fit of the latter. (c) BTO (111), LNO (200), CTO (200) and Si (220) asymmetrical reflections of the BTO(101)/CTO(110)/YSZ(001)/Si(001) sample. Lower panel: zoom of the Si (220), LNO (200) and CTO (200) reflections. The red curve is a Gaussian fit for the LNO (200) and CTO (200) reflections.*

Figure A.4 shows AFM topographic images, 5 µm x 5 µm in size (1 µm x 1 µm in the insets). The BTO(001) film on LNO/$CeO_2$/YSZ/Si(001) (Figure A.4a) presents small grains a few tens of nanometers wide, locally agglomerated in some small areas, a few nm high (see in the lower panel the height profile along the line marked in the topographic image). The overall roughness, with a root means square (rms) of 0.74 nm, is remarkably low considering the BTO thickness (t > 100 nm). The BTO(101)/(100) film LNO/$CeO_2$/YSZ/Si(111) (Figure A.4b) presents a similar morphology of small grains, with the roughness being very low (rms = 0.44 nm) and the surface very homogeneous in spite of the coexistence of the two crystalline orientations. The BTO(101) film on LNO(110)/CTO(110)/YSZ(001)/Si(001) (Figure A.4c) shows a dense morphology of large grains (a few hundred nm wide), with some grain boundaries (see two examples marked with white dotted lines) oriented along

BTO[1-10] and BTO[001] directions. The grains are very flat (see the corresponding height profile) and the overall roughness is very low (rms = 0.53 nm). Therefore, the BTO(101) films on Si(001) substrates are extremely flat in comparison with previous reports[247] and present low roughness comparable to state-of-the-art BTO(001) films on Si(001).

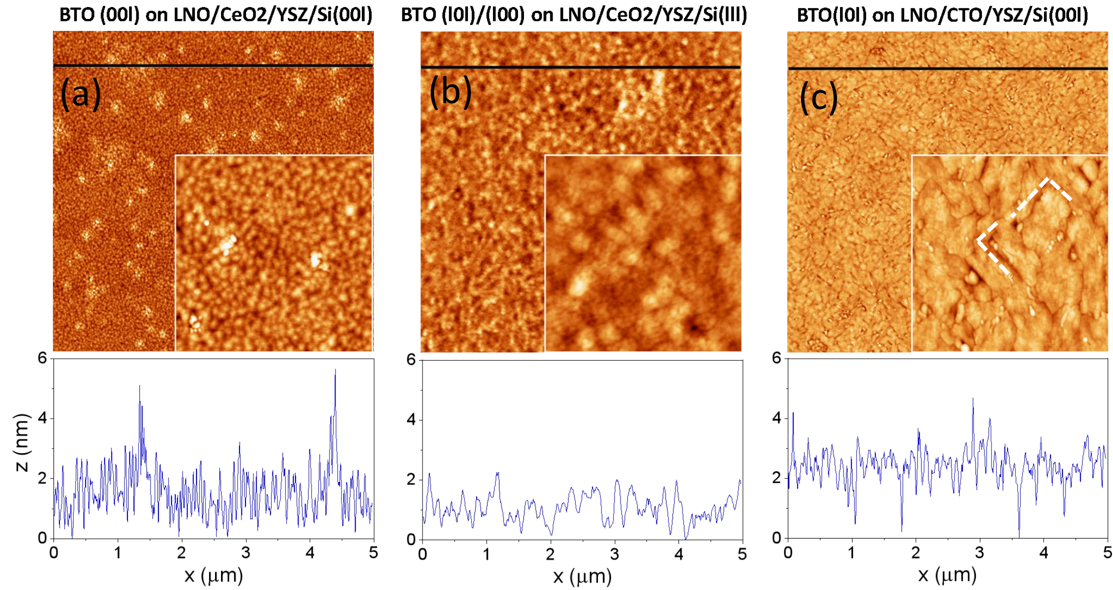


*Figure A.4 Topographic AFM images (5 μm x 5 μm) of the (a) BTO(001)/LNO/CeO₂/YSZ/Si(001), (b) BTO(101)/(100)/LNO/CeO₂/YSZ/Si(111), and (c) BTO(101)/CTO(110)/YSZ(001)/Si(001) samples. The corresponding height ranges are 7, 4 and 7 nm, respectively. Insets: 1 μm x 1 μm scanned regions, being the corresponding height ranges 5, 4, and 5 nm. Lower panels show height profiles along the horizontal lines marked in the respective 5 μm x 5 μm topographic image.*

## Electrical Characterization

As shown in Figure A.4(a), ferroelectric polarization loops of the two samples BTO(101)/(100)/LNO/$CeO_2$/YSZ/Si(111) and BTO(001)/LNO/$CeO_2$/YSZ/Si(001) were measured by a dynamic hysteresis mode, whereas the dielectric leakage current compensation was used for the sample BTO(101)/CTO(110)/YSZ(001)/Si(001) due to its higher leakage at high electric field. The (001) film has the largest polarization at high electric field, as expected considering that the polar axis of BTO is along the *c*-axis. Its remnant polarization $P_r$ is 3.2 μC/cm$^2$, whereas in the BTO(101)/(100) and BTO(101) films, $P_r$ is 1.9 and 4.5 μC/cm$^2$, respectively. Figure A.4(b) shows the leakage curves measured at room temperature. The leakage of the BTO(001) film on LNO/$CeO_2$/YSZ/Si(001) (black squares) is very low: 7 x $10^{-8}$ A cm$^{-2}$ and 2 x $10^{-3}$ A cm$^{-2}$ at 45 and 450 kV cm$^{-1}$, respectively. The leakage of the BTO(101)/(100) film on

LNO/$CeO_2$/YSZ/Si(111) on Si(111) is higher at low field (3 x $10^{-7}$ A $cm^{-2}$ at 45 kV $cm^{-1}$), whereas in the BTO(101) film on CTO(110)/YSZ(001)/Si(001) it is similar to that of the BTO(001) sample (8 x $10^{-8}$ A $cm^{-2}$ at 45 kV $cm^{-1}$). However, the leakage of this film increases sharply with the field, while the increase of the BTO(101)/(100) is smaller.

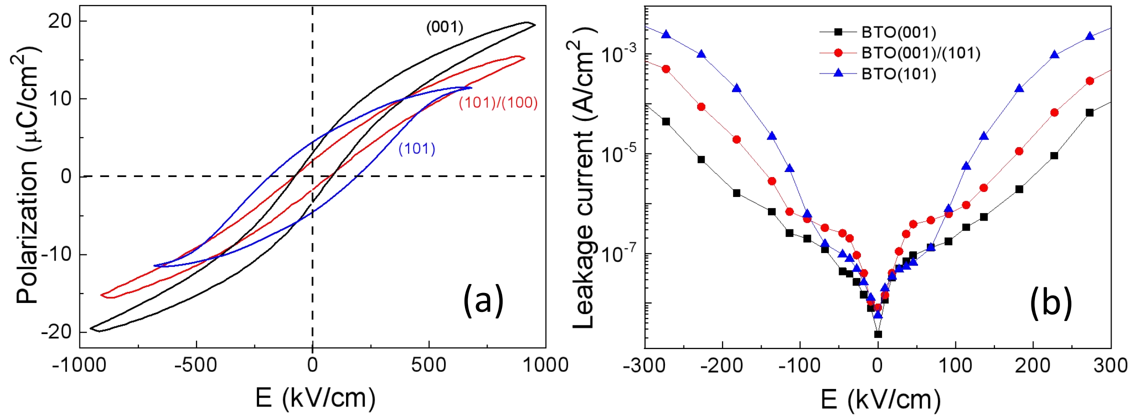


*Figure A.5 (a) Ferroelectric polarization loops, and (b) leakage current density of the BTO(001) film on LNO/$CeO_2$/YSZ/Si(001), BTO(101)/(100) film on LNO/$CeO_2$/YSZ/Si(111), and BTO(101) film on CTO(110)/YSZ(001)/Si(001).*

## Conclusion

In summary, suitable selection of buffer layers and silicon wafer orientation permits control over the crystallographic orientation in epitaxial $BaTiO_3$ films. $BaTiO_3$(001), $BaTiO_3$(101) and $BaTiO_3$(101)/(100) textures can be achieved on $LaNiO_3$/$CeO_2$/YSZ/Si(001), $LaNiO_3$/$CaTiO_3$/YSZ/Si(001), and $LaNiO_3$/$CeO_2$/YSZ/Si(111), respectively. $BaTiO_3$(001) films are fully epitaxial, whereas the other $BaTiO_3$ films present the coexistence of crystal domains. All the films, irrespective of their orientation, are extremely flat with a low rms roughness (in the 0.4 - 0.8 nm range), present low leakage (in the 7 x $10^{-8}$ A $cm^{-2}$ - 3 x $10^{-7}$ A $cm^{-2}$ range at 45 kV $cm^{-1}$) and sizeable remnant polarization in the 1.9 - 4.5 μC $cm^{-2}$ range. The films can pave the way towards devices taking advantage of the anisotropic properties of ferroelectric $BaTiO_3$.

# List of symbols and abbreviations

## Materials

| | |
|---|---|
| BTO | $BaTiO_3$ |
| HZO | $Hf_{0.5}Zr_{0.5}O_2$ |
| LAO | $LaAlO_3$ |
| LSAT | $(LaAlO_3)_{0.3}(SrAl_{0.5}Ta_{0.5}O_3)_{0.7}$ |
| LSMO | $La_{2/3}Sr_{1/3}MnO_3$ |
| LNO | $LaNiO_3$ |
| STO | $SrTiO_3$ |
| YSZ | $Y:ZrO_2$ |

## Methodologies

| | |
|---|---|
| AFM | Atomic force microscopy |
| DC | Direct current |
| DHM | Dynamic hysteresis measurement |
| DLCC | Dynamic leakage current compensation |
| *GIXRD* | Grazing incidence x-ray diffraction |
| PLD | Pulsed laser deposition |
| *RSM* | Reciprocal space map |
| RMS | Root mean square |
| *t-b* | Top-bottom electrodes configuration |
| *t-t* | Top-top electrodes configuration |
| *XRD* | X-ray diffraction |
| *XRR* | X-ray reflectivity |

## Variables

| | |
|---|---|
| *a/ip* | In-plane lattice parameter |

| | |
|---|---|
| *c/oop* | Out-of-plane lattice parameter |
| $\varepsilon_r$ | Relative permittivity |
| $\varepsilon$ | Biaxial strain |
| $E_{imp}$, $E_{dep}$ | Imprint field, depolarization field |
| $E_c$, $V_c$ | Coercive field, coercive voltage |
| FE | Ferroelectric |
| FWHM | Full width at half maximum |
| GR (gr) | Growth rate |
| $P_{O2}$ | Oxygen pressure |
| $P_r$ | Remnant polarization |
| $T_s$ | Substrate temperature |
| $t$ | Thickness |
| $T_c$ | Curie temperature |
| $\omega$ | Rocking curve |

# List of publications

***Submitted***

1. S. Estandía, N. Dix, J. Gazquez, **J. Lyu**, I. Fina, M. F. Chisholm, J. Fontcuberta, F. Sánchez. Engineering ferroelectric $Hf_{0.5}Zr_{0.5}O_2$ thin films by epitaxial stress. Submitted, 2019.

***Published (in peer review journals)***

2. **J. Lyu,** I. Fina, R. Solanas, B. Romain, G Saint-Girons, J. Fontcuberta, F. Sánchez. Enhanced ferroelectricity in epitaxial $Hf_{0.5}Zr_{0.5}O_2$ thin films integrated on Si(001) using $SrTiO_3$ templates. ***Applied Physics Letter***, 2019, 114, 222901.
3. **J. Lyu,** I. Fina, R. Solanas, J. Fontcuberta, F. Sánchez. Growth Window of Ferroelectric Epitaxial $Hf_{0.5}Zr_{0.5}O_2$ Thin Films. ***ACS Applied Electronic Materials***, 2019, 1, 220.
4. **J. Lyu,** I. Fina, J. Fontcuberta, F. Sánchez. Epitaxial Integration on Si(001) of Ferroelectric $Hf_{0.5}Zr_{0.5}O_2$ Capacitors with High Retention and Endurance. ***ACS Applied materials & interfaces***, 2019, 11, 6224.
5. **J. Lyu,** I. Fina, R. Solanas, J. Fontcuberta, F. Sánchez. Robust ferroelectricity in epitaxial $Hf_{1/2}Zr_{1/2}O_2$ thin films. ***Applied Physics Letters***, 2018, 113, 082902.
6. **J. Lyu,** I. Fina, R. Solanas, J. Fontcuberta, F. Sánchez. Selectable texture in epitaxial ferroelectric $BaTiO_3$ films integrated with silicon. ***CrystEngComm***, 2018, 20, 6225.
7. **J. Lyu,** S. Estandía, J. Gazquez, M. Chisholm, I. Fina, N. Dix, J. Fontcuberta, F. Sánchez. Control of Polar Orientation and Lattice Strain in Epitaxial $BaTiO_3$ Films on Silicon. ***ACS Applied materials & interfaces***, 2018, 10, 25529.
8. **J. Lyu,** I. Fina, R. Solanas, J. Fontcuberta, F. Sánchez. Tailoring Lattice Strain and Ferroelectric Polarization of Epitaxial $BaTiO_3$ Thin Films on Si (001). ***Scientific Reports***, 2018, 8, 495.

# List of communications

2018.03.12-14
Sant Feliu de Guíxols, Girona, Spain
**The Spring 2018 Meeting of the TO-BE COST Action**
Poster: *Tuning lattice strain and electrical properties of epitaxial ferroelectric $BaTiO_3$ films on Si(001)*

2017.09.11-13
Institute of Solid State Physics, University of Latvia, Riga, Latvia
**COST TO BE FALL MEETING 2017**
Oral Talk: *Tailoring lattice strain and ferroelectric polarization of epitaxial ferroelectric $BaTiO_3$ films on Si(001)*

2017.07.10-12
Sant Feliu de Guíxols, Girona, Spain
**NANOSELECT ANNUAL MEETING 2017 (project meeting)**
Oral Talk: *Tuning lattice strain and ferroelectric polarization of epitaxial $BaTiO_3$ thin films on Si(001)*

2016.06.08-10
Sant Feliu de Guíxols (Girona), Spain
**NANOSELECT NOE ANNUAL MEETING (project meeting)**
Poster: *Controlling lattice strain and electrical properties of epitaxial ferroelectric $BaTiO_3$ films on Silicon*

2018.03.15-17
Sant Feliu de Guíxols, Spain
**School on "Oxide Based Technologies" of the TO-BE COST Action**

2017.04.11-21
Institut d'Etudes Scientifiques de Cargèse, France
**International School of Oxide Electronics 2017**
Poster: *Tailoring lattice strain and electrical properties of epitaxial ferroelectric $BaTiO_3$ films on Si(001)*

# References

[1] Setter, N.; Damjanovic, D.; Eng, L.; Fox, G.; Gevorgian, S.; Hong, S.; Stolitchnov, I. Ferroelectric thin films: Review of materials, properties, and applications. *J. Appl. Phys.* **2006**, 100(5), 051606.
[2] Haertling, G. H. Ferroelectric ceramics: history and technology. *J. Am. Ceram. Soc.* **1999**, 82(4), 797-818.
[3] Pandya, S.; Wilbur, J.; Kim, J.; Gao, R.; Dasgupta, A.; Dames, C.; Martin, L. W. Pyroelectric energy conversion with large energy and power density in relaxor ferroelectric thin films. *Nat. Mater.* **2018**, 17(5), 432.
[4] Zhang, Q.; Whatmore, R. W. Improved ferroelectric and pyroelectric properties in Mn-doped lead zirconate titanate thin films. *J. Appl. Phys.* **2003**, 94(8), 5228-5233.
[5] Auciello, O.; Scott, J. F.; Ramesh, R. The physics of ferroelectric memories. *Phys. Today.* **1998**, 51(7), 22-27.
[6] Damjanovic, D. Ferroelectric, dielectric and piezoelectric properties of ferroeletric thin films and ceramics. *Rep. Prog. Phys.* **1998**, 61(9), 1267.
[7] Muralt, P. (2000). Ferroelectric thin films for micro-sensors and actuators: a review. *J. Micromech. Microeng.* **2000**, 10(2), 136.
[8] Chanthbouala, A.; Garcia, V.; Cherifi, R. O.; Bouzehouane, K.; Fusil, S.; Moya, X.; Bibes, M. A ferroelectric memristor. *Nat. Mater.* **2012**, 11(10), 860.
[9] Yu, S. Neuro-inspired computing with emerging nonvolatile memorys. *P. IEEE.* **2018**, 106(2), 260-285.
[10] Wessels, B. W. Ferroelectric epitaxial thin films for integrated optics. *Annu. Rev. Mater. Res.* **2007**, 37, 659-679.
[11] Chandra, P., & Littlewood, P. B. A Landau primer for ferroelectrics. *In Physics of ferroelectrics* (pp. 69-116). **2007**, Springer, Berlin, Heidelberg.
[12] Ong, L. H.; Osman, J.; Tilley, D. R. Landau theory of second-order phase transitions in ferroelectric films. *Phys. Rev. B.* **2001**, 63(14), 144109.
[13] Fridkin, V.; Ducharme, S. Ferroelectricity and Ferroelectric Phase Transition. *In Ferroelectricity at the Nanoscale* (pp. 1-9). **2014**, Springer, Berlin, Heidelberg.
[14] Daraktchiev, M.; Catalan, G.; Scott, J. F. Landau theory of ferroelectric domain walls in magnetoelectrics. *Ferroelectrics* 2008, 375(1), 122-131.
[15] Reiner, J. W.; Kolpak, A. M.; Segal, Y.; Garrity, K. F.; Ismail, S.; Ahn, C. H.; Walker, F. J. Crystalline oxides on silicon. *Adv. Mater.* **2010**, 22(26-27), 2919-2938.
[16] Defaÿ, E. Ferroelectric dielectrics integrated on silicon. *John Wiley & Sons* **2013**.
[17] Mazet, L.; Yang, S. M.; Kalinin, S. V.; Schamm, S.; Dubourdieu, C. A review of molecular beam epitaxy of ferroelectric $BaTiO_3$ films on Si, Ge and GaAs substrates and their applications. *Sci. Technol. Adv. Mat.* **2015**, 16(3), 036005.
[18] Schlom, D. G.; Chen, L. Q.; Pan, X.; Schmehl, A.; Zurbuchen, M. A. (2008). A thin film approach to engineering functionality into oxides. *J. Am. Ceram. Soc.* **2008**, 91(8), 2429-2454.
[19] Vila-Fungueiriño, J. M.; Bachelet, R.; Saint-Girons, G.; Gendry, M.; Gich, M.;

Gazquez, J.; Carretero-Genevrier, A. Integration of functional complex oxide nanomaterials on silicon. *Front. Phys.* **2015**, 3, 38.

[20] Shichi, Y.; Tanimoto, S.; Goto, T.; Kuroiwa, K.; Tarui, Y. Interaction of $PbTiO_3$ films with Si substrate. *Jpn. J. Appl. Phys.* **1994**, 33(9S), 5172.

[21] Matsubara, S.; Shohata, N.; Mikami, M. Epitaxial growth of $PbTiO_3$ on $MgAl_2O_4$/Si substrates. *Jpn. J. Appl. Phys.* **1985**, 24(S3), 10.

[22] McKee, R. A.; Walker, F. J.; Chisholm, M. F. Crystalline oxides on silicon: the first five monolayers. *Phys. Rev. Lett.* **1998**, 81(14), 3014.

[23] Maruyama, T.; Saitoh, M.; Sakai, I.; Hidaka, T.; Yano, Y.; Noguchi, T. Growth and characterization of 10-nm-thick c-axis oriented epitaxial $PbZr_{0.25}Ti_{0.75}O_3$ thin films on (100) Si substrate. *Appl. Phys. Lett.* **1998**, 73(24), 3524-3526.

[24] Yu, Z.; Ramdani, J.; Curless, J. A.; Overgaard, C. D.; Finder, J. M.; Droopad, R.; Kaushik, V. S. Epitaxial oxide thin films on Si (001). *J. Vac. Sci. Technol. B.* **2000**, 18(4), 2139-2145.

[25] Guerrero, C.; Roldan, J.; Ferrater, C.; Garcia-Cuenca, M. V.; Sanchez, F.; Varela, M. Growth and characterization of epitaxial ferroelectric $PbZr_xTi_{1-x}O_3$ thin film capacitors with $SrRuO_3$ electrodes for non-volatile memory applications. *Solid State Electron.* **2001**, 45(8), 1433-1440.

[26] Wang, Y.; Ganpule, C.; Liu, B. T.; Li, H.; Mori, K.; Hill, B.; Droopad, R. Epitaxial ferroelectric $Pb(Zr,Ti)O_3$ thin films on Si using $SrTiO_3$ template layers. *Appl. Phys. Lett.* **2002**, 80(1), 97-99.

[27] Vaithyanathan, V.; Lettieri, J.; Tian, W.; Sharan, A.; Vasudevarao, A.; Li, Y. L.; Woicik, J. C. *c*-axis oriented epitaxial $BaTiO_3$ films on (001)Si. *J. Appl. Phys.* **2006**, 100(2), 024108.

[28] Warusawithana, M. P.; Cen, C.; Sleasman, C. R.; Woicik, J. C.; Li, Y.; Kourkoutis, L. F.; Bedzyk, M. A ferroelectric oxide made directly on silicon. *Science* **2009**, 324(5925), 367-370.

[29] Dekkers, M.; Nguyen, M. D.; Steenwelle, R.; te Riele, P. M.; Blank, D. H.; Rijnders, G. Ferroelectric properties of epitaxial $Pb(Zr,Ti)O_3$ thin films on silicon by control of crystal orientation. *Appl. Phys. Lett.* **2009**, 95(1), 012902.

[30] Sakai, S.; Takahashi, M. Recent progress of ferroelectric-gate field-effect transistors and applications to nonvolatile logic and FeNAND flash memory. *Materials* **2010**, 3(11), 4950-4964.

[31] Sambri, A.; Gariglio, S.; Torres Pardo, A.; Triscone, J. M.; Stéphan, O.; Reiner, J. W.; Ahn, C. H. Enhanced critical temperature in epitaxial ferroelectric $Pb(Zr_{0.2}Ti_{0.8})O_3$ thin films on silicon. *Appl. Phys. Lett.* **2011**, 98(1), 012903.

[32] Dubourdieu, C.; Bruley, J.; Arruda, T. M.; Posadas, A.; Jordan-Sweet, J.; Frank, M. M.; Narayanan, V. Switching of ferroelectric polarization in epitaxial $BaTiO_3$ films on silicon without a conducting bottom electrode. *Nat. Nanotechnol.* **2013**, 8(10), 748.

[33] Bakaul, S. R.; Serrao, C. R.; Lee, M.; Yeung, C. W.; Sarker, A.; Hsu, S. L.; Clarkson, J. D. Single crystal functional oxides on silicon. *Nat. Commun.* **2016**, 7, 10547.

[34] Scigaj, M.; Dix, N.; Fina, I.; Bachelet, R.; Warot-Fonrose, B.; Fontcuberta, J.; Sánchez, F. Ultra-flat $BaTiO_3$ epitaxial films on Si (001) with large out-of-plane

polarization. *Appl. Phys. Lett.* **2013**, 102(11), 112905.
[35] Böscke, T. S.; Müller, J.; Bräuhaus, D.; Schröder, U.; Böttger, U. Ferroelectricity in hafnium oxide thin films. *Appl. Phys. Lett.* **2011**, 99(10), 102903.
[36] Park, M. H.; Lee, Y. H.; Kim, H. J.; Kim, Y. J.; Moon, T.; Kim, K. D.; Müller, J.; Kersch, A.; Schroeder, U.; Mikolajick, T.; Hwang, C. S. Ferroelectricity and Antiferroelectricity of Doped Thin $HfO_2$-Based Films. *Adv. Mater.* **2015**, 27, 1811−1831.
[37] Fan, Z.; Chen, J.; Wang, J. Ferroelectric $HfO_2$-based Materials for Next-Generation Ferroelectric Memories. *J. Adv. Dielectr.* **2016**, 06, 1630003.
[38] Park, M. H.; Lee, Y. H.; Kim, H. J.; Kim, Y. J.; Moon, T.; Kim, K. D.; Hyun, S. D.; Mikolajick, T.; Schroeder, U.; Hwang, C. S. Understanding the formation of the metastable ferroelectric phase in hafnia-zirconia solid solution thin films. *Nanoscale* **2018**, 10, 716−725.
[39] Merz, W. J. The Electric and Optical Behavior of $BaTiO_3$ Single-Domain Crystals. *Physical Review* **1949**, 76(8), 1221.
[40] Damodaran, A. R.; Breckenfeld, E.; Chen, Z.; Martin, L. W. Enhancement of Ferroelectric Curie Temperature in $BaTiO_3$ Films via Strain-Induced Defect Dipole Alignment. *Adv. Mater.* **2014**, 26, 6341.
[41] Fina, I.; Dix, N.; Rebled, J. M.; Gemeiner, P.; Marti, X.; Peiro, F.; Fontcuberta, J. The direct magnetoelectric effect in ferroelectric-ferromagnetic epitaxial heterostructures. *Nanoscale* **2013**, 5(17), 8037-8044.
[42] Damodaran, A. R.; Agar, J. C.; Pandya, S.; Chen, Z.; Dedon, L.; Xu, R.; Martin, L. W. New modalities of strain-control of ferroelectric thin films. *J. Phys-Condens. Mat.* **2016**, 28(26), 263001.
[43] Eltes, F.; Caimi, D.; Fallegger, F.; Sousa, M.; Connor, E.; Rossell, M. D.; Abel, S. Low-loss $BaTiO_3$-Si waveguides for nonlinear integrated photonics. *ACS Photonics* **2016**, 3(9), 1698-1703.
[44] Ścigaj, M. Functional oxide films and interfaces: ferroelectric $BaTiO_3$ films on Si (001) and conducting (110) and (111) $LaAlO_3/SrTiO_3$ interfaces. **2016**, PhD thesis.
[45] Janolin, P. E. Strain on ferroelectric thin films. *J. Mater. Sci.* **2009**, 44(19), 5025-5048.
[46] Bardal, A.; Matthee, T.; Wecker, J.; Samwer, K. Initial stages of epitaxial growth of Y-stabilized $ZrO_2$ thin films on *a*-$SiO_x$/Si(001) substrates. *J. Appl. Phys.* **1994**, 75(6), 2902-2910.
[47] Fork, D. K.; Fenner, D. B.; Connell, G. A. N.; Phillips, J. M.; Geballe, T. H. Epitaxial yttria-stabilized zirconia on hydrogen-terminated Si by pulsed laser deposition. *Appl. Phys. Lett.* **1990**, 57(11), 1137-1139.
[48] de Coux, P.; Bachelet, R.; Gatel, C.; Warot-Fonrose, B.; Fontcuberta, J.; Sánchez, F. Mechanisms of epitaxy and defects at the interface in ultrathin YSZ films on Si (001). *CrystEngComm* **2012**, 14(23), 7851-7855.
[49] Bachelet, R.; De Coux, P.; Warot-Fonrose, B.; Skumryev, V.; Fontcuberta, J.; Sánchez, F. $CoFe_2O_4$/buffer layer ultrathin heterostructures on Si (001). *J. Appl. Phys.* **2006**, 110, 086102.
[50] Sánchez, F.; Aguiar, R.; Trtik, V.; Guerrero, C.; Ferrater, C.; Varela, M. Epitaxial

growth of $SrTiO_3$ (00h), (0hh), and (hhh) thin films on buffered Si (001). *J. Mater. Res.* **1998**, 13(6), 1422-1425.
[51] Schlom, D. G.; Chen, L. Q.; Fennie, C. J.; Gopalan, V.; Muller, D. A.; Pan, X.; Uecker, R. Elastic strain engineering of ferroic oxides. *MRS Bull.* **2014**, 39(2), 118-130.
[52] Schlom, D.G.; Chen, L. Q.; Eom, C. B.; Rabe, K.M.; Streiffer, S. K.; Triscone, J. M. Strain Tuning of Ferroelectric Thin Films. *Annu. Rev. Mater. Res.* **2007**, 37, 589−626.
[53] Gutiérrez, D.; Radaelli, G.; Sánchez, F.; Bertacco, R.; Fontcuberta, J. Bandwidth-limited Control of Orbital and Magnetic Orders in Half-doped Manganites by Epitaxial Strain. *Phys. Rev. B: Condens. Matter Mater. Phys.* **2014**, 89, 075107.
[54] Li, J.; Shan, Z.; Ma, E. Elastic Strain Engineering for Unprecedented Materials Properties. *MRS Bull.* **2014**, 39, 108−114.
[55] Weber, M.C.; Guennou, M.; Dix, N.; Pesquera, D.; Sánchez, F.; Herranz, G.; Fontcuberta, J.; López-Conesa, L.; Estradé, S.; Peiró, F.; Iñiguez, J.; Kreisel, J. Multiple Strain-induced Phase Transitions in $LaNiO_3$ Thin Films. *Phys. Rev. B: Condens. Matter Mater. Phys.* **2016**, 94, 014118.
[56] Oka, D.; Fukumura, T. Crystal Engineering for Novel Functionalities with Oxide Thin Film Epitaxy. *CrystEngComm* **2017**, 19, 2144−2162.
[57] Choi, K. J.; Biegalski, M.; Li, Y. L.; Sharan, A.; Schubert, J.; Uecker, R.; Chen, L. Q. Enhancement of ferroelectricity in strained $BaTiO_3$ thin films. *Science* **2004**, 306(5698), 1005-1009.
[58] Rodriguez, J. A.; Remack, K.; Boku, K.; Udayakumar, K. R.; Aggarwal, S.; Summerfelt, S. R.; Moise, T. Reliability properties of low-voltage ferroelectric capacitors and memory arrays. *IEEE T. Device Mat. Re.* **2004**, 4(3), 436-449.
[59] McAdams, H. P.; Acklin, R.; Blake, T.; Du, X. H.; Eliason, J.; Fong, J.; Natarajan, S. A 64-Mb embedded FRAM utilizing a 130-nm 5LM Cu/FSG logic process. *IEEE J. Solid-St. Circ.* **2004**, 39(4), 667-677.
[60] Tuller, H. L.; Bishop, S. R. Point defects in oxides: tailoring materials through defect engineering. *Annu. Rev. Mater. Res.* **2011**, 41, 369-398.
[61] Sinsheimer, J.; Callori, S. J.; Ziegler, B.; Bein, B.; Chinta, P. V.; Ashrafi, A.; Dawber, M. In-situ X-ray diffraction study of the growth of highly strained epitaxial $BaTiO_3$ thin films. *Appl. Phys. Lett.* **2013**, 103(24), 242904.
[62] Yanase, N.; Abe, K.; Fukushima, N.; Kawakubo, T. Thickness dependence of ferroelectricity in heteroepitaxial $BaTiO_3$ thin film capacitors. *Jpn. J. Appl. Phys.* **1999**, 38(9S), 5305.
[63] Petraru, A.; Pertsev, N. A.; Kohlstedt, H.; Poppe, U.; Waser, R.; Solbach, A.; Klemradt, U. Polarization and lattice strains in epitaxial $BaTiO_3$ films grown by high-pressure sputtering. *J. Appl. Phys.* **2007**, 101(11), 114106.
[64] Khestanova, E.; Dix, N.; Fina, I.; Scigaj, M.; Rebled, J. M.; Magén, C.; Sánchez, F. Untangling electrostatic and strain effects on the polarization of ferroelectric superlattices. *Adv. Funct. Mater.* **2016**, 26(35), 6446-6453.
[65] Lee, H. N.; Seo, S. S. A.; Choi, W. S.; Rouleau, C. M. Growth control of oxygen stoichiometry in homoepitaxial $SrTiO_3$ films by pulsed laser epitaxy in high vacuum.

*Sci. Rep.* **2016**, 6, 19941.
[66] Barth, J. V.; Costantini, G.; Kern, K. Engineering atomic and molecular nanostructures at surfaces. *Nature* **2005**, 437, 671-679.
[67] Khestanova, E.; Dix, N.; Fina, I.; Scigaj, M.; Rebled, J. M.; Magén, C.; Sánchez, F. Untangling electrostatic and strain effects on the polarization of ferroelectric superlattices. *Adv. Funct. Mater.* **2016**, 26(35), 6446-6453.
[68] Park, Y. D.; Lim, J. A.; Lee, H. S.; Cho, K. Interface engineering in organic transistors. *Mater. Today* **2007**, 10(3), 46-54.
[69] Chen, S.; Manders, J. R.; Tsang, S. W.; So, F. Metal oxides for interface engineering in polymer solar cells. *J. Mater. Chem.* **2012**, 22(46), 24202-24212.
[70] Grancini, G.; Roldán-Carmona, C.; Zimmermann, I.; Mosconi, E.; Lee, X.; Martineau, D.; Nazeeruddin, M. K. One-year stable perovskite solar cells by 2D/3D interface engineering. *Nat. Comm.* **2012**, 8, 15684.
[71] Graetzel, M.; Janssen, R. A.; Mitzi, D. B.; Sargent, E. H. Materials interface engineering for solution-processed photovoltaics. *Nature* **2012**, 488(7411), 304.
[72] Zhou, H.; Chen, Q.; Li, G.; Luo, S.; Song, T. B.; Duan, H. S.; Yang, Y. Interface engineering of highly efficient perovskite solar cells. *Science* **2012**, 345(6196), 542-546.
[73] Ohtomo, A.; Hwang, H. Y. A high-mobility electron gas at the $LaAlO_3/SrTiO_3$ heterointerface. *Nature* **2004**, 427(6973), 423.
[74] Huijben, M.; Brinkman, A.; Koster, G.; Rijnders, G.; Hilgenkamp, H.; Blank, D. H. Structure-property relation of $SrTiO_3/LaAlO_3$ interfaces. *Adv. Mater.* **2009**, 21(17), 1665-1677.
[75] Chen, H.; Kolpak, A. M.; Ismail-Beigi, S. Electronic and magnetic properties of $SrTiO_3/LaAlO_3$ interfaces from first principles. *Adv. Mater.* **2010**, 22, 2881-2899.
[76] Herranz, G.; Sánchez, F.; Dix, N.; Scigaj, M.; Fontcuberta, J. High mobility conduction at (110) and (111) $LaAlO_3/SrTiO_3$ interfaces. *Sci. Rep.* **2012**, 2, 758.
[77] Nieh, C. W.; Lee, Y. J.; Lee, W. C.; Yang, Z. K.; Kortan, A. R.; Hong, M.; Hsu, C. H. Nanometer thick single crystal $Y_2O_3$ films epitaxially grown on Si (111) with structures approaching perfection. *Appl. Phys. Lett.* **2008**, 92(6), 061914.
[78] Tarnawska, L.; Giussani, A.; Zaumseil, P.; Schubert, M. A.; Paszkiewicz, R.; Brandt, O.; Schroeder, T. Single crystalline $Sc_2O_3/Y_2O_3$ heterostructures as novel engineered buffer approach for GaN integration on Si(111). *J. Appl. Phys.* **2010**, 108(6), 063502.
[79] Wang, J.; Anderoglu, O.; Hirth, J. P.; Misra, A.; Zhang, X. Dislocation structures of $\Sigma 3\{112\}$ twin boundaries in face centered cubic metals. *Appl. Phys. Lett.* **2009**, 95(2), 021908.
[80] Roldan, J.; Sanchez, F.; Trtik, V.; Guerrero, C.; Benitez, F.; Ferrater, C.; Varela, M. Epitaxial $SrRuO_3$ thin films on $LaAlO_3$ (100) and Si (100). *Appl. Surf. Sci.* **2000**, 154, 159-164.
[81] Lee, H. N.; Hesse, D.; Zakharov, N.; Gösele, U. Ferroelectric $Bi_{3.25}La_{0.75}Ti_3O_{12}$ films of uniform *a*-axis orientation on silicon substrates. *Science* **2002**, 296(5575), 2006.
[82] Chen, M. S.; Wu, T. B.; Wu, J. M. Effect of textured $LaNiO_3$ electrode on the

fatigue improvement of Pb($Zr_{0.53}Ti_{0.47}$)$O_3$ thin films. *Appl. Phys. Lett.* **1996**, 68(10), 1430-1432.
[83] Wu, W.; Wong, K. H.; Choy, C. L.; Zhang, Y. H. Top-interface-controlled fatigue of epitaxial Pb($Zr_{0.52}Ti_{0.48}$)$O_3$ ferroelectric thin films on $La_{0.7}Sr_{0.3}MnO_3$ electrodes. *Appl. Phys. Lett.* **2000**, 77(21), 3441-3443.
[84] Nagaraj, B.; Aggarwal, S.; Ramesh, R. Influence of contact electrodes on leakage characteristics in ferroelectric thin films. *J. Appl. Phys.* **2001**, 90(1), 375-382.
[85] Pintilie, L.; Pasuk, I.; Negrea, R.; Filip, L. D.; Pintilie, I. The effect of the top electrode interface on the hysteretic behavior of epitaxial ferroelectric Pb(Zr,Ti)$O_3$ thin films with bottom $SrRuO_3$ electrode. *J. Appl. Phys.* **2012**, 112(6), 064116.
[86] Pintilie, L.; Vrejoiu, I.; Hesse, D.; Alexe, M. The influence of the top-contact metal on the ferroelectric properties of epitaxial ferroelectric Pb($Zr_{0.2}Ti_{0.8}$)$O_3$ thin films. *J. Appl. Phys.* **2008**, 104(11), 114101.
[87] Hrib, L. M.; Boni, A. G.; Chirila, C.; Pasuk, I.; Pintilie, I.; Pintilie, L. Electrode interface control of the Schottky diode-like behavior in epitaxial Pb($Zr_{0.2}Ti_{0.8}$)$O_3$ thin films: A critical analysis. *J. Appl. Phys.* **2013**, 113(21), 214108.
[88] Lee, J.; Choi, C. H.; Park, B. H.; Noh, T. W.; Lee, J. K. Built-in voltages and asymmetric polarization switching in Pb(Zr,Ti)$O_3$ thin film capacitors. *Appl. Phys. Lett.* **1998**, 72(25), 3380-3382.
[89] Boni, A. G.; Chirila, C.; Pasuk, I.; Negrea, R.; Trupina, L.; Le Rhun, G.; Pintilie, L. Electrode interface controlled electrical properties in epitaxial Pb($Zr_{0.52}Ti_{0.48}$)$O_3$ films grown on Si substrates with $SrTiO_3$ buffer layer. *Thin Solid Films* **2015**, 593, 124-130.
[90] Kim, K.; Song, Y. J. Integration technology for ferroelectric memory devices. *Microelectron. Reliab.* **2003**, 43(3), 385-398.
[91] Takahashi, M.; Sakai, S. Self-aligned-gate metal/ferroelectric/insulator semiconductor field-effect transistors with long memory retention. *Jpn. J. Appl. Phys.* **2005**, 44(6L), L800.
[92] Setter, N.; Damjanovic, D.; Eng, L.; Fox, G.; Gevorgian, S.; Hong, S.; Stolitchnov, I. Ferroelectric thin films: Review of materials, properties and applications. *J. Appl. Phys.* **2006**, 100(5), 051606.
[93] Kushida, K.; Miki, H.; Torii, K.; Fujisaki, Y. Electrode-induced degradation of Pb($Zr_xTi_{1-x}$)$O_3$ (PZT) polarization hysteresis characteristics in Pt/PZT/Pt ferroelectric thin film capacitors. *Appl. Phys. Lett.* **1996**, 69(21), 3188-3190.
[94] Han, J. P.; Ma, T. P. Electrode dependence of hydrogen-induced degradation in ferroelectric Pb(Zr,Ti)$O_3$ and $SrBi_2Ta_2O_9$ thin films. *Appl. Phys. Lett.* **1997**, 71(9), 1267-1269.
[95] Shaw, T. M.; Trolier, S.; McIntyre, P. C. The properties of ferroelectric films at small dimensions. *Annu. Rev. Mater. Res.* **2000**, 30(1), 263-298.
[96] Ahn, C. H.; Rabe, K. M.; Triscone, J. M. Ferroelectricity at the nanoscale: local polarization in oxide thin films and heterostructures. *Science* **2004**, 303(5657), 488-491.
[97] Jeong, D. S.; Thomas, R.; Katiyar, R. S.; Scott, J. F.; Kohlstedt, H.; Petraru, A.; Hwang, C. S. Emerging memories: resistive switching mechanisms and current status.

*Rep. Prog. Phys.* **2012**, 75(7), 076502.
[98] Mikolajick, T.; Slesazeck, S.; Park, M. H.; Schroeder, U. Ferroelectric hafnium oxide for ferroelectric random-access memories and ferroelectric field-effect transistors. *MRS Bull.* **2018**, 43(5), 340-346.
[99] Tian, X.; Shibayama, S.; Nishimura, T.; Yajima, T.; Migita, S.; Toriumi, A. Evolution of ferroelectric $HfO_2$ in ultrathin region down to 3nm. *Appl. Phys. Lett.* **2018**, 112(10), 102902.
[100] Bersch, E.; Rangan, S.; Bartynski, R. A.; Garfunkel, E.; Vescovo, E. Band offsets of ultrathin high-κ oxide films with Si. *Phys. Rev. B* **2008**, 78(8), 085114.
[101] Wang, J.; Li, H. P.; Stevens, R. Hafnia and hafnia-toughened ceramics. *J. Mater. Sci.* **1992**, 27(20), 5397-5430.
[102] Ohtaka, O.; Fukui, H.; Kunisada, T.; Fujisawa, T.; Funakoshi, K.; Utsumi, W.; Kikegawa, T. Phase relations and volume changes of hafnia under high pressure and high temperature. *J. Am Ceram. Soc.* **2001**, 84(6), 1369-1373.
[103] Shimizu, T. Ferroelectricity in $HfO_2$ and related ferroelectrics. *J. Ceram. Soc. Jpn.* **2018**, 126(9), 667-674.
[104] Huan, T. D.; Sharma, V.; Rossetti Jr, G. A.; Ramprasad, R. Pathways towards ferroelectricity in hafnia. *Phys. Rev. B* **2014**, 90(6), 064111.
[105] Sang, X.; Grimley, E. D.; Schenk, T.; Schroeder, U.; LeBeau, J. M. On the structural origins of ferroelectricity in $HfO_2$ thin films. *Appl. Phys. Lett.* **2015**, 106(16), 162905.
[106] Lowther, J. E.; Dewhurst, J. K.; Leger, J. M.; Haines, J. Relative stability of $ZrO_2$ and $HfO_2$ structural phases. *Phys. Rev. B* **1999**, 60(21), 14485.
[107] Reyes-Lillo, S. E.; Garrity, K. F.; Rabe, K. M. Antiferroelectricity in thin-film $ZrO_2$ from first principles. *Phys. Rev. B* **2014**, 90(14), 140103.
[108] Muller, J.; Böscke, T. S.; Schröder, U.; Mueller, S.; Bräuhaus, D.; Böttger, U.; Mikolajick, T. Ferroelectricity in simple binary $ZrO_2$ and $HfO_2$. *Nano Lett.* **2012**, 12(8), 4318-4323.
[109] Mueller, S.; Mueller, J.; Singh, A.; Riedel, S.; Sundqvist, J.; Schroeder, U.; Mikolajick, T. Incipient ferroelectricity in Al-doped $HfO_2$ thin films. *Adv. Funct. Mater.* **2012**, 22(11), 2412-2417.
[110] Mueller, S., Adelmann, C., Singh, A., Van Elshocht, S., Schroeder, U., & Mikolajick, T. Ferroelectricity in Gd-doped $HfO_2$ thin films. *ECS J. Solid State Sc.* **2012**, 1(6), N123-N126.
[111] Starschich, S.; Griesche, D.; Schneller, T.; Böttger, U. Chemical solution deposition of ferroelectric hafnium oxide for future lead free ferroelectric devices. *ECS J. Solid State Sc.* **2015**, 4(12), P419-P423.
[112] Xu, L.; Nishimura, T.; Shibayama, S.; Yajima, T.; Migita, S.; Toriumi, A. Kinetic pathway of the ferroelectric phase formation in doped $HfO_2$ films. *J. Appl. Phys.* **2017**, 122(12), 124104.
[113] Schroeder, U.; Yurchuk, E.; Müller, J.; Martin, D.; Schenk, T.; Polakowski, P.; Mikolajick, T. Impact of different dopants on the switching properties of ferroelectric hafniumoxide. *Jpn. J. Appl. Phys.* **2014**, 53(8S1), 08LE02.
[114] Park, M. H.; Schenk, T.; Fancher, C. M.; Grimley, E. D; Zhou, C.; Richter, C.;

Schroeder, U. A comprehensive study on the structural evolution of $HfO_2$ thin films doped with various dopants. *J. Mater. Chem.C* **2017**, 5(19), 4677-4690.
[115] Starschich, S.; Boettger, U. An extensive study of the influence of dopants on the ferroelectric properties of $HfO_2$. *J. Mater. Chem.C* **2017**, 5(2), 333-338.
[116] Starschich, S.; Schenk, T.; Schroeder, U.; Boettger, U. Ferroelectric and piezoelectric properties of $Hf_{1-x}Zr_xO_2$ and pure $ZrO_2$ films. *Appl. Phys. Lett.* **2017**, 110(18), 182905.
[117] Shimizu, T.; Katayama, K.; Kiguchi, T.; Akama, A.; Konno, T. J.; Sakata, O.; Funakubo, H. The demonstration of significant ferroelectricity in epitaxial Y-doped $HfO_2$ film. *Sci. Rep.* **2016**, 6, 32931.
[118] Lee, Y. H.; Kim, H. J.; Moon, T.; Do Kim, K.; Hyun, S. D.; Park, H. W.; Hwang, C. S. Preparation and characterization of ferroelectric $Hf_{0.5}Z_{r0.5}O_2$ thin films grown by reactive sputtering. *Nanotechnology* **2017**, 28(30), 305703.
[119] Olsen, T.; Schröder, U.; Müller, S.; Krause, A.; Martin, D.; Singh, A.; Mikolajick, T. Co-sputtering yttrium into hafnium oxide thin films to produce ferroelectric properties. *Appl. Phys. Lett.* **2012**, 101(8), 082905.
[120] Shimizu, T.; Yokouchi, T.; Shiraishi, T.; Oikawa, T.; Krishnan, P. S. R.; Funakubo, H. Study on the effect of heat treatment conditions on metalorganic-chemical-vapor-deposited ferroelectric $Hf_{0.5}Z_{r0.5}O_2$ thin film on Ir electrode. *Jpn. J. Appl. Phys.* **2014**, 53(9S), 09PA04.
[121] Kim, S. J.; Narayan, D.; Lee, J. G.; Mohan, J.; Lee, J. S.; Lee, J.; Summerfelt, S. R. Large ferroelectric polarization of TiN/$Hf_{0.5}Z_{r0.5}O_2$/TiN capacitors due to stress-induced crystallization at low thermal budget. *Appl. Phys. Lett.* **2017**, 111(24), 242901.
[122] Park, M. H.; Kim, H. J.; Kim, Y. J.; Jeon, W.; Moon, T.; Hwang, C. S. Ferroelectric properties and switching endurance of $Hf_{0.5}Z_{r0.5}O_2$ films on TiN bottom and TiN or $RuO_2$ top electrodes. *Phys. Status Solid-R.* **2014**, 8(6), 532-535.
[123] Hyuk Park, M.; Joon Kim, H.; Jin Kim, Y.; Lee, W.; Kyeom Kim, H.; Seong Hwang, C. Effect of forming gas annealing on the ferroelectric properties of $Hf_{0.5}Z_{r0.5}O_2$ thin films with and without Pt electrodes. *Appl. Phys. Lett.* **2013**, 102(11), 112914.
[124] Park, M. H.; Kim, H. J.; Kim, Y. J.; Lee, W.; Moon, T.; Kim, K. D.; Hwang, C. S. Study on the degradation mechanism of the ferroelectric properties of thin $Hf_{0.5}Z_{r0.5}O_2$ films on TiN and Ir electrodes. *Appl. Phys. Lett.* **2014**, 105(7), 072902.
[125] Hoffmann, M.; Schroeder, U.; Schenk, T.; Shimizu, T.; Funakubo, H.; Sakata, O.; Kersch, A. Stabilizing the ferroelectric phase in doped hafnium oxide. *J. Appl. Phys.* **2015**, 118(7), 072006.
[126] Hyuk Park, M.; Joon Kim, H.; Jin Kim, Y.; Lee, W.; Moon, T.; Seong Hwang, C. Evolution of phases and ferroelectric properties of thin $Hf_{0.5}Z_{r0.5}O_2$ films according to the thickness and annealing temperature. *Appl. Phys. Lett.* **2013**, 102(24), 242905.
[127] Lowther, J. E.; Dewhurst, J. K.; Leger, J. M.; Haines, J. Relative stability of $ZrO_2$ and $HfO_2$ structural phases. *Phys. Rev. B* **1999**, 60(21), 14485.
[128] Curtis, C. E.; Doney, L. M.; Johnson, J. R. Some properties of hafnium oxide, hafnium silicate, calcium hafnate, and hafnium carbide. *J. Am Ceram. Soc.* **1954**,

37(10), 458-465.
[129] Kim, H. J.; Park, M. H.; Kim, Y. J.; Lee, Y. H.; Jeon, W.; Gwon, T.; Hwang, C. S. Grain size engineering for ferroelectric $Hf_{0.5}Z_{r0.5}O_2$ films by an insertion of $Al_2O_3$ interlayer. *Appl. Phys. Lett.* **2014**, 105(19), 192903.
[130] Starschich, S.; Griesche, D.; Schneller, T.; Waser, R.; Böttger, U. Chemical solution deposition of ferroelectric yttrium-doped hafnium oxide films on platinum electrodes. *Appl. Phys. Lett.* **2014**, 104(20), 202903.
[131] Riedel, S.; Polakowski, P.; Müller, J. A thermally robust and thickness independent ferroelectric phase in laminated hafnium zirconium oxide. *AIP Adv.* **2016** 6(9), 095123.
[132] Morozovska, A. N.; Glinchuk, M. D.; Eliseev, E. A. Phase transitions induced by confinement of ferroic nanoparticles. *Phys. Rev. B* **2007**, 76(1), 014102.
[133] Polking, M. J.; Urban, J. J.; Milliron, D. J.; Zheng, H.; Chan, E.; Caldwell, M. A.; Alivisatos, A. P. Size-dependent polar ordering in colloidal GeTe nanocrystals. *Nano Lett.* **2011**, 11(3), 1147-1152.
[134] Materlik, R.; Künneth, C.; Kersch, A. The origin of ferroelectricity in $Hf_{1-x}Zr_xO_2$: A computational investigation and a surface energy model. *J. Appl. Phys.* **2015**, 117(13), 134109.
[135] Lee, C. K.; Cho, E.; Lee, H. S.; Hwang, C. S.; Han, S. First-principles study on doping and phase stability of $HfO_2$. *Phys. Rev. B* **2008**, 78(1), 012102.
[136] Shannon, R. D. Revised effective ionic radii and systematic studies of interatomic distances in halides and chalcogenides. *Acta Crystallogr. A* **1976**, 32(5), 751-767.
[137] Schroeder, U.; Yurchuk, E.; Müller, J.; Martin, D.; Schenk, T.; Polakowski, P.; Mikolajick, T. Impact of different dopants on the switching properties of ferroelectric hafnium oxide. *Jpn. J. Appl. Phys.* **2014**, 53(8S1), 08LE02.
[138] Müller, J.; Schröder, U.; Böscke, T. S.; Müller, I.; Böttger, U.; Wilde, L.; Frey, L. Ferroelectricity in yttrium-doped hafnium oxide. *J. Appl. Phys.* **2011**, 110(11), 114113.
[139] Park, M. H.; Lee, Y. H.; Mikolajick, T.; Schroeder, U.; Hwang, C. S. Review and perspective on ferroelectric $HfO_2$-based thin films for memory applications. *MRS Comm*. **2018**, 8(3), 795-808.
[140] Pešić, M.; Fengler, G.; Larcher, L.; Padovani, A.; Schenk, T.; Grimley, E. D.; Mikolajick, T. Physical Mechanisms behind the Field-Cycling Behavior of $HfO_2$-Based Ferroelectric Capacitors. *Adv. Funct. Mater.* **2016**, 26(25), 4601-4612.
[141] Schenk, T.; Yurchuk, E.; Mueller, S.; Schroeder, U.; Starschich, S.; Böttger, U.; Mikolajick, T. About the deformation of ferroelectric hystereses. *Appl. Phys. Rev.* **2014**, 1(4), 041103.
[142] Schenk, T.; Hoffmann, M.; Ocker, J.; Pešić, M.; Mikolajick, T.; Schroeder, U. Complex internal bias fields in ferroelectric hafnium oxide. *ACS Appl. Mater. Inter.* **2015**, 7(36), 20224-20233.
[143] Grimley, E. D.; Schenk, T.; Sang, X.; Pešić, M.; Schroeder, U.; Mikolajick, T.; LeBeau, J. M. Structural Changes Underlying Field-Cycling Phenomena in Ferroelectric $HfO_2$ Thin Films. *Adv. Electron. Mater.* **2016**, 2(9), 1600173.

[144] Kim, H. J.; Park, M. H.; Kim, Y. J.; Lee, Y. H.; Moon, T.; Do Kim, K.; Hwang, C. S. A study on the wake-up effect of ferroelectric $Hf_{0.5}Zr_{0.5}O_2$ films by pulse-switching measurement. *Nanoscale* **2016**, 8(3), 1383-1389.
[145] Kozodaev, M. G.; Chernikova, A. G.; Korostylev, E. V.; Park, M. H.; Khakimov, R. R.; Hwang, C. S.; Markeev, A. M. Mitigating wakeup effect and improving endurance of ferroelectric $HfO_2$-$ZrO_2$ thin films by careful La-doping. *J. Appl. Phys.* **2019**, 125(3), 034101.
[146] Clima, S.; Wouters, D. J.; Adelmann, C.; Schenk, T.; Schroeder, U.; Jurczak, M.; Pourtois, G. Identification of the ferroelectric switching process and dopant dependent switching properties in orthorhombic $HfO_2$: A first principles insight. *Appl. Phys. Lett.* **2014**, 104(9), 092906.
[147] Lu, X.; Li, H.; Cao, W. Landau expansion parameters for $BaTiO_3$. *J. Appl. Phys.* **2013**, 114(22), 224106.
[148] Barabash, S. V.; Pramanik, D.; Zhai, Y.; Magyari-Kope, B.; Nishi, Y. Ferroelectric switching pathways and energetics in $(Hf,Zr)O_2$. *ECS Trans.* **2017**, 75(32), 107-121.
[149] Richter, C.; Schenk, T.; Park, M. H.; Tscharntke, F. A.; Grimley, E. D.; LeBeau, J. M.; Schroeder, U. Si doped hafnium oxide—A “fragile” ferroelectric system. *Adv. Electron. Mater.* **2017**, 3(10), 1700131.
[150] Schroeder, U.; Richter, C.; Park, M. H.; Schenk, T.; Pešić, M.; Hoffmann, M.; Chung, C. Lanthanum-doped hafnium oxide: a robust ferroelectric material. *Inorg. Chem.* **2018**, 57(5), 2752-2765.
[151] Chernikova, A. G.; Kozodaev, M. G.; Negrov, D. V.; Korostylev, E. V.; Park, M. H.; Schroeder, U.; Markeev, A. M. Improved ferroelectric switching endurance of La-doped $Hf_{0.5}Zr_{0.5}O_2$ thin films. *ACS Appl. Mater. Inter.* **2018**, 10(3), 2701-2708.
[152] Park, M. H.; Kim, H. J.; Kim, Y. J.; Lee, Y. H.; Moon, T.; Kim, K. D.; Hwang, C. S. Effect of Zr Content on the Wake-Up Effect in $Hf_{1-x}Zr_xO_2$ Films. *ACS Appl. Mater. Inter.* **2016**, 8(24), 15466-15475.
[153] Starschich, S.; Menzel, S.; Böttger, U. Pulse wake-up and breakdown investigation of ferroelectric yttrium doped $HfO_2$. *J. Appl. Phys.* **2017**, 121(15), 154102.
[154] Huang, F.; Chen, X.; Liang, X.; Qin, J.; Zhang, Y.; Huang, T.; Zhang, L. Fatigue mechanism of yttrium-doped hafnium oxide ferroelectric thin films fabricated by pulsed laser deposition. *Phys. Chem. Chem. Phys.* **2017**, 19(5), 3486-3497.
[155] Streiffer, S. T.; Eastman, J. A.; Fong, D. D.; Thompson, C.; Munkholm, A.; Murty, M. R.; Stephenson, G. B. Observation of Nanoscale 180° Stripe Domains in Ferroelectric $PbTiO_3$ Thin Films. *Phys. Rev. Lett.* **2002**, 89(6), 067601.
[156] Fong, D. D.; Stephenson, G. B.; Streiffer, S. K.; Eastman, J. A.; Auciello, O.; Fuoss, P. H.; Thompson, C. Ferroelectricity in ultrathin perovskite films. *Science* **2004**, 304(5677), 1650-1653.
[157] Highland, M. J.; Fister, T. T.; Richard, M. I.; Fong, D. D.; Fuoss, P. H.; Thompson, C.; Stephenson, G. B. Polarization switching without domain formation at the intrinsic coercive field in ultrathin ferroelectric $PbTiO_3$. *Phys. Rev. Lett.* **2010**, 105(16), 167601.

[158] Garcia, V.; Fusil, S.; Bouzehouane, K.; Enouz-Vedrenne, S.; Mathur, N. D.; Barthelemy, A.; Bibes, M. Giant tunnel electroresistance for non-destructive readout of ferroelectric states. *Nature* **2009**, 460(7251), 81.
[159] Stengel, M.; Vanderbilt, D.; Spaldin, N. A. Enhancement of ferroelectricity at metal-oxide interfaces. *Nat. Mater.* **2009**, 8(5), 392.
[160] Chu, Y. H.; Zhan, Q.; Martin, L. W.; Cruz, M. P.; Yang, P. L.; Pabst, G. W.; Schlom, D. G. Nanoscale domain control in multiferroic $BiFeO_3$ thin films. *Adv. Mater.* **2006**, 18(17), 2307-2311.
[161] Shimizu, T.; Katayama, K.; Kiguchi, T.; Akama, A.; Konno, T. J.; Funakubo, H. (2015). Growth of epitaxial orthorhombic $YO_{1.5}$-substituted $HfO_2$ thin film. *Appl. Phys. Lett.* **2015**, 107(3), 032910.
[162] Shimizu, T.; Katayama, K.; Funakubo, H. Epitaxial growth of $YO_{1.5}$ doped $HfO_2$ films on (100) YSZ substrates with various concentrations. *Ferroelectrics* **2017**, 512(1), 105-110.
[163] Mimura, T.; Katayama, K.; Shimizu, T.; Uchida, H.; Kiguchi, T.; Akama, A.; Funakubo, H. Formation of (111) orientation-controlled ferroelectric orthorhombic $HfO_2$ thin films from solid phase via annealing. *Appl. Phys. Lett.* **2016**, 109(5), 052903.
[164] Katayama, K.; Shimizu, T.; Sakata, O.; Shiraishi, T.; Nakamura, S.; Kiguchi, T.; Funakubo, H. Growth of (111)-oriented epitaxial and textured ferroelectric Y-doped $HfO_2$ films for downscaled devices. *Appl. Phys. Lett.* **2016**, 109(11), 112901.
[165] Suzuki, T.; Shimizu, T.; Mimura, T.; Uchida, H.; Funakubo, H. Epitaxial ferroelectric Y-doped $HfO_2$ film grown by the RF magnetron sputtering. *Jpn. J. Appl. Phys.* **2018**, 57(11S), 11UF15.
[166] Lee, K.; Lee, T. Y.; Yang, S. M.; Lee, D. H.; Park, J.; Chae, S. C. Ferroelectricity in epitaxial Y-doped $HfO_2$ thin film integrated on Si substrate. *Appl. Phys. Lett.* **2018**, 112(20), 202901.
[167] Kiguchi, T.; Nakamura, S.; Akama, A.; Shiraishi, T.; Konno, T. J. Solid state epitaxy of $(Hf,Zr)O_2$ thin films with orthorhombic phase. *J. Ceram. Soc. Jpn.* **2016**, 124(6), 689-693.
[168] Wei, Y.; Nukala, P.; Salverda, M.; Matzen, S.; Zhao, H. J.; Momand, J.; Kooi, B. J. A rhombohedral ferroelectric phase in epitaxially strained $Hf_{0.5}Zr_{0.5}O_2$ thin films. *Nat. Mater.* **2018**, 17(12), 1095.
[169] Li, T.; Zhang, N.; Sun, Z.; Xie, C.; Ye, M.; Mazumdar, S.; Ke, S. Epitaxial ferroelectric $Hf_{0.5}Zr_{0.5}O_2$ thin film on a buffered YSZ substrate through interface reaction. *J. Mater. Chem. C* **2018**, 6(34), 9224-9231.
[170] Yoong, H. Y.; Wu, H.; Zhao, J.; Wang, H.; Guo, R.; Xiao, J.; Yan, X. Epitaxial Ferroelectric $Hf_{0.5}Zr_{0.5}O_2$ Thin Films and Their Implementations in Memristors for Brain‐Inspired Computing. *Adv. Funct. Mater.* **2018**, 28(50), 1806037.
[171] Shiraishi, T.; Choi, S.; Kiguchi, T.; Shimizu, T.; Uchida, H.; Funakubo, H.; Konno, T. J. Fabrication of ferroelectric Fe doped $HfO_2$ epitaxial thin films by ion-beam sputtering method and their characterization. *Jpn. J. Appl. Phys.* **2018**, 57(11S), 11UF02.
[172] Li, T.; Ye, M.; Sun, Z.; Zhang, N.; Zhang, W.; Inguva, S.; Huang, H. Origin of

Ferroelectricity in Epitaxial Si-Doped $HfO_2$ Films. *ACS Appl. Mater. Inter.* **2019**, 11(4), 4139-4144..
[173] Giessibl, F. J. Advances in atomic force microscopy. *Rev. Mod. Phys.* **2003**, 75(3), 949.
[174] Liu, F.; Fina, I.; Gutiérrez, D.; Radaelli, G.; Bertacco, R.; Fontcuberta, J. Selecting Steady and Transient Photocurrent Response in $BaTiO_3$ Films. *Adv. Electron. Mater.* **2015**, 1(9), 1500171.
[175] Liu, F.; Fina, I.; Bertacco, R.; Fontcuberta, J. Unravelling and controlling hidden imprint fields in ferroelectric capacitors. *Sci. Rep.* **2016**, 6, 25028.
[176] Fina, I.; Fàbrega, L.; Langenberg, E.; Martí, X.; Sánchez, F.; Varela, M.; Fontcuberta, J. Non-ferroelectric contributions to the hysteresis cycles in manganite thin films: A comparative study of measurement techniques. *J. Appl. Phys.* **2011**, 109(7), 074105.
[177] Haeni, J. H.; Irvin, P.; Chang, W.; Uecker, R.; Reiche, P.; Li, Y. L.; Tagantsev, A. K. Room-temperature ferroelectricity in strained $SrTiO_3$. *Nature* **2004**, 430(7001), 758.
[178] Chen, Y. B.; Sun, H. P.; Katz, M. B.; Pan, X. Q.; Choi, K. J.; Jang, H. W.; Eom, C. B. Interface structure and strain relaxation in $BaTiO_3$ thin films grown on $GdScO_3$ and $DyScO_3$ substrates with buried coherent $SrRuO_3$ layer. *Appl. Phys. Lett.* **2007**, 91, 252906.
[179] Harrington, S. A.; Zhai, J.; Denev, S.; Gopalan, V.; Wang, H.; Bi, Z.; Jia, Q. Thick lead-free ferroelectric films with high Curie temperatures through nanocomposite-induced strain. *Nat. Nanotechnol.* **2011**, 6, 491.
[180] Pramanick, A.; Prewitt, A. D.; Forrester, J. S.; Jones, J. L. Domains, domain walls and defects in perovskite ferroelectric oxides: A review of present understanding and recent contributions. *Crit. Rev. Sol. Sta. Mater. Sci.* **2012**, 37, 243-275.
[181] Chen, X.; Yang, S.; Kim, J. H.; Kim, H. D.; Kim, J. S.; Rojas, G.; Guisinger, N. Ultrathin $BaTiO_3$ templates for multiferroic nanostructures. *New J. Phys.* **2011**, 13, 083037.
[182] Dix, N.; Fina, I.; Bachelet, R.; Fàbrega, L.; Kanamadi, C.; Fontcuberta, J.; Sánchez, F. Large out-of-plane ferroelectric polarization in flat epitaxial $BaTiO_3$ on $CoFe_2O_4$ heterostructures. *Appl. Phys. Lett.* **2013**, 102, 172907.
[183] Yan, H.; Inam, F.; Viola, G.; Ning, H.; Zhang, H.; Jiang, Q.; Zeng, T.; Gao, Z.; Reece, M. The Contribution of Electrical Conductivity, Dielectric Permittivity and Domain Switching in Ferroelectric Hysteresis Loops. *J. Adv. Dielectr.* **2011**, 01, 107−118.
[184] Jin, L.; Li, F.; Zhang, S. Decoding the Fingerprint of Ferroelectric Loops: Comprehension of the Material Properties and Structures. *J. Am. Ceram. Soc.* **2014**, 97, 1−27.
[185] Morishima, Y.; Niwa, E.; Hashimoto, T. Analysis of thermal stability of $LaNi_{1-x}Fe_xO_{3-\delta}$ (x = 0.0, 0.2, 0.4) by thermogravimetry and high-temperature X-ray diffraction under controlled oxygen partial pressures. *J. Therm. Anal. Calorim.* **2016**, 123, 1769−1775.
[186] Pintilie, L.; Boerasu, I.; Gomes, M. J. M.; Zhao, T.; Ramesh, R.; Alexe, M.

Metal-ferroelectric-metal structures with Schottky contacts. II. Analysis of the experimental current-voltage and capacitance voltage characteristics of Pb(Zr,Ti)$O_3$ thin films. *J. Appl. Phys.* **2005**, 98, 124104.
[187] Chen, A. P.; Khatkhatay, F.; Zhang, W.; Jacob, C.; Jiao, L.; Wang, H. Strong oxygen pressure dependence of ferroelectricity in $BaTiO_3$/$SrRuO_3$/$SrTiO_3$ epitaxial heterostructures. *J. Appl. Phys.* **2013**, 114, 124101.
[188] Li, M.; Zhou, J.; Jing, X.; Zeng, M.; Wu, S.; Gao, J.; Zhang, Z.; Gao, X.; Lu, X.; Liu, J.-M.; Alexe, M. Controlling Resistance Switching Polarities of Epitaxial $BaTiO_3$ Films by Mediation of Ferroelectricity and Oxygen Vacancies. *Adv. Electron. Mater.* **2015**, 1, 1500069.
[189] Lyu, J.; Fina, I.; Solanas, R.; Fontcuberta, J.; Sánchez, F. Tailoring Lattice Strain and Ferroelectric Polarization of Epitaxial $BaTiO_3$ Thin Films on Si(001). *Sci. Rep.* **2018**, 8, 495.
[190] Lyu, J.; Estandía, S.; Gazquez, J.; Chisholm, M. F.; Fina, I.; Dix, N.; Sánchez, F. Control of Polar Orientation and Lattice Strain in Epitaxial $BaTiO_3$ Films on Silicon. *ACS Appl. Mater. Inter.* **2018**, 10, 25529-25535.
[191] Kan, D.; Shimakawa, Y. Controlled cation stoichiometry in pulsed laser deposition-grown $BaTiO_3$ epitaxial thin films with laser fluence. *Appl. Phys. Lett.* **2011**, 99, 081907.
[192] Dasgupta, A.; Saremi, S.; Ruijuan, X.; Dedon, L. R.; Pandya, S.; Damodaran, A. R.; Martin, L. W. Nonstoichiometry, structure, and properties of $Ba_{1-x}TiO_y$ thin films. *J. Mater. Chem. C* **2018**, 6, 10751-10759.
[193] Jaber, N.; Wolfman, J.; Daumont, C.; Negulescu, B.; Ruyter, A.; Sauvage, T.; Gervais, F. Laser fluence and spot size effect on compositional and structural properties of $BiFeO_3$ thin films grown by Pulsed Laser Deposition. *Thin Solid Films* **2017**, 634, 107-111.
[194] Shelke, V.; Harshan, V. N.; Kotru, S.; Gupta, A. Effect of kinetic growth parameters on leakage current and ferroelectric behavior of $BiFeO_3$ thin films. *J. Appl. Phys.* **2009**, 106, 104114.
[195] Perriere, J.; Millon, E.; Seiler, W.; Boulmer-Leborgne, C.; Craciun, V.; Albert, O.; Etchepare, J. Comparison between ZnO films grown by femtosecond and nanosecond laser ablation. *J. Appl. Phys.* **2002**, 91, 690-696.
[196] Saremi, S.; Xu, R.; Dedon, L. R.; Mundy, J. A.; Hsu, S. L.; Chen, Z.; Martin, L. W. Enhanced electrical resistivity and properties via ion bombardment of ferroelectric thin films. *Adv. Mater.* **2016**, 28, 10750-10756.
[197] Saremi, S.; Xu, R.; Dedon, L. R.; Gao, R.; Ghosh, A.; Dasgupta, A.; & Martin, L. W. Electronic Transport and Ferroelectric Switching in Ion-Bombarded, Defect-Engineered $BiFeO_3$ Thin Films. *Adv. Mater. Inter.* **2018**, 5, 1700991.
[198] Saremi, S.; Xu, R.; Allen, F. I.; Maher, J.; Agar, J. C.; Gao, R.; Martin, L. W. Local control of defects and switching properties in ferroelectric thin films. *Phys. Rev. Mater.* **2018**, 2, 084414.
[199] Moyer, J. A.; Eaton, C.; Engel, R. Highly conductive $SrVO_3$ as a bottom electrode for functional perovskite oxides. *Adv. Mater.* **2013**, 25(26), 3578-3582.
[200] Boschker, H.; Huijben, M.; Vailionis, A.; Verbeeck, J.; van Aert, S. V.; Luysberg,

M.; Blank, D. H. Optimized fabrication of high-quality $La_{0.67}Sr_{0.33}MnO_3$ thin films considering all essential characteristics. *J. Phys. D Appl. Phys.* **2011**, 44(20), 205001.

[201] Boschker, H.; Kautz, J.; Houwman, E. P.; Siemons, W.; Blank, D. H.; Huijben, M.; Rijnders, G. High-temperature magnetic insulating phase in ultrathin $La_{0.67}Sr_{0.33}MnO_3$ films. *Phys. Rev. Lett.* **2012**, 109(15), 157207.

[202] Sánchez, F.; Ferrater, C.; Guerrero, C.; Garcia-Cuenca, M. V.;Varela, M. High-quality epitaxial $LaNiO_3$ thin films on $SrTiO_3$ (100) and $LaAlO_3$ (100). *Appl. Phys. A* **2000**, 71(1), 59-64.

[203] Fowlie, J.; Gibert, M.; Tieri, G.; Gloter, A.; Íñiguez, J.; Filippetti, A.; Kreisel, J. Conductivity and local structure of $LaNiO_3$ thin films. *Adv. Mater.* **2017**, 29(18), 1605197.

[204] Sergeenkov, S.; Cichetto Jr, L.; Zampieri, M.; Longo, E.; Araújo-Moreira, F. M. Scaling like behaviour of resistivity observed in $LaNiO_3$ thin films grown on $SrTiO_3$ substrate by pulsed laser deposition. *J. Phys-Condens. Mat.* **2015**, 27(48), 485307.

[205] Chen, J.; Luo, Y.; Ou, X.; Yuan, G.; Wang, Y.; Yang, Y.; Liu, Z. Upward ferroelectric self-polarization induced by compressive epitaxial strain in (001) $BaTiO_3$ films. *J. Appl. Phys.* **2013**, 113(20), 204105.

[206] Luo, Y.; Li, X.; Chang, L.; Gao, W.; Yuan, G.; Yin, J.; Liu, Z. Upward ferroelectric self-poling in (001)-oriented $PbZr_{0.2}Ti_{0.8}O_3$ epitaxial films with compressive strain. *AIP Adv.* **2013**, 3(12), 122101.

[207] Khomyakova, E.; Sadl, M.; Ursic, H.; Daniels, J.; Malic, B.; Bencan, A.; Rojac, T. Self-poling of $BiFeO_3$ thick films. *ACS Appl. Mater. Inter.* **2016**, 8(30), 19626.

[208] Choudhury, P. R.; Parui, J.; Chiniwar, S.; Krupanidhi, S. B. Preferential polarization and its reversal in polycrystalline $BiFeO_3/La_{0.5}Sr_{0.5}CoO_3$ heterostructures. *Solid State Comm.* **2015**, 208, 15-20.

[209] Zhang, W.; Gao, Y.; Kang, L.; Yuan, M.; Yang, Q.; Cheng, H.; Ouyang, J. Space-charge dominated epitaxial $BaTiO_3$ heterostructures. *Acta Mater.* **2015**, 85, 207.

[210] Zubko, P.; Jung, D. J.; Scott, J. F. Electrical characterization of $PbZr_{0.4}Ti_{0.6}O_3$ capacitors. *J. Appl. Phys.* **2006**, 100(11), 114113.

[211] Stengel, M.; Spaldin, N. A. Origin of the dielectric dead layer in nanoscale capacitors. *Nature* **2006**, 443(7112), 679.

[212] Tsurumaki, A.; Yamada, H.; Sawa, A. Impact of Bi Deficiencies on Ferroelectric Resistive Switching Characteristics Observed at p-Type Schottky-Like $Pt/Bi_{1-\delta}FeO_3$ Interfaces. *Adv. Funct. Mater.* **2012**, 22(5), 1040-1047.

[213] Geohegan, D.B. Fast intensified-CCD photography of $YBa_2Cu_3O_{7-x}$ laser ablation invacuum and ambient oxygen. *Appl. Phys. Lett.* **1992**, 60, 2732.

[214] Gonzalo, J.; Siegel, J.; Perea, A.; Puerto, D.; Resta, V.; Galvan M.; Afonso, C.N. Imaging Self-Sputtering and Backscattering from the Substrate during Pulsed Laser Deposition of Gold. *Phys. Rev. B* **2007**, 76, 035435.

[215] Sambri, A.; Amoruso, S.; Wang, X.; Granozio, M.; Bruzzese, R. Plume Propagation Dynamics of Complex Oxides in Oxygen. *J. Appl. Phys.* **2008**, 104, 053304.

[216] Scharf, T.; Faupel, J.; Sturm, K.; Krebs, H. Intrinsic Stress Evolution in Laser Deposited Thin Films. *J. Appl. Phys.* **2003**, 94, 4273−4278.

[217] Marrocchelli, D.; Perry, H.; Bishop, S. R. Understanding Chemical Expansion in Perovskite-structured Oxides. *Phys. Chem. Chem. Phys.* **2015**, 17, 10028−10039.

[218] Oh, D. W.; Ravichandran, J.; Liang, C. W.; Siemons, W.; Jalan, B.; Brooks, C. M.; Majumdar, A. Thermal conductivity as a metric for the crystalline quality of $SrTiO_3$ epitaxial layers. *Appl. Phys. Lett.* **2011**, 98(22), 221904.

[219] Guo, H.; Dong, S.; Rack, P. D.; Budai, J. D.; Beekman, C.; Gai, Z.; Herklotz, A. Strain doping: Reversible single-axis control of a complex oxide lattice via helium implantation. *Phys. Rev. Lett.* **2015**, 114, 256801.

[220] Mimura, T.; Shimizu, T.; Uchida, H.; Sakata, O.; Funakubo, H. Thickness-Dependent Crystal Structure and Electric Properties of Epitaxial Ferroelectric $Y_2O_3$-$HfO_2$ films. *Appl. Phys. Lett.* **2018**, 113, 102901.

[221] Pesquera, D.; Herranz, G.; Barla, A.; Pellegrin, E.; Bondino, F.; Magnano, E.; Fontcuberta, J. Surface symmetry-breaking and strain effects on orbital occupancy in transition metal perovskite epitaxial films. *Nat. Commun.* **2011**, 3, 1189.

[222] Birkholz, M. *Thin Film Analysis by X-Ray Scattering*; Wiley-VCH: Weinheim, Germany, **2005**.

[223] Sánchez, F.; Ocal, C.; Fontcuberta, J. Tailored Surfaces of Perovskite Oxide Substrates for Conducted Growth of Thin Films. *Chem. Soc. Rev.* **2014**, 43, 2272-2285.

[224] Janovec, V. On the Theory of the Coercive Field of Single-Domain Crystals of $BaTiO_3$. *Czech. J. Phys.* **1958**, 8, 3.

[225] Lee, H. N.; Nakhmanson, S. M.; Chisholm, M. F.; Christen, H. M.; Rabe, K. M.; Vanderbilt, D. Suppressed Dependence of Polarization on Epitaxial Strain in Highly Polar Ferroelectrics. *Phys. Rev. Lett.* **2007**, 98, 217602.

[226] Park, M. H.; Kim, H. J.; Kim, Y. J.; Lee, Y. H.; Moon, T.; Kim, K. D.; Hyun, S. D.; Hwang, C. S. Study on the Size Effect in $Hf_{0.5}Zr_{0.5}O_2$ Films Thinner than 8 nm Before and after Wake-up Field Cycling. *Appl. Phys. Lett.* **2015**, 107, 192907.

[227] Migita, S.; Ota, H.; Yamada, H.; Shibuya, K.; Sawa, A.; Toriumi, A. Polarization Switching Behavior of Hf-Zr-O Ferroelectric Ultrathin Films Studied through Coercive Field Characteristics. *Jpn. J. Appl. Phys.* **2018**, 57, 04FB01.

[228] Kim, T.; Park, J.; Cheong, B. H.; Jeon, S. Effects of high pressure nitrogen annealing on ferroelectric $Hf_{0.5}Zr_{0.5}O_2$ films. *Appl. Phys. Lett.* **2018**, 112, 092906.

[229] Islamov, D. R.; Gritsenko, V. A.; Perevalov, T. V.; Pustovarov, V. A.; Orlov, O. M.; Chernikova, A. G.; Krasnikov, G. Y. Identification of the nature of traps involved in the field cycling of $Hf_{0.5}Zr_{0.5}O_2$-based ferroelectric thin films. *Acta Mater.* **2019**, 166, 47-55.

[230] Tagantsev, A. K.; Gerra, G. Interface-induced phenomena in polarization response of ferroelectric thin films. *J. Appl. Phys.* **2006**, 100(5), 051607.

[231] Hsieh, Y. H.; Xue, F.; Yang, T.; Liu, H. J.; Zhu, Y.; Chen, Y. C.; Chu, Y. H. Permanent ferroelectric retention of $BiFeO_3$ mesocrystal. *Nat. Comm.* **2016**, 7, 13199.

[232] Lyu, J.; Fina, I.; Solanas, R.; Fontcuberta, J.; Sánchez, F. Robust Ferroelectricity in Epitaxial $Hf_{1/2}Zr_{1/2}O_2$ Thin Films. *Appl. Phys. Lett.* **2018**, 113, 082902.

[233] Hyuk Park, M.; Joon Kim, H.; Jin Kim, Y.; Moon, T.; Seong Hwang, C. The

Effects of Crystallographic Orientation and Strain of Thin $Hf_{0.5}Zr_{0.5}O_2$ Film on its Ferroelectricity. *Appl. Phys. Lett.* **2014**, 104, 072901.
[234] Fengler, F.P.G.; Nigon, R.; Muralt, P.; Grimley, E.D.; Sang, X.; Sessi, V.; Hentschel, R.; LeBeau, J.M.; Mikolajick, T.; Schroeder, U. Analysis of Performance Instabilities of Hafnia-Based Ferroelectrics Using Modulus Spectroscopy and Thermally Stimulated Depolarization Currents. *Adv. Electron. Mater.* **2018**, 4, 1700547.
[235] Lyu, J.; Fina, I.; Solanas, R.; Fontcuberta, J.; Sanchez, F. The Growth Window of Ferroelectric Epitaxial $Hf_{0.5}Zr_{0.5}O_2$ Thin Films. *ACS Applied Electronic Materials.* **2019**.
[236] Scott, J. F.; Kammerdinger, L.; Parris, M.; Traynor, S.; Ottenbacher, V.; Shawabkeh, V.; Oliver, W. F. Switching Kinetics of Lead Zirconate Titanate Submicron Thin film Memories. *J. Appl. Phys.* **1988**, 64, 787-792.
[237] Yan, H.; Inam, F.; Viola, G.; Ning, H.; Zhang, H.; Jiang, Q.; Zeng, T.; Gao, Z.; Reece, M. J. The Contribution of Electrical Conductivity, Dielectric Permittivity and Domain Switching in Ferroelectric Hysteresis Loops. *J. Adv. Dielectrics* **2011**, 1, 107-118.
[238] Yoo, I. K.; Desu, S. B. Mechanism of fatigue in ferroelectric thin films. *Phys. Status Solidi A* **1992**, 133, 565-573.
[239] Kim, S. J.; Mohan, J.; Lee, J.; Lee, J. S.; Lucero, A. T.; Young, C. D.; Colombo, L.; Summerfelt, S. R.; San, T.; Kim, J. Effect of Film Thickness on the Ferroelectric and Dielectric Properties of Low-Temperature (400 °C) $Hf_{0.5}Zr_{0.5}O_2$ Films, *Appl. Phys. Lett.* **2018**, 112, 172902.
[240] Chernikova, A.; Kozodaev, M.; Markeev, A.; Matveev, Yu.; Negrov, D.; Orlov, O. Confinement-free Annealing Induced Ferroelectricity in $Hf_{0.5}Zr_{0.5}O_2$ Thin Films. *Microelectron. Eng.* 2015, 147, 15–18.
[241] Moalla, R.; Vilquin, B.; Saint-Girons, G.; Sebald, G.; Baboux, N.; Bachelet, R. Dramatic Effect of Thermal Expansion Mismatch on the Structural, Dielectric, Ferroelectric and Pyroelectric Properties of Low-Cost Epitaxial PZT Films on $SrTiO_3$ and Si. *CrystEngComm* **2016**, 18, 18871891.
[242] Park, M.; Kim, H.; Kim, Y.; Moon, T.; Kim, K.; Lee, Y.; Hyun, S.; Hwang, C. Study on the Internal Field and Conduction Mechanism of Atomic Layer Deposited Ferroelectric $Hf_{0.5}Zr_{0.5}O_2$ Thin Films. *J. Mater. Chem. C* **2015**, 3, 6291-6300.
[243] Lomenzo, P. D.; Takmeel, Q.; Moghaddam, S.; Nishida, T. Annealing Behavior of Ferroelectric Si-doped $HfO_2$ Thin Films. *Thin Solid Films* **2016**, 615, 139-144.
[244] Zhao, X.; Vanderbilt, D. First-principles study of structural, vibrational, and lattice dielectric properties of hafnium oxide. *Physical Review B* **2002**, 65, 233106.
[245] Watanabe, Y.; Ota, H.; Migita, S.; Kamimuta, Y.; Iwamoto, K.; Takahashi, M.; Toriumi, A. Achievement of Higher-k and High-Φ in Phase Controlled $HfO_2$ Film Using Post Gate Electrode Deposition Annealing. *ECS Transactions* **2007**, 11, 35-45.
[246] Adelmann, C.; Tielens, H.; Dewulf, D.; Hardy, A.; Pierreux, D.; Swerts, J.; Van Elshocht, S. Atomic Layer Deposition of Gd-Doped $HfO_2$ Thin Films. *J. Electrochem. Soc.* **2010**, 157, G105-G110.
[247] Colder, H.; Domengès, B.; Jorel, C.; Marie, P.; Boisserie, M.; Guillon, S.;

Méchin, L. Structural characterisation of $BaTiO_3$ thin films deposited on $SrRuO_3$/YSZ buffered silicon substrates and silicon microcantilevers. *J. Appl. Phys.* **2014**, 115(5), 053506.
[248] Kim, D. J.; Jo, J. Y.; Kim, Y. S.; Chang, Y. J.; Lee, J. S.; Yoon, J. G.; Noh, T. W. Polarization relaxation induced by a depolarization field in ultrathin ferroelectric $BaTiO_3$ capacitors. *Phys. Rev. Lett.* **2005**, 95(23), 237602.
[249] Jo, J. Y., Kim; D. J.; Kim, Y. S.; Choe, S. B.; Song, T. K.; Yoon, J. G.; Noh, T. W. Polarization switching dynamics governed by the thermodynamic nucleation process in ultrathin ferroelectric films. *Phys. Rev. Lett.* **2006**, 97(24), 247602.
[250] Ouyang, J.; Slusker, J.; Levin, I.; Kim, D. M.; Eom, C. B.; Ramesh, R.; Roytburd, A. L. Engineering of Self-Assembled Domain Architectures with Ultra-high Piezoelectric Response in Epitaxial Ferroelectric Films. *Adv. Funct. Mater.* **2007**, 17(13), 2094-2100.
[251] Mtebwa, M.; Feigl, L.; Yudin, P.; McGilly, L. J.; Shapovalov, K.; Tagantsev, A. K.; Setter, N. Room temperature concurrent formation of ultra-dense arrays of ferroelectric domain walls. *Appl. Phys. Lett.* **2015**, 107(14), 142903.
[252] Chopra, A.; Alexe, M.; Hesse, D. Fabrication and orientation control of highly cation-ordered epitaxial $PbSc_{0.5}Ta_{0.5}O_3$ thin films on Si(100). *J. Appl. Phys.* **2015**, 117(4), 044102.
[253] Scigaj, M.; Chao, C. H.; Gázquez, J.; Fina, I.; Moalla, R.; Saint-Girons, G.; Sánchez, F. High ferroelectric polarization in *c*-oriented $BaTiO_3$ epitaxial thin films on $SrTiO_3$/Si (001). *Appl. Phys. Lett.* **2016**, 109(12), 122903.